

Stratosphere-Troposphere Coupling and Oceanic Feedbacks in an Aquaplanet Model

Natasha Elise Trencham

Space and Atmospheric Physics Group, Department of Physics, Imperial College London

Submitted in part fulfillment of the requirements for the degree of Doctor of Philosophy in
Physics of Imperial College London and the Diploma of Imperial College London

Declaration

I hereby declare that the work contained within this thesis is my own, except where otherwise explicitly indicated.

The copyright of this thesis rests with the author. Unless otherwise indicated, its contents are licensed under a Creative Commons Attribution-Non Commercial 4.0 International Licence (CC BY-NC). Under this licence, you may copy and redistribute the material in any medium or format. You may also create and distribute modified versions of the work. This is on the condition that: you credit the author and do not use it, or any derivative works, for a commercial purpose. When reusing or sharing this work, ensure you make the licence terms clear to others by naming the licence and linking to the licence text. Where a work has been adapted, you should indicate that the work has been changed and describe those changes. Please seek permission from the copyright holder for uses of this work that are not included in this licence or permitted under UK Copyright Law.

Abstract

Since the 90's, there have been many studies looking at the impact of stratospheric temperature perturbations (STP's) on the troposphere below, and the mechanisms involved. However, it is not well-understood how these interactions might be modified by atmosphere-ocean coupling. This holds particular relevance to the study of e.g. ozone depletion/recovery in the Southern Ocean region.

To investigate this, abrupt uniform, polar, and equatorial STP's – corresponding to different types of forcings - were applied to the atmosphere of MITgcm in an aquaplanet, double-drake configuration. Each was conducted in three different versions of the model: atmosphere-only, atmosphere + slab-ocean, and fully-coupled atmosphere + ocean. In the atmosphere-only model, atmospheric responses similar to those of previous studies were recorded, underscoring their generic nature. In the coupled models, an initial weakening (\sim decades), and – in the fully-coupled model - subsequent strengthening and poleward-shift (\sim centuries) of the underlying atmospheric response was produced, in polar/equatorial heating experiments. Uniform heating saw the latter process occur initially too. Sea surface temperature (SST) anomalies were found to drive these changes, with extratropical/tropical anomalies controlling the former/latter process. These were in turn attributable to changes in the zonal winds, causing anomalies in the turbulent and ocean heat fluxes, although uniform STP's saw SST changes that were more controlled by large, near-uniform anomalous downwelling longwave fluxes.

Our results highlight the importance of incorporating atmosphere-ocean coupling when studying the effects of STP's, especially over longer timescales (\gtrsim 100 years). With respect to ozone depletion in the Southern Ocean, they suggest an amplified poleward jet shift which - as greenhouse gases continue to rise – may continue and amplify further into the 21st/22nd century.

Acknowledgments

First, I would like to extend my gratitude towards my supervisors Arnaud Czaja and Joanna Haigh, for their expert help and advice over the course of my PhD. I could not have wished for more supportive supervisors.

I also wish to extend my thanks to the many other students, postdocs, and members of staff in the atmospheric physics group, who have helped me in various ways over the course of my studies. Lastly, I wish also to acknowledge the support provided by my family and friends throughout this time, without which, none of this would have been possible.

Nomenclature

β	Rossby parameter ($\text{m}^{-1}\text{s}^{-1}$)
\mathbf{F}	Eliassen Palm flux vector (m^2s^{-2})
\mathcal{F}	Frictional acceleration (ms^{-2})
Ω	Rotation rate (s^{-1})
ω	Vertical (pressure) velocity (Pa s^{-1})
Φ	Geopotential height (m)
ϕ	Latitude angle
ψ	Eulerian mass streamfunction (kgs^{-1})
ρ	Density (kgm^{-3})
σ	Model pressure/height level number
σ_B	Eady growth rate (s^{-1})
τ	Optical depth / Surface wind stress (ms^{-2})
θ	Potential temperature (K)
$\tilde{\psi}$	TEM residual mass streamfunction (kgs^{-1})
\tilde{v}	TEM residual meridional velocity (ms^{-1})
\tilde{w}	TEM residual vertical velocity (ms^{-1})
f	Coriolis parameter (s^{-1})
g	Gravitational acceleration (ms^{-2})
N	Brunt-Vaisala frequency (s^{-1})
p	Pressure (Pa)

Q	Diabatic potential temperature tendency (Ks^{-1})
q	Specific humidity (kg/kg) or potential vorticity (s^{-1})
R	Earth radius (m)
R_d	Gas constant for dry air ($\text{Jkg}^{-1}\text{K}^{-1}$)
T	Temperature (K)
U	Zonal mass transport ($\text{kgm}^{-1}\text{s}^{-1}$)
u	Zonal velocity (ms^{-1})
u_s	Surface zonal wind (ms^{-1})
u_s^*	Surface wind speed (ms^{-1})
V	Meridional mass transport ($\text{kgm}^{-1}\text{s}^{-1}$)
v	Meridional velocity (ms^{-1})
V_S	Sverdrup meridional mass transport ($\text{kgm}^{-1}\text{s}^{-1}$)
v_s	Surface meridional wind (ms^{-1})
w	Vertical velocity (ms^{-1})
x	Longitude (m)
y	Latitude (m)
z	Height (m)
AAO	Antarctic Oscillation
AO	Arctic Oscillation
DJF	December, January and February
EOF	Empirical orthogonal function
EP	Eliassen-Palm
GCM	General Circulation Model
GHG	Greenhouse gas
LW	Longwave
NAO	North Atlantic Oscillation

NH Northern hemisphere

NWP Numerical weather prediction

PV Potential vorticity

S-T Stratosphere-Troposphere

SAM Southern Annular Mode

sGCM Simplified general circulation model

SH Southern hemisphere

SLP Sea level pressure

SST Sea surface temperature

SSW Sudden stratospheric warming

STP Stratospheric temperature perturbation

SW Shortwave

TOA Top-of-atmosphere

WBC Western Boundary Current

Contents

List of Figures	11
List of Tables	27
Introduction	29
1 Background	31
1.1 Stratosphere-Troposphere Coupling	31
1.1.1 Motivation	31
1.1.2 Phenomena	32
1.1.3 Modelling studies	35
1.2 Atmosphere-ocean coupling	40
1.2.1 Tropical atmosphere-ocean coupling	40
1.2.2 Midlatitudinal atmosphere-ocean coupling	44
1.3 Stratosphere-Troposphere-Ocean Interaction	50
1.3.1 Stratospheric impacts on the ocean	50
1.3.2 Oceanic feedbacks on atmosphere	52
1.4 Conclusions	53
2 Methodology	55
2.1 Atmospheric equations	55
2.1.1 Eddy-mean flow decomposition	55
2.1.2 Quasigeostrophic equations	56
2.1.3 The Transformed Eulerian Mean (TEM) and Eliasson-Palm Flux	58
2.2 Oceanic equations	60
2.2.1 Geostrophic and Ekman flow	60
2.2.2 Sverdrup balance	61
2.3 Aquaplanet climatology	62
2.4 The Model: MITgcm	65
2.4.1 Dynamical Core	65
2.4.2 Atmospheric Physics Parameterisations	67
2.4.3 Oceanic Physics Parameterisations	71

2.5	Model configuration	73
2.6	Control climatology	75
2.6.1	Atmosphere	75
2.6.2	Surface	78
2.6.3	Ocean	80
2.7	Experiments	85
3	Effect of stratosphere-troposphere coupling	87
3.1	Climatological changes	87
3.1.1	Eulerian mean fields	88
3.1.2	TEM circulation and EP fluxes	91
3.2	Drivers of climatological change	94
3.2.1	Thermal wind and heat budget	94
3.2.2	Forcing of the TEM circulation	99
3.2.3	Eliassen-Palm fluxes	99
3.2.4	Meridional potential vorticity gradient	106
3.2.5	Equilibrium response: Conclusions	107
3.3	Temporal response	108
3.3.1	Experiment U01	108
3.3.2	Experiments P01 and T01	115
3.4	Chapter Conclusions	118
4	SST change and drivers	121
4.1	SST time-evolution and drivers: Slab-ocean setup	121
4.1.1	Global mean SST and surface fluxes time-evolution	122
4.1.2	Local SST changes and drivers	125
4.1.3	Drivers of turbulent heat flux anomalies	132
4.1.4	Summary & main conclusions	136
4.2	SST time-evolution and drivers: Fully-coupled setup	137
4.2.1	Global mean SST and surface fluxes time-evolution	137
4.2.2	Zonal mean SST time-evolution	142
4.2.3	Changes in pseudo-mixed layer heat content	144
4.2.4	Ocean circulation changes	150
4.2.5	Changes in vertical temperature structure	155
4.2.6	Summary & main conclusions	159
4.3	SST change: Fully-Coupled vs Slab-Ocean Setups	160
4.3.1	Differences in SST anomalies	160
4.3.2	Drivers of SST differences	164
4.4	Main conclusions	166
5	Effect of atmosphere-ocean coupling	168

5.1	Model hierarchy results comparison	168
5.2	SST perturbation experiments	176
5.3	U01-QFLUX SST experiment	182
5.3.1	Momentum budget	184
5.3.2	Heat budget	189
5.4	P01-QFLUX SST experiment	194
5.5	Chapter Conclusions	200
6	Conclusions & Future Work	204
6.1	Summary & Conclusions	204
6.2	Applications	209
6.3	Limitations	210
6.4	Future Work	212
	Bibliography	214
A	Atmospheric equations	226
A.1	Equations of motion	226
A.2	Geostrophic wind	227
A.3	Relationships between PV meridional gradient & EP flux divergence	227
B	Oceanic equations	229
B.1	Fundamental equations	229
C	Third-party works & permissions	231

List of Figures

1.1.1	Composite of differences in SAM index between the weak and strong stratospheric events in the period 1987-2002. Day 0 corresponds to the onset of stratospheric event, and red/blue contours correspond to positive/negative SAM values, i.e. stronger/weaker-than-normal zonal flow along 60°S. Figure taken from Thompson et al. (2005). © American Meteorological Society. Used with permission.	32
1.1.2	Control values (contours) and anomalies (colours) in SH summertime (DJF) mass streamfunction (left) and zonal winds (right), based upon 50-year integrated model response to year 2000 (vs. 1960) ozone concentrations. Figures adapted from Polvani et al. (2011). © American Meteorological Society. Used with permission.	34
1.1.3	Response of model atmosphere in Haigh et al. (2005) to applied STP's, applied (a) throughout the model stratosphere (U5; top panel), and (b) preferentially to the tropical stratosphere (E5; bottom panel). Figures display, from left-to-right: (i) zonal wind anomalies (ms^{-1} , left panels), (ii) mass streamfunction anomalies (10^{10}kgs^{-1} , middle panels), and (iii) anomalous poleward fluxes of westerly momentum by the eddies, $[u^*v^*]$ (m^2s^{-2} , right panels). Figures adapted from Haigh et al. (2005). © American Meteorological Society. Used with permission.	36
1.1.4	Proposed mechanism whereby STP's can cause alterations to the tropospheric mean zonal winds and circulation. Taken from Simpson et al. (2009). © American Meteorological Society. Used with permission.	39
1.2.1	Schematic of equatorial flow patterns along equatorial Pacific with typical (top; normal conditions) and weaker than average surface westerlies (bottom; El Niño conditions). Figure taken from Bjerknes (1966).	41
1.2.2	Schematic showing the direct, linear atmospheric response to low-level heating in the tropics (left) and midlatitudes (right) on a latitude-height plane. Arrows indicate the direction of vertical motions, and circled dots/crosses motion that is out of/into the section (i.e. westerly/easterly) respectively. Figure adapted from Hoskins & Karoly (1981). © American Meteorological Society. Used with permission.	42

1.2.3	Schematic showing how a strengthened Hadley circulation in the tropics can lead to an enhanced subtropical jet with greater vertical shear, and therein to increased baroclinicity in that region. This leads to enhanced potential vorticity mixing, and poleward heat transport by baroclinic eddies. Figure taken from Hou (1998). © American Meteorological Society. Used with permission.	43
1.2.4	The atmospheric response to shallow heating in a linear, quasigeostrophic model with a westerly, baroclinic jet at its centre. The heating is centered at 180° , and decays exponentially with height. Colours and contours correspond to temperature and geopotential height anomalies respectively. Figure adapted from Kushnir et al. (2002). © American Meteorological Society. Used with permission.	46
1.2.5	Schematic showing the relative strengths of the polar front jet (PFJ), subtropical jet (STJ), and storm tracks (dashed rectangles), under conditions of weakened (left) and strengthened (right) Hadley circulations. Wavy-arrows show the dispersion of wave-activity from polar front to subtropical jet, and open arrows show the transport of westerly momentum by eddies, maintaining the surface westerlies (W), which stay anchored to the subarctic frontal zone (SAFZ). Figure taken from Nakamura et al. (2004).	47
1.2.6	Top panels: SST's (contours, 2°C intervals and dashed contours for 10°C and 20°C) and 10m wind convergence (colours) from: (a) satellite observations, and (b) the ECMWF reanalysis data. Bottom panels: SST's (contours, same spacing) and, from the ECMWF reanalysis data (colours): (c) SLP laplacian, (d) and sign-reversed SST laplacian. Figure taken from Minobe et al. (2008).	49
1.3.1	Schematic illustrating the fast (left) and slow (right) modelled oceanic responses to a poleward-shift in the midlatitude jet, caused by a step-change in ozone-depletion. Black arrows denote anomalous ocean currents. Red (blue) arrows denote heat fluxes in (out) of the surface mixed layer. Blue patches represent the sea ice cover. Figure taken from Ferreira et al. (2015). © American Meteorological Society. Used with permission.	51
2.3.1	Multi-model mean fields, from the APE FLAT SST experiment. From left-to-right, top-to-bottom: (a) zonal wind (top-left), (b) meridional wind (top-middle), (c) vertical wind (top-right), (d) temperature (bottom-left), (e) absolute humidity (bottom-middle), and (f) relative humidity (bottom-right). Figures adapted from chapter 5 of Williamson et al. (2012).	63
2.3.2	Multi-model mean transient eddies, from the APE FLAT SST experiment: (a) $\overline{u'v'}$ eddies (left panel), and (b) $\overline{v'\theta'}$ eddies (right panel) Figures adapted from chapter 5 of Williamson et al. (2012).	64

2.4.1	Schematic of how the MITgcm hydrodynamical kernel and physics packages combine to form distinct atmospheric and oceanic models. Figure taken from the MITgcm user manual (Adcroft et al. 2018), available online at www.mitgcm.org	65
2.4.2	Instantaneous 3D plot of an atmospheric temperature field at 500hPa from MITgcm, illustrating the cubed-sphere grid used by the model. Figure taken from the MITgcm user manual (Adcroft et al. 2018), available online at www.mitgcm.org	66
2.4.3	Schematic of a single grid cell in the MITgcm, and the relative points at which zonal, meridional, and vertical velocities are defined.	67
2.5.1	3D cube-sphere aquaplanet ocean model, with double-drake ridges highlighted in yellow. Adapted from a figure on John Marshall's personal webpages at www.oceans.mit.edu	74
2.6.1	300-year mean climatological fields from control fully-coupled atmosphere-ocean run. From left-to-right, top-to-bottom: (a) zonal wind (top-left), (b) mass streamfunction (top-middle), (c) vertical wind (top-right), (d) temperature (bottom-left), (e) absolute humidity (bottom-middle), and (f) relative humidity (bottom-right).	76
2.6.2	300-year mean climatological fields from control fully-coupled atmosphere-ocean run. From left-to-right, top-to-bottom: (a) meridional westerly eddy momentum fluxes, $[\overline{uv}]_{eddy}$ (top-left), (b) meridional potential temperature eddy fluxes, $[\overline{v\theta}]_{eddy}$ (top-middle), (c) TEM residual mass streamfunction, $\tilde{\psi}$ (top-right), (d) EP fluxes (arrows) and divergences (colours) (bottom-left), (e) diabatic potential temperature tendencies (bottom-middle), and (f) advective potential temperature tendencies (bottom-right). In the EP flux diagram, the fluxes are mass-weighted as per equations (2.1.32) and (2.1.33), the contour intervals are $1.5 \times 10^{16} \text{m}^3$, and the arrows are scaled such that the horizontal and vertical arrows in the top-left have lengths $5 \times 10^{14} \text{m}^3$ and $5 \times 10^{20} \text{m}^3 \text{Pa}$ respectively.	77
2.6.3	300-year mean surface climatological fields from control fully-coupled atmosphere-ocean run. From left-to-right, top-to-bottom: (a) precipitation (top-left), (b) net heat fluxes (radiative + turbulent heat fluxes) (top-middle), (c) radiative fluxes (LW + SW fluxes) (top-right), (d) turbulent heat fluxes (sensible + latent heat fluxes) (bottom-left), (e) zonal wind stress (bottom-middle), and (f) meridional wind stress (bottom-right). The surface fluxes and stresses are positive downward (from the atmosphere, into the ocean).	79

2.6.4	300-year mean oceanic climatological fields from control fully-coupled atmosphere-ocean run. From left-to-right, top-to-bottom: (a) sea surface temperature (top-left), (b) salinity at 16m (top-middle), (c) barotropic streamfunction (top-right), (d) zonal velocity at 16m (positive eastward; bottom-left), (e) meridional velocity at 16m (positive northward; bottom-middle), and (f) vertical velocity at 32m (positive downward; bottom-right).	81
2.6.5	300-year mean oceanic climatological fields from control fully-coupled atmosphere-ocean run. From left-to-right: (a) potential temperature (left panels), (b) salinity (middle panels), and (c) meridional velocity (positive northward; right panels). Top/bottom panels correspond to values zonally-averaged over the large (0° to 90°W)/small basins (90°W to 0°) respectively.	82
2.6.6	300-year mean oceanic mixed-layer depths - absolute (left), and sigma-level (right) - from control fully-coupled atmosphere-ocean run. Contour level spacing is set at 20m/1 for the left/right plot.	84
2.6.7	300-year mean oceanic potential temperature tendencies from control fully-coupled atmosphere-ocean run due to ocean heat: (a) advection (left), and (b) diffusion (right), both vertically-integrated over the top 144m ($\int_{-144m}^0 \rho c_p \dot{\theta} dz$). Contour intervals are set to 5Wm^{-2}	85
2.7.1	Atmospheric lapse rates, $\Gamma = -dT/dz$ (colours; interval = 1K/km), and diagnosed stratosphere (black crosses), based upon 300-year mean temperature values from the fully-coupled atmosphere-ocean model control run.	86
3.1.1	Control values (contours), and anomalies (colours), in zonal-average (a) zonal wind (top panel), and (b) mass streamfunction (bottom panel) in (left-to-right): (i) U01 (left panels), (ii) P01 (middle panels) and (iii) T01 (right panels) experiments, averaged over years 1-5. Hatching indicates regions in which the confidence levels in the experiment vs control values are below 95%, as measured by a two-tail student's t-test.	89
3.1.2	Changes in (left-to-right): (a) maximum polar vortex (vor) and midlatitude jet (jet) strength (left); (b) maximum tropical Hadley (had) and Ferrel cell (fer) strength (middle); (c) maximum residual circulation strength in the tropics (trop) and extratropics (etrop) (right), in U01, P01 and T01 experiments, averaged over years 1-5.	90

3.1.3	Control values (contours), and anomalies (colours), in zonal-average (a) TEM residual mass streamfunction (top panel), and (b) EP flux divergence (anomalies = colours; contours = control values) and EP fluxes (vectors) (bottom panel) in (left-to-right): (i) U01 (left panels), (ii) P01 (middle panels) and (iii) T01 (right panels) experiments, averaged over years 1-5. Hatching in the top panels indicates regions in which the confidence levels in the experiment vs control values are below 95%, as measured by a two-tail student's t-test. In the EP flux diagram, the fluxes are mass-weighted as per equations (2.1.32) and (2.1.33), the EP flux divergences are in units of 10^{15}m^3 , and the arrows are scaled such that the horizontal and vertical arrows in the top-left have lengths $5 \times 10^{13}\text{m}^3$ and $5 \times 10^{19}\text{m}^3\text{Pa}$ respectively.	92
3.2.1	Control values (contours), and anomalies (colours), in zonal-average geostrophic wind in experiments (i) P01 (left-panel), and (ii) T01 (right panel), averaged over years 1-5. Hatching indicates regions in which the confidence levels in the experiment vs control values are below 95%, as measured by a two-tail student's t-test.	95
3.2.2	Control values (contours), and anomalies (colours), in zonal-average: (a) potential temperature (left panels), (b) diabatic potential temperature tendencies (middle panels), and (c) advective potential temperature tendencies (right panels), in experiments (i) P01 (top panels), and (ii) T01 (bottom panels), averaged over years 1-5. Hatching indicates regions in which the confidence levels in the experiment vs control values are below 95%, as measured by a two-tail student's t-test.	96
3.2.3	Control values (contours), and anomalies (colours), in zonal-average radiative potential temperature tendencies in experiments (i) P01 (left panel), and (ii) T01 (right panel), averaged over years 1-5. Hatching indicates regions in which the confidence levels in the experiment vs control values are below 95%, as measured by a two-tail student's t-test.	97
3.2.4	Control values of the total potential temperature heating rate by TEM residual circulation, $-\tilde{\omega}\partial_p[\theta]$ (contours), and anomalies (colours) caused by changes in the: (a) total heating rate, $\Delta(-\tilde{\omega}\partial_p[\theta])$ (left panels), (b) residual circulation, $-(\Delta\tilde{\omega})\partial_p[\theta]$ (middle panels), and (c) potential temperature gradient, $-\tilde{\omega}\Delta(\partial_p[\theta])$ (right panels), in experiments (i) P01 (top panels) and (ii) T01 (bottom panels), averaged over years 1-5.	98

3.2.5	Control values of TEM residual streamfunction, $\tilde{\psi}$ (contours), and anomalies (colours) in zonal-average $\tilde{\psi}$ curvature due to changes in (top-to-bottom, left-to-right): (a) vertical + meridional components (LHS of equation (2.1.27); top-left panel), (b) vertical component only (1st term on LHS of equation (2.1.27); top-right panel), (c) EP flux divergence, $\nabla \cdot \mathbf{F}$ (3rd term on RHS of equation (2.1.27); bottom-left panel), and (d) friction, \mathcal{F}_λ (2nd term on RHS of equation (2.1.27); bottom-right panel), in experiment P01, averaged over years 1-5.	100
3.2.6	Control values (contours) and anomalies (colours) of horizontal EP flux divergence, $\partial_y F^y$, in experiments (i) P01 (left panel), and (ii) T01 (right panel), averaged over years 1-5.	101
3.2.7	Control values of vertical EP flux divergences, $\partial_p F^p$ (contours), and their anomalies (colours) due to changes in: (a) total vertical EP flux divergence, $\Delta \partial_p F^p$ (left panels), (b) poleward eddy heat fluxes, $\Delta [v^* \theta^*]$ (middle panels), and (c) vertical potential temperature gradient, $\Delta \partial_p [\theta]$ (right panels), in experiments (i) P01 (top panels), and (ii) T01 (bottom panels), averaged over years 1-5.	102
3.2.8	Control values (contours) and anomalies (colours) in meridional potential vorticity gradient, q_ϕ , due to changes in: (a) total meridional PV gradient, Δq_ϕ (left panels), (b) the meridional component, $\Delta q_{\phi,y}$ (2nd component of equation(2.1.28); middle panels), and (c) the vertical component, $\Delta q_{\phi,p}$ (3rd component of equation (2.1.28); right panels), in experiments (i) P01 (top panels), and (ii) T01 (bottom panels), averaged over years 1-5.	104
3.2.9	Control values (contours) and anomalies (colours) in vertical component of meridional PV gradient, $q_{\phi,p}$, due to changes in: (a) zonal wind vertical gradient, $\Delta \partial_p u$ (left panels), and (b) potential temperature vertical gradient, $\Delta \partial_p \theta$ (right panels), in experiments (i) P01 (top panels), and (ii) T01 (bottom panels), averaged over years 1-5.	105
3.2.10	Schematic of the interaction between the mean fields and eddies in the equilibrated model.	108
3.3.1	Control values (contours), and anomalies (colours), in zonal-average (a) zonal wind (top panel), and (b) mass streamfunction (bottom panel) in U01 experiment, averaged over days (left-to-right): (i) 0-10 (left panels), (ii) 11-20 (middle panels) and (iii) 21-30 (right panels).	109

- 3.3.2 Changes in EP fluxes (arrows) divergences (colours) in U01 experiment, averaged over days (left-to-right): (i) 0-10 (left panels), (ii) 11-20 (middle panels) and (iii) 21-30 (right panels). Control values of EP flux divergences are shown as contours. In the EP flux diagram, the fluxes are mass-weighted as per equations (2.1.32) and (2.1.33), the EP flux divergences are in units of 10^{15}m^3 , and the arrows are scaled such that the horizontal and vertical arrows in the top-left have lengths $5 \times 10^{13}\text{m}^3$ and $5 \times 10^{19}\text{m}^3\text{Pa}$ respectively. 110
- 3.3.3 Control values (contours), and anomalies (colours), in zonally- and hemispherically-averaged (a) zonal wind (top panels), and (b) potential temperature (bottom panels), 340hPa to 20hPa, in U01 experiment, averaged over days (left-to-right): (i) 0-5 (left panels), (ii) 6-10 (middle panels) and (iii) 11-15 (right panels). 111
- 3.3.4 Control values (contours), and anomalies (colours) in zonally- and hemispherically-averaged (a) EP flux divergences, $\nabla \cdot \mathbf{F}$ (top panels), and (b) meridional potential vorticity gradient, q_ϕ (bottom panels), 340hPa to 60hPa, in U01 experiment, averaged over days (left-to-right): (i) 0-5 (left panels), (ii) 6-10 (middle panels) and (iii) 11-15 (right panels). Arrows correspond to anomalous EP fluxes, $\Delta \mathbf{F}$. In the EP flux diagram, the fluxes are mass-weighted as per equations (2.1.32) and (2.1.33), the EP flux divergences are in units of 10^{15}m^3 , and the arrows are scaled such that the horizontal and vertical arrows in the top-left have lengths 10^{13}m^3 and $10^{19}\text{m}^3\text{Pa}$ respectively. 112
- 3.3.5 Control values (contours), and anomalies (colours), in zonally- and hemispherically-averaged (a) vertical EP flux divergence, $\frac{dF^p}{dp}$ (top panels), and (b) vertical component of meridional PV gradient, $q_{\phi,p}$ (bottom panels), 340hPa to 60/20hPa, in U01 experiment, averaged over days 0-10. Left-to-right, panels correspond to the: (i) total values (left panels), (ii) contributions due to changes in poleward eddy heat fluxes, $\Delta[v^*\theta^*]$ (top-middle)/vertical zonal wind gradient, $\Delta\partial_p u$ (bottom-middle), and (iii) contributions due to changes in vertical potential temperature gradient, $\Delta\partial_p\theta$ (right panels). 113
- 3.3.6 For experiment P01, averaged over days 0-10, changes in: (a) zonal wind (top-left), (b) EP fluxes (arrows) and divergences (colours) (top-middle), (c) EP fluxes (arrows) and meridional PV gradient (colours) (top-right), (d) potential temperature (bottom-left), (e) vertical EP flux divergence (bottom-middle), and (f) vertical component of meridional PV gradient (bottom-right). All values are zonally- and hemispherically-averaged, and contours/colours indicate control values/anomalies. In the EP flux diagram, the fluxes are mass-weighted as per equations (2.1.32) and (2.1.33), the EP flux divergences are in units of 10^{15}m^3 , and the arrows are scaled such that the horizontal and vertical arrows in the top-left have lengths 10^{13}m^3 and $10^{19}\text{m}^3\text{Pa}$ respectively. 116

3.3.7	For experiment T01, averaged over days 0-10, changes in: (a) zonal wind (top-left), (b) EP fluxes (arrows) and divergences (colours) (top-middle), (c) EP fluxes (arrows) and meridional PV gradient (colours) (top-right), (d) potential temperature (bottom-left), (e) vertical EP flux divergence (bottom-middle), and (f) vertical component of meridional PV gradient (bottom-right). All values are zonally- and hemispherically-averaged, and contours/colours indicate control values/anomalies. In the EP flux diagram, the fluxes are mass-weighted as per equations (2.1.32) and (2.1.33), the EP flux divergences are in units of 10^{15}m^3 , and the arrows are scaled such that the horizontal and vertical arrows in the top-left have lengths 10^{13}m^3 and $10^{19}\text{m}^3\text{Pa}$ respectively.	117
3.4.1	Schematic showing mechanism whereby downward propagation of easterly zonal wind anomalies (circled crosses) and simultaneous induction of westerly anomalies on its equatorward flank (circled dot) may be achieved. Arrows show the directions of anomalous EP flux components. Mechanism is depicted for the Southern Hemisphere, with approximate latitudes of the zonal wind anomalies indicated along the (horizontal) latitude axis.	119
4.1.1	Time-evolution of global-average 360-day running mean (a) sea surface temperatures (top panels), and (b) anomalous surface heat fluxes and its radiative and turbulent heat flux components (bottom panels), positive upward, for experiments (left-to-right): (i) U01 (left panels), (ii) P01 (middle panels), and (iii) T01 (right panels), in slab-ocean double-drake set-up.	123
4.1.2	Time-evolution of global-average 360-day running mean anomalous (a) turbulent surface fluxes (top panels), and (b) radiative surface fluxes (bottom panels), positive upwards, for experiments (left-to-right): (i) U01 (left panels), (ii) P01 (middle panels), and (iii) T01 (right panels), in slab-ocean double-drake set-up.	124
4.1.3	(a) (Top panels) Changes in zonal-mean sea surface temperatures in slab-ocean setup, averaged over years 0-5 (red), 5-10 (green), and 10-25 (blue), and (b) (bottom panels) time-evolution of control values (contours) and anomalies (colours) in zonal-average sea surface temperatures, in experiments (left-to-right): (i) U01 (left panels), (ii) P01 (middle panels), and (iii) T01 (right panels).	126
4.1.4	Control values (contours) and anomalies (colours) in (a) sea surface temperatures (top panels), and (b) net surface heat fluxes (bottom panels), positive upwards, averaged over years 0-10, for experiments: (i) U01 (left panels), (ii) P01 (middle panels), and (iii) T01 (right panels), in slab-ocean double-drake set-up. Hatching in the top panels indicates regions in which the confidence levels in the experiment vs control values are below 95%, as measured by a two-tail student's t-test.	128

4.1.5	Control values (contours) and anomalies (colours) in surface (a) turbulent heat fluxes (top panels), and (b) radiative fluxes (bottom panels), positive upwards, averaged over years 0-10, for experiments: (i) U01 (left panels), (ii) P01 (middle panels), and (iii) T01 (right panels), in slab-ocean double-drake set-up.	129
4.1.6	Control values (contours) and anomalies (colours) in surface (a) sensible heat fluxes (top panels), and (b) latent heat fluxes (bottom panels), positive upwards, averaged over years 0-10, for experiments: (i) U01 (left panels), (ii) P01 (middle panels), and (iii) T01 (right panels), in slab-ocean double-drake set-up.	130
4.1.7	Control values (contours) and anomalies (colours) in surface longwave fluxes: (a) downward LW fluxes (top panels), and (b) upward LW fluxes (bottom panels), positive upwards, averaged over years 0-10, for experiments: (i) U01 (left panels), (ii) P01 (middle panels), and (iii) T01 (right panels), in slab-ocean double-drake set-up.	131
4.1.8	Control values (contours) and anomalies (colours) of surface wind times: (a) surface humidity difference, $u_s^*(q_{sat} - q_s)$ (top panels), and (b) surface temperature difference, $u_s^*(SST - T_s)$ (bottom panels), averaged over years 0-10 of experiment P01 in slab-ocean double-drake setup. From left-to-right, the anomalies in the panels give the (i) total anomaly, $\Delta(u_s^*(X_{sea} - X_{air}))$ (left panels), (ii) anomaly due to changes in surface wind, $(\Delta u_s^*)(X_{sea} - X_s)$ (middle panels), and (iii) anomaly due to changes in surface temperature/humidity difference, $u_s^*(\Delta(X_{sea} - X_s))$ (right panels).	133
4.1.9	Control values (contours) and anomalies (colours) in surface wind squared: (a) total, $u^2 + v^2$ (left) and (b) zonal, u^2 (right), averaged over years 0-10 of experiment P01 in slab-ocean double-drake set-up.	134
4.1.10	Time-evolution of global-average latent (top panels)/sensible (bottom panels) heat flux anomalies (black lines), and global-average surface wind times: (a) surface temperature difference, $u_s^*(SST - T_s)$ (top panels), and (b) surface humidity difference, $u_s^*(q_{sat} - q_s)$ (bottom panels) anomalies (blue lines), in experiments (i) U01 (left panels), (ii) P01 (middle panels), and (iii) T01 (right panels), in slab-ocean double-drake setup.	135
4.2.1	Time-evolution of global-average (a) sea surface temperatures (top panels), and (b) surface heat flux anomalies (black), and its radiative (blue) and turbulent heat (red) flux components (bottom panels), for experiments (left-to-right): (i) U01 (left panels), (ii) P01 (middle panels), and (iii) T01 (right panels), in fully-coupled double-drake set-up.	138

4.2.2	Time-evolution of global-average anomalous (a) turbulent surface fluxes (top panels), and (b) radiative surface fluxes (bottom panels), positive upwards, for experiments (left-to-right): (i) U01 (left panels), (ii) P01 (middle panels), and (iii) T01 (right panels), in fully-coupled double-drake set-up.	139
4.2.3	(a) (Top panels) Changes in zonal-mean sea surface temperatures in fully-coupled setup, averaged over years 0-25 (red), 125-150 (green), and 250-275 (blue), and (b) (bottom panels) time-evolution of control values (contours) and anomalies (colours) in zonal-average sea surface temperatures, in experiments (left-to-right): (i) U01 (left panels), (ii) P01 (middle panels), and (iii) T01 (right panels). Errorbars in the top panel are based upon the standard deviations of the ensemble-mean values, calculated along the time dimension.	143
4.2.4	Control values (contours) and anomalies (colours) in vertically-integrated (0-144m): (a) heat content, averaged over years 250-300 (left panels), (b) net surface heat fluxes, averaged over years 0-300 (middle panels), and (c) net advective + diffusive fluxes, averaged over years 0-300 (right panels), (positive = warming), in experiments: (i) P01 (top panels), and (ii) T01 (bottom panels) in fully-coupled double-drake setup. Hatching in the left panels indicates regions in which the confidence levels in the experiment vs control values are below 95%, as measured by a two-tail student's t-test.	145
4.2.5	Control values (contours) and anomalies (colours) in total vertically-integrated (0-144m): (a) net surface heat fluxes (radiative + turbulent) (top-left), (b) radiative heat fluxes (top-middle), (c) turbulent heat fluxes (top-right), (d) net ocean heat transport fluxes (advective + diffusive) (bottom-left), (e) advective heat fluxes (bottom-middle), and (f) diffusive heat fluxes (bottom-right), (positive = warming), averaged over years 0-300 of experiment P01 in fully-coupled setup.	146
4.2.6	Control values (contours) and anomalies (colours) in total vertically-integrated (0-144m) surface heat fluxes: (a) net longwave (left), and (b) sensible heat (right), (positive = warming), averaged over years 0-300 of experiment P01 in fully-coupled double-drake set-up.	147
4.2.7	Control values of advective heat fluxes (contours), and anomalies in mean flow advective heat fluxes, $-\bar{\mathbf{u}} \cdot \nabla \bar{\theta}$ (colours) due to changes in: (a) total, $-\Delta(\bar{\mathbf{u}} \cdot \nabla \bar{\theta})$, (top-left), (b) horizontal advection, $\Delta(-\bar{u}\partial_x\bar{\theta} - \bar{v}\partial_y\bar{\theta})$ (top-middle), (c) vertical advection, $-\Delta\bar{w}\partial_z\bar{\theta}$ (top-right), (d) mean flow, $-(\Delta\bar{\mathbf{u}}) \cdot \nabla \bar{\theta}$ (bottom-left), (e) potential temperatures, $-\bar{\mathbf{u}} \cdot \Delta(\nabla \bar{\theta})$ (bottom-middle), and (f) mean flow and potential temperatures, $-(\Delta\bar{\mathbf{u}}) \cdot \Delta(\nabla \bar{\theta})$ (bottom-right), (positive = warming), averaged over years 0-300 of P01 in fully-coupled setup.	148

- 4.2.8 Control values (contours) and anomalies (colours) in: (a) vertically-integrated (0-144m) meridional mass transport, $V = \int_{-144m}^0 \rho v dz$ (positive northward; left panels), (b) vertically-integrated (0-144m) zonal mass transport, $U = \int_{-144m}^0 \rho u dz$ (positive eastward; middle panels), and (c) vertical velocities at $z=-144m$ (positive upward; right panels), for experiments (i) P01 (top panels), and (ii) T01 (bottom panels), averaged over years 0-300 of fully-coupled setup. Hatching indicates regions in which the confidence levels in the experiment vs control values are below 95%, as measured by a two-tail student's t-test. . 151
- 4.2.9 Control values (contours) and anomalies (colours) in vertically-integrated (0-144m): (a) meridional mass transport, $V = \int_{-144m}^0 \rho v dz$ (positive northward; top panels), and (b) zonal mass transport, $U = \int_{-144m}^0 \rho u dz$ (positive eastward; bottom panels), driven by changes in the: (i) Ekman + geostrophic flows, $\mathbf{u_E} + \mathbf{u_G}$ (left panels), (ii) geostrophic flows only, $\mathbf{u_G}$ (middle panels), and (iii) Ekman flows only, $\mathbf{u_E}$ (right panels), averaged over years 0-300 of experiment P01 in fully-coupled setup. Hatching in the top-right panel indicates regions in which the confidence levels in the experiment vs control values are below 95%, as measured by a two-tail student's t-test. 152
- 4.2.10 Control values (contours) and anomalies (colours) in the geostrophic vertical velocities, w_G , at depth: (a) $z=-144m$ (left panel), and (b) $z=0m$ (right panel), averaged over years 0-300 of experiment P01 in fully-coupled setup. . 153
- 4.2.11 Control values (contours) and anomalies (colours) in the total column-integrated meridional mass transport, $V = \int_{-3400m}^0 \rho v dz$ (positive northward), calculated from the: (a) Sverdrup mass balance (equation (2.2.7); left panel), and (b) Eulerian mean fields (right panel), averaged over years 0-300 of experiment P01 in fully-coupled setup. Hatching indicates regions in which the confidence levels in the experiment vs control values are below 95%, as measured by a two-tail student's t-test. 154
- 4.2.12 Control values (contours) and anomalies (colours) in zonal-mean oceanic potential temperature, averaged over years: (a) 0-10 (top panels), and (b) 250-300 (bottom panels), for experiments: (i) U01 (left panels), (ii) P01 (middle panels), and (iii) T01 (right panels). 156
- 4.2.13 Control values of potential temperature (contours), and anomalies (colours) in zonal-mean oceanic stationary-mean advective potential temperature tendency, $-\bar{\mathbf{u}} \cdot \nabla \bar{\theta}$, due to changes: (a) total, $-\Delta(\bar{\mathbf{u}} \cdot \nabla \bar{\theta})$, (top-left), (b) meridional advection, $-\Delta \bar{v} \partial_y \bar{\theta}$ (top-middle), (c) vertical advection, $-\Delta \bar{w} \partial_z \bar{\theta}$ (top-right), (d) mean flow, $-(\Delta \bar{\mathbf{u}}) \cdot \nabla \bar{\theta}$ (bottom-left), (e) potential temperatures, $-\bar{\mathbf{u}} \cdot \Delta(\nabla \bar{\theta})$ (bottom-middle), and (f) mean flow and potential temperatures, $-(\Delta \bar{\mathbf{u}}) \cdot \Delta(\nabla \bar{\theta})$ (bottom-right), (positive = warming), averaged over years 0-300 of P01 in fully-coupled setup. 157

4.3.1	(a) (Top panel) Absolute changes in zonal-mean sea surface temperatures in slab-ocean setup years 0-50 (red line) and fully-coupled setup years 0-50 (green line) and 250-300 (blue line). (b) (Bottom panel) Difference in zonal-mean sea surface temperature anomalies between fully-coupled setup years 0-50/250-300 (green/blue line) and slab-ocean setup years 0-50. Shown for experiments (left-to-right): (i) U01 (left panels), (ii) P01 (middle panels) and (iii) T01 (right panels). Errorbars plotted are based on standard deviations of the ensemble-average SST anomalies, calculated along time dimension.	161
4.3.2	Control values (contours) and anomalies (colours) in sea surface temperatures, averaged over first 50 years, in setups (a) slab-ocean (top panel) and (b) fully-coupled (bottom panel), for experiments (left-to-right): (i) U01 (left panels), (ii) P01 (middle panels), and (iii) T01 (right panels).	162
4.3.3	Schematic showing the main drivers of SST changes seen in the slab-ocean (left) and fully-coupled setup (right), in different regions of the global ocean (DLR = downward longwave radiation; THF = turbulent heat fluxes; OHF = ocean heat fluxes).	164
5.1.1	Changes (colours) in (a) zonal wind (top panel) and (b) mass streamfunction (bottom panel) anomalies in (left-to-right): (i) U01 (left panels), (ii) P01 (middle panels) and (iii) T01 (right panels), in slab-ocean setup years 0-50 vs atmosphere-only setup years 0-30. Contours display the control values in the atmosphere-only setup. Hatching indicates regions in which the confidence levels in the coupled anomalies vs uncoupled anomalies are below 95%, as measured by a two-tail student's t-test.	169
5.1.2	Changes (colours) in (a) zonal wind (top panel) and (b) mass streamfunction (bottom panel) anomalies in (left-to-right): (i) U01 (left panels), (ii) P01 (middle panels) and (iii) T01 (right panels), in fully-coupled setup years 0-50 vs atmosphere-only setup years 0-30. Contours display the control values in the atmosphere-only setup. Hatching indicates regions in which the confidence levels in the coupled anomalies vs uncoupled anomalies are below 95%, as measured by a two-tail student's t-test.	170
5.1.3	Changes (colours) in (a) zonal wind (top panel) and (b) mass streamfunction (bottom panel) anomalies in (left-to-right): (i) U01 (left panels), (ii) P01 (middle panels) and (iii) T01 (right panels) experiments, in fully-coupled setup years 250-300 vs atmosphere-only setup years 0-30. Contours display the control values in the atmosphere-only setup. Hatching indicates regions in which the confidence levels in the coupled anomalies vs uncoupled anomalies are below 95%, as measured by a two-tail student's t-test.	171

5.1.4	Changes in (a) maximum polar vortex (vor) and midlatitude jet (jet) strength (top panel), and (b) maximum tropical Hadley (had) and Ferrel cell (fer) strength (bottom panel) in (left-to-right): (i) U01 (left panels), (ii) P01 (middle panels) and (iii) T01 (right panels) experiments, in atmosphere-only (sst), slab-ocean (qflux), and fully-coupled (cpl) setups, averaged over years indicated (yX-Y).	172
5.2.1	Sea surface temperature anomalies used in SST perturbation experiments, derived from SST changes in the (a) slab-ocean setup (top panel), and (b) fully-coupled setup (bottom panel) in experiments (left-to-right): (i) U01 (left panels), (ii) P01 (middle panels) and (iii) T01 (right panels).	175
5.2.2	Projections of the full zonal wind (u) and mass streamfunction (psi) anomalies, seen in response to SST-perturbation experiments, onto difference in anomalies between atmosphere-only and (a) slab-ocean setup, years 25-50 (top panel), (b) fully-coupled setup, years 0-300 (bottom panel), in experiments (left-to-right): (i) U01 (left panels), (ii) P01 (middle panels) and (iii) T01 (right panels). The black dots indicate the result of projecting the difference in the anomalies between the different setups onto itself, and the error-bars' length are set as the standard deviation of the time-average projections of the different ensemble members.	177
5.2.3	Control values (contours) and anomalies (colours) in (a) zonal wind (left panels), (b) mass streamfunction (middle panels), and (c) potential temperature (right panels), in response to uniform SST-perturbation experiments: (i) sst-1k np (top panels), and (ii) sst-1k np (bottom panels). Hatching indicates regions in which the confidence levels in the experiment vs control values are below 95%, as measured by a two-tail student's t-test.	179
5.2.4	Projections of zonal wind (u) and mass streamfunction (psi) anomalies in atmosphere-only (sst), slab-ocean (qflux) and fully-coupled (cpl) setups, averaged over years 0-30, 0-50, and 250-100 as stated, in experiments (left-to-right): (i) U01 (left panels), (ii) P01 (middle panels) and (iii) T01 (right panels), onto corresponding anomalies seen in SST perturbation experiment sst-1k np. Errorbars' length are set as the standard deviations between ensemble members.	180
5.3.1	Control values (contours) and anomalies (colours) in various climatological fields in response to SST perturbation experiment sst-qflux-U01 np, averaged over years 0-5: (a) zonal wind (top-left), (b) Eulerian streamfunction (top-middle), (c) TEM residual streamfunction (top-right), (d) temperature (bottom-left), (e) relative humidity (bottom-middle), and (f) absolute humidity (bottom-right). Hatching indicates regions in which the confidence levels in the experiment vs control values are below 95%, as measured by a two-tail student's t-test.	183

- 5.3.2 Control values (contours) and anomalies (colours) in: (a) Coriolis westerly acceleration, $f[v]$ (top-left), (b) westerly acceleration by uv eddies, $-\frac{\partial[u^*v^*]}{\partial y}$ (top-middle), (c) frictional deceleration, $\overline{F_x}$ (top-right), (d) TEM residual circulation (bottom-left), (e) EP fluxes (arrows) and divergences (colours = anomalies; colours = control values) (bottom-middle), and (f) meridional PV gradient, q_ϕ (bottom-right), in response to SST perturbation experiment sst-qflux-U01 np, averaged over years 0-5. In the EP flux diagram, the fluxes are mass-weighted as per equations (2.1.32) and (2.1.33), the EP flux divergences are in units of 10^{15}m^3 , and the arrows are scaled such that the horizontal and vertical arrows in the top-left have lengths $5 \times 10^{13}\text{m}^3$ and $5 \times 10^{19}\text{m}^3\text{Pa}$ respectively. Hatching in all but the bottom-middle and bottom-right panels indicates regions in which the confidence levels in the experiment vs control values are below 95%, as measured by a two-tail student's t-test. 185
- 5.3.3 Control values (contours) and anomalies (colours) in (a) Eady growth rate, σ_B (top panel), and (b) 3rd meridional PV gradient component, $q_{\phi,p}$ (bottom panel), due to changes in: (i) both vertical potential temperature and zonal wind gradients, $\Delta\partial_p\theta$ and $\Delta\partial_pu$ (left panel), (ii) vertical zonal wind gradient only, $\Delta\partial_pu$ (middle panel), and (iii) vertical potential temperature gradient only, $\Delta\partial_p\theta$ (right panel), in response to SST perturbation experiment sst-qflux-U01 np, averaged over years 0-5. 187
- 5.3.4 Control values (contours) and anomalies (colours) in: (a) zonal winds (top-left), (b) mass streamfunction (top-middle), (c) EP fluxes (arrows) and divergences (colours = anomalies; colours = control values) (top-right), (d) Coriolis acceleration, $f[v]$ (bottom-left), (e) acceleration by uv eddies, $-\frac{\partial[u^*v^*]}{\partial y}$ (bottom-middle), and (f) meridional PV gradient, q_ϕ (bottom-right), in response to SST perturbation experiment sst-qflux-U01 np, averaged over days 0-5. In the EP flux diagram, the fluxes are mass-weighted as per equations (2.1.32) and (2.1.33), the EP flux divergences are in units of 10^{15}m^3 , and the arrows are scaled such that the horizontal and vertical arrows in the top-left have lengths $5 \times 10^{13}\text{m}^3$ and $5 \times 10^{19}\text{m}^3\text{Pa}$ respectively. 188
- 5.3.5 Control values (contours) and anomalies (colours) in diabatic potential temperature tendencies in response to SST perturbation experiment sst-qflux-U01 np, averaged over years 0-5, due to changes in: (a) all diabatic processes (top-left), (b) convection (top-middle), (c) condensation (top-right), (d) radiation (bottom-left), (e) diffusion (bottom-middle), and (f) dissipation (bottom-right). Hatching indicates regions in which the confidence levels in the experiment vs control values are below 95%, as measured by a two-tail student's t-test. 191

5.3.6	Control values (contours) and anomalies (colours) in advective potential temperature tendencies in response to SST perturbation experiment sst-qflux-U01 np, averaged over years 0-5, due to changes in heating by: (a) total advection (top-left), (b) TEM residual mean flow, $\tilde{\omega} [\theta]$, (top-middle), (c) vertical mean flow, $[\omega] [\theta]$ (top-right), (d) meridional eddies, $[u^*v^*]$ (bottom-left), (e) vertical eddies, $[\omega^*\theta^*]$ (bottom-middle), and (f) meridional mean flow, $[v] [\theta]$ (bottom-right). Hatching indicates regions in which the confidence levels in the experiment vs control values are below 95%, as measured by a two-tail student's t-test.	192
5.3.7	Control values (contours) and anomalies (colours) in (a) potential temperature (left), (b) diabatic potential temperature tendencies (middle), and (c) convective potential temperature tendencies (right), in response to SST perturbation experiment sst-qflux-U01 np, averaged over days 0-15.	193
5.4.1	Control values (contours) and anomalies (colours) in various climatological fields in response to SST perturbation experiment sst-qflux-P01 np, averaged over years 0-5: (a) zonal wind (top-left), (b) Eulerian streamfunction (top-middle), (c) temperature (top-right), (d) relative humidity (bottom-left), (e) absolute humidity (bottom-middle), and (f) diabatic potential temperature tendency (bottom-right). Hatching indicates regions in which the confidence levels in the experiment vs control values are below 95%, as measured by a two-tail student's t-test.	196
5.4.2	Control values (contours) and anomalies (colours) in: (a) EP flux divergence, $\nabla \cdot \mathbf{F}$, including anomalous EP fluxes (arrows) (top-left), (b) meridional EP flux gradient, $\frac{\partial F^y}{\partial y}$ (top-middle), (c) vertical EP flux gradient, $\frac{\partial F^p}{\partial p}$ (top-right), (d) meridional PV gradient, q_ϕ (bottom-left), (e) meridional PV gradient 2nd component in equation (2.1.28), $q_{\phi,y}$ (bottom-middle), and (f) (e) meridional PV gradient 3rd component in equation (2.1.28), $q_{\phi,p}$ (bottom-right), in response to SST perturbation experiment sst-qflux-P01 np, averaged over years 0-5. In the EP flux diagram, the fluxes are mass-weighted as per equations (2.1.32) and (2.1.33), the EP flux divergences are in units of 10^{15}m^3 , and the arrows are scaled such that the horizontal and vertical arrows in the top-left have lengths $5 \times 10^{13}\text{m}^3$ and $5 \times 10^{19}\text{m}^3\text{Pa}$ respectively.	197
5.4.3	Control values (contours) and anomalies (colours) in (a) Eady growth rate, σ_B (top panel), and (b) 3rd meridional PV gradient component, $q_{\phi,p}$ (bottom panel), due to changes in: (i) both vertical potential temperature and zonal wind gradients, $\Delta\partial_p\theta$ and $\Delta\partial_pu$ (left panel), (ii) vertical zonal wind gradient only, $\Delta\partial_pu$ (middle panel), and (iii) vertical potential temperature gradient only, $\Delta\partial_p\theta$ (right panel), in response to SST perturbation experiment sst-qflux-P01 np, averaged over years 0-5.	199

- 5.5.1 Schematic showing mechanism whereby a strengthened and expanded Hadley cell (solid black rectangle) leads to an increase in subtropical baroclinicity, with westerly/easterly acceleration (dotted/crossed circles) in the upper/lower subtropical troposphere. This causes a dipole anomaly in the third meridional PV gradient component - $q_{\varphi,p}$ in equation (2.1.28) - above/below the region of maximum baroclinicity increase (grey/white ovals), which acts as a waveguide, causing anomalous upward and equatorward EP fluxes in the midlatitudes, as well as anomalous downward EP fluxes in the subtropics (arrows), as the waves move towards/away from regions of increased/decreased meridional PV gradient. This induces a strengthening of the midlatitude zonal winds and circulation, with westerly zonal wind acceleration throughout the midlatitude troposphere, and a strengthened Ferrel cell (dashed black rectangle). Please note that the exact positions of the anomalous EP flux arrows and meridional PV gradient anomalies are not to be taken as precise, and are intended more for illustrative purposes. Mechanism is depicted for the Southern Hemisphere, with approximate latitudes of the zonal wind anomalies indicated along the (horizontal) latitude axis. 201
- 6.1.1 Schematics showing the changes in atmospheric and oceanic circulation patterns (solid and dashed black cells), surface zonal winds (red pluses/blue minuses), surface sensible heat fluxes (red arrows), thermocline depths, and SST, in experiment P01, setups: (i) slab-ocean (left), and (ii) fully-coupled (right). Red/blue shading indicate regions of heating/cooling by the changes in ocean vertical currents, causing local changes in the penetration depth of the thermocline. 207

List of Tables

2.5.1 Table giving the cell-centre pressure and depth values corresponding to each model level (σ) in the atmosphere and ocean respectively.	73
5.2.1 List of descriptors used to describe and identify the different SST-perturbation experiments.	176

Introduction

Historically, stratosphere-troposphere coupling has been viewed as a one-way interaction, with upward-propagating synoptic-scale waves driving changes in the stratosphere above, such as the Quasi-Biennial Oscillation (QBO), the Brewer-Dobson circulation, and sudden stratospheric warming (SSW) events (Shepherd 2002). However, since the 1990's, a growing body of observational and computational evidence, showing a downward influence of the stratosphere upon the troposphere, has emerged. These studies span a broad range of stratospheric phenomena and timescales, from SSW events (~ 3 -4 weeks) (Baldwin & Dunkerton 1999; Sigmond et al. 2013), to solar-cycle induced ozone variations (~ 5 years) (Gray et al. 2010), to long-term anthropogenic depletion and subsequent recovery of stratospheric ozone ($\gtrsim 10$ years) (Polvani et al. 2011; Son et al. 2018). Moreover, simulations with imposed stratospheric temperature/zonal wind perturbations have illustrated that many of the associated tropospheric dynamical changes can be forced by these stratospheric changes alone (Haigh et al. 2005; White et al. 2020). In more recent years, increases in computing power have given rise to similar studies performed using models of greater resolution and complexity, including models that fully-resolve and represent stratospheric processes (Hitchcock & Simpson 2014, 2016), and coupled atmosphere-ocean models (Armour et al. 2016). However, relatively few studies have looked at the impact the presence of these additional interactions have upon the underlying response to stratospheric perturbations: in particular, the impact of atmosphere-ocean coupling (e.g, Sigmond et al. 2010).

Changes in ocean heat content and circulation have the potential to influence the overlying atmosphere via changes in surface temperatures (SST's), and there is a large body of evidence supporting this ocean-atmosphere feedback, by both tropical (e.g. Matsuno 1966; Gill 1980) and, to a lesser extent, midlatitude SST's (e.g. Kushnir et al. 2002). The mechanisms governing these couplings vary, from the direct conversion of static into mechanical energy in the tropics via the mean flows (Held & Hou 1980; Held 2000), to the control of SST fronts on the strength and position of storm tracks in the midlatitudes (Brayshaw et al. 2008). Furthermore, recent studies have drawn links between shifts in the poleward Hadley cell edges, and shifts in the extratropical circulations, zonal winds, and storm tracks (Kang & Polvani 2011; Ceppi & Hartmann 2013), demonstrating the ability of tropical SST's to indirectly influence the extratropical atmosphere via changes in the tropical circulation. Moreover, recent modeling studies - looking at the oceanic response to step-changes in stratospheric ozone (Ferreira et al. 2015)

and associated surface wind stresses (Cai 2006) - have shown a response in the ocean circulation and SST patterns. Thus, taken together, it seems entirely plausible that atmosphere-ocean coupling could have a significant impact on the underlying tropospheric response to stratospheric perturbations.

The central aim of this thesis is to explore the impact of stratospheric temperature perturbations (STP's) on the troposphere below, using an intermediate-complexity General Circulation Model (GCM), in a double-drake, aquaplanet setup, with parameterisations of various physical processes, and, in particular, with varying degrees of atmosphere-ocean coupling present. In doing so, we shall be able to answer the following question: what is the impact on the ocean by the STP's, and how, if at all, does this modify the underlying atmospheric response?

The organisation of this thesis shall be as follows. Chapter 1 will provide a detailed overview of relevant literature as it pertains to the topic of this thesis, including the results of existing studies on stratosphere-troposphere, atmosphere-ocean, and stratosphere-troposphere-ocean coupling. Chapter 2 shall provide an overview of the methodology behind the study, detailing the mathematical tools and model to be used, its configuration and setup, and the stratospheric-forcing experiments to be performed using it. Chapter 3 shall outline the results of the experiments in the atmosphere-only version of the model, and the mechanisms involved. Chapter 4 shall outline the SST changes induced by the experiments in the two coupled versions of the model, and their drivers. Chapter 5 shall then attempt to bring these strands together, and look at the precise impact of the induced SST changes on the atmosphere above. Chapter 6 will then attempt to summarise the results of the chapters 3-5, discuss the main conclusions from, and limitations of, the study, and suggest future work to build upon, expand, or improve what has been achieved.

Chapter 1

Background

We will start with a review of the relevant literature, as it pertains to the topic of this thesis: the impact of STP's on the troposphere below, and how it might be affected by atmosphere-ocean coupling. As such, we will split our review into three sub-reviews, looking at, in order: (i) stratosphere-troposphere coupling; (ii) atmosphere-ocean coupling; and (iii) stratosphere-troposphere-ocean coupling.

1.1 Stratosphere-Troposphere Coupling

1.1.1 Motivation

The two lowermost regions of the atmosphere are known as the troposphere and the stratosphere. These two regions comprise approximately 95% of the atmospheric mass, and over 99% of the total mass of water vapour and aerosols (Andrews et al. 2010). Of these two layers, the troposphere holds the most relevance to human life, being the region in which almost all weather processes take place and, above all, being the region in which we live. Nevertheless, the stratosphere is still extremely important to us, primarily, because of its chemical composition: it contains over 90% of atmospheric ozone, O_3 , a strong absorber of UV radiation between about 200nm and 300nm, and an important greenhouse gas.

The depletion of stratospheric ozone - catalysed by man-made chlorofluorocarbons (CFC's) - through the 1980's and 1990's, its recent slowdown, and projected reversal and recovery, is a well-documented story - see, for example, Solomon (1999), Newchurch et al. (2003), and Eyring (2010). What has been historically less well understood and studied is what impact such changes in chemical composition might have on the troposphere below. In particular, what effect might stratospheric cooling/warming, caused by ozone depletion/recovery, have on the troposphere? The answer to this question also holds relevance for studying the effects of varying levels of stratospheric ozone due to variations in solar irradiance over the 11-year solar cycle. This would improve the performance of real-time numerical weather prediction (NWP) models,

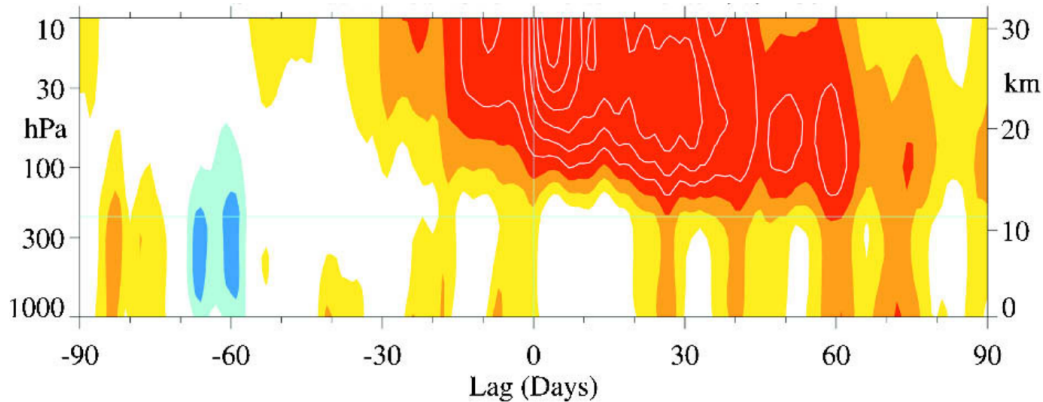


Figure 1.1.1: Composite of differences in SAM index between the weak and strong stratospheric events in the period 1987-2002. Day 0 corresponds to the onset of stratospheric event, and red/blue contours correspond to positive/negative SAM values, i.e. stronger/weaker-than-normal zonal flow along 60°S. Figure taken from Thompson et al. (2005). © American Meteorological Society. Used with permission.

which typically do not include real-time ozone data assimilation due to computational cost and complexity (Met Office 2021). It also holds relevance to, more generally, studying what effect changes in stratospheric concentrations of other gaseous substances, such as carbon dioxide, CO_2 , and volcanic-born aerosols, might have on the troposphere.

1.1.2 Phenomena

Sudden Stratospheric Warming (SSW) Events

Some of the earliest pieces of observational evidence for a stratospheric influence on the troposphere were found through studies of the annular modes in both hemispheres. These are the leading modes of variability in the extratropical circulation, and are formally defined as the leading order empirical orthogonal functions (EOF) of sea level pressure, zonally symmetric geopotential height, or zonal wind speed (Thompson & Wallace 2000). In the Northern Hemisphere, it is referred to as either the Northern Annular Mode (NAM), or, more commonly, the Arctic Oscillation (AO), and in the Southern Hemisphere, as either the Southern Annular Mode (SAM), or the Antarctic Oscillation (AAO). Typically defined close to the surface, the annular modes can actually be defined and calculated at any particular height or pressure level, into the stratosphere, and are calculated taking the difference in pressure/temperature/geopotential height at that altitude between two given latitudes: one in the midlatitudes, and one in the high/polar latitudes. A low/high index of annular mode corresponds to a strengthened/weakened meridional gradient in pressure/temperature/geopotential. By thermal wind arguments - see equation 2.1.11 - this will be accompanied with a band of strengthened/weakened westerlies along the enhanced/weakened meridional gradient axis.

In the early 2000's, several studies noted that periods of high and low annular mode index in the troposphere, in both hemispheres, were foreshadowed, by a period of around 2-3 weeks, by the same sign of annular mode index in the stratosphere, some of which were triggered by sudden stratospheric warming (SSW) events (Baldwin & Dunkerton 1999; Thompson et al. 2005). A composite of the difference between certain high- and low-SAM index events in the periods 1987-2002 is shown in figure 1.1.1, and clearly shows a signal originating in the stratosphere on day 0, and penetrating through to the troposphere by days 30-60. This then leads to changes in the surface climate that can persist for around 60 days after the event. It should be noted that not every SSW event, or period of high or low annular mode in the stratosphere, has preceded an associated change in the troposphere, and that most of these events with associated changes in the troposphere occurred at times of the year when the conditions are most conducive to wave-mean flow interactions in the stratosphere: midwinter in the Northern Hemisphere, and late spring in the Southern Hemisphere (Zhou et al. 2002; Baldwin & Dunkerton 1999; Thompson & Wallace 2000). Given the fact that annular modes account for a large proportion of the observed variation in weather patterns in the extratropics, understanding the nature of this observed coupling could potentially lead to much enhanced predictive power for numerical weather models (Baldwin et al. 2003). Indeed, such an enhanced predictive power of surface weather following strong/weak polar vortex events, at lead times of 2 weeks to 2 months, has been demonstrated by performing hindcast simulations, with the models initialised at the time of onset of the sudden stratospheric warmings/coolings (Sigmond et al. 2013; Domeisen et al. 2020).

Stratospheric ozone

Modeling studies which looked to simulate the changes in stratospheric ozone in the latter-half of the 20th century, found that such changes were the key drivers behind variations in the Southern Hemisphere climatology over that timeperiod (Polvani et al. 2011). Stronger ozone depletion in the late-spring would lead to an intensification and poleward-displacement of the midlatitude tropospheric jet, and a broadening of the summer Hadley cell and its subtropical dry zones (see figure 1.1.2) (Son et al. 2010; Polvani et al. 2011). Moreover, this effect was found to be 2-3 times stronger than that associated with increased greenhouse gases (GHGs) (Polvani et al. 2011). A subsequent study, which revisited these simulations, but using models from the Chemistry-Climate Model Initiative (CCMI), found similar results, and showed them to be robust across the models, irrespective of chemistry-atmosphere-ocean coupling (Son et al. 2018). Furthermore, simulations of projected rises in greenhouse gases and ozone recovery over the coming decades indicate that effects of the latter will tend to mitigate the former, effectively canceling out the projected poleward shift of the SH midlatitude jet in response to rising GHGs (Gerber & Son 2014).

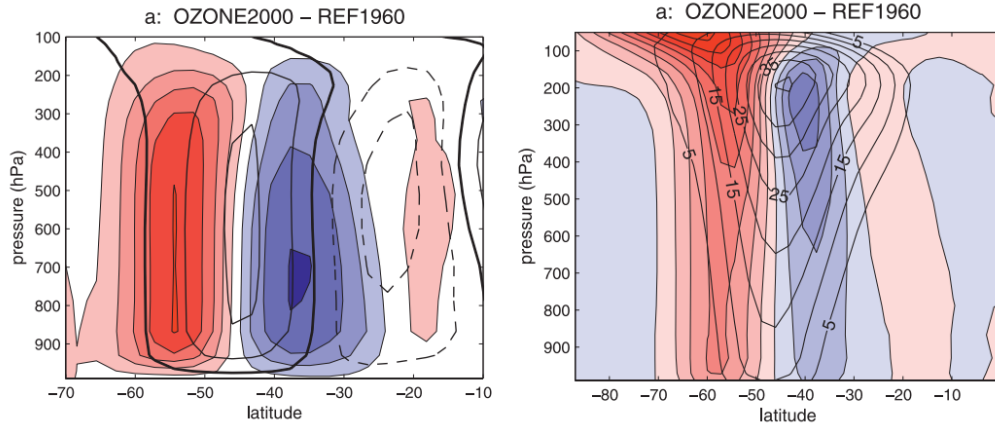


Figure 1.1.2: Control values (contours) and anomalies (colours) in SH summertime (DJF) mass streamfunction (left) and zonal winds (right), based upon 50-year integrated model response to year 2000 (vs. 1960) ozone concentrations. Figures adapted from Polvani et al. (2011). © American Meteorological Society. Used with permission.

Solar cycle

Another phenomenon which shows evidence of a downward influence of stratospheric changes upon the troposphere below is the 11-year solar cycle. Over this period - during which the levels of solar activity as measured by sunspot number go from a maximum, to a minimum, to another maximum value - solar UV irradiance shows considerable variation, with recent solar cycles showing variation of around 6% at around 200nm (Gray et al. 2010). This leads to a similar variation in levels of stratospheric ozone, with a difference of up to 4% in ozone levels between solar minimum and solar maximum (Soukharev & Hood 2006). Such variation is caused by a combination of: (i) changes to the ozone production rate by photolysis of molecular oxygen, primarily occurring in the low-latitude stratosphere at upper levels (Haigh 1994); (ii) changes to the ozone catalytic destruction rate by trace species, caused by changes in the precipitation rate of energetic charged particles, primarily occurring at polar latitudes (e.g. Randall et al. 2007). Furthermore, these two processes can also induce stratospheric circulation changes, leading to transport-induced variations in ozone concentrations (e.g. Gray et al. 2009).

Such variations in levels of stratospheric ozone cause corresponding changes in stratospheric temperatures and - via thermal wind balance, equation (2.1.11) - zonal winds, by as much as $+1^{\circ}\text{C}$ and -2m/s in the lower tropical stratosphere, and as much as $+3^{\circ}\text{C}$ and -1m/s in the middle polar stratosphere, between solar minimum and maximum (Frame & Gray 2010). Through a combination of GCM and reanalysis data, there is evidence of a downward influence of these stratospheric signals on the troposphere below, with solar maximum conditions shown to give rise to a poleward-shift in the midlatitude jets and circulations, as well as a poleward-expansion of the Hadley cell (e.g. Haigh & Blackburn 2006).

1.1.3 Modelling studies

Simplified GCM's

Ever since observational evidence for a downward influence of the stratosphere on the troposphere first arose, modelers have sought evidence for their manifestation in General Circulation Models (GCM's). Of particular interest to this thesis, are those that utilised simplified GCM's, or sGCM's: these are GCM's with a full representation of the dynamics, but only highly parameterised representations of physical processes, such as convection, diffusion, and absorption and emission of radiation. In such studies, heating/cooling perturbations were applied to the stratosphere of the sGCM, and a significant response in the troposphere was produced. The results of these studies will be explored in the following.

The work of Polvani & Kushner in the early 2000's, on this topic of stratosphere-troposphere coupling, focused on applying cooling perturbations to the polar stratospheric lapse rate of an sGCM, corresponding to a strengthening of the polar vortex (Kushner & Polvani 2004, 2006; Polvani & Kushner 2002). In these studies, such stratospheric cooling produced a significant response in the troposphere: a strengthening and poleward displacement of the tropospheric jet, the magnitude of which correlated positively with the magnitude of cooling perturbation applied. Whilst issues relating to details of the model state caused the magnitude of the shift of the tropospheric jet to be revised down, from 15° to about 3° for a stratospheric cooling lapse rate of $\gamma=4^\circ\text{Ckm}^{-1}$ (Gerber & Polvani 2009), the qualitative details of the tropospheric response have nonetheless proved robust, and project almost entirely and positively to the model's annular mode, in good agreement with aforementioned observations (Kushner & Polvani 2004; Polvani & Kushner 2002). Moreover, by isolating the thermal and eddy-driving terms, they found that the downward transmission of a signal from the stratosphere to the troposphere was only possible with the tropospheric eddy-driving terms present, although the full tropospheric response seemed to require a two-way coupling between stratosphere and troposphere (Kushner & Polvani 2004).

Lorenz & DeWeaver (2007) performed similar experiments, this time imposing a uniform cooling of 3.5°C on the stratosphere, such that the tropopause is moved to a lower pressure-level: a scenario akin to what might be expected in response to increased stratospheric CO_2 concentrations. Their results showed a strengthening and poleward shift of the midlatitude tropospheric jets, accompanied by a strengthening and poleward and upward shift of the eddy kinetic energy and momentum fluxes. These results showed good agreement with the results of IPCC models, although only one model, GFDL, had the daily model output necessary for calculating transient eddy fluxes.

The work of Haigh et al. (2005) focused more on heating perturbations applied to the lower stratospheres of sGCM's, applied either uniformly, or preferentially around the poles/equator, primarily to investigate the tropospheric response to variations in solar activity over the 11-year solar cycle. Uniform stratospheric heating was found to lead to a weakening of the tropospheric midlatitude jets and mean meridional circulations. Moreover, the positions of the jets and Hadley cells were found to be sensitive to the latitudinal positions of the applied temperature

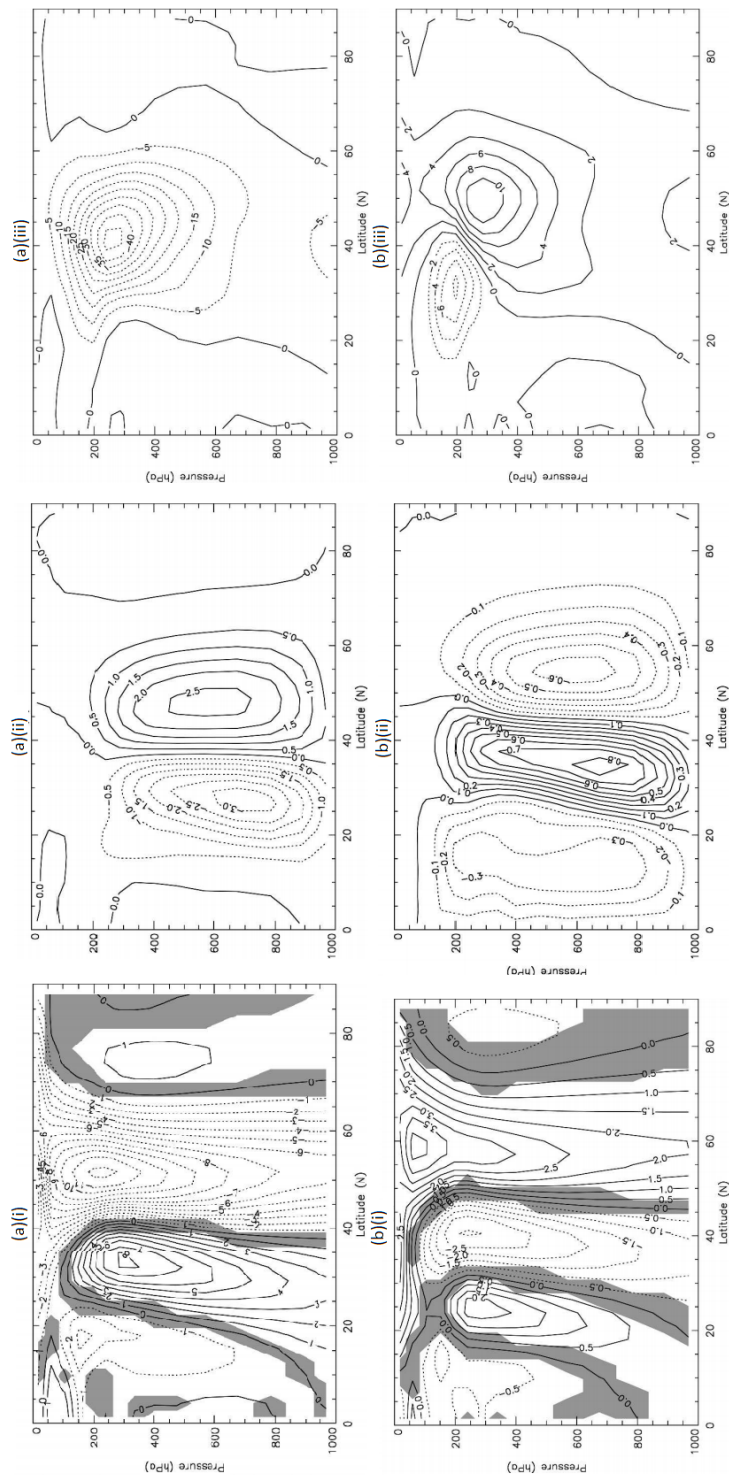


Figure 1.1.3: Response of model atmosphere in Haigh et al. (2005) to applied STP's, applied (a) throughout the model stratosphere (U5; top panel), and (b) preferentially to the tropical stratosphere (E5; bottom panel). Figures display, from left-to-right: (i) zonal wind anomalies (ms^{-1} , left panels), (ii) mass streamfunction anomalies (10^{10}kg s^{-1} , middle panels), and (iii) anomalous poleward fluxes of westerly momentum by the eddies, $[u^*v]$ ($\text{m}^2 \text{s}^{-2}$, right panels). Figures adapted from Haigh et al. (2005). © American Meteorological Society. Used with permission.

perturbations, with uniform and high-latitude perturbations shifting them equatorward, and low-latitude perturbations shifting them poleward (see figure 1.1.3). This work suggested that it is the meridional temperature gradient that is important when determining the sign of the tropospheric response to STP's.

Lorenz & DeWeaver (2007) explored this issue of the sensitivity of the tropospheric response to the location of any heating perturbations in an sGCM from a more general standpoint: using a similar methodology to Haigh et al. (2005), they placed 5°C heating perturbations of width 20° and height 150hPa at all positions in the latitude-pressure plane, and examined the response of the zonal wind. Whilst they found, like Haigh et al. (2005), that heating perturbations placed around the stratospheric equator and poles caused the midlatitude jet to shift poleward and equatorward respectively, they found an analogous response could also be produced by applying the perturbations at the same latitudes, but below the tropopause. Furthermore, they found that, when placed between 35° and 55°, the sign of the response of the zonal winds would change with the height at which the perturbation was applied, with the midlatitude jet moving equatorward when the perturbation was applied above the tropopause or near the surface, 1000-800hPa, and polewards when the perturbation was applied below the tropopause and above 800hPa. This work suggested that it is not only the meridional temperature gradient, in both stratosphere and troposphere, that is important in determining the sign of the tropospheric response to heating perturbations, but also whether the heating perturbation is placed above or below the tropopause, leading to a raising or lowering of tropopause height, respectively.

In Simpson et al. (2009), similar experiments with a similar response to that found in Haigh et al. (2005) were performed and recorded, but with the mechanisms responsible for the downward transmission of a signal from the stratosphere to the troposphere being closely examined. Changes in horizontal eddy momentum flux - initially caused by changes in vertical temperature gradients, and zonal wind accelerations in the stratosphere and troposphere, caused by changes in horizontal temperature gradient - were found to provide a crucial pathway and positive feedback mechanism, whereby stratospheric heating perturbations were able to cause changes in the mean meridional circulations and, in turn, in the tropospheric zonal wind. Further work on similar experiments in Simpson et al. (2010) highlighted the variability in atmospheric response to imposed STP's, depending upon the state and location of the mean zonal winds, with low-latitude and narrower jets exhibiting a stronger response to applied tropical stratospheric heating perturbations.

Garfinkel et al. (2013) further investigated this issue of the dependence of the response of the zonal winds to applied stratospheric forcing upon their control state. This was achieved by performing experiments in which the strength and width of the polar vortex was varied identically in three model configurations, in which the tropospheric jets were centred at 30°, 40°, and 50°. The strongest response was found when the jets were centred at 40°. The likely cause for this variation in response was found to be the stronger tropospheric eddy feedback present when the jet was centred at 40°.

In an attempt to determine the relative roles of the synoptic- and planetary-eddies in driving

the tropospheric response to sudden stratospheric warmings, Domeisen et al. (2013) performed experiments in which heating perturbations were applied to the stratospheric polar vortex, causing it to decelerate, in two model configurations: one with a full interactive wave spectrum, and one with fully-interactive planetary waves but only fixed, time-mean synoptic wave forcing. The presence of synoptic wave feedbacks was found to be crucial in determining the tropospheric response, with the zonal winds shifting equatorwards/polewards relative to their control state in their presence/absence. A similar experimental setup was utilised by Smith & Scott (2016), only this time truncating the influence of planetary waves, in an attempt to decipher their role in the model response to applied polar stratospheric cooling. It found, in contrast, that in the absence of planetary wave feedbacks, the tropospheric jet formed and persisted at lower latitudes in response to enhanced polar stratospheric cooling. It would therefore appear that the presence of both planetary- and synoptic-scale eddy feedbacks, and the interaction between the two, are essential to producing the full model response to applied polar stratospheric forcing.

More complex GCM's

In experiments which utilised a comprehensive, stratosphere-resolving GCM, the Canadian Middle Atmosphere Model (CMAM), Hitchcock & Simpson (2014, 2016) were able to emulate the equatorward shift of the midlatitude jet characteristic of SSW events in response to the applied forcing of the polar vortex, and found that it was well explained by the simple model of tropospheric eddy feedbacks proposed by Lorenz & Hartmann (2001). Moreover, they found that the synoptic-scale eddies - whilst contributing the most to the shift - responded almost entirely to alterations in the internal tropospheric eddy feedbacks, whilst the planetary-scale eddies appeared to be forced directly by changes in the stratospheric state. This would imply a mechanism involving direct forcing of the planetary waves by changes in the stratosphere, amplified by synoptic-wave feedbacks in the troposphere. Similar experiments by White et al. (2020), performed using the intermediate complexity Model of an Idealized Moist Atmosphere (MiMA), incorporated with a full radiative transfer model, reproduced a similar equatorward shift of the midlatitude jet, and affirmed the key role of synoptic eddies in driving the persistent shift at long lags.

Mechanism

There exist many mechanisms by which a perturbation in the stratosphere exerts a downward influence on the tropospheric circulation below. These include the mechanisms of mass redistribution, downward control, potential vorticity inversion, radiative processes, planetary wave reflection, and wave-mean flow interactions, with synoptic scale eddies and planetary waves. Whilst some or all of these mechanisms may play a part in real-world occurrences of downward influence by the stratosphere on the troposphere, in the context of the aforementioned studies involving heating/cooling perturbations applied to the stratospheres of sGCM's, most are either insufficient to account for the observed model changes, or simply irrelevant. In particular, any

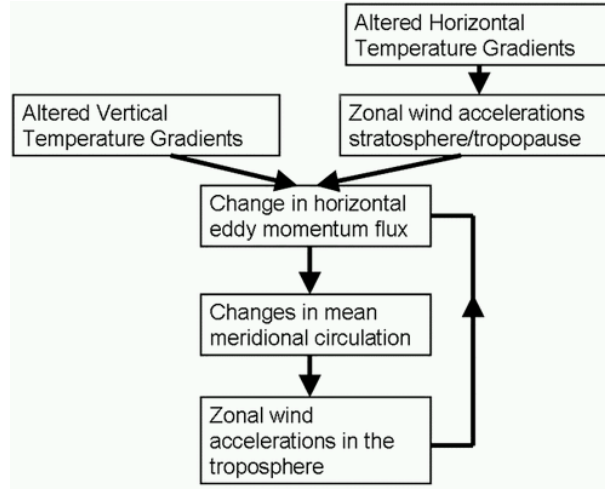


Figure 1.1.4: Proposed mechanism whereby STP’s can cause alterations to the tropospheric mean zonal winds and circulation. Taken from Simpson et al. (2009). © American Meteorological Society. Used with permission.

direct mechanisms, such as mass redistribution, downward control, and potential vorticity inversion, suffer from the fact that the stratospheric mass is much smaller than the tropospheric mass. This means that anomalies in stratospheric forcing or potential vorticity - which exert an influence on the troposphere below via their mass-weighted vertically-integrated quantities - can only exert only minimal influence via these mechanisms on their own (see e.g. Simpson 2009). Furthermore, whilst mechanisms involving planetary waves might provide promising pathways for instances of stratospheric downward influence in NH winter, such mechanisms necessitate the existence of large-scale mountain ranges, such as the Rockies and Himalayas, in order to produce low wavenumber planetary waves in the first instance. Hence, their relevance to studies involving S-T coupling in more simplified models and setups, or locations (e.g. the Southern Hemisphere) with little or no orography, is minimal.

Thus, the primary mechanism of stratosphere-troposphere coupling that this study will focus on, is that of wave-mean flow interaction involving synoptic-scale/baroclinic, eddies. Such eddies are produced by baroclinic instability in regions of steep temperature gradient, and as such are found primarily in the midlatitudes, in both hemispheres. They are important to the meridional transport of heat and momentum, and are responsible for maintaining the strong westerly tropospheric jets in the midlatitudes (for more details, see section 2.1). Thus, if any change in the stratosphere can exert an influence on the propagation of these eddies, it is reasonable to expect that this may have a significant impact on the tropospheric circulation.

One form of wave-mean flow interaction with synoptic scale eddies that we will focus on, is that outlined in Simpson et al. (2009). The mechanism is summarised schematically in figure 1.1.4, and can be described as follows: anomalous stratospheric heating causes alterations to the vertical and meridional temperature gradients around the tropopause, with the latter re-

sulting in zonal wind accelerations/decelerations (via thermal wind, equation (2.1.11)), affecting the vertical zonal wind shear. These combine to alter the meridional potential vorticity (PV) gradients (see equation (2.1.28)) thereby altering the quasigeostrophic index of refraction (see equation (2.1.29)), and hence, the direction of eddy propagation, producing anomalous horizontal eddy momentum fluxes and eddy heat fluxes. These flux anomalies drive both local zonal wind changes around the tropopause and upper troposphere, and anomalous meridional circulations that extend down throughout the troposphere, resulting in temperature and zonal wind changes that reach down to the surface. Tropospheric zonal wind anomalies then provide a positive-feedback onto themselves - via their impact on local horizontal eddy momentum fluxes - due to their effects on local refractive index and baroclinicity.

1.2 Atmosphere-ocean coupling

Now that we have laid out the evidence for a stratospheric influence upon the troposphere - in particular, for that of STP's upon the troposphere - in both observations and in simulations, and have established the main candidate mechanism through which STP's are able to exert a dynamical influence on the troposphere in intermediate-complexity GCM aquaplanet experiments with fixed SST, what remains to be seen is how all this is changed by the presence of an ocean that can interact with the atmosphere above, thermally and mechanically. To understand what potential impact this might have on the stratosphere-troposphere coupling, one clearly needs an understanding of how the atmosphere and ocean can interact with each other. This is what shall be examined in this subsection.

1.2.1 Tropical atmosphere-ocean coupling

Phenomena

In the tropics, atmosphere-ocean coupling is a strong, two-way interaction, with local atmospheric variations - in surface wind, and temperature and humidity - able to imprint themselves upon the ocean and vice versa. An explanation for this strong coupling can be found in the higher temperatures in these regions, which lead - via the Clausius-Clapeyron relation, equation (2.4.7) - to a proportionally greater increase in humidity and moist static energy in the atmosphere. Thus, moist processes such as convection and condensation become very powerful in the tropics, and allow for very strong atmosphere-ocean energy feedbacks.

The classic example of tropical atmosphere-ocean interaction is the El Niño-Southern Oscillation (ENSO) phenomenon. During an El Niño event, anomalously weak surface westerlies along the equatorial Pacific cause an anomalous eastward flow of warm Indian and Indonesian waters, flooding over cold Southern American waters, and thereby relaxing the usual wind-driven west-east sea level and temperature gradients along the equatorial Pacific (see fig. 1.2.1). During a La Nina event, the opposite occurs, and anomalously strong surface westerlies cause an enhancement of the west-east sea level and temperature gradients in the Pacific.

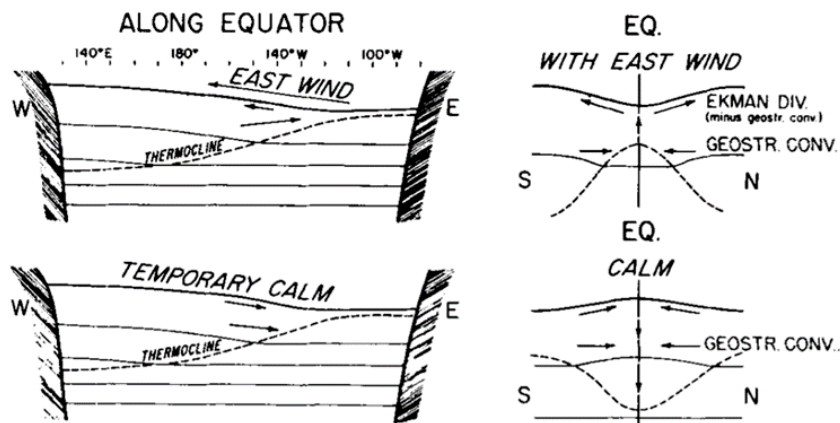


Figure 1.2.1: Schematic of equatorial flow patterns along equatorial Pacific with typical (top; normal conditions) and weaker than average surface westerlies (bottom; El Niño conditions). Figure taken from Bjerknes (1966).

The Southern Oscillation is the atmospheric analogue of El Niño/La Niña, involving east-west shifts in tropical atmospheric mass between the Indian Ocean and West Pacific Ocean and the central and eastern Pacific Ocean. It is typically measured by the Southern Oscillation Index (SOI), which takes the difference in sea-level pressure (SLP) between two points on the western and eastern edges of the Pacific, e.g. Easter Island and Darwin:

$$SOI = 10 \times \frac{SLP_{Tahiti} - SLP_{Darwin}}{\sigma}$$

where SLP_{Tahiti} and SLP_{Darwin} are the sea-level pressures at Tahiti and Darwin respectively, and σ is the standard deviation of the numerator. El Niño/La Niña events are found to correspond to negative/positive values of the SOI, i.e., weakened/strengthened differences in west-east Pacific SLP, and correspondingly diminished/enhanced west-east Walker circulations over the equatorial Pacific (Peixoto & Oort 1992). Also, in the zonally-averaged picture, El Niño events are found to correspond to strengthened tropical Hadley circulations and subtropical westerly jets, and overall warmer/colder atmospheric and sea surface temperatures in the tropics/midlatitudes (Pan & Oort 1983). Most of these changes in zonally-averaged quantities are attributable to more local changes over the eastern tropical Pacific (Bjerknes 1969).

Mechanisms

Gill (1980) constructed a simple analytic model to investigate the response of the tropical atmosphere to diabatic heating, based upon that of Matsuno (1966), in which the beta-plane approximation is applied to the horizontal momentum equations, horizontal advection is neglected, and small perturbations to the steady-state are considered. Solutions to the resulting momentum and continuity equations would resemble the tropical Pacific Walker and Hadley

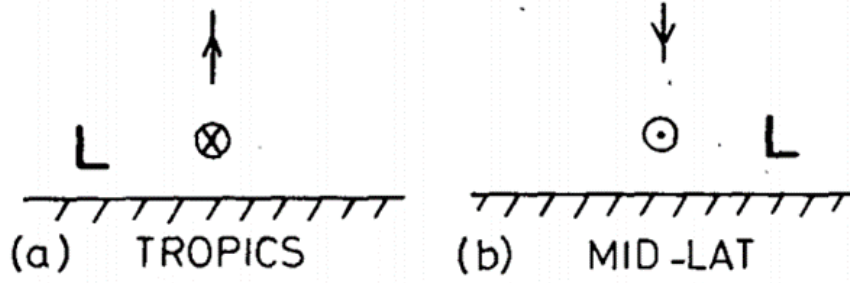


Figure 1.2.2: Schematic showing the direct, linear atmospheric response to low-level heating in the tropics (left) and midlatitudes (right) on a latitude-height plane. Arrows indicate the direction of vertical motions, and circled dots/crosses motion that is out of/into the section (i.e. westerly/easterly) respectively. Figure adapted from Hoskins & Karoly (1981). © American Meteorological Society. Used with permission.

circulations, with equatorial inflow into the region of localised heating, and outflow on its poleward flanks, with cyclonic lows situated to the west of the heating. The heating anomaly would induce upward motions in its vicinity, causing vortex-stretching ($\partial_z w > 0$), and hence vorticity creation. This must be balanced by a poleward flow ($\beta v > 0$) at low-level around the heating anomaly - see the left panel of figure 1.2.2 - although in the zonally-averaged picture this is balanced by a return flow west of the heat source.

Turning to zonally-symmetric models, Held & Hou (1980) created an analytic model of a zonally-symmetric flow, in which the upper-branch of the Hadley cell was angular-momentum conserving - such that the meridional advection of westerly momentum was balanced by Coriolis acceleration, $f[v] = -[v]\partial_y[u]$ (see equation (2.1.8)) - whilst the lower-branch was damped by friction. As in Gill (1980), equatorial heating would induce upward motions, balanced by cool descent polewards, and the overall circulation pattern resembles a Hadley cell. Furthermore, Coriolis accelerations on the upper branch of the cell produces a westerly flow which gets stronger with latitude. Under this model, the latitudinal extent of the Hadley cell, ϕ_H , scales as:

$$\phi_H \propto (H\Delta_e\theta)^{\frac{1}{2}} \quad (1.2.1)$$

where H is the height of the circulation outflow, and $\Delta_e\theta$ is the equator-to-pole radiative-equilibrium temperature difference (Vallis 2006; Vallis et al. 2015). The strength of the circulation, Ψ_H , can be expressed in a similar manner, and scales as:

$$\Psi_H \propto (\Delta_e\theta)^{\frac{5}{2}} \quad (1.2.2)$$

under this theory (Vallis 2006). Whilst it does accurately reproduce many of the features of the tropical Hadley circulations and subtropical westerlies, and can be extended to account

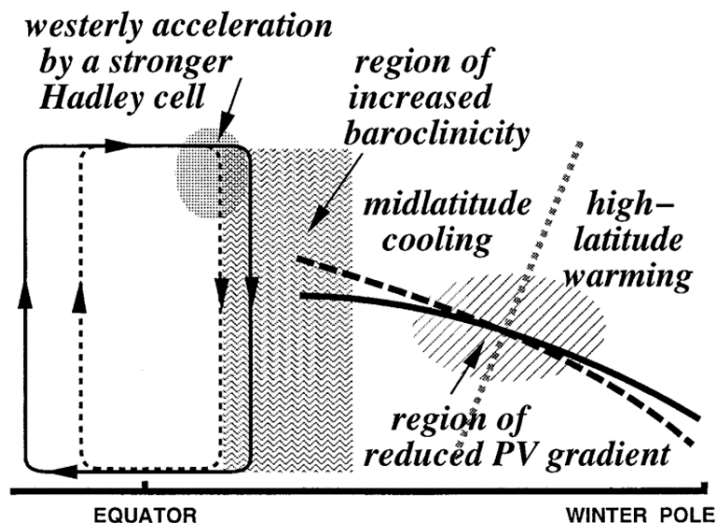


Figure 1.2.3: Schematic showing how a strengthened Hadley circulation in the tropics can lead to an enhanced subtropical jet with greater vertical shear, and therein to increased baroclinicity in that region. This leads to enhanced potential vorticity mixing, and poleward heat transport by baroclinic eddies. Figure taken from Hou (1998). © American Meteorological Society. Used with permission.

for seasonal variations of the Hadley cells by varying the latitude about which tropical diabatic heating is centred (Lindzen & Hou 1988), the validity of the Held-Hou model is limited by the constraint that the eddy forcing be negligible, equivalent to requiring the local Rossby number, $Ro = -\zeta/f \simeq 1$ along the upper branches of the cell away from the equator (Schneider 2006). Whilst this approximation is reasonable for the winter Hadley cell ($Ro \gtrsim 0.9$), it is less so for the equinoctial ($Ro \lesssim 0.7$) and summer ($Ro \lesssim 0.5$) cells, upon which the divergence of eddy momentum fluxes exerts a significant forcing (Schneider 2006). Moreover, the subtropical westerlies produced have very strong vertical shears, which would be reduced in the presence of eddies via baroclinic instability.

The Held-Hou model can be modified to account for these effects by requiring that the cell terminate at or before a critical latitude, ϕ_c , at which the modelled vertical wind shear would reach a baroclinically unstable value. This is the approach taken by Held (2000), and yields a critical latitude which scales as:

$$\phi_c \propto (H\Delta_v\theta)^{\frac{1}{4}} \quad (1.2.3)$$

where $\Delta_v\theta$ is the gross dry static stability, equal to surface-to-tropopause potential temperature difference (Vallis et al. 2015). This scaling has been shown to be accurate across a broad range of models and parameters (Walker & Schneider 2006; Frierson et al. 2007).

Changes in Hadley cell strength and extent also have the potential to influence extratropical

dynamics, thereby allowing a means by which tropical SST's can exert an influence on the extratropical atmosphere. Hou (1998) showed, using GCM simulations, that a tropical heating-induced Hadley cell strengthening and polewards-expansion can be accompanied by a westerly acceleration and increased vertical wind shear in the subtropics and midlatitudes. This enhanced baroclinicity outside of the tropics led to an enhanced PV mixing and poleward heat transport by baroclinic eddies, leading to reduced meridional and PV gradients in those regions. Figure 1.2.3 shows a schematic of this process. More recently, there have been numerous studies which have - by analysing the output of various model simulations and reanalysis data - pointed to a positive correlation in shifts in the poleward edge of the Hadley cell, and both poleward shifts and increases in strength in the eddy-driven midlatitude jet (Kang & Polvani 2011; Ceppi & Hartmann 2013; Staten & Reichler 2014). This correlation is strongest in the Southern Hemisphere, and during austral summer (Kang & Polvani 2011; Ceppi & Hartmann 2013), and the studies estimate that a 1° shift in the Hadley cell edge should be accompanied by a 1.5° - 2° shift in the eddy-driven jet. The connection between changes in the Hadley cell and midlatitude jet is provided by poleward eddy momentum fluxes - $[u^*v^*]$ in equation (2.1.8) - and their divergence/convergence patterns. A poleward shift in this pattern will induce a poleward-expansion/-shift in the upper Hadley and Ferrel cell branches, and the eddy-driven jet, to the extent that these features are controlled by these eddy fluxes.

Furthermore, changes in the Hadley cell can be linked to shifts in the positions of extratropical storm tracks - characterised as the maxima of poleward eddy heat fluxes - via the dependence of both on meridional temperature gradients. An increase in subtropical temperature gradient around the Hadley cell terminus, for instance, would cause an equatorward-shift of the storm tracks, as their diffusive nature causes the poleward eddy heat fluxes to shift with the temperature gradient profile. An increase in tropical static stability, conversely, which would induce an poleward-expansion in the Hadley cells via equation (1.2.3), would also induce a poleward-shift in the storm tracks, via the downstream impact on the meridional temperature gradients (Mbengue & Schneider 2018).

1.2.2 Midlatitudinal atmosphere-ocean coupling

Phenomena

In contrast to the situation in the tropics, atmosphere-ocean interactions in the extratropics tend to operate in mainly one direction only, with changes in the surface winds, temperature and humidity gradients forcing anomalous surface heat fluxes and Ekman currents, which in turn drive local SST changes, surface heat fluxes being the dominant driver over most of the extratropical ocean (Cayan 1992a,b,c; Seager et al. 2000). That said, extratropical SST anomalies exhibit large, basin-size scales, and - as the surface expressions of temperature anomalies throughout a well-mixed oceanic mixed layer - a long persistence, with an e-folding timescale of 3-5 months (Barnett 1981; Frankignoul & Reynolds 1983). Moreover, correlations between certain extratropical SST anomalies formed in the spring and those in the autumn suggest a

pattern of inter-seasonal ‘re-emergence’, with the SST anomalies being sequestered within the thermocline during the summer, and reemerging in response to stirring by surface heat fluxes and winds later in the year (Alexander et al. 1999). Evidence for this process having an influence on the extratropical atmosphere has been found in covariances between 500hPa wintertime geopotential heights, and the SST up to six months earlier, with the atmospheric response resembling that of the North Atlantic Oscillation (NAO) (Czaja & Frankignoul 1999, 2002).

Thus, whilst the influence of the extratropical SST’s on the atmosphere above might not be very strong on short timescales, their robustness, scale and persistence – including patterns of inter-seasonal reemergence – has the potential to grant them influence over large-scale atmospheric patterns on longer timescales, of the order of months or longer.

Mechanisms

The response of the extratropical atmosphere to local SST anomalies is, in contrast to the atmospheric response – both in the tropics and extratropics – to tropical SST anomalies, relatively weak and hard to detect, and often dwarfed by the atmospheric variability in that region (see e.g. Ferranti et al. 1994). Moreover, the precise nature of the response is dependent on a number of variables such as the background mean flows, the strength of the eddy-mean flow interaction, diabatic processes, etc. (see, e.g. Kushnir et al. 2002). This is owing to it being modulated by a number of mechanisms, which likely interact with each other, producing a response that is highly sensitive and nonlinear, making it difficult to model. Nonetheless, progress has been made in recent decades in elucidating some of the mechanisms at play, which we will now discuss.

First, is the linear baroclinic response. If the entire lower half of the troposphere were to come into thermal equilibrium with a temperature anomaly, δT , placed at its bottom boundary, then, by integrating equation (A.1.3) and applying equation (A.1.5), that would yield a proportionate perturbation to the geopotential height, $\delta\Phi \propto \Phi_0(\delta T/T_0)$ (Kushnir et al. 2002; see fig 1.2.4). As per equation (A.2.2), this would also induce a change in the zonal winds, with westerly deceleration/acceleration on the equatorward/poleward flanks of the geopotential height anomaly. The heating itself would necessarily have to be balanced by advection, which at the near-surface level in the midlatitudes would imply an anomalous equatorward flow, advecting cold air from higher latitudes. This would produce a negative vorticity ($\beta v < 0$), which must be balanced by vortex-shrinking via downwelling ($\partial_z w < 0$) (Hoskins & Karoly, 1981; see right panel of figure 1.2.2).

Generally, however, the midlatitude response to SST forcing does not resemble the linear baroclinic response alone, but is modified greatly by the presence of nonlinear forcing terms. The greatest source of nonlinear forcing in the midlatitudes is probably the stationary and transient eddies, or storm tracks. These appear as quadratic quantities in the quasigeostrophic atmospheric equations – see equations (2.1.12) and (2.1.13) – and thereby act as nonlinear source/sink terms for heat and momentum (Kushnir et al. 2002). These stationary and transient

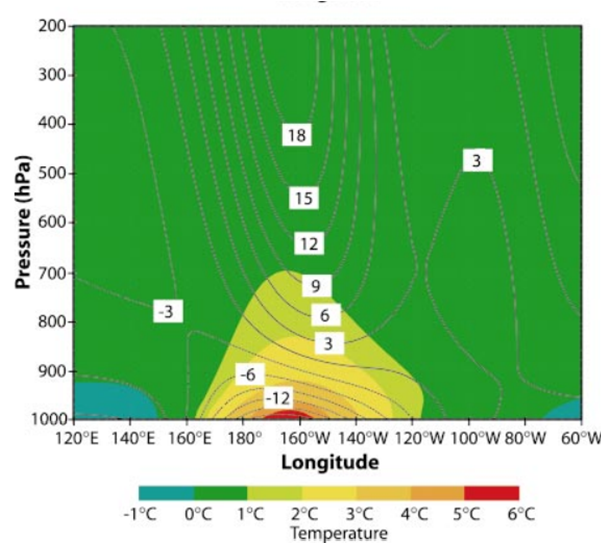


Figure 1.2.4: The atmospheric response to shallow heating in a linear, quasigeostrophic model with a westerly, baroclinic jet at its centre. The heating is centered at 180° , and decays exponentially with height. Colours and contours correspond to temperature and geopotential height anomalies respectively. Figure adapted from Kushnir et al. (2002). © American Meteorological Society. Used with permission.

eddy feedbacks onto the midlatitude mean flows, and are crucial in forcing the Ferrel circulations and midlatitude westerly jets.

The largest source of energy for midlatitude storm tracks is baroclinic conversion/instability – a mechanism whereby the potential energy can be released by motion in a fluid with non-parallel isobars and isotherms – which peaks in the region of maximum baroclinicity, as measured by the Eady growth rate, equation (2.1.18) (Chang et al. 2002). When low-level baroclinicity is increased – as might happen in response to e.g. an increased local SST meridional gradient – this generally leads to strengthened storm tracks, which feed back onto the mean flow, strengthening the surface westerlies, and shifting the midlatitude jet towards the region of enhanced baroclinicity (Brayshaw et al. 2008; Chen et al. 2010). Moreover, the nature of the atmospheric response to changes in baroclinicity is highly dependent upon the state of the mean-flow, and not just confined to the region of forcing, with a stronger/weaker subtropical jet generally leading to a less/more well-separated eddy-driven jet in response to an enhancement of midlatitude baroclinicity (Brayshaw et al. 2008). Furthermore, it has been suggested that – whilst initially they cause a reduction in baroclinicity through increased poleward heat flux, decreasing the meridional temperature gradient – increases in baroclinic eddy activity, in the steady-state limit, can actually lead to enhanced baroclinicity, providing a positive feedback for the generation and maintenance of such eddies (Robinson 2000).

Another point of particular relevance to this study is the suggestion that ocean feedbacks along midlatitude SST frontal zones help to anchor and maintain storm tracks against the

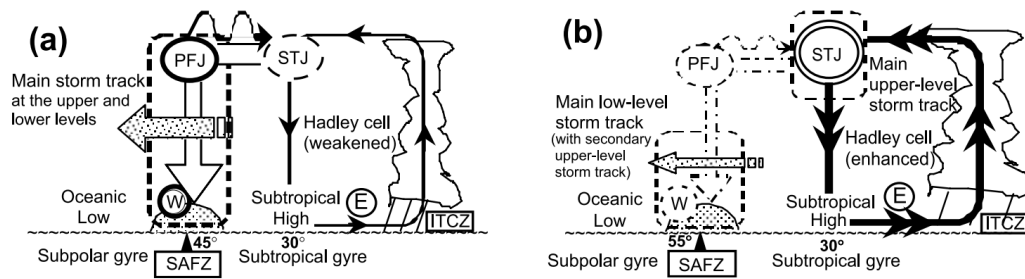


Figure 1.2.5: Schematic showing the relative strengths of the polar front jet (PFJ), subtropical jet (STJ), and storm tracks (dashed rectangles), under conditions of weakened (left) and strengthened (right) Hadley circulations. Wavy-arrows show the dispersion of wave-activity from polar front to subtropical jet, and open arrows show the transport of westerly momentum by eddies, maintaining the surface westerlies (W), which stay anchored to the subarctic frontal zone (SAFZ). Figure taken from Nakamura et al. (2004).

relaxing effects of poleward eddy heat transport. This idea was put forth by Nakamura et al. (2004), with strong surface zonal wind stresses in the region of the polar-front (aka. eddy-driven) jet driving the ocean circulation locally, reinforcing the SST front, and sustaining - along with vigorous storm track activity - its mixed layer structure. Since the ocean has a higher thermal capacity, and hence, responds much more slowly to thermal and dynamic changes, such features would then act to restore near-surface baroclinicity via turbulent heat exchange with the atmosphere above, as eddy heat transport acts to reduce it, at least in the short term.

These ideas were subsequently affirmed by Sampe et al. (2010), which used idealised GCM experiments to look at the impact the presence/absence of a midlatitude SST front had on storm tracks and the polar-front jet. It found that elimination of the midlatitude SST front led to a significant reduction in eddy activity, and an equatorward shift in the polar frontal jet and subtropical high pressure belt. Furthermore, a distinction between regimes in which the subtropical jet is relatively strong/weak - as forced by an enhanced/weakened Hadley cell via a Held-Hou mechanism - was drawn; see figure 1.2.5. In the latter, eddy-activity gets trapped by the core of the strongly baroclinic subtropical jet, weakening the polar front jet and storm tracks, and thereby reducing their sensitivity to changes in the midlatitude SST front (Nakamura et al. 2004).

Western boundary currents (WBC's)

In recent years - building upon the idea of Nakamura et al. (2004) that midlatitude SST fronts can help to anchor and maintain storm tracks against the thermal-relaxation effects of baroclinic eddies - there has been much research into atmosphere-ocean coupling along western boundary currents, such as Kurushio and the Gulf Stream. These are warm, deep and fast-flowing currents that form the western edges of oceanic gyres, and transport large amounts of heat polewards. They are therefore regions of sharp and narrow SST fronts, with high variability (Kwon et al.

2010). It is therefore conceivable that they might exert a significant influence on the atmosphere above, both in their large-scale influence in transporting large amounts of heat polewards, and also through the formation and maintenance of storm tracks along their SST fronts.

Through a combination of satellite and reanalysis data, Minobe et al. (2008) showed that there was a narrow band of precipitation, cloud formation, and deep upward vertical motion, anchored along the warm flank of the Gulf Stream, off the eastern North American coastline. These features were found to be consistent with a pattern of increased surface wind convergence, which in turn was well-explained by local boundary layer pressure adjustments to SST curvatures - see figure 1.2.6. Moreover, smoothing of the SST's effectively removed the narrow rain band, highlighting the pivotal importance of the sharp SST front in its maintenance. Similarly, Taguchi et al. (2009) ran regional simulations in which the atmosphere was allowed to respond to evolving SST distributions in the Kuroshio and Oyashio Extension (KOE) region, based upon data from the 2003/4 cold season, with and without smoothing of the finescale SST fronts. Comparison between two simulations revealed locally enhanced meridional gradients of turbulent fluxes of heat and moisture when the finescale SST fronts were resolved, favorable to the restoration of cross-frontal sea-air temperature gradients, and thereby to the development and maintenance of storm tracks. Moreover, smoothing of the SST's was shown to lead to a reduction and equatorward-shift in storm track activity.

As well as looking at the direct influence of WBC SST fronts on the atmosphere, there have been numerous studies showing an atmospheric impact from their variability. For instance, Frankignoul et al. (2011) showed meridional shifts in the Kuroshio and the Oyashio Extensions had significant impacts upon the large-scale atmospheric circulations, inducing responses similar to the North Pacific Oscillation/Western Pacific Pattern in a positive phase for a northward displacement of the Oyashio extension, based upon lagged regression analysis of historical SST and temperature data. Likewise, O'Reilly & Czaja (2015) found - by looking at reanalysis data from the period 1992-2011 - that a less/more meandering Kuroshio extension, with stronger/weaker SST meridional gradients, was associated with increased atmospheric transient eddy heat transport in the western/eastern Pacific region, consistent with increases/decreases in low-level baroclinicity.

Moreover, various GCM experiments - in which the atmospheric response to SST fronts along WBC's have been simulated using different model resolutions - have underscored the importance of model resolution in determining the overall atmospheric response. For instance, Smirnov et al. (2015) simulated the atmospheric response to a northward shift in the Oyashio Extension at two model resolutions - 0.25° and 1° - using the global Community Atmosphere Model, version 5 (CAM5). The two model resolutions produced similar vertical diabatic heating profiles in response to the shift, but different advective responses, with the high-resolution model balancing the diabatic heating with an anomalous poleward eddy heat and moisture transport, whilst the low-resolution model balanced it with a low-level equatorward flow of cold air, equivalent to the linear response to shallow extratropical heating of Hoskins & Karoly (1981). Moreover, the high-resolution model exhibited a weaker response in the surface winds, but a stronger anomalous

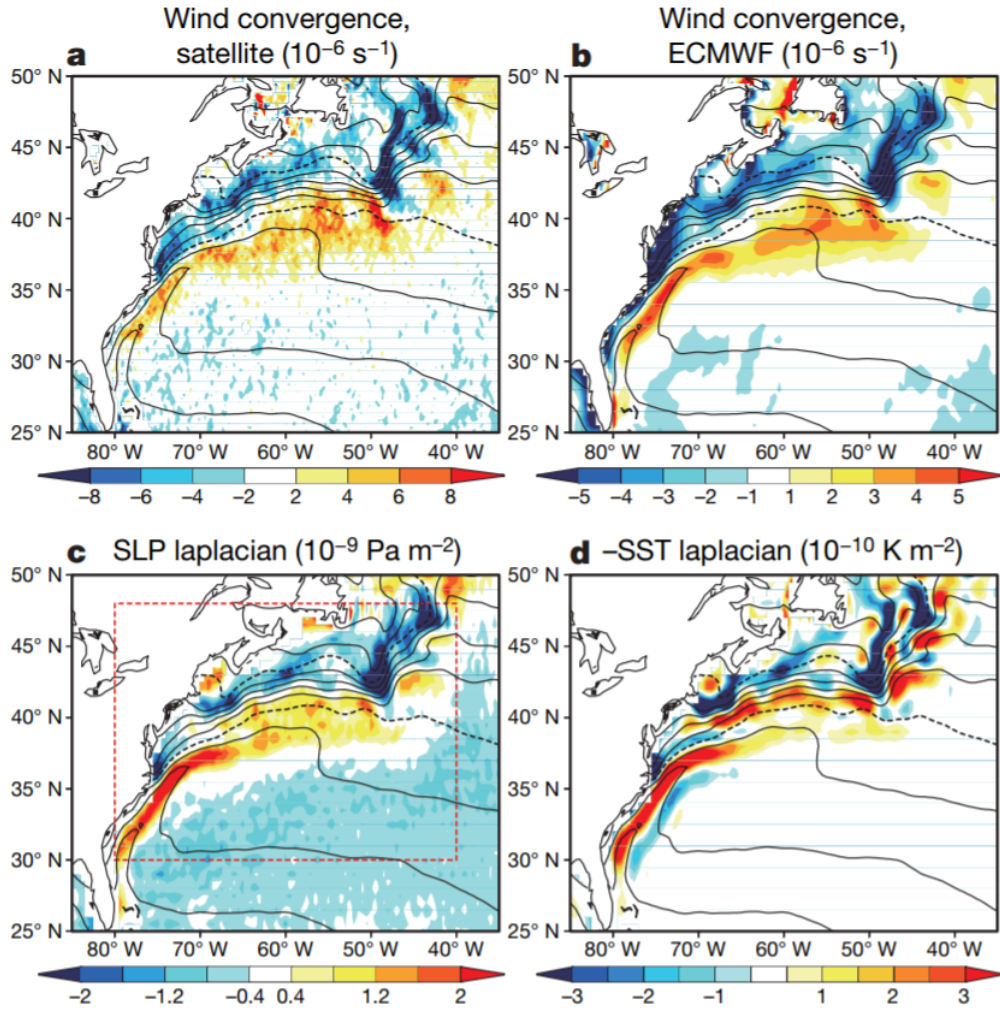


Figure 1.2.6: Top panels: SST's (contours, 2°C intervals and dashed contours for 10°C and 20°C) and 10m wind convergence (colours) from: (a) satellite observations, and (b) the ECMWF reanalysis data. Bottom panels: SST's (contours, same spacing) and, from the ECMWF reanalysis data (colours): (c) SLP laplacian, (d) and sign-reversed SST laplacian. Figure taken from Minobe et al. (2008).

vertical circulation, extending throughout the troposphere. Overall, the high-resolution model response was shown to be much more similar to the real-world response to a northward shift in the Oyashio Extension.

Similarly, Ma et al. (2017) simulated the regional atmospheric response the SST front in the Kuroshio Extension region, with and without mesoscale oceanic eddies present, using high- (27km) and low- (162km) resolution versions of the Weather Research and Forecasting (WRF) Model. Whilst both versions of the model were found to accurately reproduce the overall patterns of rainfall, jet stream, and storm track induced by the full SST front with mesoscale eddies - with slight underestimates of the rainfall and storm track activity by the low-resolution model - elimination of the eddies produced a definite southward shift in the jet stream and storm track in the high-resolution model only. These differences in response were attributed to the inability of the low-resolution model to capture the small-scale diabatic heating associated with mesoscale oceanic eddies and cyclogenesis. More recently, Foussard et al. (2019) ran simulations in an idealised setup with a zonally-symmetric SST field, with sharp meridional gradient in the midlatitudes, with and without mesoscale eddies added to the SST front. The eddies were found to shift the storm track and eddy-driven jet poleward, owing to an enhanced diabatic heating within the storms associated with greater polewards advection of moisture.

It is therefore clear from these experiments that: (i) SST fronts along WBC's exert a significant influence upon the atmosphere above through its generation and maintenance of storm tracks, in agreement with Nakamura et al. (2004), and (ii) that shifts in their position and strength can therefore significantly impact the overlying atmosphere. Moreover, mesoscale eddies appear to play a significant role in the atmosphere-ocean coupling along these fronts, and only relatively high-resolution models ($\lesssim 100\text{km}$) appear capable of providing an accurate representation of this type of coupling.

1.3 Stratosphere-Troposphere-Ocean Interaction

Having outlined the relevant aspects of stratosphere-troposphere and atmosphere-ocean coupling, we will in this last subsection look at the existing body of work which seeks to decipher any possible interactions or feedbacks between these two different couplings. We will split our analysis into two separate subsections, looking at: (i) the impact of tropospheric changes caused by stratospheric perturbations on the oceans below (the top-down coupling), and (ii) the impact of oceanic feedbacks on these atmospheric changes (the bottom-up coupling).

1.3.1 Stratospheric impacts on the ocean

The work of Cai et al. (2005), Cai (2006), and Cai & Cowan (2007), looked at the simulated trends in surface wind stress curl in the Southern Hemisphere in response to forcing by increasing greenhouse gases and decreasing stratospheric ozone - based on past data and future projections - and the response it produced in simulations of the oceanic circulation. Both forc-

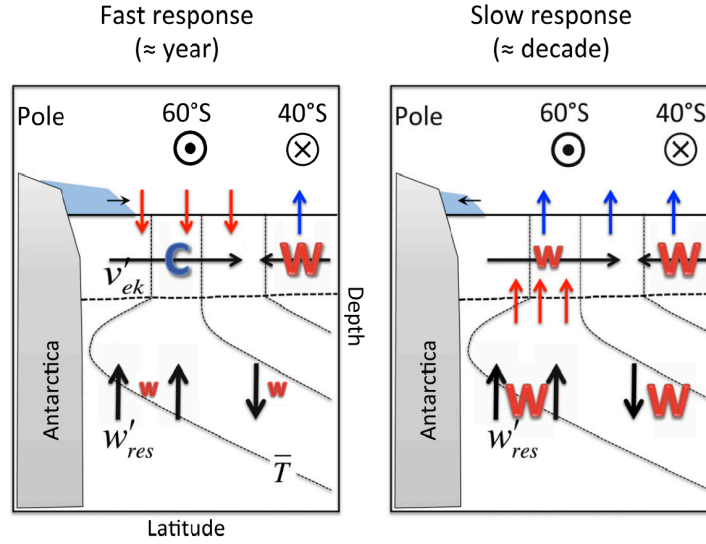


Figure 1.3.1: Schematic illustrating the fast (left) and slow (right) modelled oceanic responses to a poleward-shift in the midlatitude jet, caused by a step-change in ozone-depletion. Black arrows denote anomalous ocean currents. Red (blue) arrows denote heat fluxes in (out) of the surface mixed layer. Blue patches represent the sea ice cover. Figure taken from Ferreira et al. (2015). © American Meteorological Society. Used with permission.

ings were shown to produce a similar southward strengthening of the entire southern midlatitude ocean circulation, including the subtropical gyres, and particularly the East Australia Current (EAC). This in turn would lead to a greater poleward oceanic transport of heat, and thus an amplified warming of the midlatitude Southern Hemisphere SST's. Moreover, it was shown that most of this trend in the latter half of the 20th century was attributable to declining levels of stratospheric ozone.

Wang et al. (2014) extended this work by looking at the projected trends in stratospheric ozone and greenhouse gases over the 21st century, and the simulated changes in wind stress curl and ocean circulation they would produce. During the period of ozone recovery (2006-2045), there was little change in SH ocean circulation, as the rising levels of ozone acted to counteract any poleward shift due to rising levels of greenhouse gases. Subsequently, the trends in the summertime oceanic supergyre circulation were shown to vary depending upon the emissions scenario, its poleward shift projected to stabilise (RCP4.5) or accelerate (RCP8.5) in the ozone post-recovery period.

Ferreira et al. (2015) looked at the simulated response of two coupled atmosphere-ocean models - one the MITgcm in an aquaplanet, double drake setup, similar to that described in section 2.5 - to a step-change in ozone depletion, with the inclusion of a seasonal cycle in stratospheric ozone levels. In the Southern Ocean region, they found an initial 'fast' response in both models, characterised by a dipolar SST anomaly, with warm/cold anomalies equatorward/poleward of about 50°S, lasting for the initial 2-20 years. After this, a 'slow' response, characterised by a

monopole of warming, would take over. These responses were found to be driven by surface wind-induced changes to the ocean circulation, with the fast response driven by an enhanced equatorward Ekman drift, and the slow response by anomalous upwelling, itself a consequence of the former phenomenon. The two responses are shown schematically in figure 1.3.1.

Following a similar methodology, Kostov et al. (2017) looked at the response of the Southern Ocean SST's to a step-increase in Southern Annular Mode (SAM) index, across a variety of coupled models included in the Climate Modeling Intercomparison Project phase 5 (CMIP5). Whilst many models showed a similar, non-monotonic response, with initial cooling followed by subsequent warming, the diversity in model responses was large, with some models exhibiting a persistent cooling, and others a very abrupt shift from cooling to warming after only three years. Further investigation showed much of this intermodel spread to be explained by differences in the model ocean state: those with stronger meridional SST gradients exhibited a stronger initial cooling, whilst those with a stronger vertical temperature inversion in the Southern Ocean region exhibited a greater magnitude of 'slow' warming. The time-evolution of each model's Southern Ocean SSTs was dictated by the relative strengths of these two competing responses.

A similar inter-model diversity in response to a step-change in ozone was observed in Seviour et al. (2019), and was found to be well-reproduced by varying a single subgrid-scale mixing parameter, which would have the effect of varying the magnitude of oceanic temperature inversion. This lent support to the hypothesis of Kostov et al. (2017), that it was the variation in oceanic meridional and vertical temperature gradients in the mean model state that was the source of inter-model spread. However, by using this relationship to constrain the response of the real-world Southern Ocean to realistic ozone depletion, it found that this response alone was insufficient to explain the extended cooling seen from 1980 to the present. Whilst the exact causes of this extended cooling remain unclear, factors such as the passive northward advection of heat by the ocean circulation, in response to rising levels of greenhouse gases, most likely play a role (Armour et al. 2016).

1.3.2 Oceanic feedbacks on atmosphere

Sigmond et al. (2010) attempted to answer the question of whether or not atmosphere-ocean coupling had a significant impact upon the atmospheric response to stratospheric ozone depletion. It addressed this by performing realistic, seasonally-varying ozone perturbation experiments with the Canadian Middle Atmosphere Model (CMAM), both with and without a fully-coupled ocean model present, over a 100-year period. It found that, whilst the coupled model impacted the model's internal variability, causing an increased persistence in SAM-related atmospheric fluctuations, it had no discernible impact on the externally-forced atmospheric response to stratospheric ozone fluctuations.

Ogawa et al. (2015) performed GCM aquaplanet simulations of realistic, seasonally-recurring ozone depletion, both with and without a strong midlatitude SST front centred around 45°S present, run for a 52-year period. It found that, whilst both simulations would produce westerly

accelerations in the stratosphere between 45°S to 60°S in October to January, only with the midlatitude SST front present, was that signal able to penetrate into the troposphere and down to the surface, with a lag of about one month. It must however be stated that - given that the SST fields in these simulations were prescribed and not responding to the stratosphere-induced atmospheric changes, and with very large differences between the two prescribed SST fields - this is not so much evidence of an oceanic feedback upon the atmospheric response to stratospheric changes, as evidence of the importance of the mean atmospheric state in producing the full tropospheric response to said stratospheric changes. Since the SST front is key in maintaining the extratropical mean atmospheric fields, as discussed in section 1.2.2, its elimination would understandably have a great impact upon those mean fields, and therefore their response to external forcing.

In recent years, there has also been emerging evidence of an oceanic feedback onto solar-cycle induced tropospheric changes. By analysing trends in long-term mean SLP and SST over the period 1870-2010, Gray et al. (2013) showed a signal resembling the positive phase of the NAO in the years following a solar maximum, which maximises at a lag of approximately 3-4 years. Scaife et al. (2013) proposed a mechanism for this lagged response, based upon the known impact of the NAO on the North Atlantic ocean - forcing a tripole pattern of anomalous SST's - the persistence of these ocean heat content anomalies, and their subsequent feedback on the atmosphere. Subsequent studies (Andrews et al. 2015; Misios et al. 2016; Gray et al. 2016) have confirmed this lagged surface response to solar cycle variability and the mechanisms involved, with the ocean heat content anomalies being sequestered within the thermocline during the winter months, remaining intact underneath a shallow mixed layer that forms in summer, and re-emerging in the winter.

1.4 Conclusions

From section 1.1, it is clear that there is a very strong body of evidence - both from observations and simulations - for an influence of STP's on the troposphere below, over both the short-term (SSW's, ~weeks), and long-term (solar-cycle/anthropogenic ozone changes, ~years). Such atmospheric changes have the potential - via altered surface heat fluxes and Ekman currents - to alter the SST's of an underlying ocean. Certainly, the modeling studies outlined in section 1.3.1, support this hypothesis, indicating that stratospheric ozone depletion will induce - via altered Ekman currents - alterations to the wind-driven oceanic circulation, which in turn impact the oceanic heat transport and SST's, although the sign of the SST anomaly in the Southern Ocean region may be sensitive to the timescale in question.

From section 1.2, it is also evident that such SST changes have the capacity to induce changes in tropospheric dynamics, although the degree of, and mechanisms behind, such atmosphere-ocean coupling vary depending upon the latitudinal region of the SST anomaly, and also the atmospheric latitude region with which it is communicating. Relatively little research into the

oceanic feedbacks upon this type of stratosphere-troposphere coupling has been done and, from section 1.3.2, the existing results do not really provide any clear consensus, save for perhaps causing an increased persistence in the atmospheric signal.

Thus, the groundwork for a study which looks at the impact of atmosphere-ocean coupling upon the tropospheric response to STP's, the main subject of this thesis, has been laid. In the following chapters, I will present the results of my research into this topic.

Chapter 2

Methodology

Having laid the foundations for our understanding of the motivations behind the project and its scope, in this chapter, we shall provide an overview of its methodology. We shall start with a brief outline of relevant atmospheric and oceanic equations which shall be of use in our analysis, accompanied by a brief discussion of aquaplanet climatology. We will then move on to provide an overview of the model to be used, the MITgcm, its packages, precise setup and configuration. We will then outline the stratospheric-forcing experiments, and how they will be implemented within the model.

2.1 Atmospheric equations

In this section, we will present mathematical formulae that pertain to the dynamics and thermodynamics of the atmosphere. These formulae all ultimately stem from the primitive equations of motion, presented in section A.1. Moreover, they shall be of use later in analysing the results of experiments in which perturbations are applied to the model atmosphere.

2.1.1 Eddy-mean flow decomposition

More often than not, in our analyses of model output, we will be looking at zonally- and/or time-averaged quantities. For any given quantity, say A , its time-mean will be denoted with an overbar, \bar{A} , and its zonal-mean by square brackets, $[A]$. Deviations from these averaged quantities are known as EDDIES, and are defined as:

$$A = \bar{A} + A' = [A] + A^* \tag{2.1.1}$$

with A' indicating a temporal eddy and A^* indicating a zonal eddy. When both time- and zonal-means are utilised, a given field A has the following decomposition into mean and eddy quantities:

$$A = [\bar{A}] + [A'] + \bar{A}'^* + A'^* \quad (2.1.2)$$

When dealing with compound quantities - say AB - as will often be the case in our analyses, the number of quantities multiplies to $2 \times 2 = 4$ when dealing with the type of decomposition in equation (2.1.1), or $4 \times 4 = 16$ when dealing with the type of decomposition in equation (2.1.2). However, taking the time- and/or zonal-mean cuts this down to $4/2 = 2$ and $16/2/2 = 4$, giving the following decompositions:

$$\overline{AB} = \bar{A}\bar{B} + \overline{A'B'} \quad (2.1.3)$$

$$[AB] = [A][B] + [A^*B^*] \quad (2.1.4)$$

$$[\overline{AB}] = [\bar{A}][\bar{B}] + \overline{[A'] [B']} + [\bar{A}'^* \bar{B}^*] + \overline{[A'^* B'^*]} \quad (2.1.5)$$

In equation (2.1.5), we label the different terms on the RHS as the stationary mean (sm), transient mean (tm), stationary eddy (se), and transient eddy (te), respectively. We can group together the two transient terms into the term $\overline{[A'B']} = \overline{[A'] [B']} + \overline{[A'^* B'^*]}$, which we call the transient flux (tf), simplifying the decomposition into:

$$[\overline{AB}] = [\bar{A}][\bar{B}] + \overline{[A'B']} + [\bar{A}'^* \bar{B}^*] \quad (2.1.6)$$

Simplifying further still, we can group together all the eddies into one term, which we label as $[\overline{AB}]_{eddy} = \overline{[A'B']} + [\bar{A}'^* \bar{B}^*]$, and call simply the eddy flux (ef), giving the decomposition:

$$[\overline{AB}] = [\bar{A}][\bar{B}] + [\overline{AB}]_{eddy} \quad (2.1.7)$$

2.1.2 Quasigeostrophic equations

In our analyses of the results of experiments, we will focus especially on the zonally-averaged heat and momentum budgets in the latitude-pressure plane. Rewriting the fundamental set of atmospheric equations - equations (A.1.1), (A.1.8), (A.1.4) and (A.2.4) in section A.1 - using spherical coordinates (λ, ϕ, p) and zonally-averaging, we obtain the following set of equations:

$$\frac{\partial [u]}{\partial t} + \frac{\partial ([uv] \cos^2 \phi)}{R \cos^2 \phi \partial \phi} + \frac{\partial ([u\omega])}{\partial p} = f[v] + [\mathcal{F}_\lambda] \quad (2.1.8)$$

$$\frac{\partial [\theta]}{\partial t} + \frac{\partial ([v\theta] \cos \phi)}{R \cos \phi \partial \phi} + \frac{\partial ([\omega\theta])}{\partial p} = [Q] \quad (2.1.9)$$

$$\frac{\partial [v]}{R \cos \phi \partial \phi} + \frac{\partial [\omega]}{\partial p} = 0 \quad (2.1.10)$$

$$f \frac{\partial [u]}{\partial p} = \frac{1}{\rho [\theta]} \frac{\partial [\theta]}{R \partial \phi} \quad (2.1.11)$$

Utilising the decomposition of equation (2.1.4), and quasi-geostrophic scaling assumptions - terms involving $[u]$, v and θ become order-one quantities, whilst those involving other quantities such as ω and $[v]$ are of the order of the Rossby number, which is taken to be small - we arrive at the quasigeostrophic form of equations (2.1.8) and (2.1.9):

$$\frac{\partial [u]}{\partial t} + \frac{\partial ([u^* v^*] \cos^2 \phi)}{R \cos^2 \phi \partial \phi} = f [v] + [\mathcal{F}_\lambda] \quad (2.1.12)$$

$$\frac{\partial [\theta]}{\partial t} + \frac{\partial ([\omega] [\theta])}{\partial p} + \frac{\partial ([v^* \theta^*] \cos \phi)}{R \cos \phi \partial \phi} = [Q] \quad (2.1.13)$$

Together with equations (2.1.10) and (2.1.11), these equations form a set of four equations in four unknown quantities: $[u]$, $[v]$, $[\omega]$ and $[\theta]$. All eddy, frictional and diabatic terms are regarded as forcing terms. In this light, one can see the role of the eddy-momentum and eddy-heat fluxes in forcing the zonal-mean atmospheric motions.

Another useful quantity, which is conserved under the conditions of quasigeostrophic motion, is the potential vorticity, q , which takes the following zonally-averaged form in this framework:

$$[q] = f - \frac{\partial ([u] \cos \phi)}{R \cos \phi \partial \phi} - \frac{f}{R_d} \frac{\partial}{\partial p} \left(\frac{p [\theta]}{[T]} \frac{\partial_p [\Phi]}{\partial_p [\theta]} \right) \quad (2.1.14)$$

When it comes to identifying the mean meridional circulations, it can be highly instructive to diagnose an atmospheric mass streamfunction, Ψ , defined with respect to the zonal mean velocities as:

$$[v] = g \frac{\partial \Psi}{\partial p} \quad (2.1.15)$$

$$[\omega] = -g \frac{\partial \Psi}{\partial y} \quad (2.1.16)$$

Such a streamfunction then automatically obeys the mass conversation equation in the zonal mean, and can be calculated by inverting either of these equations:

$$\Psi(\phi, p) = \frac{2\pi R \cos \phi}{g} \int_{p_0}^p [v] dp' = -\frac{2\pi R^2 \cos \phi}{g} \int_{\phi_0}^{\phi} [\omega] d\phi' \quad (2.1.17)$$

Another useful quantity is the Eady growth rate. This is a measure of baroclinic instability, derived from the Eady model (Eady 1949), and takes the following form in z-/p-coordinates:

$$\sigma_B = 0.31g |f| \frac{\partial_z u}{N} = 0.31g |f| \frac{\partial_z u}{\sqrt{\frac{g}{\theta} \partial_z \theta}} = -0.31g |f| \frac{\partial_p u}{\sqrt{-\frac{R_d T}{p \theta} \partial_p \theta}} \quad (2.1.18)$$

where N is the Brunt-Vaisala (buoyancy) frequency.

2.1.3 The Transformed Eulerian Mean (TEM) and Eliassen-Palm Flux

Since much of our analyses will be looking at the forcing of the atmospheric mean-flow by eddy fluxes, we will also frequently work in the Transformed Eulerian Mean (TEM) framework, developed by Andrews & McIntyre (1976), in which a 'residual mean circulation', \tilde{v} and $\tilde{\omega}$, is defined as:

$$\tilde{v} = [v] - \frac{\partial}{\partial p} \left(\frac{[v^* \theta^*]}{\partial \theta / \partial p} \right) \quad (2.1.19)$$

$$\tilde{\omega} = [\omega] + \frac{1}{R \cos \phi} \frac{\partial}{\partial \phi} \left(\frac{[v^* \theta^*] \cos \phi}{\partial \theta / \partial p} \right) \quad (2.1.20)$$

Formally, this defines the part of the zonal mean circulation which is not balanced by eddy enthalpy flux convergence (Peixoto & Oort 1992). These fields obey the continuity equation, and hence one can define a residual streamfunction, $\tilde{\psi}$, analogously to equation (2.1.17) :

$$\tilde{\psi} = \frac{2\pi R \cos \phi}{g} \int_{p_0}^p \tilde{v} dp' = -\frac{2\pi R^2 \cos \phi}{g} \int_{\phi_0}^{\phi} \tilde{\omega} d\phi' = \psi - \left(\frac{[v^* \theta^*]}{\partial \theta / \partial p} \right) \quad (2.1.21)$$

Under this framework, it is useful to utilise a vector quantity known as the Eliassen-Palm (EP) flux, $\mathbf{F} = (F^y, F^p)$, first formulated by Eliassen (1960), whose components in latitude-pressure coordinates are defined as:

$$F^y = -R \cos \phi [u^* v^*] \quad (2.1.22)$$

$$F^p = f R \cos \phi \frac{[v^* \theta^*]}{\partial \theta / \partial p} \quad (2.1.23)$$

Calculating the divergence of this vector in the latitude-pressure plane yields:

$$\nabla \cdot \mathbf{F} = \frac{\partial (F^y \cos \phi)}{R \cos \phi \partial \phi} + \frac{\partial F^p}{\partial p} = -\frac{\partial ([u^* v^*] \cos \phi)}{\cos \phi \partial \phi} + f R \cos \phi \frac{\partial}{\partial p} \left(\frac{[v^* \theta^*]}{\partial [\theta] / \partial p} \right) \quad (2.1.24)$$

Taken all together, equations (2.1.12) and (2.1.13) take the following form in this framework:

$$\frac{\partial [u]}{\partial t} = f \tilde{v} + [\mathcal{F}_\lambda] + \frac{1}{R \cos \phi} \nabla \cdot \mathbf{F} \quad (2.1.25)$$

$$\frac{\partial [\theta]}{\partial t} + \frac{\partial (\tilde{\omega} [\theta])}{\partial p} = [Q] \quad (2.1.26)$$

Thus, in the TEM framework, $\nabla \cdot \mathbf{F}$ represents the only internal forcing of the mean state by eddies under the quasi-geostrophic approximation. Differentiating these equations with respect

to p and θ , respectively, and combining with the thermal wind relation, equation (2.1.11), we obtain a second-order differential equation in $\tilde{\psi}$:

$$\left\{ \frac{f^2 g}{2\pi R \cos \phi} \frac{\partial^2}{\partial p^2} - \frac{g}{2\pi R \cos \phi \rho [\theta]} \frac{\partial}{R \partial \phi} \left(\frac{\partial [\theta]}{\partial p} \frac{\partial}{R \partial \phi} \right) \right\} \tilde{\psi} = \frac{1}{\rho [\theta]} \frac{\partial [Q]}{R \partial \phi} - f \frac{\partial}{\partial p} \left([\mathcal{F}_\lambda] + \frac{1}{R \cos \phi} \nabla \cdot \mathbf{F} \right) \quad (2.1.27)$$

The time-independent nature of this equation makes it a useful diagnostic when investigating any forcing of the TEM residual circulation.

It can be shown that, under quasigeostrophic theory assumptions, the EP flux divergence is equivalent to the poleward eddy flux of potential vorticity (PV), $\nabla \cdot \mathbf{F} = [v^* q^*]$ - for a derivation, see for example Vallis (2006). Thus, if the eddy fluxes are downgradient - i.e. $[v^* q^*] \propto -\partial_\phi [q]$ - we would expect the EP fluxes to diverge/converge around regions of negative/positive meridional PV gradient, $\partial_\phi [q]$, as given by the formula:

$$\partial_\phi [q] = 2\Omega \cos \phi - \frac{\partial}{\partial \phi} \left(\frac{\partial ([u] \cos \phi)}{R \cos \phi \partial \phi} \right) + \frac{f^2 R}{R_d} \frac{\partial}{\partial p} \left(\frac{p [\theta]}{[T]} \frac{\partial_p [u]}{\partial_p [\theta]} \right) := [q]_{\phi,\beta} + [q]_{\phi,y} + [q]_{\phi,p} \quad (2.1.28)$$

found by differentiating equation (2.1.14) and simplifying with equation (2.1.11), and where we have labeled the individual component terms from left-to-right as $[q]_{\phi,\beta}$, $[q]_{\phi,y}$ and $[q]_{\phi,p}$ respectively. Similarly, under the assumption of downgradient poleward eddy heat fluxes, $[v^* \theta^*] \propto -\partial_\phi [\theta]$, we would expect the vertical EP flux components, F^p , to diverge/converge around regions of negative/positive $[q]_{\phi,p}$. And, if local zonal wind changes are driven by the convergence of eddy momentum fluxes, $-\frac{\partial([u^* v^*] \cos \phi)}{\cos \phi \partial \phi}$ - as is the case in the upper midlatitude troposphere - we would expect the meridional EP flux components F^y , to converge/diverge around regions of negative/positive $[q]_{\phi,y}$. For more details, see section A.3.

Moreover, Karoly & Hoskins (1982) showed that, under linear WKB theory, waves will tend to refract towards/away from regions of high/low refractive index, n , as given by the formula:

$$n^2 = \frac{R \partial_\phi [q]}{([u] - c)} - \left(\frac{k}{\cos \phi} \right)^2 - \left(\frac{f}{2NH} \right)^2 \quad (2.1.29)$$

where c is the zonal phase speed, k is the wavenumber, N is the buoyancy frequency and H is the density scale height.

TEM and EP Flux Diagrams

When it comes to constructing EP-flux diagrams, it is standard to follow the methodology of Edmon et al. (1980), and, instead of $\nabla \cdot \mathbf{F}$, to use the $\nabla \cdot \mathbf{F}$ weighted by the mass of an annular

ring, $dm = \frac{2\pi R^2}{g} \cos \phi d\phi dp$:

$$\int \nabla \cdot \mathbf{F} dm = \frac{2\pi R^2}{g} \iint \nabla \cdot \mathbf{F} \cos \phi d\phi dp = \iint \Delta d\phi dp \quad (2.1.30)$$

where

$$\Delta = \frac{\partial \hat{F}^\phi}{\partial \phi} + \frac{\partial \hat{F}^p}{\partial p} \quad (2.1.31)$$

and we have replaced the individual EP-flux vector components with the mass-weighted components:

$$\hat{F}^\phi = \frac{2\pi R}{g} \cos \phi F^\phi = -\frac{2\pi R^2}{g} \cos^2 \phi [u^* v^*] \quad (2.1.32)$$

$$\hat{F}^p = \frac{2\pi R^2}{g} \cos \phi F^p = \frac{2\pi R^3 f}{g} \cos^2 \phi \frac{[v^* \theta^*]}{\partial \theta / \partial p} \quad (2.1.33)$$

These components together form our mass-weighted EP-flux vector, $\hat{\mathbf{F}} = (\hat{F}^\phi, \hat{F}^p)$.

2.2 Oceanic equations

2.2.1 Geostrophic and Ekman flow

The fundamental oceanic equations of motion and state are provided in section B.1. In the steady-state, $\frac{d\mathbf{u}}{dt} = 0$, the equation for the horizontal flow can be rearranged to give:

$$\mathbf{u} = \hat{k} \times \frac{1}{\rho f} \left(\nabla p - \frac{\partial \tau}{\partial z} \right) := \mathbf{u}_G + \mathbf{u}_E \quad (2.2.1)$$

where we have defined two separate components to the flow - the geostrophic flow, \mathbf{u}_G , and the Ekman flow, \mathbf{u}_E - defined as:

$$\mathbf{u}_G = \hat{k} \times \frac{1}{\rho f} \nabla p = \frac{1}{\rho f} \left(-\frac{\partial p}{\partial y}, \frac{\partial p}{\partial x} \right) \quad (2.2.2)$$

$$\mathbf{u}_E = -\hat{k} \times \frac{1}{\rho f} \frac{\partial \tau}{\partial z} = \frac{1}{\rho f} \left(\frac{\partial \tau_y}{\partial z}, -\frac{\partial \tau_x}{\partial z} \right) \quad (2.2.3)$$

The geostrophic flow - as with the atmospheric geostrophic flow - is that which results from a balance between the Coriolis and pressure gradient force, and it can be defined at any point within the ocean column. The Ekman flow is a boundary-layer flow, resulting from a balance between the Coriolis and frictional forces, with the latter being a result of atmospheric surface wind stresses. The layer within which this surface wind stress is felt is called the mixed layer, with the stresses and Ekman velocities going to zero outside of this layer.

By taking the divergences of equations (2.2.1) and (2.2.3), simplifying with the continuity equation, and vertically-integrating - subject to the boundary condition that $w = 0$ at the surface - we obtain the following equations for the Ekman and geostrophic vertical velocities:

$$w_E(0) = -\frac{1}{\rho} \hat{k} \cdot \nabla \times \left(\frac{\tau(0)}{f} \right) = -w_G(0) \quad (2.2.4)$$

$$w_G(-h) = w_G(0) + \int_{-h}^0 \frac{\beta v_G}{f} dz \quad (2.2.5)$$

2.2.2 Sverdrup balance

By taking the curl of equation (2.2.1), applying the chain rule under the assumption of constant density, and simplifying with the continuity equation - see e.g. Pedlosky (1996) for a full derivation - one obtains the following equation:

$$\rho f \frac{\partial w}{\partial z} + \frac{\partial}{\partial z} \hat{k} \cdot \nabla \times \tau = \rho \beta v \quad (2.2.6)$$

By vertically-integrating this equation over the entire ocean column, and taking $w = 0$ at the top and bottom boundaries, we obtain the following expression for the total vertically-integrated meridional mass transport:

$$\beta V_S \equiv \beta \int_{-H}^0 \rho v dz = \hat{k} \cdot \nabla \times \tau(0) \quad (2.2.7)$$

This expression is known as the **SVERDRUP BALANCE**, and states that the net meridional mass transport by the entire ocean column is entirely determined by the surface wind stress curl. Furthermore, by integrating the meridional component of equation (2.2.3) over the mixed layer of depth δ , and setting $h=H$ in equation (2.2.5), such that we integrate v_G over the entire ocean column, we obtain the following equations for the total meridional mass transport by the individual Ekman and geostrophic components to the flow, V_E , and V_G , respectively:

$$\beta V_E \equiv \beta \int_{-\delta}^0 \rho v_E dz = \frac{\beta}{f} \int_{-\delta}^0 \frac{\partial \tau_x}{\partial z} dz = \frac{\beta}{f} \tau_x(0) \quad (2.2.8)$$

$$\beta V_G \equiv \beta \int_{-H}^0 \rho v_G dz = -\rho f w_G(0) = f \hat{k} \cdot \nabla \times (\tau(0)/f) \quad (2.2.9)$$

Application of the chain rule for vectors to the RHS of equation (2.2.9) then leads to the following identity:

$$\beta (V_G + V_E) = \beta V_S \quad (2.2.10)$$

Thus, the Sverdrup balance itself can be decomposed into individual geostrophic and Ekman components. Accordingly, we observe that even the meridional geostrophic flow, which has no explicit dependence on surface wind stress via its definition in equation (2.2.2), does have an implicit dependence upon it, via equation (2.2.10).

2.3 Aquaplanet climatology

In this section, we will provide a brief overview of the type of atmospheric climatology seen on an aquaplanet, focusing upon the results of the Aquaplanet Experiment (APE), detailed in Williamson et al. (2012). This study used a multi-model ensemble, with parameters and parameterisations standardised between the models, and the SST set to certain zonally- and hemispherically-symmetric profiles. Note that, whilst the models would omit orography in preference of an axially-symmetric planet covered by water, physical parameters such as albedo - as well as the SST profiles - were set to mimic Earth-like values. Hence, the climatology would be closer to that of Earth than a true waterworld, in which the albedo would be much lower.

One of the SST profiles the multi-model ensemble was set to - which is the one whose climatology we will explore here - was the FLAT SST profile, in which the SST was prescribed as:

$$\text{SST} = \begin{cases} 27 [1 - \sin^4(\frac{90}{60}\varphi)] & \text{if } |\varphi| < 60^\circ \\ 0 & \text{if } |\varphi| \geq 60^\circ \end{cases} \quad (2.3.1)$$

The multi-model mean values of the atmospheric zonal, meridional, and vertical winds, temperatures, and absolute and relative humidities, found by the APE using this SST profile, are displayed in figure 2.3.1.

Looking at the meridional and vertical winds in the top-middle and top-right panels, we see two definite circulation cells, extending from about 0 to 30°, and 30° to 60°, resembling Hadley and Ferrel cells respectively. Although difficult to judge from the plots, there also appears to be a much weaker third cell - a polar cell - polewards of 60°. In the zonal winds, we see a distinct westerly midlatitude jet, with a core at around 200hPa and 50°, conjoined with a subtropical jet on its equatorial flank, and a polar vortex in the stratosphere above, centred around 60°. Overall, the observed climatology is similar to that seen on Earth, especially in the Southern Hemisphere, where there is less orography, and the midlatitude jet is generally more well-separated from the subtropical jet than in the Northern Hemisphere. Thus, in spite of its simplicity and zonal-symmetry, this aquaplanet setup does a good job reproducing an Earth-like climatology.

Along the descending poleward branch of the tropical Hadley cell, located at around 30°, we see a strong vertical shear in the zonal winds (top-left), and a region of very low relative humidities, centered around 600hPa (bottom-right). The latter is the result of much condensation of water vapour, as air rises and moves poleward in the equatorial region. By the time it reaches

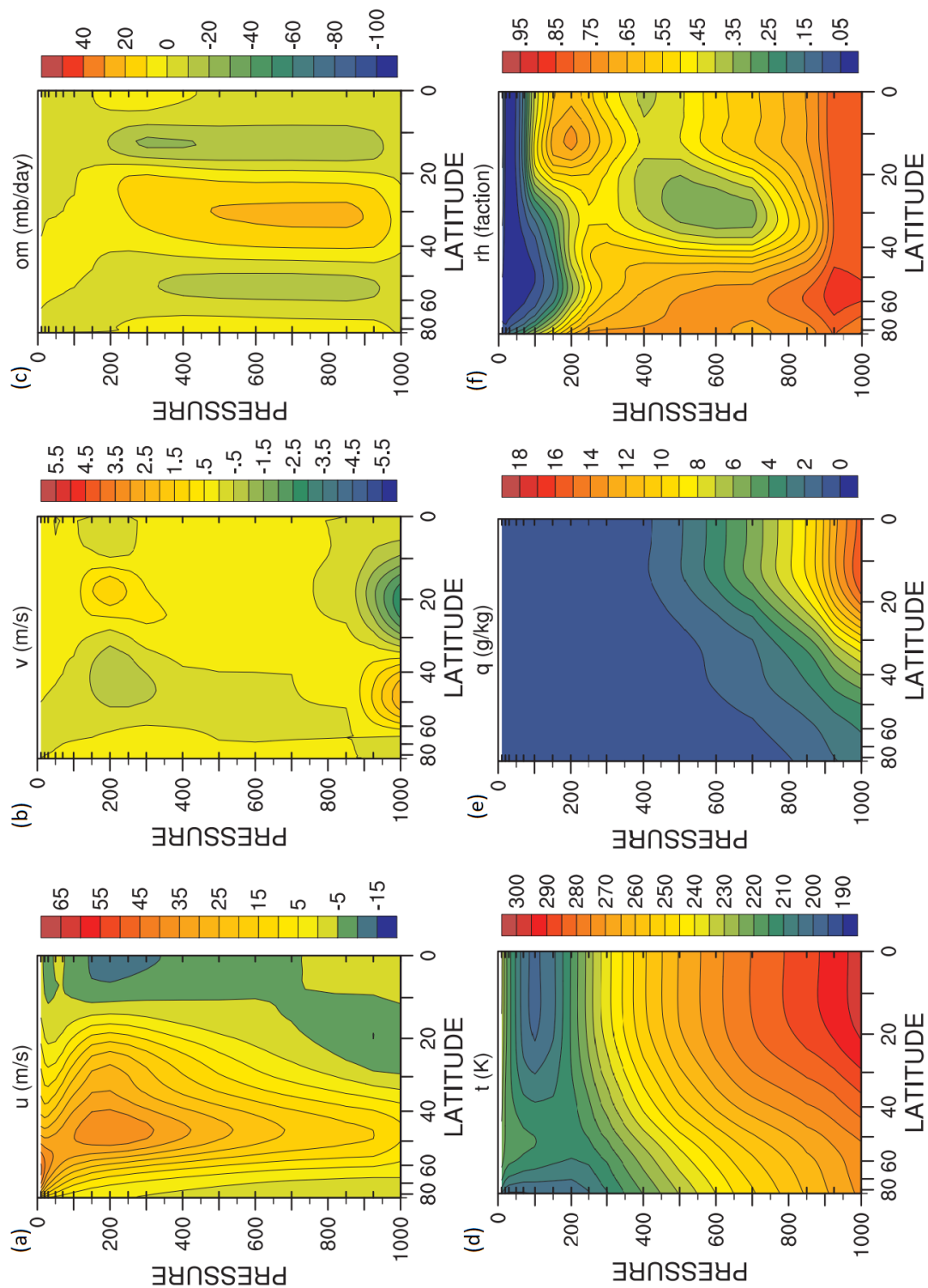


Figure 2.3.1: Multi-model mean fields, from the APE FLAT SST experiment. From left-to-right, top-to-bottom: (a) zonal wind (top-left), (b) meridional wind (top-middle), (c) vertical wind (top-right), (d) temperature (bottom-left), (e) absolute humidity (bottom-middle), and (f) relative humidity (bottom-right). Figures adapted from chapter 5 of Williamson et al. (2012).

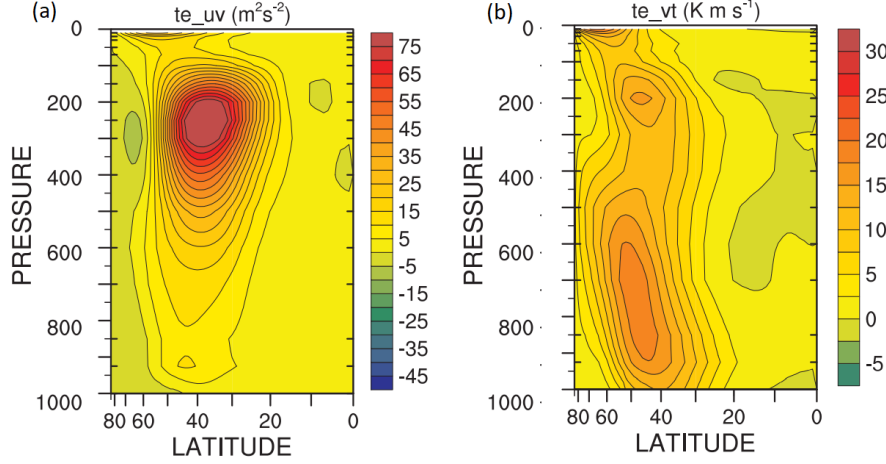


Figure 2.3.2: Multi-model mean transient eddies, from the APE FLAT SST experiment: (a) $\overline{u'v'}$ eddies (left panel), and (b) $\overline{v'\theta'}$ eddies (right panel) Figures adapted from chapter 5 of Williamson et al. (2012).

the subtropics, the air has lost much of its absolute humidity, and its relative humidity drops further as it descends into warmer temperatures. The former is a result of positive/negative Coriolis accelerations along the upper-/lower-branches of the tropical Hadley cell - the term $f[v]$ in equation (2.1.12). This induces upper-level westerlies and lower-level easterlies which get stronger with latitude, thereby causing the large vertical zonal wind shear along the poleward boundary of the Hadley cell. Furthermore, it is in agreement - via the thermal wind relation, equation (2.1.11) - with the sharp meridional gradients in temperature (bottom-left) we see in the subtropics.

In the midlatitudes, we see a continuation of this pattern of pronounced meridional temperature and vertical zonal wind gradients. The poleward eddy fluxes of westerly momentum and heat - shown in figure 2.3.2 - grow significantly in this region, with maxima at around 40° and 250hPa, and 50° respectively. The maxima in eddy momentum fluxes coincides with the equatorial flank of the midlatitude jet, and the poleward edge of the subtropical jet, a region of very sharp vertical zonal wind shear. As per equation (2.1.12), the divergence/convergence of eddy momentum fluxes equatorward/poleward of the maxima would lead to westerly deceleration/acceleration. Moreover, following equations (2.1.25) and (2.1.24), the divergence/convergence of eddy heat fluxes in the upper/lower midlatitudes seen in figure 2.3.2 would cause a vertical redistribution of this westerly momentum flux into that region, causing westerly deceleration/acceleration, and thereby reducing the vertical wind shear in that region. This is all reflected by the eddy-driven midlatitude jet we observe in that region, with a core just poleward of the maxima in eddy-momentum fluxes, and westerlies which extend down to the surface, leading to an overall reduced vertical wind shear relative to the subtropics. In thermal-wind agreement, we see slightly reduced meridional temperature gradients in the mid-

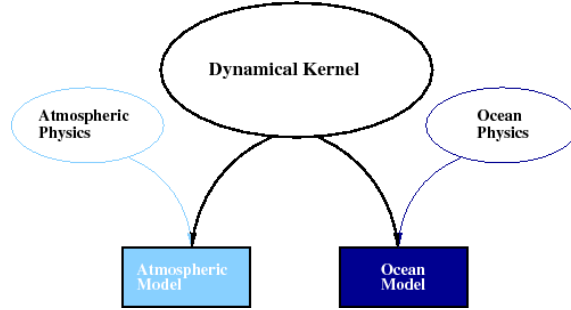


Figure 2.4.1: Schematic of how the MITgcm hydrodynamical kernel and physics packages combine to form distinct atmospheric and oceanic models. Figure taken from the MITgcm user manual (Adcroft et al. 2018), available online at www.mitgcm.org.

latitudes, reflecting the convergence of poleward eddy heat fluxes in the midlatitudes. These eddy momentum and heat flux convergence/divergence patterns are also what drives the upper and poleward/equatorward branches of the Ferrel cell we see in the midlatitudes, via equations (2.1.8) and (2.1.9).

2.4 The Model: MITgcm

Having laid out the mathematical tools and background relevant to our study, we will now describe key features of the model to be used, the MITgcm.

2.4.1 Dynamical Core

The MITgcm has a full hydrodynamical kernel: it fully solves the momentum, continuity, equation of state, thermodynamic, and tracer equations, for a given set of boundary conditions, for both the atmosphere and the ocean. Particular to the MITgcm is the fact that it utilises isomorphisms between the full equations of motion for the atmosphere and ocean, allowing it to operate with a single hydrodynamical core. Hence, particular vector and scalar quantities, such as velocity and geopotential height, are translated into generalised variables that have a different interpretation, depending on whether one is dealing with the atmosphere or the ocean. For example, instead of using pressure or height as its vertical coordinate, it uses the generalised vertical coordinate r , which becomes pressure/height when dealing with an atmosphere/ocean. By using one dynamical core instead of two, the MITgcm allows for a more streamlined approach to incorporating full atmosphere-ocean coupling, which will be of particular use to this study when it comes to looking at oceanic feedbacks on atmospheric changes.

For both the ocean and the atmosphere, the dynamical kernel is also paired with its own particular set of physics packages - atmospheric or oceanic physics - to form its own complete version of the model, with both dynamical and physical processes represented: see figure 2.4.1. The physics packages used are generally parameterisations of irreversible, diabatic and subgrid-

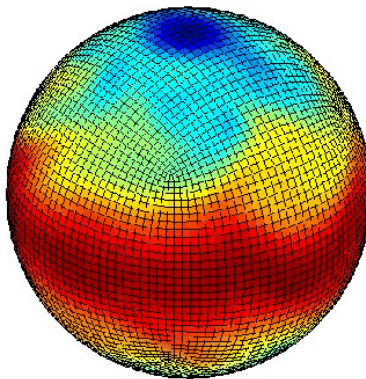


Figure 2.4.2: Instantaneous 3D plot of an atmospheric temperature field at 500hPa from MITgcm, illustrating the cubed-sphere grid used by the model. Figure taken from the MITgcm user manual (Adcroft et al. 2018), available online at www.mitgcm.org.

scale processes such as convection, diffusion, and radiative heating. These will be discussed in detail in the following subsections. By utilising a single dynamical core and parameterisations of other physical processes, the model is able to run fast, cheaply and efficiently, whilst at the same time not being overly-simplistic. Moreover, when we contrast this model with the types of simplified GCM's commonly used in previous studies, looking at the impact of STP's on the troposphere - see section 1.1.3 - it is clearly a more complex model, with more sophisticated physics parameterisations. Thus, when we come to analyse the results of applying STP's, even in an atmosphere-only setup, we should theoretically be able to - via comparison with the results of similar experiments with sGCM's from previous studies - be able to see what difference, if any, these superior physics parameterisations make to the results.

Another particular feature of the MITgcm is that, rather than the conventional latitude-longitude grid, the model uses a 'cubed-sphere' grid: the spherical topology of the model is projected onto six 32x32 square-shaped grids (CS32 grid), with the poles at the centres of two faces, and the other four faces centred around the equator. Figure 2.4.2 provides an illustration of how this grid maps back onto the original spherical topology. The utilisation of this type of grid removes the issue of convergence of the model equations at singularities around the poles, although it does introduce four corners into the midlatitudes of each hemisphere. Hence, care must be taken to ensure that the model is not running with a particular preference for wavenumber-4 behaviour. Another advantage over the conventional latitude-longitude grid is that the grid boxes have a more uniform size across the whole sphere. This means that convergence of the model equations can be achieved at the same resolution, but with larger timesteps, compared to a model with a conventional latitude-longitude grid, again allowing for a model which can run reasonably fast.

Since it is run on a cubed-sphere grid, the model uses vector-invariant forms of the momentum equations, such that they are independent on the type of gridding used. The model output is then given on the cubed-sphere grid, and must be regridded onto a latitude-longitude grid via

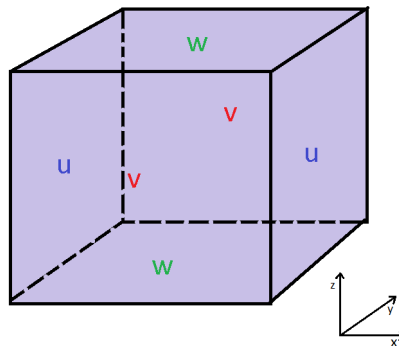


Figure 2.4.3: Schematic of a single grid cell in the MITgcm, and the relative points at which zonal, meridional, and vertical velocities are defined.

the Matlab routines, `cube2latlon.m` and `rotateuv2uvEN.m`, included as part of the MITgcm package. If performing further calculations with these variables, such as calculating the angular momentum or heat budget, it is better, for accuracy reasons, to perform all calculations on the cubed-sphere, and regrid to a latitude-longitude grid after, since the regridding process introduces small errors into the variables. An alternative approach is provided by, where possible, using vector-invariant quantities, such as vorticity, in lieu of their vector-dependent counterparts, such as velocity, and using corresponding vector-invariant forms of the essential equations.

Another feature of the gridding is that the separate zonal, meridional, and vertical components to the velocity field (u , v and w) and the tracer fields of humidity/salinity and potential temperature (s/q and θ) are defined at different points on each grid cell. As shown schematically in figure 2.4.3, the different velocity components are defined separately on the six cell faces, with the zonal, meridional, and vertical velocities defined on the east/west, north/south, and top/bottom cell faces respectively, whilst the tracers are defined at cell-centre. Moreover, compound quantities, such as $w\theta$, are defined at the same cell face as the velocity component, meaning interpolation of cell-centred values must be performed. These features of the gridding system are another reason why it is preferable to calculate derived quantities on the cubed-sphere grid first, and why great care must be taken when regridding to a latitude-longitude grid.

2.4.2 Atmospheric Physics Parameterisations

The module that encodes the atmospheric physics for MITgcm, `atm_phys.F90`, contains parameterisations for the surface stresses, turbulent heat fluxes, diffusion within the boundary layer, large-scale condensation, moist convection, and radiative transfer. It follows O’Gorman & Schneider (2008), and is based upon parameterisations presented in Frierson et al. (2006) and Frierson (2007). Here we will provide an outline of these parameterisations.

The model is run in one of three configurations: atmosphere-only (sst), slab-ocean (qflux),

or fully-coupled atmosphere-ocean (cpl). When run in the slab-ocean configuration, the ocean is treated as a well-mixed, static slab of water of constant depth, h , and salinity, that has a purely thermodynamic interaction with the atmosphere above. The net effects of oceanic circulation on the SST can be parameterised by a constant flux term, Q_{flux} , in the energy-balance equation, to give:

$$\rho c_p \frac{dSST}{dt} h = - (S + L_v E - \alpha SW_s^\downarrow - LW_s^\downarrow + \sigma T_s^4) - Q_{flux} \equiv -NSF - Q_{flux} \quad (2.4.1)$$

where S is the sensible heat flux, E is the evaporative flux, α is the albedo, SW_s^\downarrow and LW_s^\downarrow are the downward fluxes of shortwave and longwave radiation at the surface respectively, T_s is the surface temperature, and NSF is the net surface heat flux. All surface fluxes are defined positive upwards. Hence, when in equilibrium ($\frac{dSST}{dt}=0$), we have that $NSF = -Q_{flux}$.

When run in the fully-coupled configuration, the Q_{flux} term is replaced with the net advective and diffusive temperature tendencies caused by the oceanic circulation, and surface heat exchange with the atmosphere is confined only to the top model ocean layer, such that equation (2.4.1) only applies to the top model layer. Below this layer, the oceanic temperature tendencies are entirely controlled by the oceanic advective and diffusive heat fluxes. In the atmosphere-only configuration, there is no Q_{flux} term, and the SST is held constant.

The surface stress, sensible heat and evaporative fluxes, respectively, are parameterised using standard drag laws:

$$\tau = \rho_a C |\mathbf{v}_a| \mathbf{v}_a \quad (2.4.2)$$

$$S = \rho_a c_p C |\mathbf{v}_a| (\theta_a - T_s) \quad (2.4.3)$$

$$E = \rho_a C |\mathbf{v}_a| (q_a - q_0^*) \quad (2.4.4)$$

where q_0^* is the saturation specific humidity corresponding to the surface temperature, and ρ_a , \mathbf{v}_a , θ_a and q_a are the atmospheric density, wind speed, potential temperature and specific humidity, evaluated at the lowest model level, respectively. The drag coefficient, C , is calculated in accordance with Monin-Obukunov similarity (MOS) theory, and vanishes for values of the Bulk Richardson number:

$$Ri(z) = \frac{gz (\theta_v(z) - \theta_v(z')) / \theta_v(z')}{|\mathbf{v}(z)|^2} \quad (2.4.5)$$

that exceed the critical Richardson's number, Ri_c , where $z = z_a$ - the height of the lowest model level - and $z' = 0$.

Diffusion occurs within a boundary layer of depth h , such that the Bulk Richardson number, evaluated with $z = h$ and $z' = z_a$, exceeds $Ri_c = 1$. The diffusion coefficient, K , is calculated in accordance with MOS theory, and takes the functional forms outlined in Troen & Mahrt

(1986), and, again, vanishes for values of Ri that are less than $Ri_c = 1$. All the drag and diffusion coefficients are calculated with a roughness length, $z_0 = 0.05m$, for momentum, heat and moisture. The diffusive heating term takes the form:

$$Q = \frac{\partial}{\partial z} \left(K \frac{\partial \theta}{\partial z} \right) \quad (2.4.6)$$

Large-scale condensation occurs in the model when a grid-box becomes saturated, i.e. $q > q^*$, where q^* is the saturation specific humidity, calculated from the saturation vapour pressure, e^* , using $q^* = \varepsilon e^*/p$, with $\varepsilon = R_d/R_v$, where R_d is the gas constant for dry air, R_v is the gas constant for water vapour, and p is the pressure. The saturation vapour pressure itself is calculated from the Clausius-Clapeyron equation:

$$e^*(T) = e_0^* e^{-(L_v/R_v)[(1/T)-(1/T_0)]} \quad (2.4.7)$$

with fixed latent heat of vaporisation, $L_v = 2.5 \times 10^6 Jkg^{-1}$, and e_0^* is a reference value for the saturation vapour pressure at reference temperature $T_0 = 273.16K$. Upon saturation, the humidity of the gridbox is then adjusted as per:

$$\delta q = \frac{q^* - q}{1 + \frac{L_v}{c_p} \frac{dq^*}{dT}} \quad (2.4.8)$$

and the condensate falls out with no re-evaporation. Clouds are not included in the model parameterisations.

Moist convection is performed using a simple Betts-Miller scheme (BMS). Temperature and humidity are relaxed towards reference profiles, q_{ref} and T_{ref} - describing a moist adiabat up to the lifting condensation level (LCL), and a dry adiabat above, with 70% relative humidity relative to this temperature profile - using:

$$\delta q = -\frac{q - q_{ref}}{\tau_{SBM}} \quad (2.4.9)$$

$$\delta T = -\frac{T - T_{ref}}{\tau_{SBM}} \quad (2.4.10)$$

with convective relaxation time, $\tau_{SBM} = 2$ hours. The precipitation due to drying and warming, respectively, are then calculated:

$$P_q = -\int_{p_0}^{p_{LZB}} \delta q \frac{dp'}{g} \quad (2.4.11)$$

$$P_T = -\int_{p_0}^{p_{LZB}} \frac{c_p}{L_v} \delta T \frac{dp'}{g} \quad (2.4.12)$$

with the integrals ranging from the surface to the level of zero buoyancy (LZB). For convection to occur, one must have $P_T > 0$, indicating that the convective available potential energy

(CAPE) is greater than the convective inhibition (CIN). If, in addition, one has $P_q > 0$ - indicating that the column contains more moisture than the reference profile - deep convection will occur, and the temperature and humidity profiles are relaxed up to the reference profiles up to the LZB, in such a manner as to conserve enthalpy. If, rather, one has $P_q < 0$, as well as $P_T > 0$, then the temperature profile is relaxed to the reference profile up to the pressure level, p , such that:

$$P_q = - \int_{p_0}^p \delta q \frac{dp'}{g} = 0 \quad (2.4.13)$$

There is no diurnal or seasonal cycle in the model, with the aquaplanet kept at a perpetual equinox, and with top-of-the-atmosphere (TOA) insolation given by:

$$R_S = R_{S_0} [1 + \Delta_S p_2(\theta)] \quad (2.4.14)$$

where

$$p_2(\theta) = \frac{1}{4} [1 - 3 \sin^2(\theta)] \quad (2.4.15)$$

is the second Legendre polynomial, $R_{S_0} = 1360/4 \text{ W m}^{-2}$ - the annual global mean insolation - and $\Delta_S = 1.4$.

Radiation scheme

The atm_phys.F package contains an optional radiation module, radiation_mod.F90, which contains parameterisations for radiative transport using a grey atmosphere scheme. The exact parameterisation which will be used in conducting experiments for this study are those developed by Geen (2015), which compromise separate empirical parameterisations for window and non-window longwave emission and transmission, and downward shortwave transmission.

The parameterisation utilises the standard two-stream approximation. In the longwave, the upwelling, U , and downwelling, D , fluxes are given by:

$$\frac{dU_{LW}}{d\tau} = (U_{LW} - B) \quad (2.4.16)$$

$$\frac{dD_{LW}}{d\tau} = (B - D_{LW}) \quad (2.4.17)$$

with blackbody emission, B , given by:

$$B = \sigma_{SB} T^4 \quad (2.4.18)$$

where σ_{SB} is the Stefan-Boltzmann constant, and with surface and TOA boundary conditions:

$$(U_{LW})_{surface} = \sigma_{SB} T_s^4 \quad (2.4.19)$$

$$(D_{LW})_{TOA} = 0 \quad (2.4.20)$$

Under this scheme, the behaviour of two different 'bands' of longwave radiation are parameterised: a normal 'interactive' longwave band, with wavelengths in the region of $4 - 8\mu\text{m}$ or $14 - 100\mu\text{m}$, and a window band, with wavelengths in the region of $8 - 14\mu\text{m}$. The window band is set to comprise a specified fraction - 0.3732 - of longwave emission, calculated as the spectral window for water vapour. This window band is subject to much less atmospheric absorption than the other longwave band.

For the shortwave fluxes, there is no assumed emission, and any reflected radiation is taken to escape to space, simplifying the above set of equations to:

$$\frac{dD_{SW}}{d\tau} = -D_{SW} \quad (2.4.21)$$

$$U_{SW} = (1 - \alpha) (D_{SW})_{surface} \quad (2.4.22)$$

with TOA boundary condition:

$$(D_{SW})_{TOA} = R_S \quad (2.4.23)$$

The optical depths for the longwave, window, and shortwave schemes are calculated using the following empirical parameterisations:

$$\frac{d\tau^{LW}}{d\sigma} = 0.15493 + 351.48q^{\frac{1}{2}} \quad (2.4.24)$$

$$\frac{d\tau^{WIN}}{d\sigma} = 0.2150 + 147.11q + 10814q^2 \quad (2.4.25)$$

$$\frac{d\tau^{SW}}{d\sigma} = 0.0596 + \exp \left[\frac{0.01887}{\tau^{SW} + 0.009522} + \frac{0.01887}{(\tau^{SW} + 0.5194)^2} \right] \quad (2.4.26)$$

where τ is optical depth, σ is model pressure-level, and q is the specific humidity, kg/kg . These parameterisations capture the radiative effects of water vapour, and trace amounts of carbon dioxide, but neglect ozone. This can affect the tropopause height, particularly at the poles, where the ozone tends to accumulate due to the Brewer-Dobson circulation.

2.4.3 Oceanic Physics Parameterisations

When run in its fully-coupled atmosphere-ocean configuration, all net surface stresses, radiative, heat and water fluxes, from the atmosphere into the ocean, are transmitted to/absorbed by the top model layer only. Outside of this top layer, the only physical or subgridscale processes that are parameterised by the model are the advection and diffusion of tracers - salinity and temperature - by geostrophic eddies, with convection being implicit as vertical diffusion. These

processes are parameterised by the Gent-McWilliams/Redi (GMRedi) scheme, which itself is comprised of two separate schemes.

The first, the Redi scheme, follows Redi (1982), and diffuses tracers along isopycnals via a diffusion operator oriented along the local isopycnal, introducing the following term into the tendency equation of tracer, τ :

$$\nabla \cdot \kappa_\rho \mathbf{K}_{\text{Redi}} \nabla \tau \quad (2.4.27)$$

where κ_ρ is the along-isopycnal diffusivity, and \mathbf{K}_{Redi} is the 2-rank tensor, which projects $\nabla \tau$ onto the isopycnal surface:

$$\mathbf{K}_{\text{Redi}} = \frac{1}{1 + |\mathbf{S}|^2} \begin{pmatrix} 1 + S_y^2 & -S_x S_y & S_x \\ -S_x S_y & 1 + S_x^2 & S_y \\ S_x & S_y & |\mathbf{S}|^2 \end{pmatrix} \quad (2.4.28)$$

and \mathbf{S} is the isoneutral slope vector:

$$\mathbf{S} = (S_x, S_y) = \left(-\frac{\partial_x \sigma}{\partial_z \sigma}, \frac{\partial_y \sigma}{\partial_z \sigma} \right) \quad (2.4.29)$$

where σ is the dimensionless model level. Under the small slope approximation, $|\mathbf{S}|^2 \ll 1$, and the Redi projection tensor approximates to:

$$\mathbf{K}_{\text{Redi}} \simeq \frac{1}{1 + |\mathbf{S}|^2} \begin{pmatrix} 1 & 0 & S_x \\ 0 & 1 & S_y \\ S_x & S_y & |\mathbf{S}|^2 \end{pmatrix} \quad (2.4.30)$$

The second scheme, the GM scheme, follows Gent & McWilliams (1990) and Gent et al. (1995), and adiabatically advects tracers via a bolus velocity, \mathbf{u}^* , introducing the following term into the tracer tendency equation:

$$-\nabla \cdot \tau \mathbf{u}^* \quad (2.4.31)$$

The bolus velocity field is defined as the curl of a streamfunction, \mathbf{F}^* , itself defined in terms of the isoneutral slope components:

$$\mathbf{u}^* = \nabla \times \mathbf{F}^* \quad (2.4.32)$$

$$\mathbf{F}^* = (F_x, F_y, 0) = (-\kappa_{GM} S_y, \kappa_{GM} S_x) \quad (2.4.33)$$

and κ_{GM} is a function of non-dimensional constant, α , length scale, L , and the vertically-averaged Eady growth rate, $\overline{\sigma_B}^z$:

σ	1	2	3	4	5	6	7	8	9
Pressure (hPa)	980	940	900	860	820	780	740	700	660
Depth (m)	16	55	111	190	298	438	611	817	1055
σ	10	11	12	13	14	15	16	17	18
Pressure (hPa)	620	580	540	500	460	420	380	340	300
Depth (m)	1326	1630	1967	2337	2739	3174	-	-	-
σ	19	20	21	22	23	24	25		
Pressure (hPa)	260	220	180	140	100	60	20		
Depth (m)	-	-	-	-	-	-	-		

Table 2.5.1: Table giving the cell-centre pressure and depth values corresponding to each model level (σ) in the atmosphere and ocean respectively.

$$\kappa_{GM} = \alpha L^2 \overline{\sigma_B}^z = \alpha L^2 \frac{\overline{|f|^2}^z}{\sqrt{Ri}} \quad (2.4.34)$$

We note that, within the model, the components of the bolus streamfunction, ψ_{GM} , are defined in terms of the components of streamfunction \mathbf{F}^* , as:

$$(\psi_{GM,x}, \psi_{GM,y}) = (F_y, -F_x) = (\kappa_{GM} S_x, \kappa_{GM} S_y) \quad (2.4.35)$$

2.5 Model configuration

As mentioned earlier, we will run the model in three configurations: atmosphere-only (sst), slab-ocean (qflux), and fully-coupled atmosphere-ocean (cpl). The model atmospheres have identical configurations in each setup, with 25 equally-spaced pressure levels of width 40hPa, from 1000hPa at the surface, to 0hPa at the top-of-atmosphere. In the atmosphere-only and slab-ocean setups, the ocean is a mixed layer of depth 50m, with SST that is held fixed/evolves as per equation (2.4.1) respectively. In the fully-coupled setup, the ocean is a fully-dynamical ocean, with 15 unevenly spaced depth-levels, from 0 to 3400m depth, the vertical height of each level rising with increasing depth, from 32m for the top layer, to 452m for the bottom layer. Table 2.5.1 gives the cell-centred pressure and depth values which correspond to each atmosphere and ocean model level. On both the atmosphere and ocean, analogous boundary conditions are placed, with $w=0$ at both the top of the atmosphere and bottom of the ocean, and a moving nonlinear free surface at the interface between the two media. The grid resolution is C32, or 32x32 grid points on each face of the cube-sphere, giving a total resolution of 192x32. This corresponds to a resolution of approximately 2.8° at the equator, and up to around 3.9° at 45° latitude.

To arrive at the control setup of our fully-coupled atmosphere-ocean model, the global ocean is placed in an aquaplanet, double-drake configuration, illustrated by figure 2.5.1: the entire planet is covered by a global ocean, of constant 3400m depth, with no orography, except for two

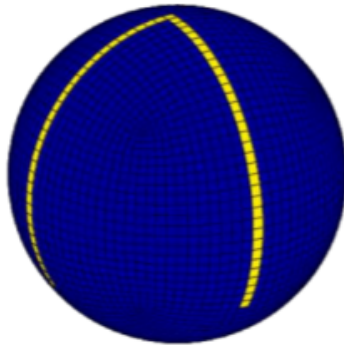


Figure 2.5.1: 3D cube-sphere aquaplanet ocean model, with double-drake ridges highlighted in yellow. Adapted from a figure on John Marshall’s personal webpages at www.oceans.mit.edu.

oceanic ridges at a 90° longitudinal separation, and extending latitudinally from 90°N to 30°S . However, the albedo is set closer to that of the Earth than that of the open ocean, at 37%. This is done primarily to achieve an atmospheric climatology similar to that of Earth, which has an albedo of around 30%, whilst also accounting for the fact that the atmospheric physics package contains no cloud physics parameterisations, as cloud cover would typically raise the planetary albedo. Moreover, lower planetary albedos were found to lead to overly-strong, or even unstable, tropospheric zonal winds, extending high up into the model atmosphere, whilst higher albedos would have the opposite effect. The model is run for approximately 2000 years until equilibrium is reached, which we define as being when the global-average net surface heat flux - as defined in equation (2.4.1) - becomes and remains consistently below 0.1Wm^{-2} , averaging over a timeperiod of around 10 years.

Once the control setup and climate of the fully-coupled atmosphere-ocean model has been arrived at, from there we diagnose and calibrate the slab-ocean and atmosphere-only model control setups to match this control climatology. This is achieved by taking 300-year time-averaged values of the fully-coupled model control setup’s SST’s and net surface heat fluxes (NSF), inverting the latter into the Q-flux term via equation (2.4.1), setting $\frac{dSST}{dt} = 0$ such that $Q_{flux} = -NSF$. These SST and Q-flux values are then imposed in a slab-ocean setup. In the case of the slab-ocean setup, the SST’s are allowed to evolve according to equation (2.4.1), whereas in the atmosphere-only setup, they are held fixed at the fully-coupled control values. As with the fully-coupled atmosphere-ocean version of the model, the models are then allowed to run until they reach equilibrium, which takes approximately 10 years and 200 days in the slab-ocean and atmosphere-only setups respectively. The end result is three control model setups, in which the atmospheres and SSTs look almost identical, but with varying degrees of atmosphere-ocean coupling present. We will now provide a description of these control climatologies in the following subsection.

2.6 Control climatology

2.6.1 Atmosphere

Figure 2.6.1 displays the control values of various atmospheric fields in the control fully-coupled atmosphere-ocean setup. The slab-ocean and atmosphere-ocean control climatologies are almost identical. We see that the model atmosphere possesses a two-cell circulation structure, with Hadley and Ferrel cells of approximate latitudinal extent of around 30° , located between 0° to 60° , in both hemispheres. As with the ordinary atmosphere, we observe almost-flat temperature and humidity gradients in the tropical and equatorial regions respectively, with a significant negative meridional humidity gradient in the subtropics, causing that region to have very low relative humidities, down to a minimum of about 45%. These meridional humidity gradients within the tropics reflect the patterns of vertical wind in that region, with moist, rising parcels of air around the equator, and falling, desaturated parcels around the subtropics, as air parcels follow the Hadley circulation in those regions.

In the stratosphere, we observe strong polar vortices centred around 60° , of maximum speed 35m/s at the top-of-atmosphere. In the troposphere, we see a single midlatitude jet in each hemisphere, centred around 40° , and with maxima of around 30m/s around the tropopause level at 250hPa. The patterns of zonal winds in the extratropical troposphere and stratosphere reflect the patterns in the meridional temperature gradients, as per the thermal wind relation, equation (2.1.11).

Overall, the climatology is quite similar to that seen in the APE-FLAT SST experiment, as detailed in section 2.3. The main differences are in the subtropics/midlatitudes, with an equatorward-shifted region of subtropical descent, and narrower and equatorward-shifted Ferrel cells and eddy-driven midlatitude jets, the latter of which has merged with the subtropical jet to form a single-jet structure. That said, these differences - particularly the differences in jet structure - are probably smaller than they appear at first glance, owing to the nonlinear latitude axis used in the APE climatology plots, which affords greater breadth to features in the tropics, versus the mid-to-high latitudes. Moreover, the APE-FLAT SST profile is steeper in the midlatitudes, with a greater tropical SST (27°C vs. 23°C), and similar SST at 60° . This would leader to a stronger meridional temperature gradient in the midlatitudes, and thus a stronger zonal wind vertical shear, and possibly also greater eddy fluxes into the midlatitudes. These differences combined should explain the main differences in climatology we see in the midlatitudes between these different setups.

The top-left and -right panels of figure 2.6.2 display the meridional eddy fluxes of westerly momentum and potential temperature, $[\overline{uv}]_{eddy}$ and $[\overline{v\theta}]_{eddy}$, respectively. As with Earth and the APE, local maxima in poleward eddy momentum flux exist around the locations of the midlatitude jet cores and polar vortices, meaning that, as per equation (2.1.12), the eddies transport westerly momentum away from the tropics/low latitudes, and into the midlatitudes/high latitudes in the troposphere/stratosphere. This accelerates the poleward flanks of the midlatitude

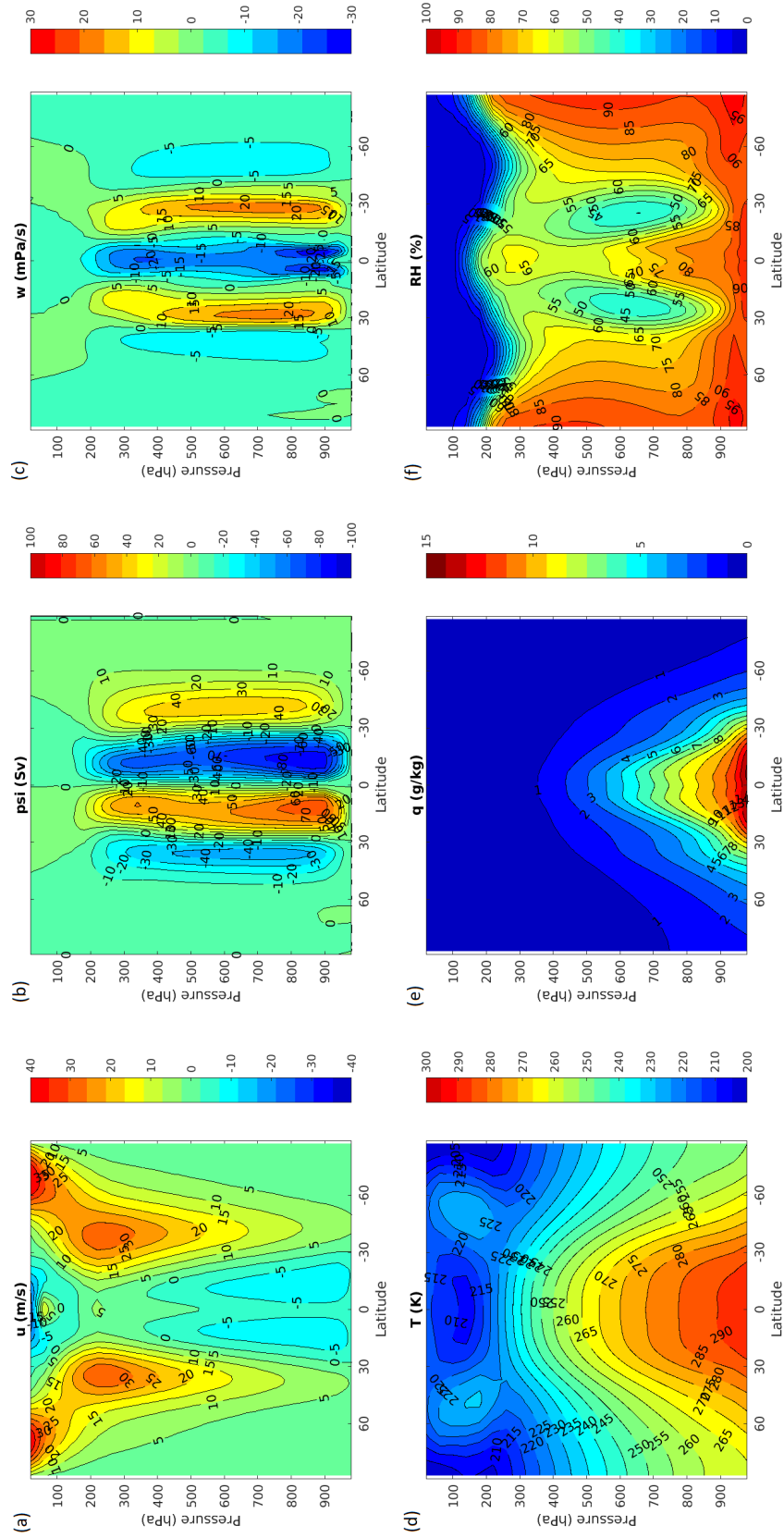


Figure 2.6.1: 300-year mean climatological fields from control fully-coupled atmosphere-ocean run. From left-to-right, top-to-bottom: (a) zonal wind (top-left), (b) mass streamfunction (top-middle), (c) vertical wind (top-right), (d) temperature (bottom-left), (e) absolute humidity (bottom-middle), and (f) relative humidity (bottom-right).

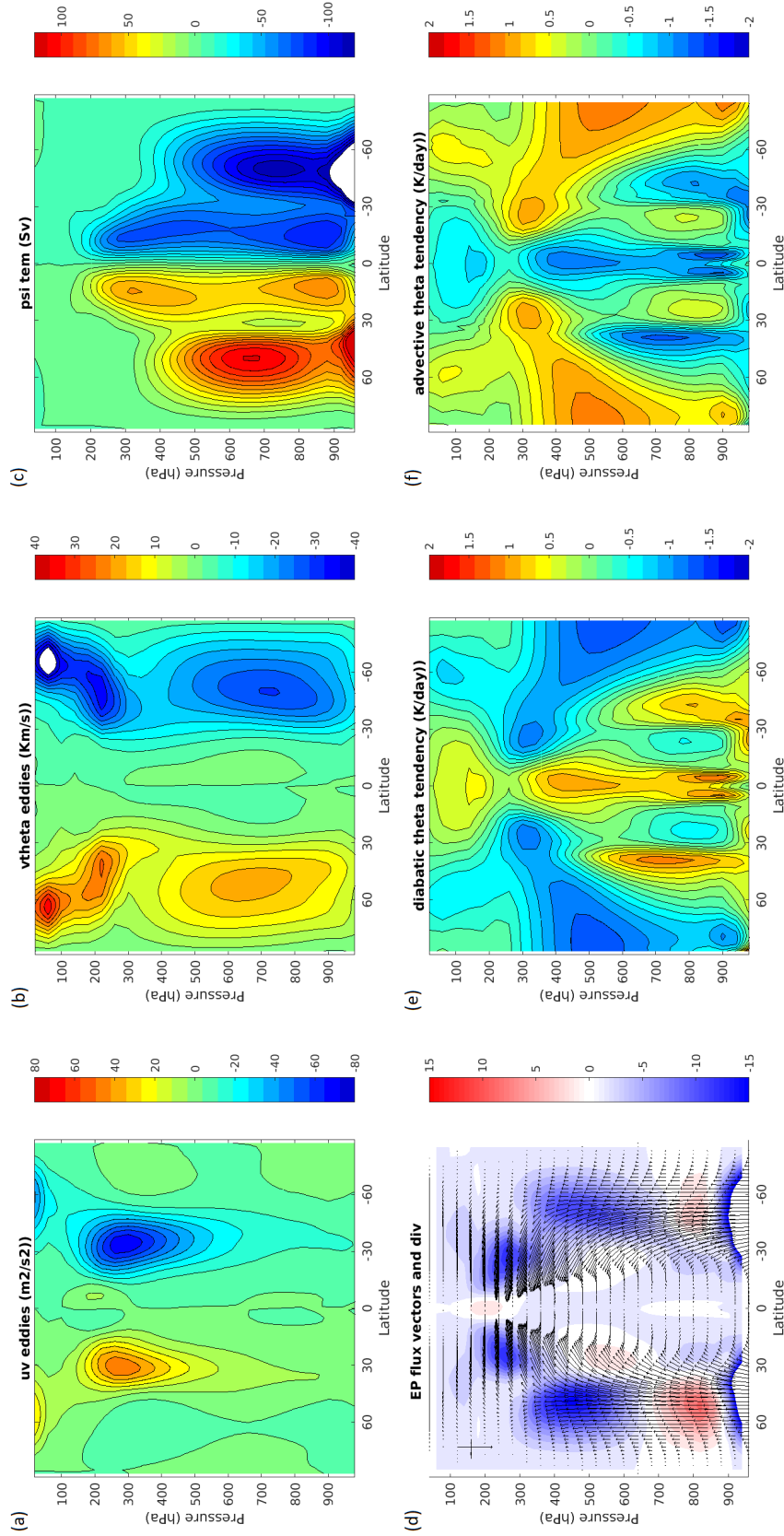


Figure 2.6.2: 300-year mean climatological fields from control fully-coupled atmosphere-ocean run. From left-to-right, top-to-bottom: (a) meridional westerly eddy momentum fluxes, $[\overline{uv}]_{eddy}$ (top-left), (b) meridional potential temperature eddy fluxes, $[\overline{v\theta}]_{eddy}$ (top-middle), (c) TEM residual mass streamfunction, $\tilde{\psi}$ (top-right), (d) EP fluxes (colours) and divergences (arrows), $[\overline{v\theta}]_{eddy}$ (top-right), (e) diabolic potential temperature tendencies (bottom-left), and (f) advective potential temperature tendencies (bottom-right). In the EP flux diagram, the fluxes are mass-weighted as per equations (2.1.32) and (2.1.33), the contour intervals are $1.5 \times 10^{16} m^3$ and $5 \times 10^{20} m^3 Pa$ respectively. The fluxes are scaled such that the horizontal and vertical arrows in the top-left have lengths $5 \times 10^{14} m^3$ and $5 \times 10^{20} m^3 Pa$ respectively.

tropospheric jets, and the stratospheric vortices. In the meridional eddy heat fluxes, we see significant, poleward eddy fluxes of heat in the mid-to-high latitudes, with local maxima at around 45° and 700hPa in the troposphere, causing a net flow of heat away from the subtropics, 20° - 45° , and into the extratropics, 45° - 90° , in the troposphere, and similar equatorward/poleward of the polar vortex in the stratosphere.

The top-right and bottom-left panels of figure 2.6.2 display the control values of the TEM residual circulation, EP fluxes and their divergences, respectively, calculated as per equations (2.1.21), (2.1.32), (2.1.33) and (2.1.30). There is a strong correspondence between the Eulerian and residual streamfunctions in the tropics, whilst in the midlatitudes, the large meridional eddy heat fluxes force the residual circulations in that region to circulate in the opposite sense to the Ferrel cells. We similarly see large upward EP fluxes in this region, which grow/diverge as they move upwards in the lower troposphere, and diminish/converge as they move upward in the upper troposphere, in agreement with the general pattern of $\frac{\partial[v^*\theta^*]}{\partial p}$, which is positive/negative in the midlatitude lower/upper troposphere. In the upper troposphere, the lower latitude EP fluxes tilt progressively more towards the equator, converging at around 30° and 250hPa, again reflecting the patterns of the eddy-momentum fluxes in this region.

The bottom-middle and -right panels of figure 2.6.2 display the equilibrium diabatic and advective atmospheric heating rates. The two are obviously equal and opposite, balancing equation (2.1.9), with the diabatic heating driving heating in the tropics and midlatitude lower troposphere, and cooling elsewhere, driving the observed equator-to-pole temperature gradient, whilst the advective heating does the exact opposite. Decomposition of the diabatic heating term into its individual components, as parameterised by the physics packages described in section 2.4.2, reveals that the low-latitude heating is largely driven by convection in the tropics, and condensation in the midlatitudes, and the dominant cooling we see elsewhere is largely radiative. Likewise, when we look at the individual components to advective heating, we see that, to a large degree, it is driven by the $[\overline{v\theta}]_{eddy}$ and $[\overline{\omega}][\overline{\theta}]$ heat fluxes, or equivalently, the $\frac{\partial(\overline{\omega}[\overline{\theta}])}{\partial p}$ term on the LHS of equation (2.1.26), indicating that the residual TEM circulation does indeed fairly well capture the net heating/cooling by the total advective heat fluxes. To see this demonstrated, see section 3.2.1.

2.6.2 Surface

Figure 2.6.3 displays the control values for surface precipitation (top-left), heat fluxes (top-middle/-right and bottom-left), and wind stresses (bottom-middle/-right). Within the tropics, we observe high levels of precipitation (top-left) and downward surface heat fluxes (top-middle) around the equator, and the converse in the subtropics. Looking at the radiative and turbulent heat fluxes - shown in the top-right and bottom-left panels - we see that these latitudinal variations in surface heat flux are driven by decreasing levels of downward radiative fluxes - largely shortwave fluxes, when we decompose this term - and increasing levels of upward turbulent heat fluxes - largely latent heat fluxes - as we move polewards within this region.

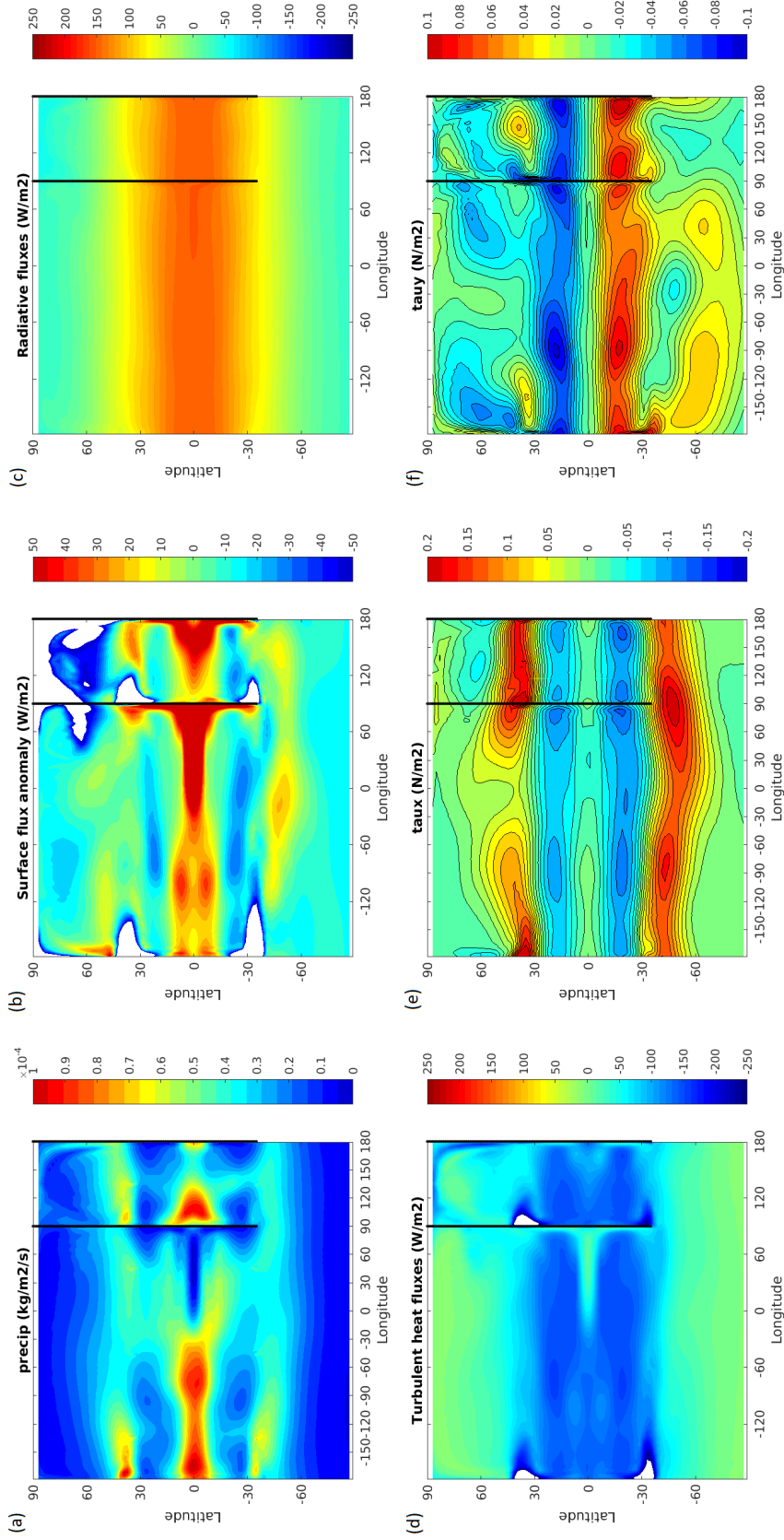


Figure 2.6.3: 300-year mean surface climatological fields from control fully-coupled atmosphere-ocean run. From left-to-right, top-to-bottom: (a) precipitation (top-left), (b) net heat fluxes (radiative + turbulent heat fluxes) (top-middle), (c) radiative fluxes (LW + SW fluxes) (top-right), (d) turbulent heat fluxes (sensible + latent heat fluxes) (bottom-left), (e) zonal wind stress (bottom-middle), and (f) meridional wind stress (bottom-right). The surface fluxes and stresses are positive downward (from the atmosphere, into the ocean).

This latter feature can be explained by the relative levels of humidity around the equator versus the subtropics, discussed in section 2.6.1, leading to a relatively high surface humidity gradient, $\delta q = q_{sat} - q_{surf}$, in the subtropics, and thus higher levels of evaporation. A similar argument can be used to explain the low precipitation values in the subtropics, and has already been outlined in section 2.6.1 to account for the low relative humidities in the subtropics, insofar as the poleward-moving air parcels have already precipitated around the equator.

In the extratropics, there is an initial increase in levels of precipitation and upward surface heat fluxes 30° - 40° , around the subtropical gyres (see section 2.6.3). Similar to the equatorial region, this is probably due to higher levels of relative humidity in this region, causing greater precipitation, plus also strong surface westerlies, leading to stronger upward latent heat fluxes via the bulk formula (see equation (2.4.4)). Polewards of this, the fluxes of precipitation and heat become very weak as we move into the cold and dry high latitudes. Only in the high-latitude small basin do we see significant fluxes of precipitation and upward turbulent heat flux. This can be attributed to the relatively high sea surface temperatures in this region - see figure 2.6.4 in section 2.6.3 - leading high levels of evaporation. Given this, it is evident in this region that the warm SST's are not driven by the surface heat fluxes, but the oceanic heat fluxes, which - as per equation (2.4.1) - must balance the former at equilibrium.

The surface wind stresses - shown in the bottom-middle and -right panels of figure 2.6.3 - reflect the meridional patterns of surface zonal and meridional wind, with negative/positive values of zonal wind stress in precisely the regions where the surface zonal winds are easterly/westerly, and negative/positive values of meridional wind stress in the tropical NH/SH, reflecting the strong equatorward surface winds which form the bottom branches of the tropical Hadley cells. Further poleward, the meridional wind stresses exhibit a more zonally-asymmetric character, with wavenumber-2/3 patterns, reflecting the dominance of eddy-mediated meridional momentum transport in the extratropics.

2.6.3 Ocean

Figure 2.6.4 displays the surface or near-surface values of ocean temperature, salinity, zonal, meridional, and vertical velocity, and the total depth-integrated horizontal barotropic streamfunction, in the control run of the fully-coupled atmosphere-ocean setup. As with the atmosphere, we see a reasonably good correspondence with the actual oceanic climatology on Earth, especially when one considers the relative simplicity of the ocean model. In the Northern Hemisphere, the ocean currents form equatorial (0° to 15° ; counterclockwise), subtropical (15° to 40° ; clockwise), and polar (40° and up; counterclockwise) gyres in the North Hemisphere basins. In the Southern Hemisphere, they form narrow equatorial and subtropical gyres 0° to 35° , polewards of which lies a strong west-east circumpolar current, strongest in the midlatitudes. Along the equator and in the midlatitudes, diverging meridional currents force upwelling, whilst in the subtropics converging meridional currents force downwelling, via the continuity equation. Taken together, these currents imply an overturning circulation in the tropics similar to a Hadley cell,

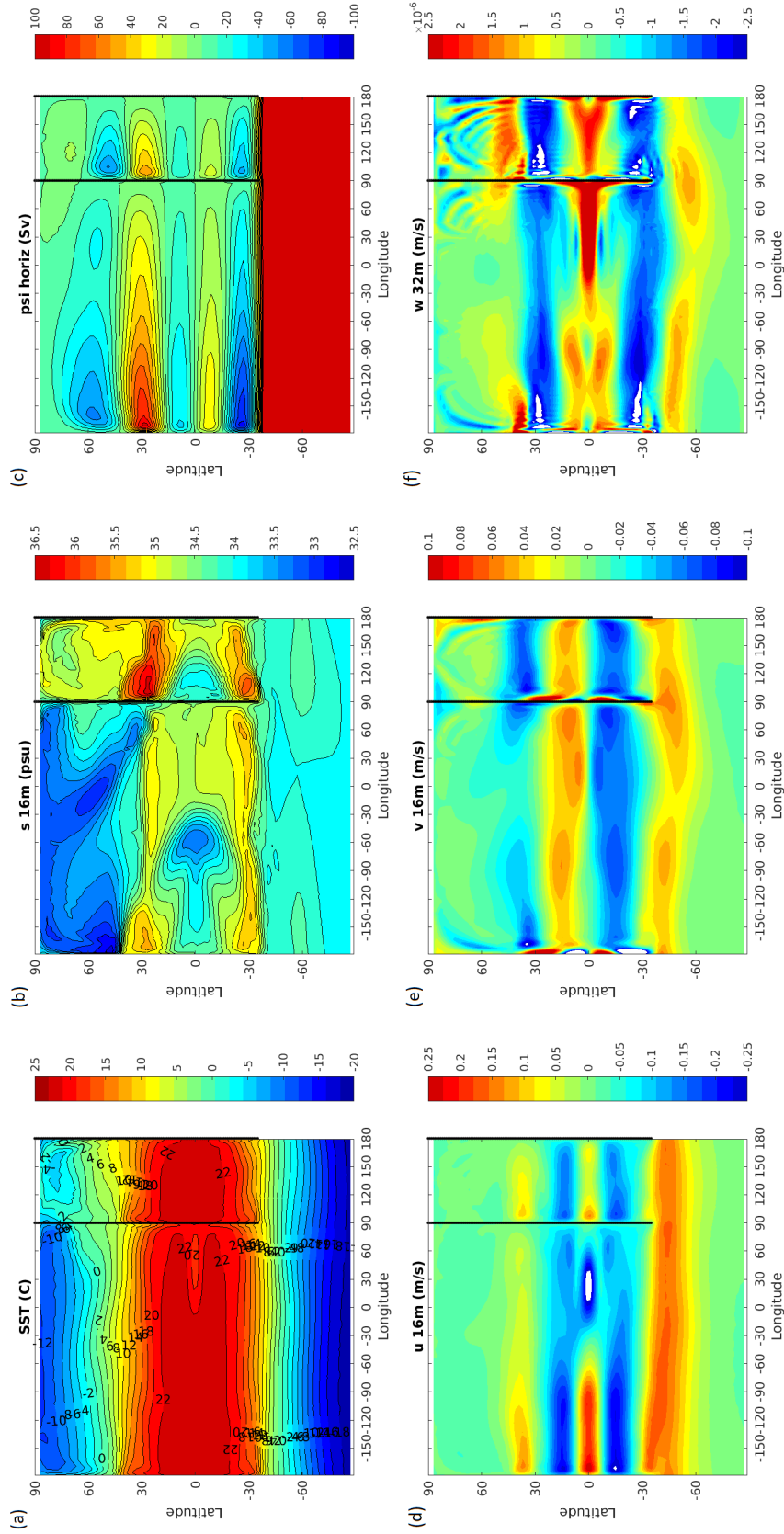


Figure 2.6.4: 300-year mean oceanic climatological fields from control fully-coupled atmosphere-ocean run. From left-to-right, top-to-bottom: (a) sea surface temperature (top-left), (b) salinity at 16m (top-middle), (c) barotropic streamfunction (top-right), (d) zonal velocity at 16m (positive eastward; bottom-left), (e) meridional velocity at 16m (positive northward; bottom-middle), and (f) vertical velocity at 32m (positive downward; bottom-right).

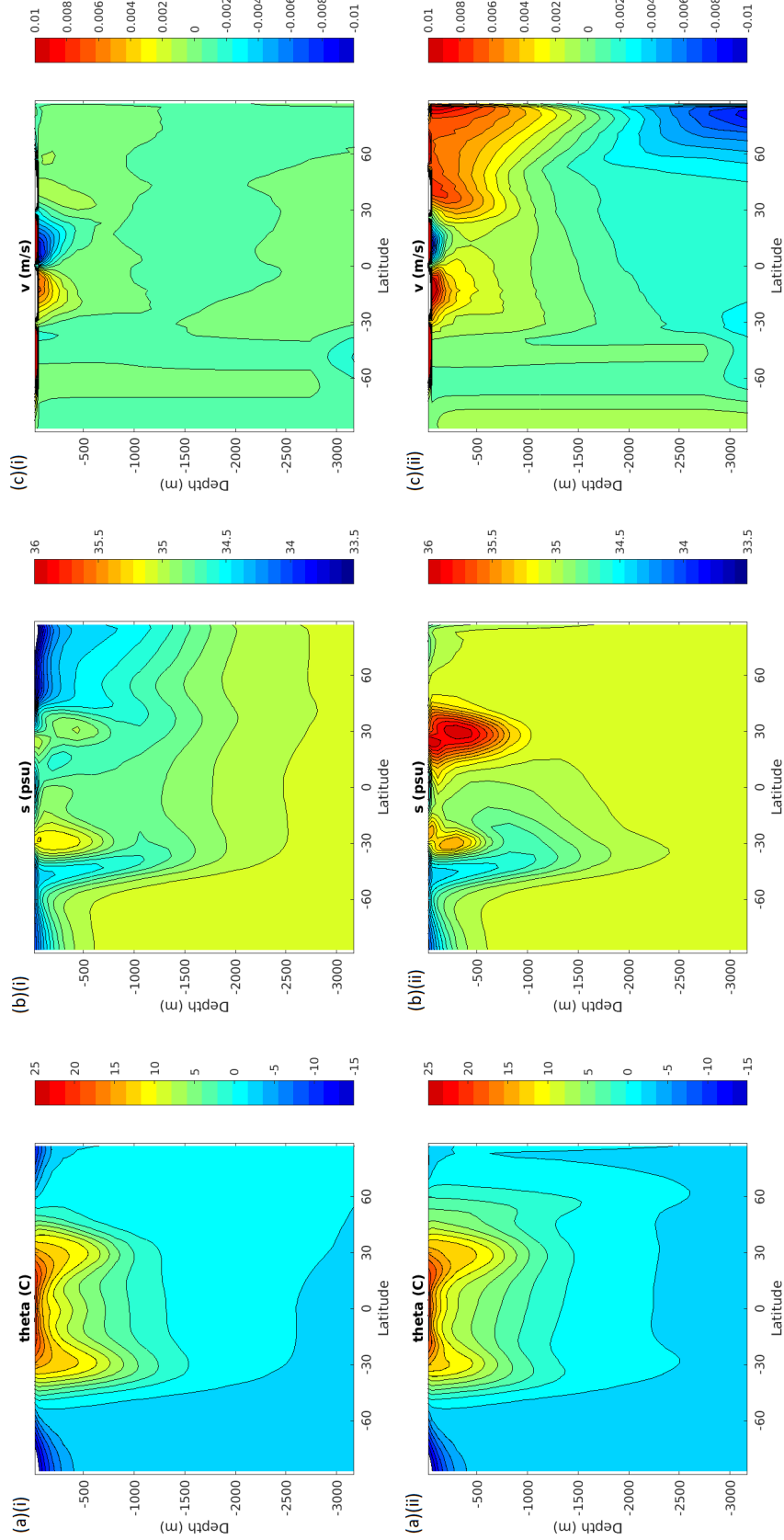


Figure 2.6.5: 300-year mean oceanic climatological fields from control fully-coupled atmosphere-ocean run. From left-to-right: (a) potential temperature (left panels), (b) salinity (middle panels), and (c) meridional velocity (positive northward; right panels). Top/bottom panels correspond to values zonally-averaged over the large (0° to 90°W)/small basins (90°W to 0°) respectively.

and could explain the relatively flat sea surface temperatures we see in the tropics, as well as the sharp temperature and salinity gradients we see at its boundary around 30° . In addition, the excess salinity we see in the subtropics compared with the equatorial region can be explained with reference to the precipitation patterns, shown in figure 2.6.3. Hence, whilst the equatorial region sees copious freshening of the water via precipitation, in the subtropics the lack of precipitation, and overlying hot, dry air causes excess evaporation, hence making the water more saline.

Figure 2.6.5 displays the potential temperatures (left panels), salinities (middle panels), and meridional velocities (right panels) on a latitude-depth grid, zonally-averaged over the large (top panels) and small (bottom panels) basins respectively. We see how, in the tropical-/polar-latitudes, temperature - and to a lesser extent the salinity - broadly decreases/increases with increasing depth, demarcating the tropical-/extratropical- thermocline/halocline, or pycnocline collectively. Also, around 30° , there are sharp meridional gradients in the temperature and salinity fields, with temperature and salinity increasing/decreasing sharply as one moves equatorward/poleward, in both hemispheres. This demarcates the boundary between tropical and extratropical pycnoclines, and coincides with the poleward, downwelling branch of the tropical overturning 'cell' we see in both hemispheres, above 500m, in the tropics.

Another important feature to point out is the deep overturning circulation seen north of 30°S in the small basin, shown in the bottom-right panel of figure 2.6.5. This overturning circulation - with waters in the top 1000m moving north from 30°S to 90°N , and then downwards and flowing back southwards through the deep ocean - is mainly absent in the large basin, shown in the top-right panel. It can also help to explain the very large accumulation of salinity - and to a lesser extent heat - centred around 30°N and 400m in the small basin, as heat and salinity are advected away from Southern Ocean region, and into the North Atlantic region of the small basin.

It must also be noted - as seen in the top-left panel of figure 2.6.4 and the left panels of figure 2.6.5 - that the oceanic temperatures in the high-latitudes are often below 0°C , with SST's reaching as low as -18°C in the polar Southern Ocean region. These low temperatures are a consequence of two details of the setup: the relatively high albedo used, at 37%, and the lack of an ocean ice physics package. The former point has already been explained in section 2.5 as necessary for providing stable and realistic atmospheric zonal winds. The latter was more a result of the relevant package not being compatible with the gray radiation package used within the atmospheric model, outlined in section 2.4.2. Clearly, more work needs to be done to make these packages compatible with each other, and perhaps to make the radiation package more stable in general. However - as discussed in section 1.2.2 - the extratropical atmosphere responds more to changes in extratropical meridional SST gradient than to changes in absolute extratropical SST. Furthermore - as shall be seen in section 5 - the feedback on the atmosphere is largely controlled by the changes in tropical SST. Thus, it is the author's view that the absence of sea ice - and consequent very low polar oceanic temperatures - should not greatly impact upon the validity of our results.

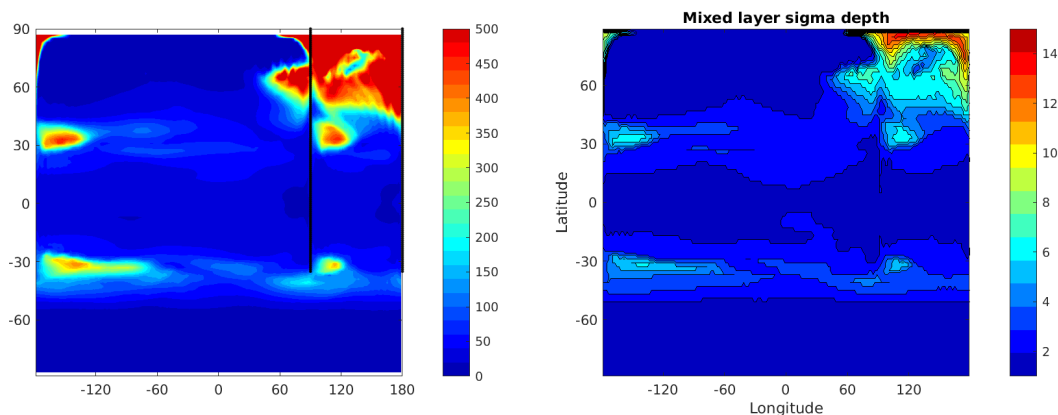


Figure 2.6.6: 300-year mean oceanic mixed-layer depths - absolute (left), and sigma-level (right) - from control fully-coupled atmosphere-ocean run. Contour level spacing is set at 20m/1 for the left/right plot.

Mixed layer

Figure 2.6.6 shows the oceanic mixed layer depths - both absolute as calculated by the model, and interpolated onto sigma-levels - in the control fully-coupled atmosphere-ocean run. We see that, for the most part, the oceanic mixed layer is relatively shallow, with depths below 60m in the vast majority of the global ocean, and below 20/40m in the high-latitude Southern Ocean, North Pacific, and equatorial regions, providing a sigma-level depth of one and essentially exposing the thermocline to the surface in those regions. The regions where we do have mixed layers of significant depth correspond roughly to the locations of the poleward subtropical gyres' boundaries (see figure 2.6.4), and the high-latitude North Atlantic region. Overall, global-mean and -median values for the mixed layer depth are calculated to be 119m and 98m respectively. In subsequent analyses, we will therefore treat $z=0-144\text{m}$, or the top three sigma-layers, $\sigma = 1-3$, as our oceanic pseudo-mixed layer.

Figure 2.6.7 shows the oceanic advective and diffusive heat fluxes, integrated over our oceanic pseudo-mixed layer. Large advective cooling/heating is seen in the equatorial/subtropical regions, largely driven by patterns of upwelling, cold water along the equator, and downwelling, water warm along the subtropics. Further poleward, the advective heat fluxes become dominated by horizontal heat fluxes, with cooling/heating in the middle-/high-latitudes driven by equatorward-/poleward-flows of water in those regions - see section 4.2.3 for more details. As expected, significant diffusive heating is seen in the regions where the mixed layer depth exceeds 144m, and further investigation identifies this diffusive heating as driven by vertical diffusion, or equivalently convection. We therefore see how the diffusive fluxes into/out of our pseudo-mixed layer are broadly negligible, except for the regions with higher calculated mixed-layer depths.

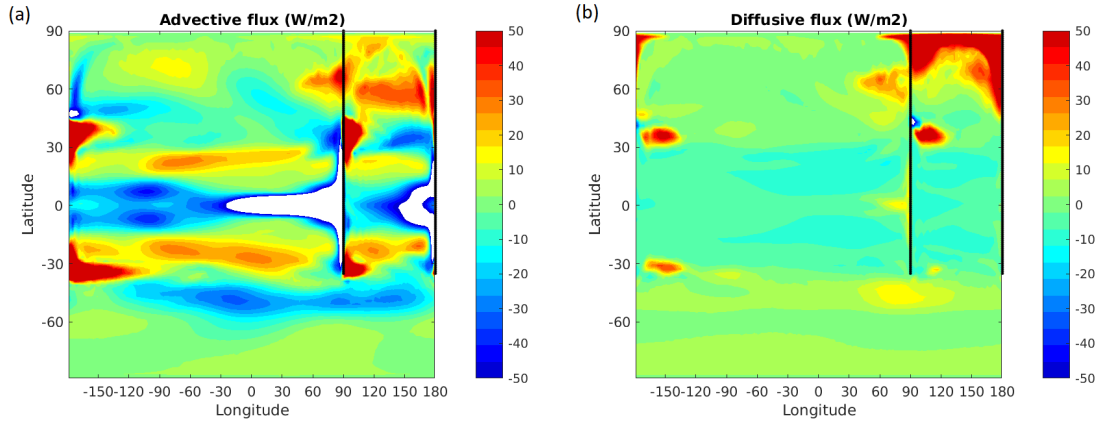


Figure 2.6.7: 300-year mean oceanic potential temperature tendencies from control fully-coupled atmosphere-ocean run due to ocean heat: (a) advection (left), and (b) diffusion (right), both vertically-integrated over the top 144m ($\int_{-144m}^0 \rho c_p \dot{\theta} dz$). Contour intervals are set to 5 Wm^{-2} .

2.7 Experiments

Having outlined the model used, the configurations it is placed in, and the climatology of the control run, we will now provide an outline of the experiments to be conducted in these model setups, and their implementation.

The main aim of the project is to investigate the impact of atmosphere-ocean coupling upon the tropospheric response to applied STP's. This will be achieved by conducting experiments in which fixed temperature tendency perturbations, $\delta \dot{T}$, are applied to the model stratosphere via their addition to the radiative temperature tendency term, Q_{rad} , and comparing the results we obtain between the different setups: atmosphere-only, slab-ocean and fully-coupled atmosphere-ocean.

The first step is thus to identify the model stratosphere. The tropopause - the boundary between the troposphere and stratosphere - is diagnosed following the criteria set forth by the World Meteorological Agency (see Slownik 1992):

The boundary between the troposphere and the stratosphere, where an abrupt change in lapse rate usually occurs. It is defined as the lowest level at which the lapse rate decreases to 2°C/km or less, provided that the average lapse rate between this level and all higher levels within 2 km does not exceed 2°C/km .

The stratosphere is then diagnosed as the atmospheric model levels above this initial, threshold change in the lapse rate. Figure 2.7.1 shows the lapse rates (colours) and stratosphere (black crosses/hatching) as defined by this criteria, for the fully-coupled atmosphere-ocean control run. Since variations in the lapse rate are small between the different model setups, the stratospheres are identically prescribed in each setup.

Having diagnosed the model stratosphere, fixed perturbations to the radiative temperature

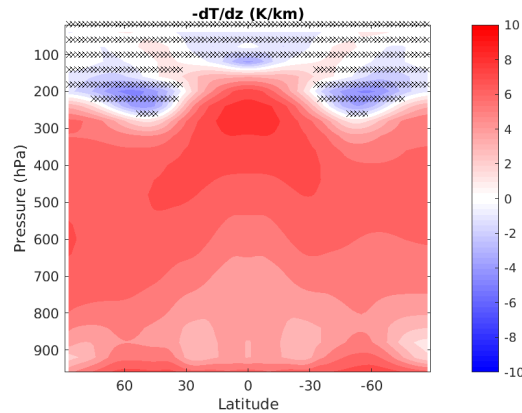


Figure 2.7.1: Atmospheric lapse rates, $\Gamma = -dT/dz$ (colours; interval = 1K/km), and diagnosed stratosphere (black crosses), based upon 300-year mean temperature values from the fully-coupled atmosphere-ocean model control run.

tendency, Q_{rad} , are added in this region of the model atmosphere. Three different types of STP, defined by their latitudinal extent, are applied in separate experiments:

- U01 (Uniform): A uniform temperature perturbation of +0.1K/day is applied throughout the stratosphere;
- P01 (Polar): A temperature perturbation of +0.1K/day is applied throughout the polar stratosphere (60°-90°) only, in both hemispheres;
- T01 (Tropical): A temperature perturbation of +0.1K/day is applied throughout the tropical stratosphere (0°-30°) only, in both hemispheres.

This methodology is similar to that of Haigh et al. (2005), and seeks to capture the type of STP's which might be caused by different phenomena and chemical species, albeit greatly simplified. The models are then run with these STP's present, in an ensemble size of 6 (atmosphere-only/slab-ocean)/8 (fully-coupled), for 5 years (atmosphere-only)/50 years (slab-ocean)/300 years (fully-coupled), and compared with their equivalent control runs. The following chapters will outline the results of these experiments, with chapter 3 focusing on the effects of the perturbations on the model atmosphere in the atmosphere-only setup, chapter 4 looking at the effect upon the SST's in the coupled setups, and chapter 5 exploring the difference in atmospheric response between the different model setups. Each chapter will attempt to divine the mechanism(s) driving the responses we see, and what the chain of causality is in triggering them. Our final chapter, chapter 6, will attempt to bring together the results of these three chapters into a single coherent picture and framework, outlining how the model troposphere and ocean responds to different STP's, via what mechanism(s), and how these interactions feedback onto each other, if at all. We will then broaden out the discussion to look at the implications of our results, and what future work might be done to build upon this research.

Chapter 3

Effect of stratosphere-troposphere coupling

In this first results chapter, we will look at the results of our STP experiments, outlined in section 2.7, in the atmosphere-only (i.e. fixed SST) version of the model. In particular, we will look at the equilibrium changes to such large-scale atmospheric structures as the Hadley and Ferrel cells, midlatitude jets, and polar vortices, and attempt - by the application of various mathematical diagnostics outlined in section 2 - to establish a mechanism whereby they occur. In an attempt to break causality, we will also look at the temporal evolution of the model, as it responds to the applied stratospheric perturbations over the first 200 days of its evolution.

In the end, we aim to have a concrete understanding of how the model atmosphere responds to our various STP's, and via what mechanism(s) this response is produced. We will then be able to compare our results to those of previous studies using similar perturbations, but with more/less simplified models, outlined in section 1.1. This will enable us to determine, for example, whether the precise parameterisations of physical atmospheric processes, the presence/absence of a realistic topography and well-resolved stratosphere, significantly modifies the atmospheric response to said STP's. Also, it will serve as extra validation for our use of the MITgcm in investigating stratosphere-troposphere coupling, which is a necessary prerequisite to then investigating how said coupling is modified by atmosphere-ocean coupling.

3.1 Climatological changes

We start first by outlining the equilibrium response of various zonal-mean climatological fields to the different STP's. In this version of the model, a new equilibrium takes approximately ~200 days to reach. Thus, we will focus mostly on ensemble-averaged (ensemble size = 6) quantities,

time-averaged over years 0-5 or 1-5 of each spinup.

3.1.1 Eulerian mean fields

Figures 3.1.1 and 3.1.2 display the equilibrium anomalies in the zonal wind and Eulerian mass streamfunction induced by our STP experiments, and the associated changes in the maximum strength of the polar vortices, midlatitude jets, Hadley and Ferrel cells, and residual streamfunction, calculated over the last four years of the five years for which the ensembles were run. These latter quantities are calculated by finding, within a certain section of the atmosphere (e.g. above 220hPa and polewards of 45° for the polar vortices), the maximum value of zonal wind speed or circulation strength. This is done for both control and experimental runs, and the difference between the two is then calculated. Note that the location of the maxima can change between the control and experimental runs, and that we are therefore not measuring the change in strength at a fixed location in the atmosphere per se.

Focusing first on the zonal winds, both U01 and P01 exhibit a weakening of the polar vortices in the stratosphere, located polewards of 50° (top-left and top-middle panels of figure 3.1.1; blue/orange bars in left panel of figure 3.1.2). We also observe, in U01, an equatorward shifting of the midlatitude tropospheric jets, with reductions in strength of their poleward flanks, and increases in strength of their equatorward flanks. For P01, we see less of a shift, and more an overall increase/decrease in jet strength in the midlatitudes/polar latitudes. Looking at the left-panel of figure 3.1.2, for P01, the magnitudes of maximum polar vortex weakening and midlatitude jet core strengthening are significantly larger in magnitude, at close to -20m/s and $+2\text{m/s}$ respectively, compared to around just -2m/s and $+1\text{m/s}$ for U01. Also, whilst U01 appears to shift the midlatitude jets slightly downward, no such shift is apparent in P01. In contrast to these results, T01 (top-right panel of figure 3.1.1; yellow bars in left panel of figure 3.1.2) exhibits a strengthening of the polar vortices of about $+10\text{m/s}$, and a decrease/increase in jet strength in the subtropics-to-low-midlatitudes/high-midlatitudes-to-polar-latitudes, with the jet core reducing in strength by approximately -2m/s . Qualitatively, it is much like the opposite of what we see in experiment P01.

Looking at the responses of the Eulerian mean circulations, similar to the midlatitude jets, U01 (bottom-left panel of figure 3.1.1; blue bars in middle panel of figure 3.1.2) exhibits an equatorward shift and strengthening of the Ferrel cells, whilst P01 (bottom-middle panel of figure 3.1.1; orange bars in middle panel of figure 3.1.2) shows more of an overall strengthening and slight reduction in their polewards extent, their maximum strength increasing by approximately $+2\text{Sv}$ and $+6/8\text{Sv}$ in experiments U01 and P01 respectively. In the Hadley cells, we observe an increase in strength, by about $+1\text{Sv}$ and $+2\text{Sv}$ in U01 and P01 respectively, and, in the case of U01, a slight equatorwards contraction, as the Ferrel cells shift. T01 (bottom-right panel of figure 3.1.1; yellow bars in middle panel of figure 3.1.2), similar to its zonal wind response, exhibits a slight weakening its Ferrel cells, by about -3 to -4Sv , and a degree of polewards expansion, whilst its Hadley cells show no significant changes, indicated by the hatching in that

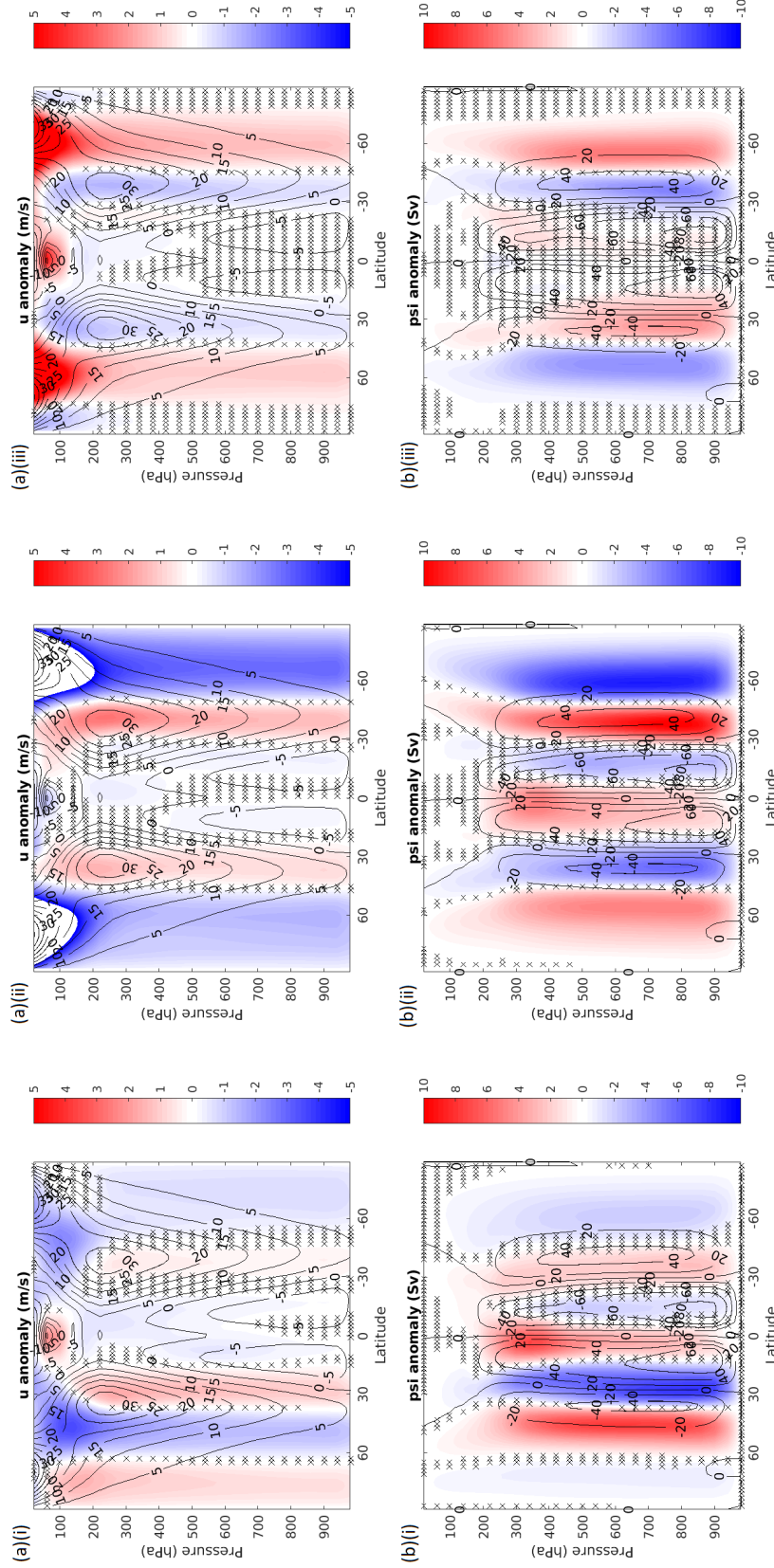


Figure 3.1.1: Control values (contours), and anomalies (colours), in zonal-average (a) zonal wind (top panel), and (b) mass streamfunction (bottom panel) in (left-to-right): (i) U01 (left panels), (ii) P01 (middle panels) and (iii) T01 (right panels) experiments, averaged over years 1-5. Hatching indicates regions in which the confidence levels in the experiment vs control values are below 95%, as measured by a two-tail student's t-test.

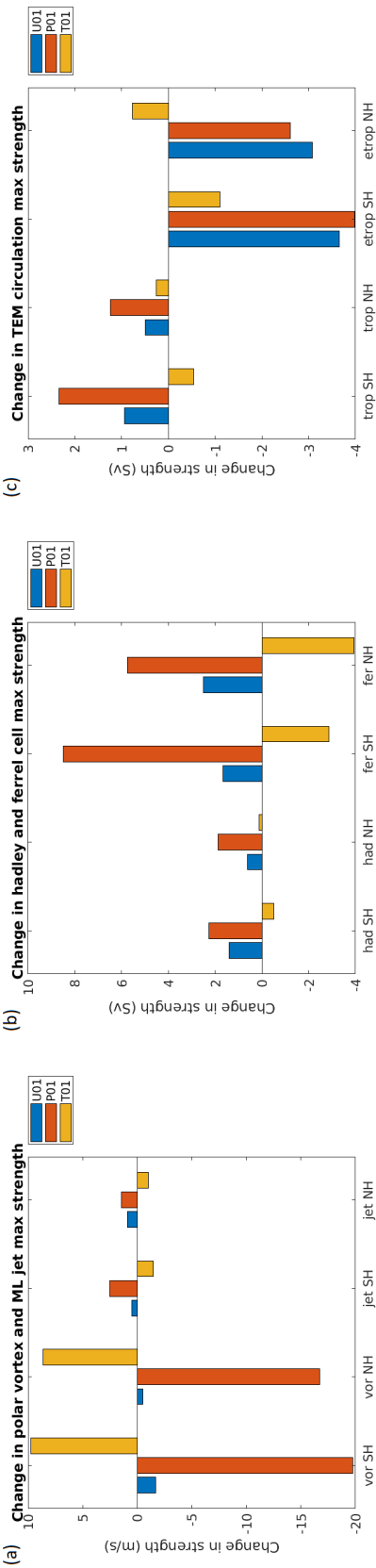


Figure 3.1.2: Changes in (left-to-right): (a) maximum polar vortex (vor) and midlatitude jet (jet) strength (left); (b) maximum tropical Hadley (had) and Ferrel cell (fer) strength (middle); (c) maximum residual circulation strength in the tropics (trop) and extratropics (etrop) (right), in U01, P01 and T01 experiments, averaged over years 1-5.

region.

We therefore see how the different STP's produce quite different atmospheric responses, with experiments U01/P01 forcing a weakening of the polar vortices, an equatorward shift/midlatitude strengthening, polar weakening of the Ferrel cells and midlatitude jets, and a strengthening of the Hadley cells, whilst T01 shows a response akin to the opposite of that seen in P01. We also see how quantitatively different the responses are, with P01 exhibiting the largest changes in zonal wind and circulation strength, followed by T01, and then U01 (except for the Hadley cells, for which T01 shows no significant change in strength). Importantly, these results are in good qualitative agreement with those of the previous studies outlined in section 1.1. The agreement, in particular, with the results of Haigh et al. (2005), which used similar STP's in an sGCM, is particularly encouraging.

It is also worth noting the difference in model response between the hemispheres within the same experiment. In all experiments, we note a greater polar vortex weakening/strengthening in the Southern Hemisphere (vor SH/NH in left panel of figure 3.1.2), and in P01 and T01 the changes in midlatitude jet strength are also of a greater magnitude in the Southern Hemisphere (compare jet SH/NH in left panel of figure 3.1.2). We also observe, in U01 and P01, a greater Hadley cell strengthening in the Southern Hemisphere (had SH/NH in middle panel of figure 3.1.2). With respect to the Ferrel cell changes in strength (fer SH/NH in middle panel of figure 3.1.2), they are greater in magnitude in the Southern Hemisphere for P01, and in the Northern Hemisphere for U01 and T01.

3.1.2 TEM circulation and EP fluxes

Figure 3.1.3 displays the changes in the TEM residual circulation (top panels), EP fluxes and divergences (bottom panels) in experiments U01-T01, and the right panel of figure 3.1.2 provides quantitative estimates for the impact on the strength of the residual streamfunction in both the tropics and extratropics. These latter quantities were calculated in a similar way to the changes in strength of the Hadley and Ferrel cells, outlined in the previous section.

Looking at these figures, experiment U01's and P01's residual circulations (top-left and top-middle panels of figure 3.1.3; blue/orange bars in right panel of figure 3.1.2) exhibit a slight strengthening in the equatorial region, increasing in strength by around +1Sv and +2Sv respectively, and an equatorward narrowing. These changes parallel closely the changes in the Eulerian mean circulations at these latitudes, reflecting the dominance of the mean flows over the eddies in controlling the circulations in the tropics. In the extratropics, the picture changes, with both experiments exhibiting an overall weakening in the TEM residual circulations, with reductions in maximum strength of around -2.5 to -4 Sv there. The contrast with the strengthening of the Ferrel cells indicates the dominant role of altered $[v^*\theta^*]$ eddy fluxes in driving the residual circulation changes there. In experiment T01 (top-right panel of figure 3.1.3; yellow bars in right panel of figure 3.1.2), we observe a slight strengthening of the TEM circulation at around 30°, and a slight weakening immediately polewards of it.

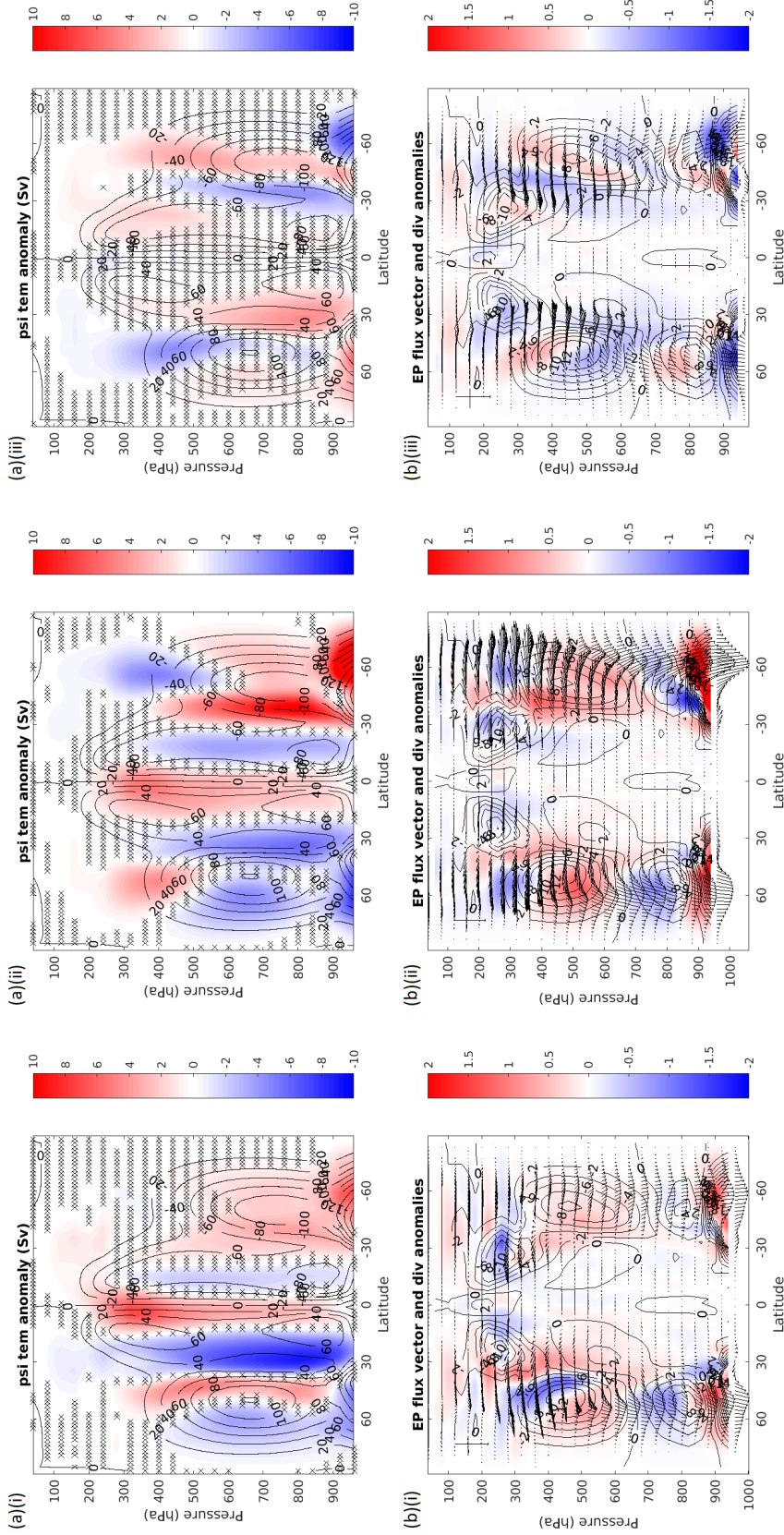


Figure 3.1.3: Control values (contours), and anomalies (colours), in zonal-average (a) TEM residual mass streamfunction (top panel), and (b) EP flux divergence (anomalies = colours; contours = control values) and EP fluxes (vectors) (bottom panel) in (left-to-right): (i) U01 (left panels), (ii) P01 (middle panels) and (iii) T01 (right panels) experiments, averaged over years 1-5. Hatching in the top panels indicates regions in which the confidence levels in the experiment vs control values are below 95%, as measured by a two-tail student's t-test. In the EP flux diagram, the fluxes are mass-weighted as per equations (2.1.32) and (2.1.33), the EP flux divergences are in units of 10^{15}m^3 , and the arrows are scaled such that the horizontal and vertical arrows in the top-left have lengths $5 \times 10^{13} \text{m}^3$ and $5 \times 10^{19} \text{m}^3 \text{Pa}$ respectively.

Looking at the changes in EP fluxes in the troposphere, both U01 and P01 (bottom-left and bottom-middle panels of figure 3.1.3) show a general reduction in their magnitude of upper-tropospheric convergence/lower-tropospheric divergence in the midlatitudes, and increased poleward and downward EP fluxes there. Contrast this with the pattern of EP fluxes and divergences in the control simulation, given in figure 2.6.2 of section 2.6, which displays more-or-less the opposite pattern to these anomalies. This therefore indicates a significant reduction in EP flux activity in the midlatitudes in these experiments. In experiment T01 (bottom-right panel of figure 3.1.3), we observe almost the exact opposite response, with increases in upper-tropospheric convergence/lower-tropospheric divergence in the midlatitudes, accompanied by an overall upward and equatorward anomalous EP flux. This projects positively onto the control pattern, and would therefore indicate an increased level of EP flux activity in the midlatitudes. Also, we note a +/- EP flux divergence anomaly dipole at around the 300hPa level, with the +/- anomaly occurring equatorward/poleward of around 40° in the U01 and P01 experiments, and the inverse for T01. This indicates a slight upward and equatorward/downward and poleward shift in the patterns of EP flux convergence in the upper midlatitude troposphere for U01 and P01/T01. This is reflected too by changes in the residual circulation around these locations, with increases/decreases in the mass streamfunction between approximately 40° - 60° and 500-200hPa for experiments U01 and P01/T01.

So, whilst experiments U01 and P01 show reductions in the strength of their residual circulations and patterns of EP flux activity and convergence in the midlatitudes, experiment T01 shows enhancements. Moreover, as was the case with the Eulerian fields, experiment P01 tends to exhibit the largest strength of response, as measured by the changes in strength in its residual circulation in the extratropics, whilst T01 appears to exhibit the weakest response, with barely any change in strength detected.

Again, we also note the differences in model response between the hemispheres within each experiment. Both U01 and P01 would appear to have larger changes in maximum TEM circulation strength - both in the tropics and in the extratropics - in the Southern Hemisphere (trop/etrop SH/NH in right panel of figure 3.1.2). For T01, the picture is less clear: it would appear to have a different sign of response in maximum TEM circulation strength, with reductions in strength in the Southern Hemisphere and increases in strength in the Northern Hemisphere. However, given the lack of significance in the TEM circulation response we see in figure 3.1.3, nothing concrete can be concluded from this.

Summary

- Experiments U01 and P01 cause a:
 - weakening of the polar vortices;
 - strengthening of the tropical easterlies;

- strengthening and equatorward shifting (U01)/contraction (P01) of the midlatitude jets;
 - strengthening of the Hadley cells;
 - strengthening and equatorial shifting (U01)/contraction (P01) of the Ferrel cells;
 - weakening and slight upwards expansion of the TEM residual circulations, patterns of EP flux divergence, and EP flux activity in the extratropics.
- Experiment T01 causes a:
 - strengthening of the polar vortices;
 - weakening and poleward expansion of the midlatitude jets;
 - weakening and poleward expansion of the Ferrel cells;
 - strengthening and slight downwards contraction of the patterns of EP flux divergence and EP flux activity in the extratropics.
 - The magnitude of atmospheric changes are generally greatest for experiment P01/in the Southern Hemisphere, and weakest for experiment U01/in the Northern Hemisphere, with the exception of the changes in residual circulation and EP fluxes in the extratropics, which are weakest for experiment T01 (and strongest for P01).

3.2 Drivers of climatological change

Thus far, we have laid out the main changes we see in the zonal winds, mean circulations - both Eulerian and TEM residual - and, through the EP fluxes, the eddy heat and momentum fluxes, in response to applied STP's. These results are in broad agreement with the results of previous studies using more simplistic GCM's, such as Haigh et al. (2005) and Simpson et al. (2009), as well as some with more complex GCM's, such as White et al. (2020), which probably belies a fundamental dependence on large-scale dynamical processes, as opposed to the details of physical parameterisations, model topography, etc. In the following section, we will seek to find out what is driving these climatological changes by analysing the equilibrium-mean values of various budgets and their component terms. Note that, because of the similarity in atmospheric response seen in experiments U01 and P01, we will tend to omit the former in our analyses.

3.2.1 Thermal wind and heat budget

Figure 3.2.1 displays the corresponding changes in zonal wind in response to changes in the temperature field - shown in the left panels of figure 3.2.2 - as calculated by vertical integration of the thermal-wind relation, given by equation (2.1.11). We observe how closely the calculated thermal wind changes mirror the actual changes in zonal wind, shown in figure 3.1.1. Thus - minus the changes in surface zonal wind, which must be given as a boundary condition and thus

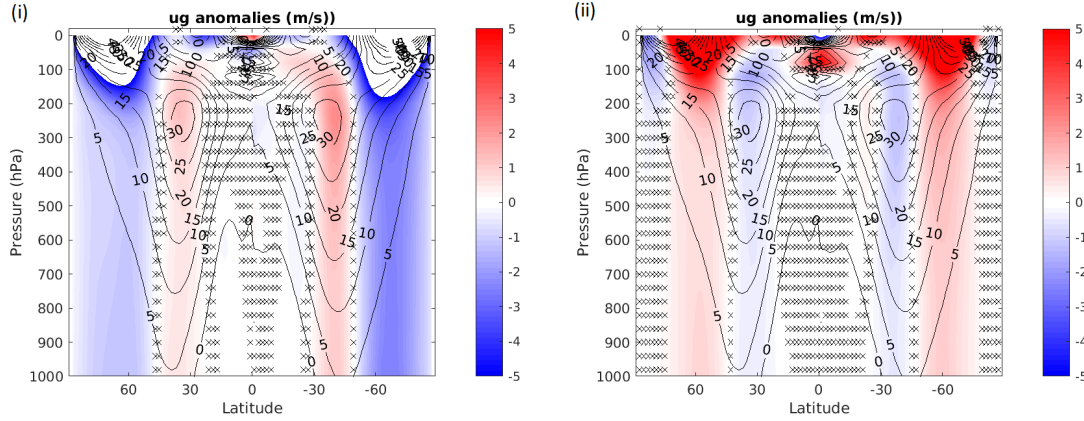


Figure 3.2.1: Control values (contours), and anomalies (colours), in zonal-average geostrophic wind in experiments (i) P01 (left-panel), and (ii) T01 (right panel), averaged over years 1-5. Hatching indicates regions in which the confidence levels in the experiment vs control values are below 95%, as measured by a two-tail student's t-test.

cannot be calculated from the thermal wind relation - the question of what is forcing the zonal winds becomes that of what is forcing the meridional potential temperature gradient.

Figure 3.2.2 displays the anomalous potential temperature tendencies - as might be diagnosed from the potential temperature tendency equation (2.1.9) - due to diabatic heating/cooling, $[Q]$ (middle panels), and advective heating/cooling, $-[v\partial_y\theta] - [\omega\partial_p\theta]$ (right panels) - as well as the changes in absolute potential temperature (left panels). We observe how the anomalous potential temperature appears to be largely forced in the extratropical troposphere, and also in much of the stratosphere, by the changes in advective heating. This is particularly true for the meridional temperature gradients, with the patterns of anomalous advective heating in the troposphere forcing reductions (more positive)/enhancements (more negative) in the meridional temperature gradient in experiment P01/T01 in the subtropics, enhancements/reductions in the midlatitudes in P01/T01, and reductions/enhancements in the higher latitudes in P01/T01. Such changes to the meridional temperature gradient would reproduce the main changes in geostrophic zonal wind we observe in the troposphere.

In the parts of the stratosphere outside the areas of direct thermal forcing (i.e. 30° to 90° in T01; 0° to 60° in P01), the dominance of anomalous advective heating and cooling also holds, forcing enhancements/reductions in the meridional temperature gradients in the high/low latitudes in T01/P01, which in turn would force positive/negative geostrophic wind anomalies. In the areas of direct thermal forcing, predictably, the changes in diabatic heating - into which the direct STP's are packaged as constants in the radiative heating rate - appear more dominant, at least in forcing the observed local changes in meridional temperature gradient. These changes in diabatic heating in the stratosphere are dominated by the changes in radiative heating rate - see figure 3.2.3 - confirming that it really largely is the applied STP's. This is less the case for P01, for which the STP's appear offset by enhanced radiative cooling, which is most probably

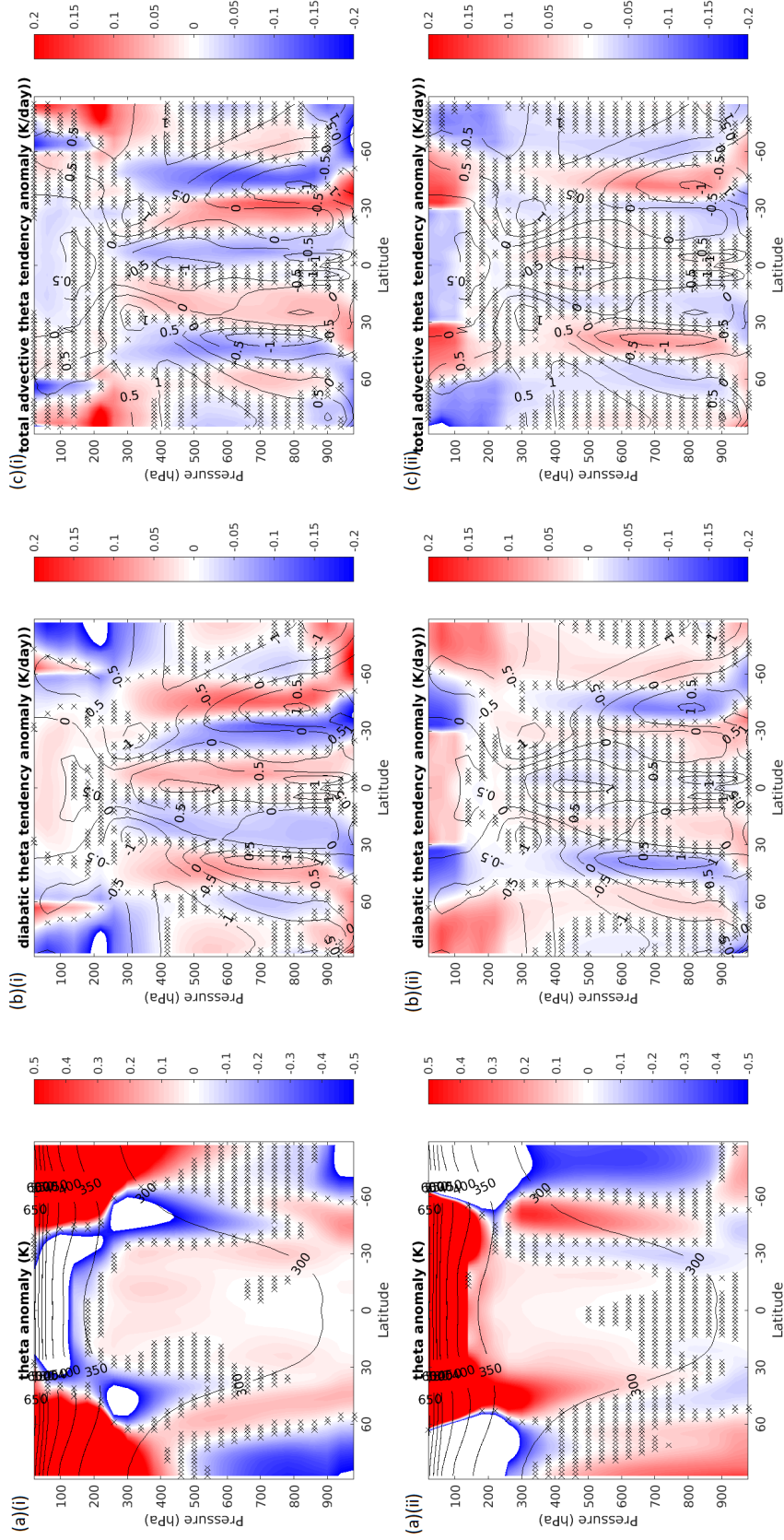


Figure 3.2.2: Control values (contours), and anomalies (colours), in zonal-average: (a) potential temperature (left panels), (b) diabatic potential temperature tendencies (middle panels), and (c) advective potential temperature tendencies (right panels), in experiments (i) P01 (top panels), and (ii) T01 (bottom panels), averaged over years 1-5. Hatching indicates regions in which the confidence levels in the experiment vs control values are below 95%, as measured by a two-tail student's t-test.

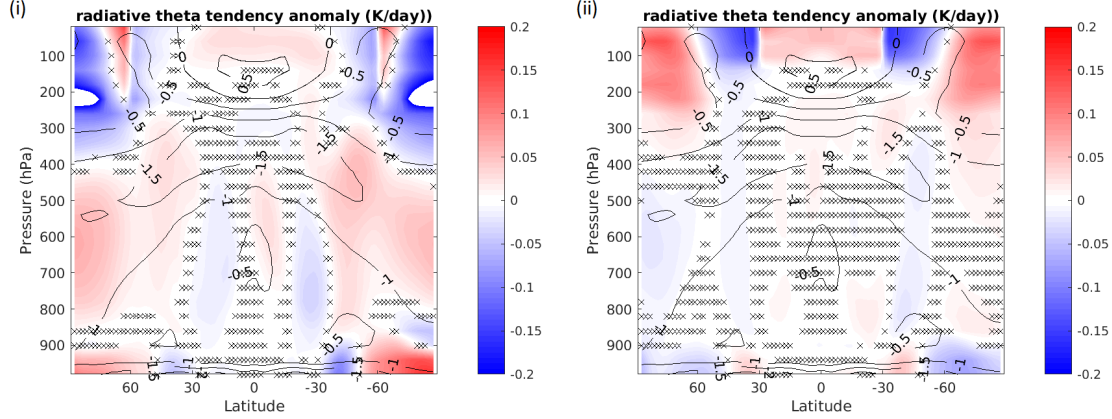


Figure 3.2.3: Control values (contours), and anomalies (colours), in zonal-average radiative potential temperature tendencies in experiments (i) P01 (left panel), and (ii) T01 (right panel), averaged over years 1-5. Hatching indicates regions in which the confidence levels in the experiment vs control values are below 95%, as measured by a two-tail student's t-test.

the result of the higher polar stratospheric temperatures, leading to higher rates of LW emission.

To further analyse the anomalous advective heating term, we look at the changes in net heating by the TEM residual circulation, $-\tilde{\omega}\partial_p[\theta]$ in 2.1.26, displayed in the left panels of figure 3.2.4. Given the close resemblance with the total advective heating rate anomalies in the right panels of figure 3.2.2, we can conclude that the anomalous advective heating rate is forced in large part by changes in the TEM residual circulation heating rate. We can then further analyse this term, by splitting it into its contribution due to the changes in residual circulation, $\tilde{\omega}$, and changes in the vertical potential temperature gradient, $\partial_p[\theta]$, as follows:

$$\Delta\left(\frac{\partial(\tilde{\omega}[\theta])}{\partial p}\right) \simeq \frac{\partial((\Delta\tilde{\omega})[\theta])}{\partial p} + \frac{\partial(\tilde{\omega}(\Delta[\theta]))}{\partial p} \quad (3.2.1)$$

where we have ignored second-order terms. These individual contributions to the TEM residual circulation heating rate are shown in the middle and right panels respectively of figure 3.2.4. Comparing the individual contributions with the overall heating rate in the left panels, it would appear that it is the contribution due to the changes in the residual circulation - the first term on the RHS of equation (3.2.1) - that is driving the overall anomalous heating rate. The second term only makes a significant contribution around the tropical tropopause, and the high latitude - poleward of 60° - troposphere, where the feedback onto the first term is generally negative. Only around the tropical tropopause does this second term appear to override the first term, in experiment T01.

Summary

- The zonal wind anomalies are in agreement with the meridional temperature gradient anomalies via the thermal-wind relation;

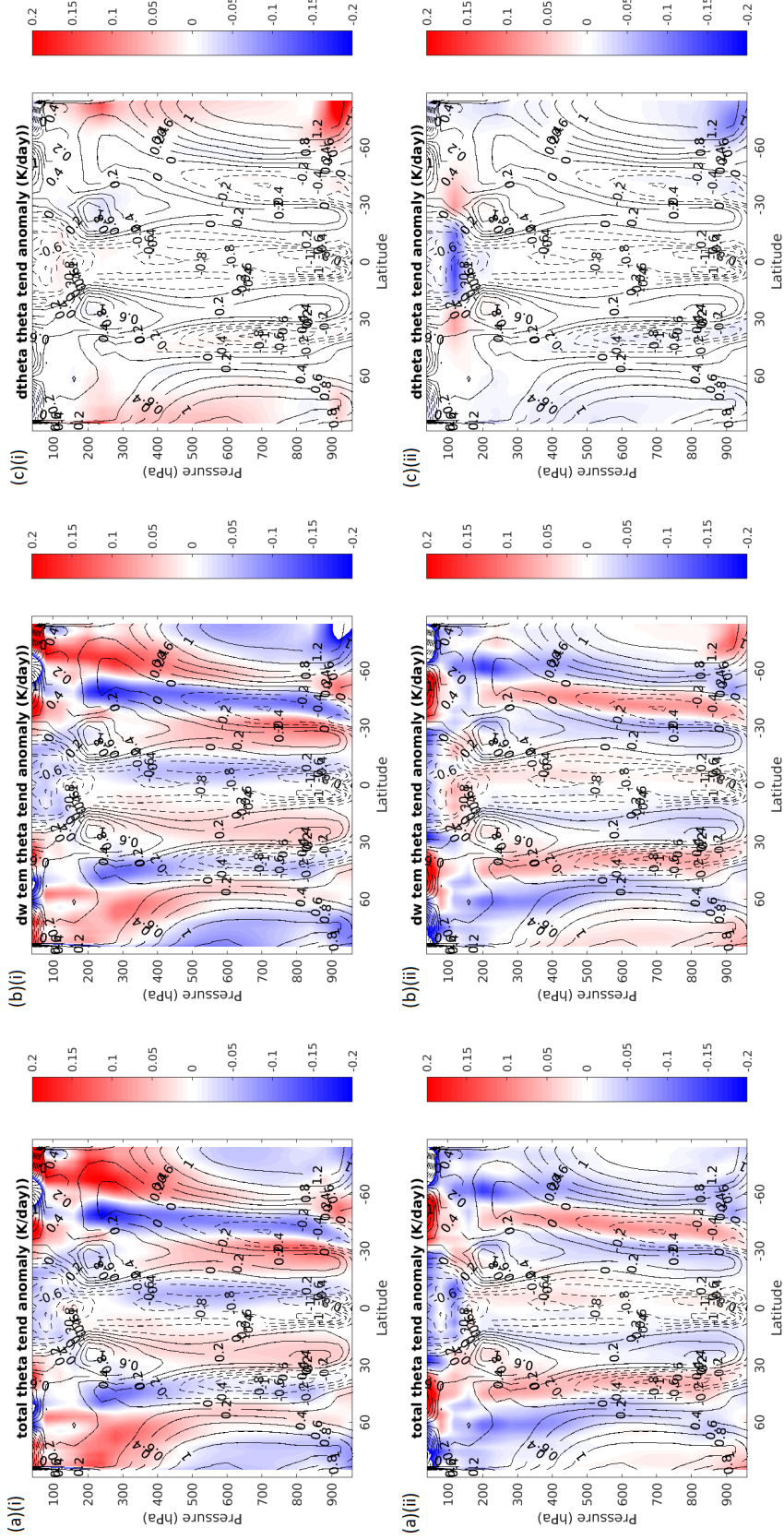


Figure 3.2.4: Control values of the total potential temperature heating rate by TEM residual circulation, $-\tilde{\omega}\partial_p[\theta]$ (contours), and anomalies (colours) caused by changes in the: (a) total heating rate, $\Delta(-\tilde{\omega}\partial_p[\theta])$ (left panels), (b) residual circulation, $-(\Delta\tilde{\omega})\partial_p[\theta]$ (middle panels), and (c) potential temperature gradient, $-\tilde{\omega}\Delta(\partial_p[\theta])$ (right panels), in experiments (i) P01 (top panels) and (ii) T01 (bottom panels), averaged over years 1-5.

- Outside the areas of direct radiative forcing, changes in potential temperature meridional gradient are in broad agreement with the changes in the advective heating;
- Anomalous advective heating/cooling is dominated by changes in the TEM residual circulation heating rate, which in turn is driven largely by changes in the TEM residual vertical velocity, $\Delta\tilde{\omega}$.

3.2.2 Forcing of the TEM circulation

In an attempt to identify what is forcing changes in the TEM residual circulation, $\tilde{\psi}$, and thus in turn forcing changes in potential temperature and geostrophic wind, we turn to equation (2.1.27). This equation, through its lack of time-derivatives, is an elliptic equation which should be obeyed by the residual mass streamfunction, $\tilde{\psi}$, at all times, and provides a means of directly linking changes in diabatic heating, frictional dissipation, and EP flux divergence to changes in the residual circulation.

The top-left panel of figure 3.2.5 shows the total change in residual streamfunction 'curvature', as calculated by summing the two terms on the LHS of equation (2.1.27), for experiment P01. We can compare this with the individual contribution by the first term on the LHS, the vertical 'curvature' term, shown in the top-right panel, and it would appear that it is the anomalous contribution by this term that dominates the overall LHS of the equation. We can also compare the total LHS anomaly to its contribution by the individual forcing terms on the RHS of equation (2.1.27), shown in the bottom panels of figure 2.1.27. As with the second term on the LHS, we have omitted the first term on the RHS of the equation - the contribution by the diabatic heating - which is found to broadly resemble the former term, with both having broadly negligible anomalous contributions. Outside of the near-surface atmospheric boundary layer, where anomalous frictional dissipation makes a significant contribution to the overall 'curvature', the EP flux divergence term appears to be dominating the RHS of equation (2.1.27) throughout most of the extratropical troposphere, and hence driving changes in the residual circulation there.

Summary

- The changes in extratropical TEM residual circulation, outside of the boundary layer, are mostly driven by changes in the EP flux divergence, $\nabla \cdot \mathbf{F}$.

3.2.3 Eliassen-Palm fluxes

In section 3.1.2 we laid out and analysed the changes in the EP fluxes and their divergences in the equilibrium mean of our stratospheric forcing experiments. Decomposition of the EP flux divergence budget into its individual contributions from the vertical and meridional flux anomalies - $\partial_y F^y$ and $\partial_p F^p$ - is given in figure 3.2.6, and the left panels of figure 3.2.7, respectively.

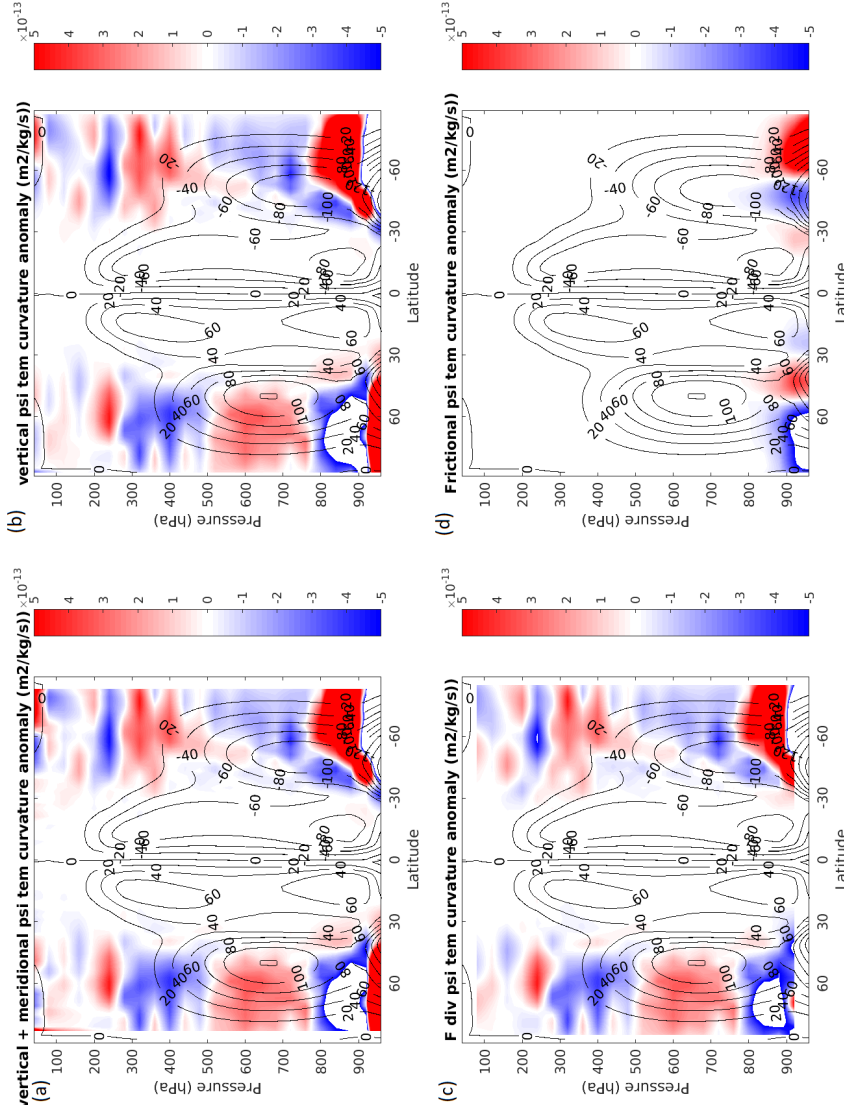


Figure 3.2.5: Control values of TEM residual streamfunction, $\tilde{\psi}$ (contours), and anomalies (colours) in zonal-average $\tilde{\psi}$ curvature due to changes in (top-to-bottom, left-to-right): (a) vertical + meridional components (LHS of equation (2.1.27); top-left panel), (b) vertical component only (1st term on LHS of equation (2.1.27); top-right panel), (c) EP flux divergence, $\nabla \cdot \mathbf{F}$ (3rd term on RHS of equation (2.1.27); bottom-left panel), and (d) friction, \mathcal{F}_λ (2nd term on RHS of equation (2.1.27); bottom-right panel), in experiment P01, averaged over years 1-5.

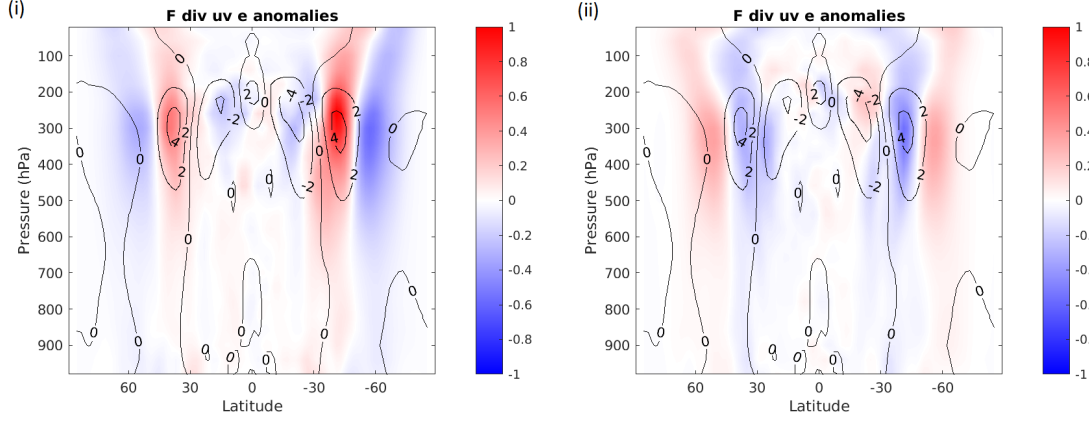


Figure 3.2.6: Control values (contours) and anomalies (colours) of horizontal EP flux divergence, $\partial_y F^y$, in experiments (i) P01 (left panel), and (ii) T01 (right panel), averaged over years 1-5.

In the midlatitude upper troposphere - between about 200-400hPa and 30°-60° - the contribution by the meridional EP flux anomalies is significant, and is reflective of the changes in extratropical zonal winds observed there, with anomalous convergence/divergence in regions of anomalous zonal wind deceleration/acceleration. Since the meridional EP fluxes are, by definition, proportional to $-[u^*v^*]$ - see equation (2.1.22) - its horizontal convergence/divergence is proportional to the horizontal divergence/convergence of poleward eddy zonal momentum fluxes, and thus, to zonal wind decelerations/accelerations by said eddy momentum fluxes. We can thus trace the changes in zonal wind in the upper troposphere - and, by vertical integration of equation (2.1.12), throughout the atmospheric column as a whole - to these changes in the meridional EP flux convergence there.

Lower down in the extratropical troposphere, the changes in vertical EP flux divergence are much more significant, and generally reproduce the anomalies in overall EP flux divergence seen in figure 3.1.3. Similar to how, polewards of about 45°, the meridional EP flux divergences exhibited negative/positive anomalies in P01/T01, from a similar latitude polewards, we observe reductions/enhancements in the patterns of lower tropospheric divergence and upper tropospheric convergence, in the vertical EP fluxes. This is all suggestive of a reduction/amplification of the action of vertical EP fluxes, with respect to taking zonal momentum in the upper troposphere and pumping it into the lower troposphere in the midlatitudes. This is achieved, physically, via their role in forcing the Ferrel circulations, and thereby inducing zonal wind Coriolis decelerations aloft, and accelerations close to the surface in the midlatitudes.

We can further analyse the contribution of the vertical EP fluxes to the overall EP flux divergence anomalies by splitting it into its contributions due to changes in the poleward eddy heat fluxes, $[v^*\theta^*]$, and potential temperature vertical gradient, $\partial_p[\theta]$, as per:

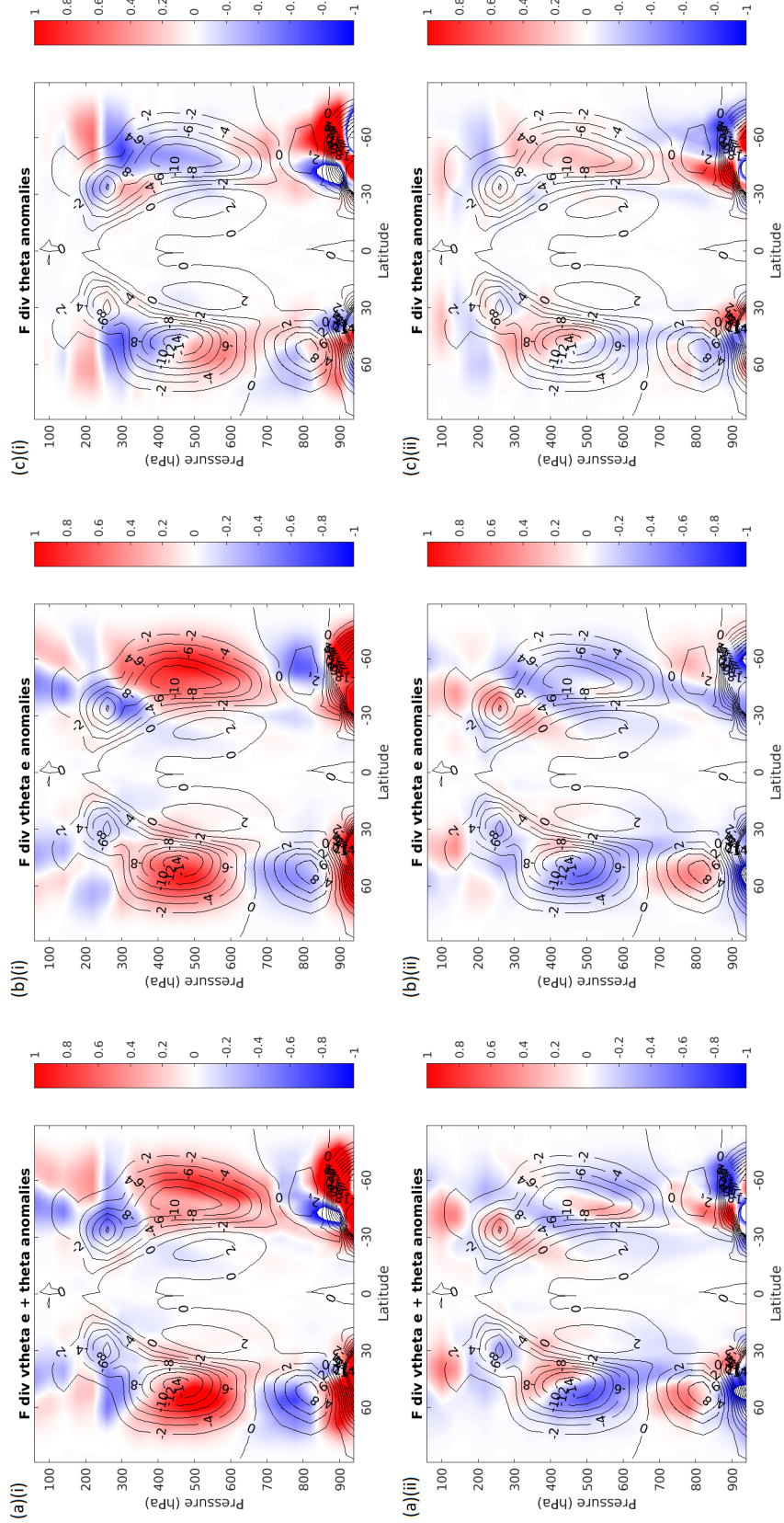


Figure 3.2.7: Control values of vertical EP flux divergences, $\partial_p F^p$ (contours), and their anomalies (colours) due to changes in: (a) total vertical EP flux divergence, $\Delta \partial_p F^p$ (left panels), (b) poleward eddy heat fluxes, $\Delta [v^* \theta^*]$ (middle panels), and (c) vertical potential temperature gradient, $\Delta \partial_p [\theta]$ (right panels), in experiments (i) P01 (top panels), and (ii) T01 (bottom panels), averaged over years 1-5.

$$\Delta \left(\frac{dF^p}{dp} \right) = \Delta \left(fR \cos \phi \frac{\partial}{\partial p} \left(\frac{[v^* \theta^*]}{\partial [\theta] / \partial p} \right) \right) = fR \cos \phi \frac{\partial}{\partial p} \left(\frac{\Delta ([v^* \theta^*])}{(\partial [\theta] / \partial p)} - \frac{[v^* \theta^*] \Delta (\partial [\theta] / \partial p)}{(\partial [\theta] / \partial p)^2} \right) \quad (3.2.2)$$

These individual contributions to the overall vertical EP flux divergence anomalies are shown in the middle and right panels of figure 3.2.7 respectively. We observe how it is the first term on the RHS of equation (3.2.2) - the contribution from the $[v^* \theta^*]$ eddy anomalies - which appears to dominate throughout most of the atmosphere. This is broadly the case, with the exception - for experiment P01 - of the extratropical tropopause region - between 300hPa to 200hPa, and polewards of around 40° - where the second term appears dominant. Incidentally, this is also a region where the model tropopause is relatively low, just above a region of large EP flux convergence, and where we see, in P01, large, positive stratospheric temperature anomalies aloft, forced by the applied STP's. This would in turn lead to large changes in the vertical temperature gradient around the tropopause in that region, leading to the observed changes in vertical EP flux divergence we see there. This might also be suggestive of a possible pathway, whereby changes to stratospheric temperature in the extratropics are able to force changes in the troposphere below.

Summary

- Changes in EP flux divergence, $\nabla \cdot \mathbf{F}$, in the extratropics are driven primarily by changes in the:
 - meridional EP fluxes, $F^y = -R \cos \phi [u^* v^*]$, and their divergences in the upper subtropical to midlatitude troposphere;
 - vertical EP fluxes, $F^p = fR \cos \phi [v^* \theta^*] / \partial_p [\theta]$, and their divergences in the rest of the extratropical atmosphere, driven by changes in the:
 - * vertical potential temperature gradient, $\partial_p [\theta]$, around the extratropical tropopause (P01);
 - * poleward eddy heat fluxes, $[v^* \theta^*]$, in rest of the extratropical atmosphere.
- Changes in the upper-tropospheric horizontal EP flux divergence, $\frac{dF^y}{dy}$, reflect the changes in zonal wind in both the upper-troposphere, and the entire atmospheric column as a whole;
- Reductions/Amplifications in the midlatitude vertical EP fluxes and divergences in experiments P01/T01 reflect the negative/positive anomalies in horizontal EP flux divergence, $\frac{dF^y}{dy}$, seen in the upper troposphere around those latitudes.

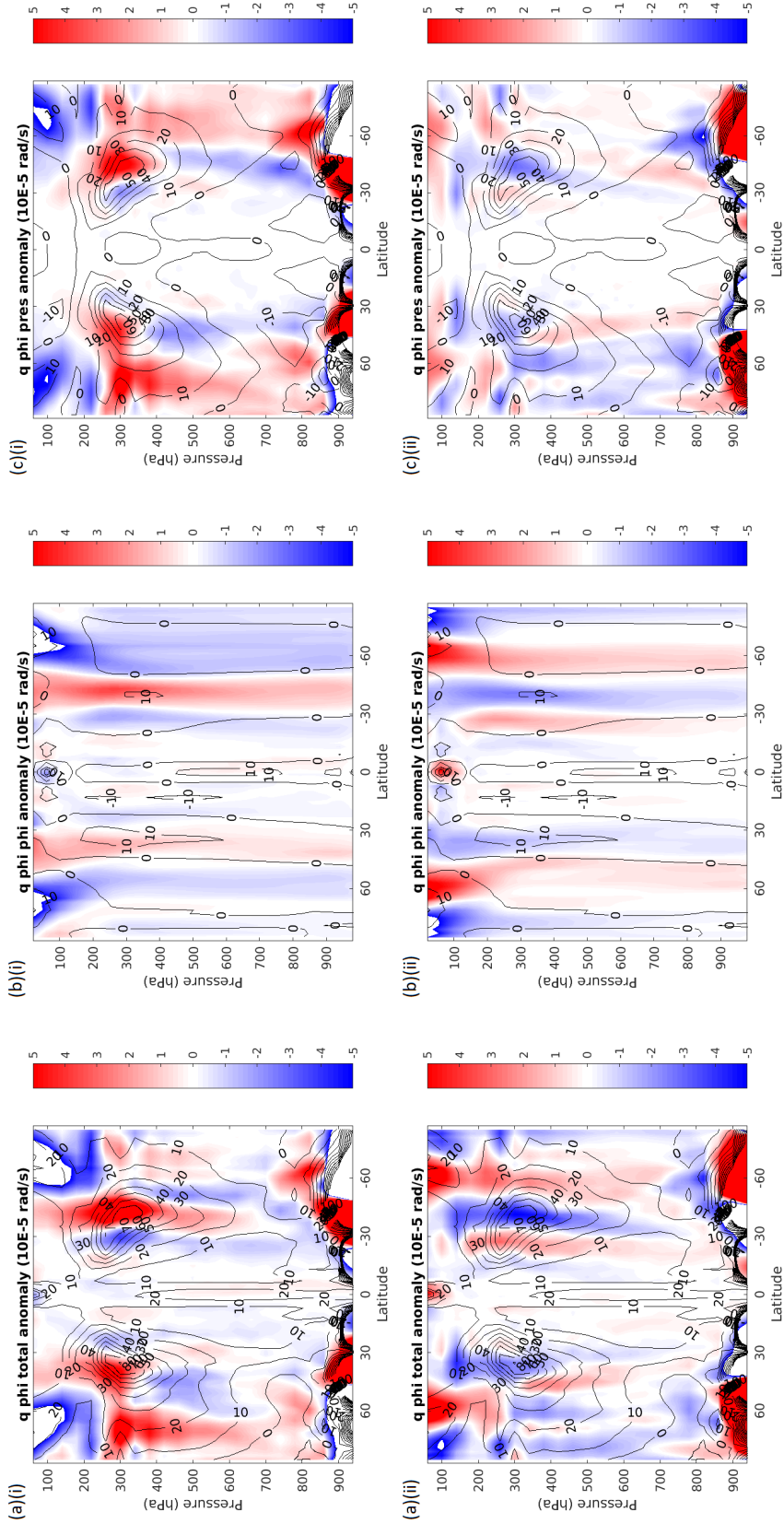


Figure 3.2.8: Control values (contours) and anomalies (colours) in meridional potential vorticity gradient, q_ϕ , due to changes in: (a) total meridional PV gradient, Δq_ϕ (left panels), (b) the meridional component, $\Delta q_{\phi,y}$ (2nd component of equation (2.1.28); middle panels), and (c) the vertical component, $\Delta q_{\phi,p}$ (3rd component of equation (2.1.28); right panels), in experiments (i) P01 (top panels), and (ii) T01 (bottom panels), averaged over years 1-5.

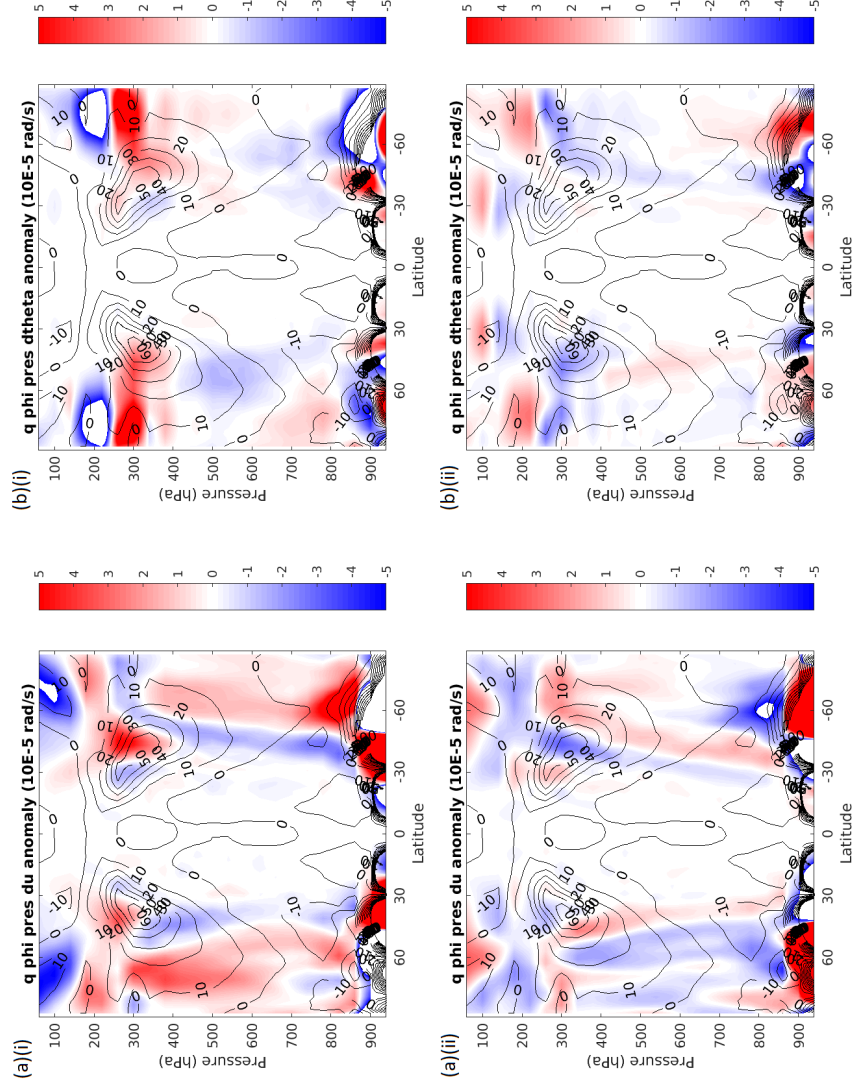


Figure 3.2.9: Control values (contours) and anomalies (colours) in vertical component of meridional PV gradient, $q_{\phi,p}$, due to changes in: (a) zonal wind vertical gradient, $\Delta \partial_p u$ (left panels), and (b) potential temperature vertical gradient, $\Delta \partial_p \theta$ (right panels), in experiments (i) P01 (top panels), and (ii) T01 (bottom panels), averaged over years 1-5.

3.2.4 Meridional potential vorticity gradient

To understand what is driving the observed changes in EP fluxes and EP flux divergence, we turn our analysis to the meridional potential vorticity (PV) gradient, $\partial_\phi [q]$. In the framework of quasigeostrophic theory, this quantity can be decomposed into three separate components as per equation (2.1.28), and EP fluxes should converge/diverge around areas of positive/negative meridional PV gradient.

The left panels of figure 3.2.8 show the total equilibrium changes in meridional PV gradient, $\partial_\phi [q]$, in experiments P01 & T01. The general pattern in the extratropical upper troposphere - where the control values of $\partial_\phi [q]$ are large and positive, and where EP much flux convergence tends to occur - is that of, in experiment P01, strengthening around the subtropical maximum, and reductions polewards in the midlatitude troposphere and high-latitude stratosphere. In experiment T01, it is more-or-less the opposite situation, with reductions around the subtropical maximum, and increases polewards. This too reflects the observed changes in the zonal winds, with increases/decreases in regions of zonal wind acceleration/deceleration. Given that - from the previous section - zonal wind accelerations/decelerations in the upper troposphere were associated with anomalous horizontal EP flux divergence/convergence, we can see how the observed changes in meridional PV gradient might be linked with those of the zonal winds.

Following equation (2.1.28), we can decompose the total change in meridional PV gradient, Δq_ϕ , into two components: the contribution by the second term on the RHS, $\Delta q_{\phi,y}$, which responds to changes in zonal wind meridional curvature, and the contribution by the third term on the RHS, $\Delta q_{\phi,p}$, which responds to changes in the vertical zonal wind and potential temperature vertical gradients and curvatures. The contributions of these two separate terms to the overall meridional PV gradient anomaly in experiments P01 and T01 are shown in the middle and right panels of figure 3.2.8 respectively.

We observe the apparent dominance of the third term, $\Delta q_{\phi,p}$, throughout most of the extratropical atmosphere. We also see a strong contribution in the midlatitude upper atmosphere by the second term, $\Delta q_{\phi,y}$. Moreover, there is a strong correspondence between the regions of positive/negative $\Delta q_{\phi,y}$ and positive/negative $\Delta \left(\frac{dF^y}{dy} \right)$. Such a correspondence also exists between regions of positive/negative $\Delta q_{\phi,p}$ and negative/positive $\Delta \left(\frac{dF^p}{dp} \right)$, although it is not as strong, and exists more in the midlatitude upper atmosphere than elsewhere. Under the assumption of anomalous poleward eddy heat fluxes that are downgradient to the temperature field, and poleward eddy westerly momentum fluxes which drive local changes in the zonal winds, these relationships make sense and are validated mathematically - see section A.3 for a mathematical derivation.

Looking more deeply into the changes in the third meridional PV gradient component, $q_{\phi,p}$, as we did for the vertical EP flux divergence anomalies in section 3.2.3, we have dissected it into its components, due to changes in vertical zonal wind gradient, $\Delta \partial_p u$, and vertical potential temperature gradient, $\Delta \partial_p \theta$. These are shown in the left and right panels of figure 3.2.9 respectively. We observe the apparent dominance of the former term throughout most of the

atmosphere, except around the tropopause level, where the contribution from the vertical potential temperature gradient appears significant, if not dominant. This is especially the case poleward of 60° , where we observe a +/- and -/+ dipole for experiments P01 and T01 respectively, around the 250hPa level, and equatorward of 40° in experiment T01, where we observe a +/- dipole around the 100hPa level. All appear forced by the changes in vertical potential temperature gradient and - like the observed changes in vertical EP flux divergence forced by changes in vertical potential temperature gradient around the tropopause - could potentially provide a pathway whereby directly applied STP's are able to influence the propagation of EP flux vectors in the troposphere below, and thereby alter the mean zonal winds and circulations.

In fact, similar to the correspondence between overall changes in $\left(\frac{dF^p}{dp}\right)$ and overall changes in $q_{\phi,p}$, we see a similar correspondence between their individual components due to changes in the zonal wind and potential temperature gradients. This is most apparent in the upper atmosphere, and for anomalies due to changes in vertical potential temperature gradients, which exhibit -/+ and +/- anomaly dipoles around the polar tropopause for experiments P01 and T01 respectively, which coincide with +/- and -/+ anomaly dipoles in $\left(\frac{dF^p}{dp}\right)$ also caused by changes in $\partial_p\theta$.

Summary

- The changes in horizontal and vertical EP flux divergence, $\nabla \cdot \mathbf{F}$, are related to changes in horizontal and vertical meridional PV gradient component, q_ϕ , with:
 - positive/negative values of $\Delta\left(\frac{dF^y}{dy}\right)$ corresponding to positive/negative values of $\Delta q_{\phi,y}$;
 - positive/negative values of $\Delta\left(\frac{dF^p}{dp}\right)$ corresponding to negative/positive values of $\Delta q_{\phi,p}$ in the midlatitude upper atmosphere: this goes for both the total anomalies, and the individual components due to changes in zonal wind, $\Delta\partial_p u$, and changes in vertical potential temperature gradient, $\Delta\partial_p\theta$.

3.2.5 Equilibrium response: Conclusions

After much analysis, we have arrived at the following picture of how the different anomalous mean fields and eddies are interrelated in the model equilibrium mean:

- Via the thermal wind and heat budget, changes in the vertical zonal wind and meridional temperature gradients are dictated by changes in the residual circulation, which in turn, were found to be forced - via the EP flux divergence - by changes in the poleward transport of westerly momentum and heat by eddies. Moreover, changes in the horizontal and vertical EP flux divergences have a direct role in forcing changes in the zonal winds via equation (2.1.25);
- Changes in the mean zonal wind and temperature fields and their gradients are also able - via causing changes in the meridional PV gradient - to induce changes in the strength and propagation of EP fluxes.

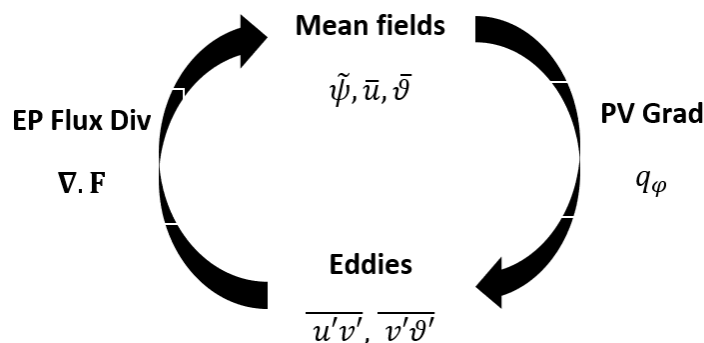


Figure 3.2.10: Schematic of the interaction between the mean fields and eddies in the equilibrated model.

Figure 3.2.10 provides a schematic of this two-way interaction between the mean fields and eddies, mediated via changes in the EP flux divergence and meridional PV gradient. This is similar to the eddy-mean flow feedback mechanisms described by Lorenz & Hartmann (2001), and Simpson et al. (2009). We therefore have a clear picture of how changes in the different eddy and mean fields are connected to each other, but no clear idea of how this interaction gets going. This will be the subject of the next subsection.

3.3 Temporal response

Thus far, we have analysed only the equilibrium atmospheric response to applied STP's, and attempted to make sense of it by analysing the equilibrium values of various budget terms. This has given us a good understanding of the interdependence of various dynamical terms, and shown the centrality of the changes in EP fluxes and their divergences - themselves forced by changes in the meridional PV gradient anomaly - in driving the observed changes in the zonal winds, circulation, and potential temperature. It has not, however, given us a clear idea of the chain of causality, from applied STP's, to changes in the zonal winds and circulations in troposphere. In this last subsection, therefore, we will focus on analysing the time-evolution of the atmospheric response in our STP experiments during the initial 30 days of each spinup, with the aim of establishing a precise chain of causality.

3.3.1 Experiment U01

Figure 3.3.1 displays the evolution of zonal wind and mass streamfunction anomalies for the U01 experiment over the initial 30 days of the spinup, using a 24-member ensemble with daily time-averaged output. We observe how the initial zonal wind anomalies appear to originate in the model stratosphere, with negative anomalies located between 30° and 60° in the initial 0-10

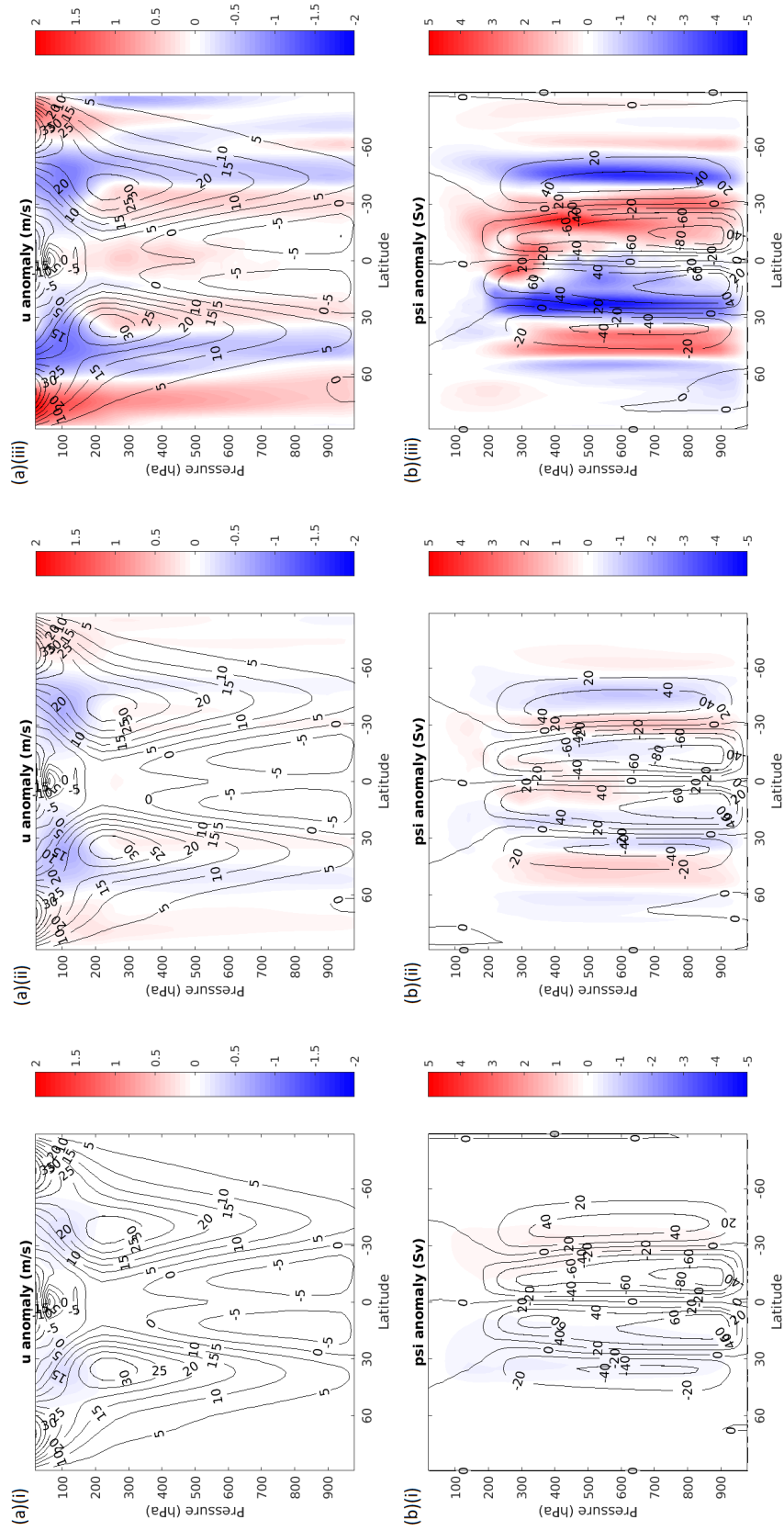


Figure 3.3.1: Control values (contours), and anomalies (colours), in zonal-average (a) zonal wind (top panel), and (b) mass streamfunction (bottom panel) in U01 experiment, averaged over days (left-to-right): (i) 0-10 (left panels), (ii) 11-20 (middle panels) and (iii) 21-30 (right panels).

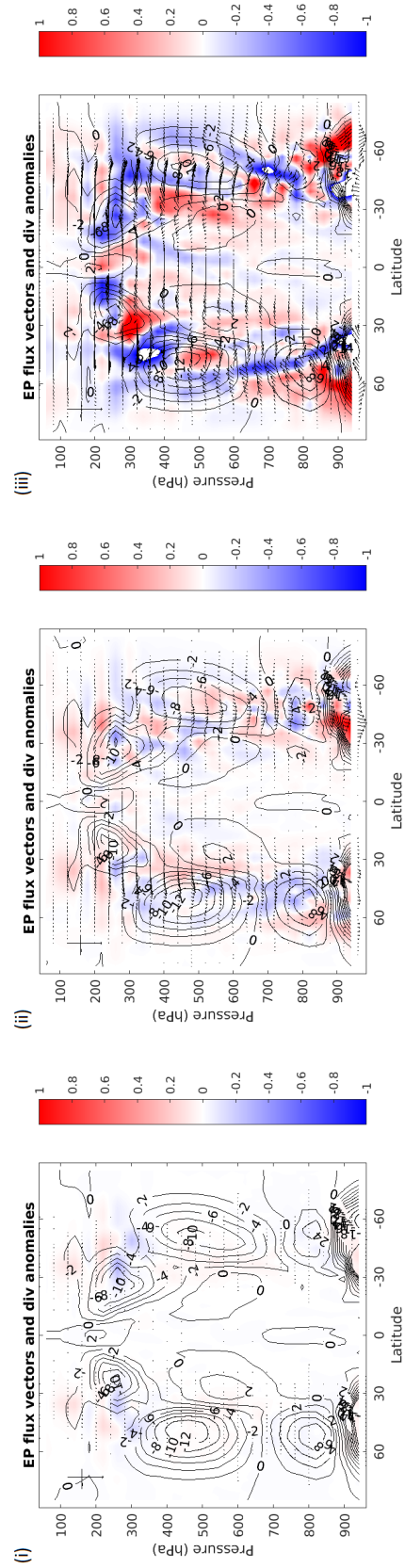


Figure 3.3.2: Changes in EP fluxes (arrows) divergences (colours) in U01 experiment, averaged over days (left-to-right): (i) 0-10 (left panels), (ii) 11-20 (middle panels) and (iii) 21-30 (right panels). Control values of EP flux divergences are shown as contours. In the EP flux diagram, the fluxes are mass-weighted as per equations (2.1.32) and (2.1.33), the EP flux divergences are in units of 10^{15}m^3 , and the arrows are scaled such that the horizontal and vertical arrows in the top-left have lengths $5 \times 10^{13} \text{m}^3$ and $5 \times 10^{19} \text{m}^3 \text{Pa}$ respectively.

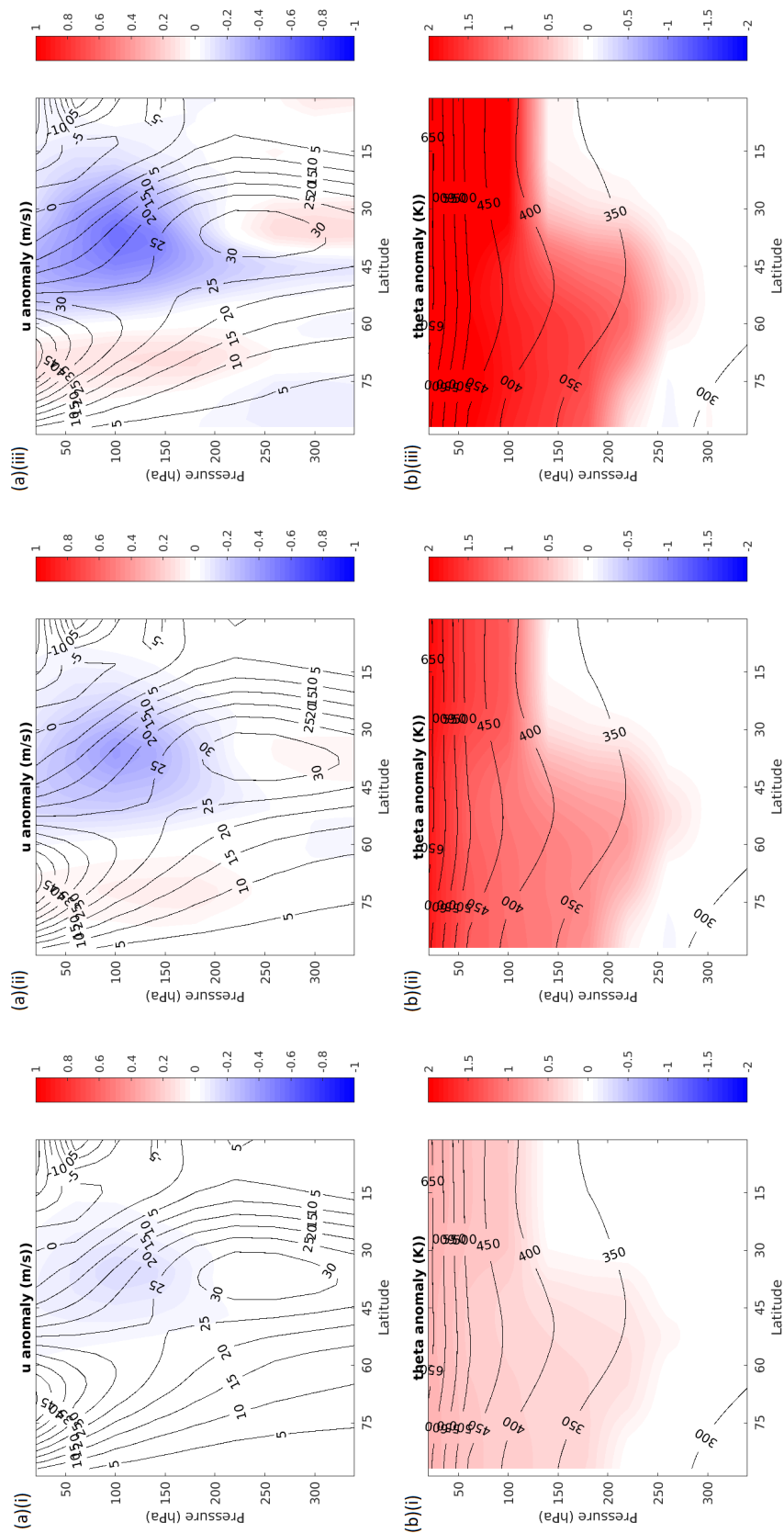


Figure 3.3.3: Control values (contours), and anomalies (colours), in zonally- and hemispherically-averaged (a) zonal wind (top panels), and (b) potential temperature (bottom panels), 340hPa to 20hPa, in U01 experiment, averaged over days (left-to-right): (i) 0-5 (left panels), (ii) 6-10 (middle panels) and (iii) 11-15 (right panels).

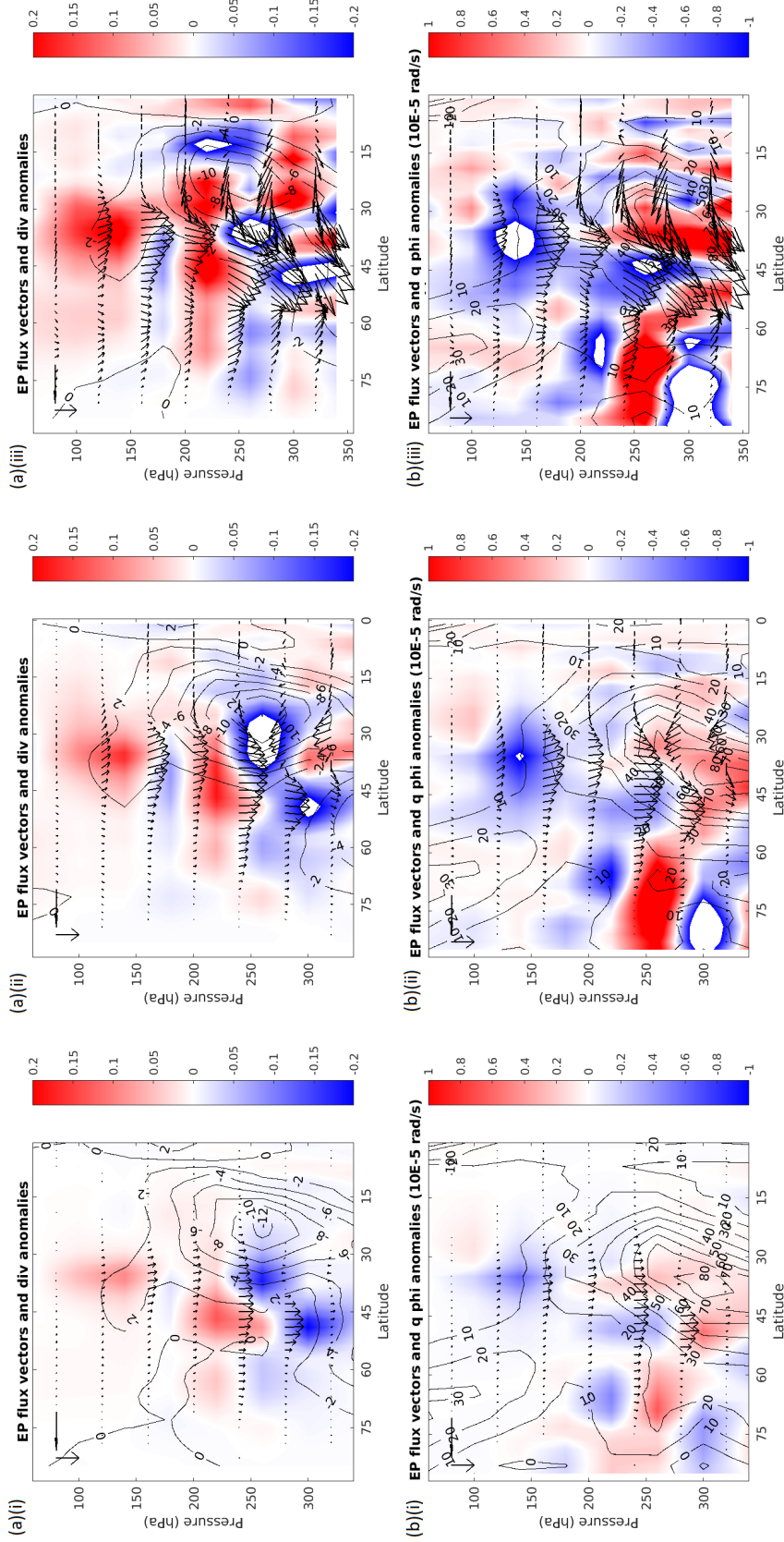


Figure 3.3.4: Control values (contours), and anomalies (colours) in zonally- and hemispherically-averaged (a) EP flux divergences, $\nabla \cdot \mathbf{F}$ (top panels), and (b) meridional potential vorticity gradient, q_ϕ (bottom panels), 340hPa to 60hPa, in U01 experiment, averaged over days (left-to-right): (i) 0-5 (left panels), (ii) 6-10 (middle panels) and (iii) 11-15 (right panels). Arrows correspond to anomalous EP fluxes, $\Delta \mathbf{F}$. In the EP flux diagram, the fluxes are mass-weighted as per equations (2.1.32) and (2.1.33), the EP flux divergences are in units of 10^{15}m^3 , and the arrows are scaled such that the horizontal and vertical arrows in the top-left have lengths 10^{13}m^3 and $10^{19} \text{m}^3 \text{Pa}$ respectively.

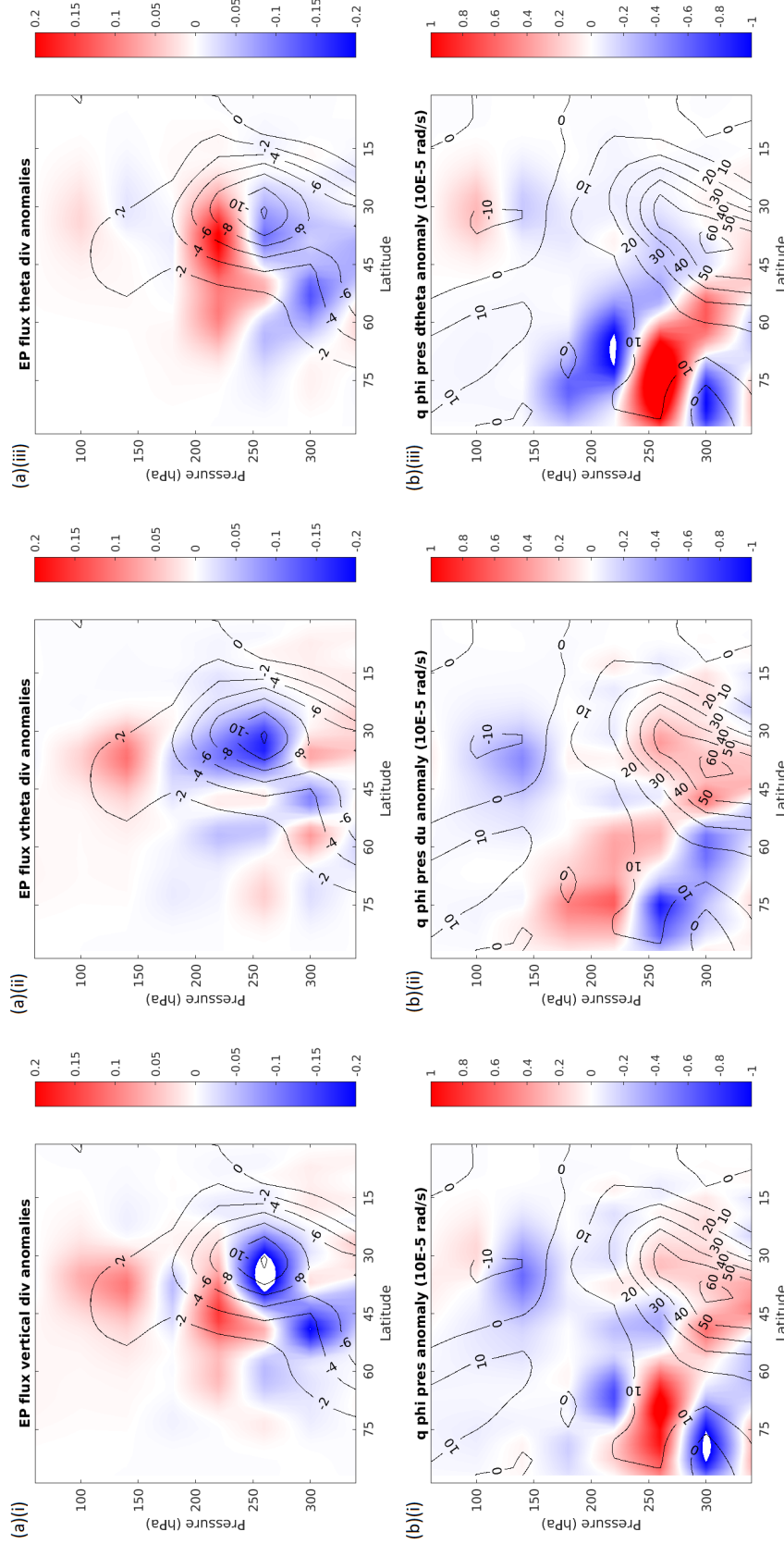


Figure 3.3.5: Control values (contours), and anomalies (colours), in zonally- and hemispherically-averaged (a) vertical EP flux divergence, $\frac{dF_p^v}{dp}$ (top panels), and (b) vertical component of meridional PV gradient, $q_{\phi,p}$ (bottom panels), 340hPa to 60/20hPa, in U01 experiment, averaged over days 0-10. Left-to-right, panels correspond to the: (i) total values (left panels), (ii) contributions due to changes in poleward eddy heat fluxes, $\Delta[v^*\theta^*]$ (top-middle)/vertical zonal wind gradient, $\Delta\partial_p u$ (bottom-middle), and (iii) contributions due to changes in vertical potential temperature gradient, $\Delta\partial_p\theta$ (right panels).

days. These anomalies then propagate down into the troposphere over the subsequent 10-30 days period, alongside the emergence and downward propagation of positive anomalies poleward of 60° , and also in the model troposphere around 30° , below the negative anomalies. A similar pattern is seen in the mass streamfunction, with anomalies that originate in the stratosphere between 30° and 60° in the initial 0-10 days, and the other anomalies in the troposphere subsequently emerging in the 11-20 day period, and then strengthening in the 21-30 day period.

The changes in EP fluxes and EP flux divergence in experiment U01 over these timeperiods are shown in figure 3.3.2. We observe how, during the initial 0-10 day period, a signal is only apparent around the tropopause level, between 200 to 300hPa and 30° to 60° in both hemispheres, with a net downward EP flux and \pm dipole pattern in the divergence. It isn't until days 11-20 that a signal begins to emerge in the extratropical troposphere below, with net downward EP fluxes flowing from the tropopause above, balanced by a net poleward flow in the subtropical upper troposphere. Beyond that, the picture becomes noisy as tropospheric variability takes over.

It is therefore clear that the initial signal in the zonal winds, mass streamfunction, and EP fluxes originates in the stratosphere and tropopause region in the first 0-10 days, subsequently extending down into the troposphere over days 11-20, and strengthening over days 21-30. To gain a clearer picture of how exactly the signal propagates down from the stratosphere into the troposphere, we turn to analysing the changes in the stratosphere and upper troposphere over the initial 15 days.

Figure 3.3.3 displays the changes in the zonal winds and potential temperature above 400hPa, averaged over both hemispheres, over days 0-5 (left panels), 6-10 (middle panels) and 11-15 (right panels) of experiment U01. In the initial 0-5 days, the only signal is in the stratosphere, with a fairly uniform warming of about $+0.2^\circ\text{C}$, and a negative zonal wind anomaly of around -0.05m/s located between 30° to 45° above 200hPa. These signals get stronger over the subsequent days, and positive anomalies in the zonal wind begin to emerge, one immediately below the negative zonal wind anomaly in the troposphere below, between 30° to 45° below 250hPa, and another to its north on the poleward flank of the polar vortex, above 250hPa and poleward of 60° . These signals initially emerge in days 6-10, and subsequently strengthen in days 11-15, whilst the negative zonal wind anomaly in the stratosphere also begins to extend down into the troposphere below around 45° , from days 11-15.

Figure 3.3.4 displays the changes in EP fluxes, $\mathbf{F} = (F^y, F^p)$ (arrows; top and bottom panels), EP flux divergences, $\nabla \cdot \mathbf{F}$ (top panels), and meridional potential vorticity gradient, q_ϕ (bottom panels), over the same atmospheric regions and timeperiods. Beginning in days 0-5, we see an anomalous downward EP flux between 30° to 60° and 200 to 300hPa, accompanied by \pm and $-/+$ dipole anomalies in the EP flux divergence and PV gradient respectively, showing a net divergence of EP fluxes away from the lower stratosphere and convergence into the upper troposphere, as the meridional PV gradient decreases aloft and increases below. In the subsequent days, this signal in the extratropics amplifies, whilst in the tropics an anomalous upward and poleward EP flux emerges in the upper troposphere, between 15° to 30° and below 250hPa,

starting in days 6-10, balancing the anomalous downward EP fluxes in the extratropics. Days 11-15 shows an amplification of the meridional and vertical components of these anomalous EP fluxes, such that a clear pattern of anomalous EP fluxes, rising in the tropical upper troposphere, traveling polewards, and then descending in the extratropics, has emerged.

Looking more closely at these anomalies, figure equatorial3.3.5 displays the separate contributions to the EP flux divergence (top panels) and meridional PV gradient (bottom panels) anomalies, averaged over days 0-10, by their total vertical components (left panels), and individual contributions from changes in the poleward eddy heat fluxes/zonal winds (middle panels), and potential temperatures (right panels). Comparing with the overall EP flux divergence and PV meridional gradient anomalies in figure 3.3.4, we see that the vertical components - $\frac{dF^p}{dp}$ and $q_{\phi,p}$ (3rd term on RHS of equation (2.1.28)) - dominate the overall anomalies, as with most of the model atmosphere in the equilibrium mean. Furthermore, the contributions to these components by the changes in poleward eddy heat fluxes/zonal winds and potential temperatures appear equally important, although the former/latter appears somewhat more dominant close to/away from the jet core, centred at 40° and 250hPa. Given the large changes in vertical zonal wind shear we see in this region, this is not altogether surprising.

Summary

- Zonal wind and mass streamfunction anomalies originate in the stratosphere in the initial 0-10 days of the spinup, and slowly strengthen and propagate down into the troposphere over the subsequent 10-30 day period;
- EP flux divergence and meridional PV gradient anomalies around the extratropical tropopause are present in the initial 0-10 days of the spinup, and emerge and strengthen in the rest of the troposphere over the 10-30 day period;
- A dipolar change in the vertical component of EP flux divergence $\nabla \cdot \mathbf{F}$, $\frac{dF^p}{dp}$, around the extratropical tropopause is present in the initial 0-10 days, and appears to force changes in horizontal EP fluxes and their convergence, $\frac{dF^y}{dy}$, and by extension forces zonal wind changes in the troposphere below;
- The dipolar changes in $\nabla \cdot \mathbf{F}$ around the extratropical tropopause are forced by changes in vertical potential temperature gradient and eddy poleward heat flux, $\partial_p [\theta]$ and $[v^* \theta^*]$;
- The dipolar changes in q_ϕ around the extratropical tropopause are forced by changes in vertical potential temperature and zonal wind gradient, $\partial_p [\theta]$ and $\partial_p [u]$, or equally vertical and meridional potential temperature gradient, $\partial_p [\theta]$ and $\partial_y [\theta]$.

3.3.2 Experiments P01 and T01

In the previous subsection, we focused on analysing the atmospheric response in experiment U01 during the first 0-30 days. To investigate whether a similar mechanism applies when we have

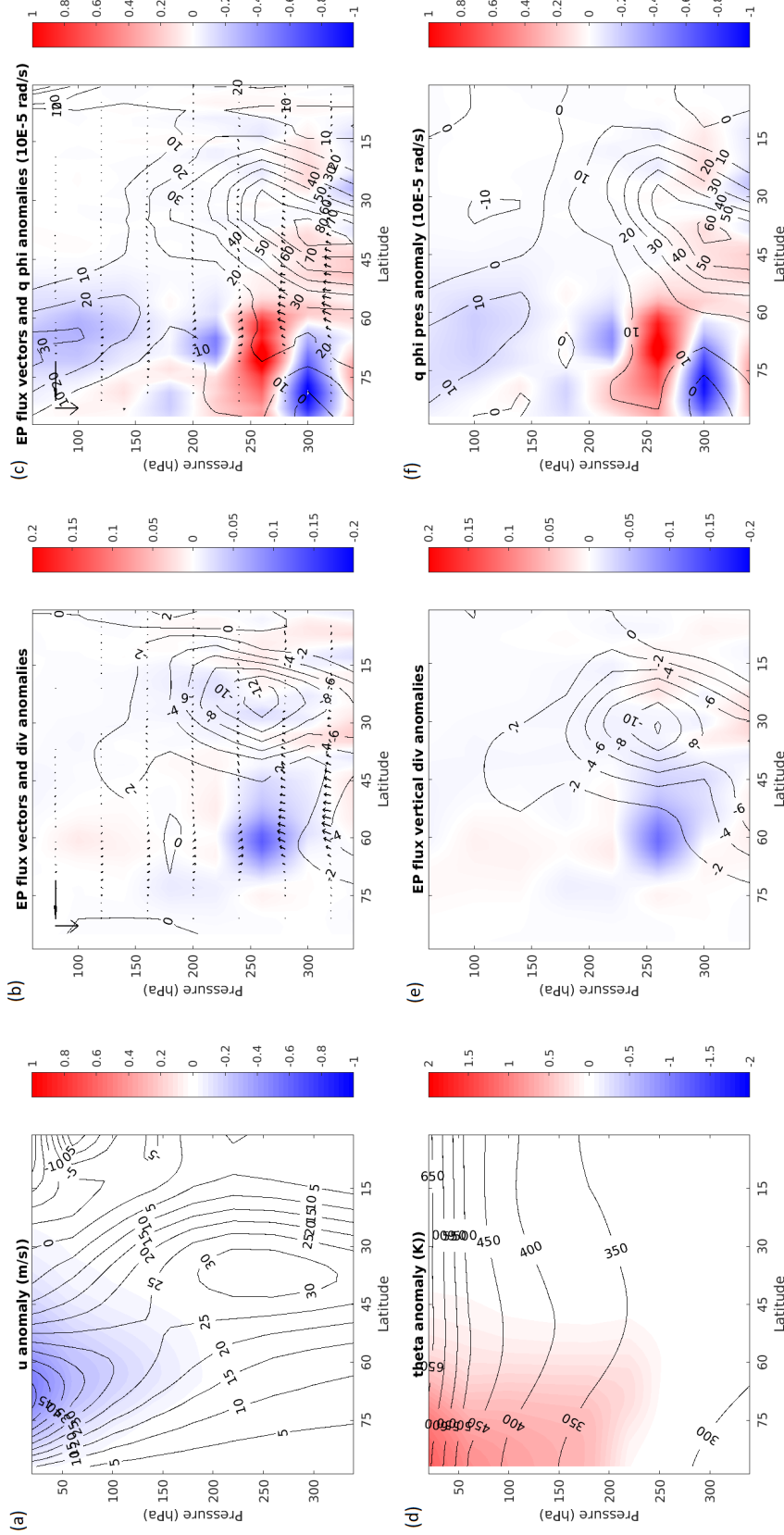


Figure 3.3.6: For experiment P01, averaged over days 0-10, changes in: (a) zonal wind (top-left), (b) EP fluxes (arrows) and divergences (colours) (top-middle), (c) EP fluxes (arrows) and meridional PV gradient (colours) (top-right), (d) potential temperature (bottom-left), (e) vertical EP flux divergence (bottom-middle), and (f) vertical component of meridional PV gradient (bottom-right). All values are zonally- and hemispherically-averaged, and contours/colours indicate control values/anomalies. In the EP flux diagram, the fluxes are mass-weighted as per equations (2.1.32) and (2.1.33), the EP flux divergences are in units of 10^{15}m^3 , and the arrows are scaled such that the horizontal and vertical arrows in the top-left have lengths 10^{13}m^3 and $10^{19}\text{m}^3\text{Pa}$ respectively.

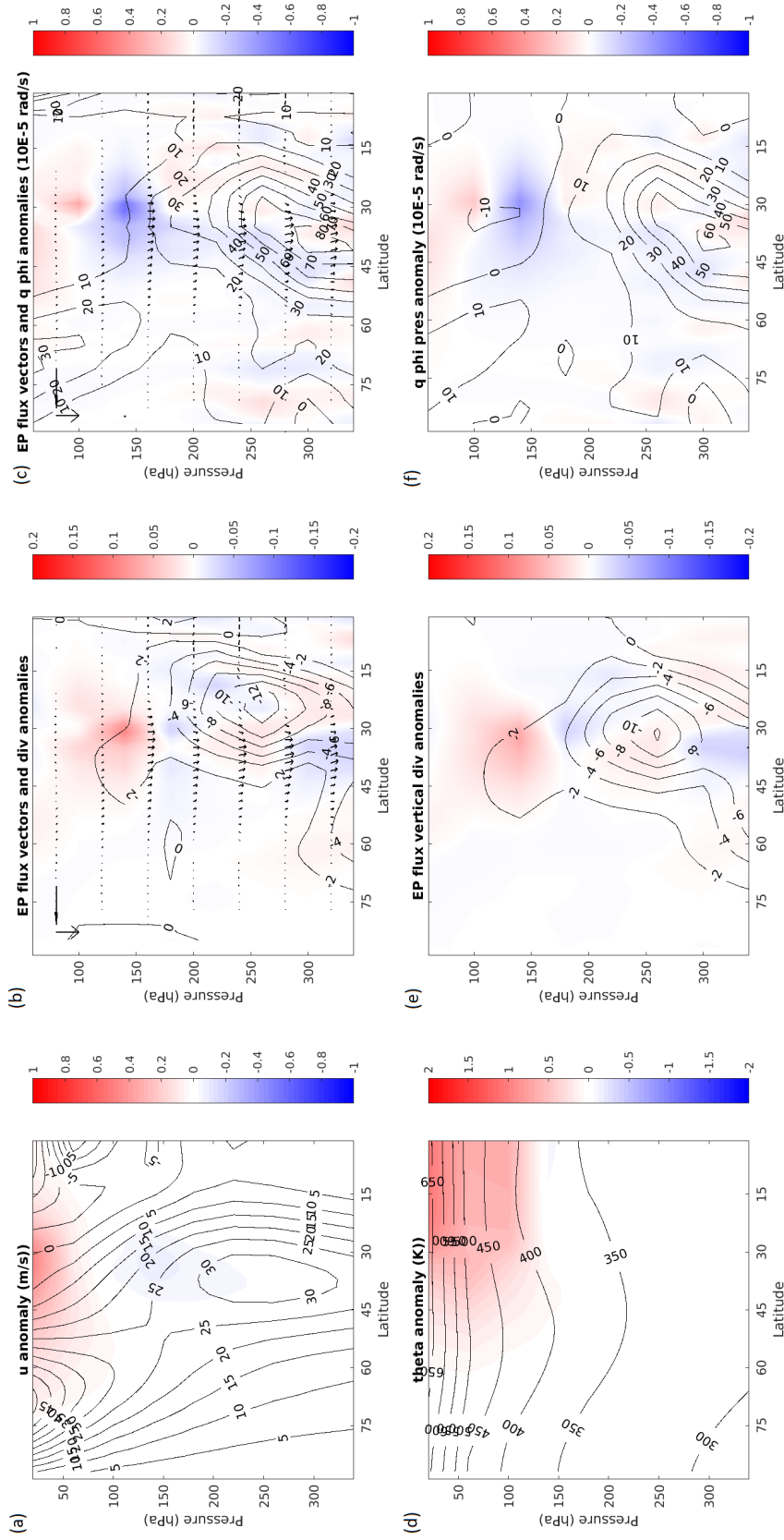


Figure 3.3.7: For experiment T01, averaged over days 0-10, changes in: (a) zonal wind (top-left), (b) EP fluxes (arrows) and divergences (colours) (top-middle), (c) EP fluxes (arrows) and meridional PV gradient (colours) (top-right), (d) potential temperature (bottom-left), (e) vertical EP flux divergence (bottom-middle), and (f) vertical component of meridional PV gradient (bottom-right). All values are zonally- and hemispherically-averaged, and contours/colours indicate control values/anomalies. In the EP flux diagram, the fluxes are mass-weighted as per equations (2.1.32) and (2.1.33), the EP flux divergences are in units of 10^{15}m^3 , and the arrows are scaled such that the horizontal and vertical arrows in the top-left have lengths 10^{13}m^3 and $10^{19}\text{m}^3\text{Pa}$ respectively.

temperature perturbations that are confined to a specific part of the stratosphere, we now turn to analysing the results of experiments P01 and T01 over this timeperiod. Figures 3.3.6 and 3.3.7 display the changes in zonal wind, potential temperature, EP fluxes and divergences, and PV meridional gradient - both total and their vertical components - in the top 400hPa, during the initial 0-10 days of experiments P01 and T01. In both experiments, as in U01, there is only a signal in the stratosphere with the zonal winds and potential temperature at this point, with negative/positive zonal wind anomalies, and positive potential temperature anomalies in the high-/low-latitudes in experiment P01/T01. At the bottom boundaries of these stratospheric anomalies, we observe +/- dipoles of anomalous EP flux divergence, and -/+ dipoles of anomalous PV meridional gradient, causing anomalous net downward EP fluxes at those latitudes, diverging away from the stratosphere and converging into the upper troposphere. Closer inspection again indicates that these anomalies in the EP flux divergence and PV meridional gradient are dominated by their vertical components.

We are thus led to much the same conclusions as in experiment U01: that the changes in EP fluxes around the tropopause level, present in the initial 0-10days and responsible for the subsequent changes in tropospheric dynamics, are initially forced by changes in vertical potential temperature and zonal wind gradients around the tropopause, which themselves are the direct, forced consequences of applied STP's. The changes in EP fluxes are such that we get an anomalous net downward flux from the stratosphere into the upper troposphere around the latitudes of forcing, inducing an anomalous poleward/equatorward EP flux from the tropical/extratropical upper troposphere in experiment P01/T01. This shifts the pattern and strength of convergence of eddy-momentum fluxes in the upper troposphere, shifting and altering the strength of the zonal winds and circulations. These changes in the mean fields then quickly filter down to the lower troposphere, via their feedbacks onto the meridional PV gradient and patterns of EP flux convergence and divergence.

3.4 Chapter Conclusions

In this last subsection, we will attempt to summarise the main conclusions from our results in this chapter. In section 3.1 it was found that the response of the model atmosphere in its atmosphere-only configuration to STP's was (P01/T01):

- polar vortices weakened/strengthened;
- Hadley cells and tropical easterlies strengthened/weakened;
- Ferrel cells and midlatitude jets strengthened/weakened and contracts/expands equatorward/poleward;
- poleward eddy heat fluxes - and associated EP fluxes, divergences and TEM circulation patterns - in the mid-to-high latitudes weakened/strengthened.

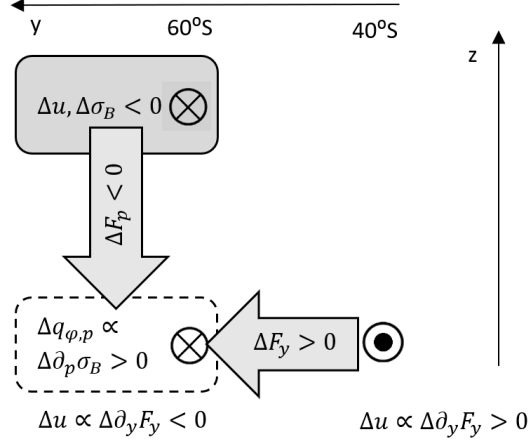


Figure 3.4.1: Schematic showing mechanism whereby downward propagation of easterly zonal wind anomalies (circled crosses) and simultaneous induction of westerly anomalies on its equatorward flank (circled dot) may be achieved. Arrows show the directions of anomalous EP flux components. Mechanism is depicted for the Southern Hemisphere, with approximate latitudes of the zonal wind anomalies indicated along the (horizontal) latitude axis.

Moreover, the tropospheric response to U01 was found to resemble a weakened version of P01, not dissimilar to P01 (strong) + T01 (weak). Overall, the atmospheric response showed a good qualitative resemblance to that found in response to similar experiments with an sGCM in Haigh et al. (2005) and Simpson et al. (2009), although quantitatively it was much weaker in the troposphere for experiments U01 and P01. It also showed good correspondence with observations/simulations of the SH atmospheric response during austral summer (DJF) to ozone depletion/recovery (Polvani et al. 2011; Son et al. 2010, 2018), with experiments T01/P01 mirroring closely the SH atmospheric response to ozone depletion/recovery. These results therefore underscore the generic nature of this type of stratosphere-troposphere coupling, especially when looking at the Southern Hemisphere, and its apparent lack of dependence upon e.g. topography, land-sea contrasts, and physical parameterisations. They also add confidence to our use of the MITgcm in this particular aquaplanet setup, through its ability to capture atmospheric responses that are qualitatively and quantitatively similar to that seen in both observations and simulations with more complex models, in response to realistic STP's.

In section 3.2, the changes in tropospheric dynamics were found to be forced by changes in the EP flux divergences, which themselves would respond to changes in zonal wind and temperature via the meridional PV gradient, implying a feedback between the eddies and mean state. Investigation into the time-evolution of the atmospheric response to applied STP's in section 3.3 showed that the direct changes in stratospheric zonal wind and temperature - as forced by the perturbations - would induce changes in the patterns of EP flux divergence that crossed the tropopause, thereby initiating changes in the tropopause below via a mechanism similar to that in figure 1.1.4 in section 1.1.

Figure 3.4.1 shows a schematic of this mechanism, illustrating how high-latitude easterly stratospheric zonal wind anomalies might be able to simultaneously propagate down through the troposphere, and induce westerly anomalies on their equatorial flank. Easterly zonal wind anomalies aloft induce a local reduction in baroclinicity, σ_B , and thereby induce an increase in PV meridional gradient third component, $q_{\phi,p}$, below. This causes an increased poleward wave-flux into the region (poleward horizontal arrow), causing westerly momentum to be siphoned away from that region by eddy-momentum fluxes into lower latitudes, thereby inducing local easterly anomalies, and westerly anomalies on its equatorward flank. It also causes an inhibition of upward wave fluxes (downward vertical arrow), shielding the zonal wind anomalies aloft, and reducing poleward eddy fluxes of heat, $[v^*\theta^*]$, as they respond to local reductions in meridional temperature gradient, $\partial_y\theta$. An equivalent mechanism for experiment T01 can be found by reversing the signs of everything. This mechanism is supported by the equilibrium responses of experiments P01 and T01, detailed in sections 3.1 and 3.2, and is essentially the same mechanism as is put forth by Simpson et al. (2009). Moreover, the details of its operation in experiment P01 are highly similar to that found in modelling studies of SSW's, such as White et al. (2020). Again, this all serves to highlight the generic nature of the coupling, and the mechanism behind it.

Chapter 4

SST change and drivers

In the previous chapter, we established precisely how different STP's influence the tropospheric climate below in an aquaplanet, atmosphere-only model, and via what mechanism. The next logical step, therefore, would be to establish how such responses are modified by the presence of a global ocean. That said, we already know from section 1.2 that the way(s) in which a thermal and/or dynamical ocean is able to cause changes in the atmosphere above is via changes in its sea surface temperatures, both absolute and their gradients. It therefore becomes essential to understand exactly how the model SST's respond to the stratospheric forcing, and via what mechanism(s), as a precursor to understanding how this then feeds-back onto the atmosphere.

In this chapter, therefore, we will focus upon detailing and explaining the changes in SST we observe in both coupled versions of the model - slab-ocean and fully-coupled - in response to our stratospheric heating experiments. The central aim will be to have an understanding, by the end, of how exactly the atmospheric changes we saw in the previous chapter force changes in the models' sea surface temperatures, what those changes look like, and whether these lead to significant differences in SST's between the fully-coupled and slab-ocean setups.

4.1 SST time-evolution and drivers: Slab-ocean setup

We will start by identifying and analysing the changes in SST in our simplest coupled setup: the slab-ocean setup. Since, in this setup, there are no actual ocean dynamics, and the oceanic heat transport at each latitude and longitude rather is quantified as a fixed flux value - i.e. the Q_{flux} - then, according to equation (2.4.1), the only thing that is able to alter SST's are changes in the net surface heat flux. Thus, in the following analyses, we will aim to diagnose the changes in SST we see in the slab-ocean setup in response to our STP's, and explain them, with reference to the observed changes in surface heat flux, its individual components, and their respective atmospheric drivers.

4.1.1 Global mean SST and surface fluxes time-evolution

The top and bottom panels of figure 4.1.1 display the time-evolution of global-average 360-day running mean sea surface temperatures (top panels) and anomalous surface heat fluxes (bottom panels; positive upward) of the STP experiments in the slab-ocean setup, over the initial 9000 days, or 25 years, of their evolution.

In each experiment, we observe a similar long-term pattern of rising SSTs, powered by a net downward anomalous surface heat flux, which in turn is driven largely by an anomalous downward radiative flux. Note the difference in scale between the overall changes in SST and surface heat fluxes between experiments U01 (left panels) and P01 (middle panels)/T01 (right panels), with the former exhibiting overall SST and turbulent/radiative flux changes of $+0.8^{\circ}\text{C}$ and $\pm 1\text{Wm}^{-2}$, and the latter closer to $+0.3^{\circ}\text{C}$ and $\pm 0.4\text{Wm}^{-2}$. This scale difference is also evident in the initial downward net surface flux anomalies, which are -0.5Wm^{-2} for U01 and -0.2Wm^{-2} for P01/T01. However, note that, as what we are looking at are 360-day running mean values, these 'initial' anomalies are rather picking up values from as far ahead as 180 days. In any case, this difference in the scale of SST and surface flux anomalies can be understood as simply the consequence of there being overall greater thermal stratospheric forcing present in experiment U01 vs P01/T01, as its entire stratosphere is being perturbed, not just a 30° -wide band in each hemisphere.

When we look at the decomposition of that net positive downward radiative flux into its longwave and shortwave components, shown in the bottom panels of figure 4.1.2, we see that it is, in the long-term, driven by anomalous downward longwave radiative fluxes. These anomalous downward longwave fluxes must originate from net increases in the temperature of the atmosphere above, resulting in greater thermal emission.

As our definition of reaching a new equilibrium state in this setup, we state that it has been reached once the global-average net surface flux reaches and remains consistently below a magnitude of 0.1W/m^2 . Since our slab-ocean setups have a mixed-layer depth of 50m, this would equate to a global-average SST rate of change of approximately $\frac{0.1\text{W/m}^2}{1000\text{kg/m}^3 \cdot 50\text{m} \cdot 4200\text{J/kg/K}} \simeq 0.015\text{K/year}$. Looking back at the bottom panels of figure 4.1.1, we see that this threshold has been reached across the different experiments at around 4000 days, or 11 years.

Another notable feature of the time-evolution of the global-average surface fluxes and its different components is how, during the initial 1000 days, or 3 years, of each experiment, the net global-average turbulent heat flux is, like the global-average net surface flux, positive downward and, as such, playing a significant role in driving the changes in global-average SST over that timeperiod. This is more the case for experiments U01 and P01, and, looking at the decomposition of this term in the top panels of figure 4.1.2, we see that it is driven primarily by changes in the surface latent heat fluxes. This dominance of the global-average turbulent heat fluxes by the latent heat fluxes is the case at all times in each experimental spinup, not just the first 1000 days. Moreover, we observe the general trend in sensible and latent heat flux anomalies being of opposite sign to one another, with the latent/sensible heat fluxes being negative/positive

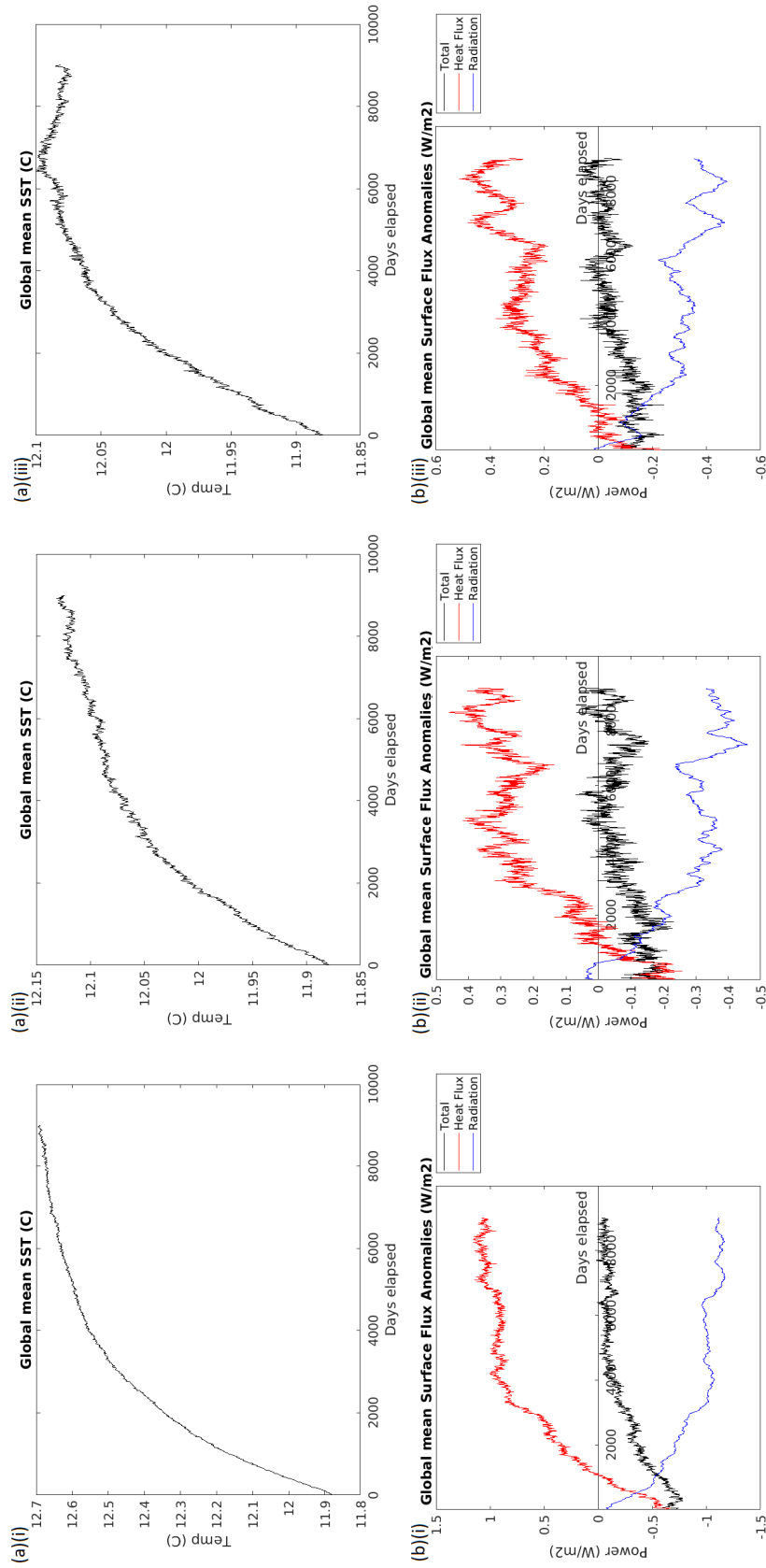


Figure 4.1.1: Time-evolution of global-average 360-day running mean (a) sea surface temperatures (top panels), and (b) anomalous surface heat fluxes and its radiative and turbulent heat flux components (bottom panels), positive upward, for experiments (left-to-right): (i) U01 (left panels), (ii) P01 (middle panels), and (iii) T01 (right panels), in slab-ocean double-drake set-up.

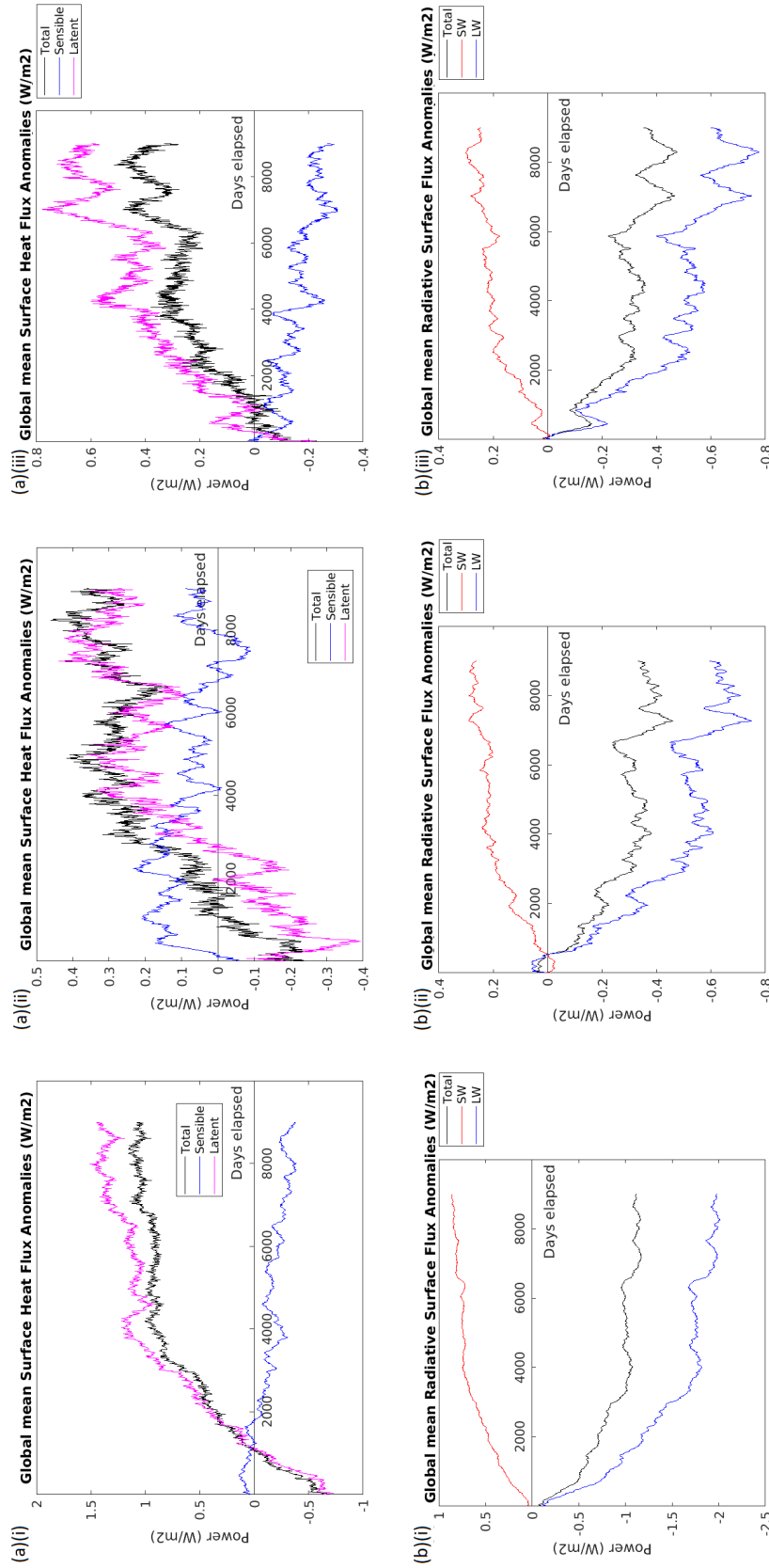


Figure 4.1.2: Time-evolution of global-average 360-day running mean anomalous (a) turbulent surface fluxes (top panels), and (b) radiative surface fluxes (bottom panels), positive upwards, for experiments (left-to-right): (i) U01 (left panels), (ii) P01 (middle panels), and (iii) T01 (right panels), in slab-ocean double-drake set-up.

initially (~ 0 -1000 days), and then positive/negative subsequently, suggesting that the latter is damping the former.

This is also the case for LW and SW radiative surface fluxes, with the former and latter anomalously negative and positive respectively, combining to give an overall negative - i.e. downward - surface radiative heat flux. Since all SW radiation incident at the surface is either absorbed or reflected out to space - see section 2.4.2 for more details - such a positive anomaly must indicate a reduction in downwelling SW radiation. Given that the amount of incident SW radiation at the top-of-atmosphere is a constant in the model, this can only be achieved by an increase in SW optical depth, τ , which in turn can only be achieved by an increase in atmospheric water vapour content. Such an increase in atmospheric water vapour would also, incidentally, lead to increased optical depths in the LW radiation bands too, leading to greater LW absorption. However, as we previously stated, increases in atmospheric temperature would lead to increased LW emission. Thus, we expect there to be simultaneously greater atmospheric LW emission and absorption, leading to an overall increased incidence of downward LW radiation at the surface.

Summary

- In all slab-ocean experiments, global-average SST rises steadily over approximately 11 years, driven by an anomalous global-average net downward surface heat flux of $0.5/0.2 \text{ Wm}^{-2}$ for experiments U01/P01 & T01;
- Initially (0-1000 days), global-average SST appears to be driven by anomalous turbulent latent heat fluxes, then subsequently by anomalous downward LW radiative fluxes;
- Increases in atmospheric heat and water vapour content must be responsible for the observed trends in the radiative heat fluxes (LW and SW respectively).

4.1.2 Local SST changes and drivers

Up until now, we have only looked at changes in global-average SST and its drivers. Whilst this is an important thing to consider, arguably more pertinent to the study of atmosphere-ocean coupling is looking at the changes in zonal-average SST and SST gradient as they occur at each given latitude. For, as was detailed in section 1.2, the same changes in SST and/or SST gradient can produce vastly different atmospheric responses depending upon where they are placed latitudinally, and in relation to such structures as the subtropical jets, storm tracks, and Hadley cells. Thus, we now turn our attention to studying the SST changes as they occur at each latitude and longitude, and their drivers.

The bottom panels of figure 4.1.3 show the changes in SST over the initial 25 years of each spinup. We observe that, when it comes to the changes in the meridional SST profile, and especially SST meridional gradient profile, these appear to be set quite early on, during the first 1000 days approximately of experiments P01 and T01. This is further confirmed by looking

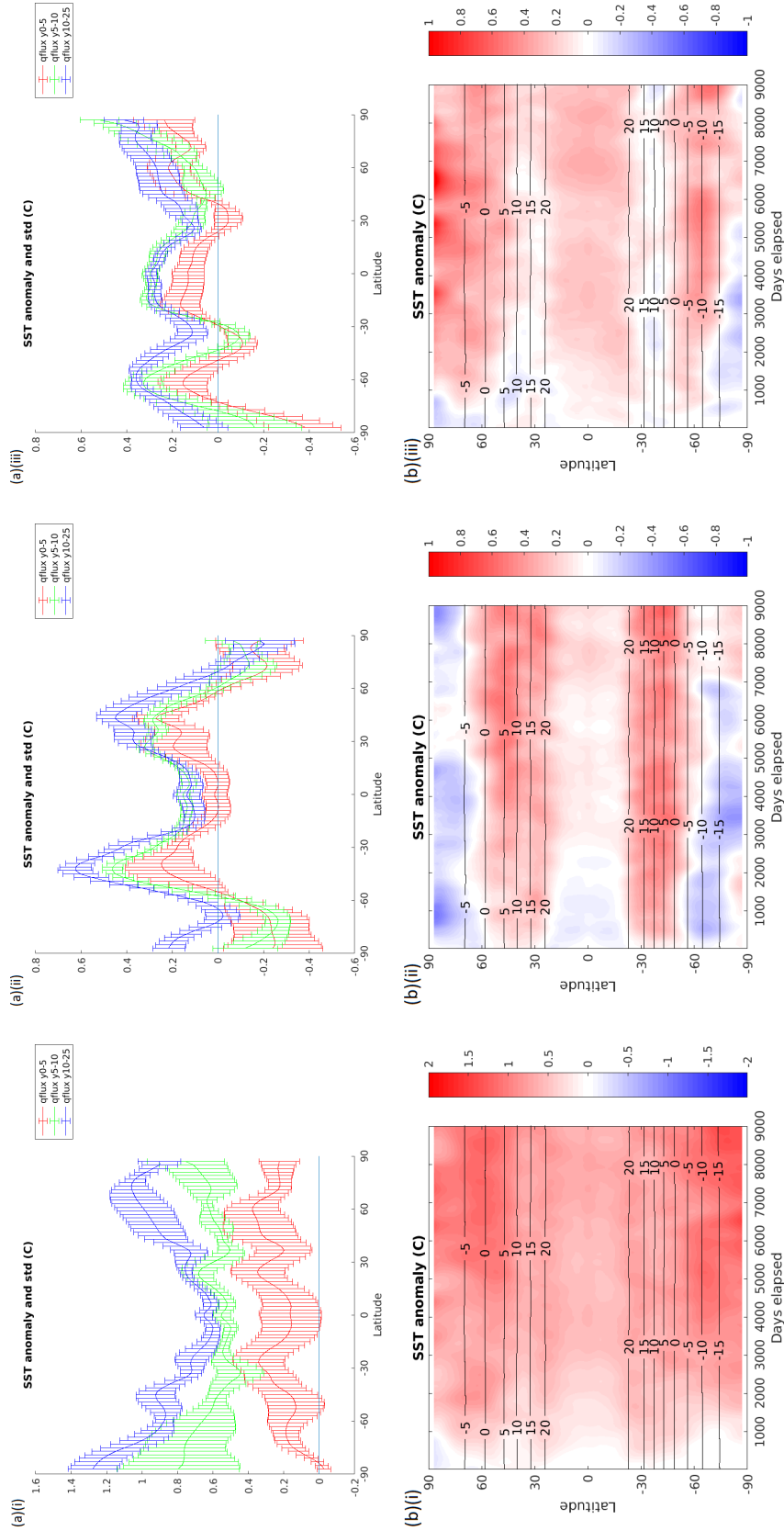


Figure 4.1.3: (a) (Top panels) Changes in zonal-mean sea surface temperatures in slab-ocean setup, averaged over years 0-5 (red), 5-10 (green), and 10-25 (blue), and (b) (bottom panels) time-evolution of control values (contours) and anomalies (colours) in zonal-average sea surface temperatures, in experiments (left-to-right): (i) U01 (left panels), (ii) P01 (middle panels), and (iii) T01 (right panels).

at the top panels of 4.1.3, which show the zonal-mean SST anomalies for each experiment, averaged over different time periods. For P01 and T01, there are relatively few changes in the SST anomalies between years 0-5, and years 5-10/10-25, save a fairly uniform and small SST increase from years 0-5 to 10-25. For U01, there are significant SST changes between years 0-5 and 5-10, with increases in SST at every latitude, ranging from $+0.4^{\circ}\text{C}$ around the equator, to around $+0.8^{\circ}\text{C}$ around the poles.

Figure 4.1.4 shows the SST (top panels) and net surface heat flux (bottom panels) anomalies, averaged over the first 10 years of each experiment in the slab-ocean setup. We note the broadly good correspondence between the top and bottom panels, with anomalous warm/cold SST anomalies aligning with regions of anomalous downward (negative)/upward (positive) net surface heat flux, affirming that the former are driven by the latter. The decomposition of the net surface heat flux anomalies into its contributions by radiative and turbulent surface heat flux anomalies is shown for each experiment in figure 4.1.5. We see that, broadly speaking, the tropics is dominated by anomalous downward radiative fluxes, damped by upward turbulent heat fluxes, giving an overall anomalous downward heat flux, especially in experiments U01 and T01. In the extratropics, the situation is reversed, with anomalous turbulent heat fluxes dominating, and the radiative fluxes generally providing a smaller, negative feedback, with the exception of regions such as the high-latitude Southern Ocean, large basin, and North Atlantic region of the small basin, in experiments U01 and P01, where the negative radiative flux anomalies contribute significantly.

Figures 4.1.6 and 4.1.7 go further, decomposing the total turbulent heat fluxes and radiative fluxes into their contributions by the sensible/latent heat fluxes, and downward/upward LW radiative fluxes (SW anomalies were found to be negligible). What is immediately striking is how the sensible/latent heat and downward/upward LW fluxes appear broadly equal and opposite to one another, with anomalous upward/downward latent heat fluxes in regions of anomalous downward/upward sensible heat fluxes, and similar for the upward and downward LW fluxes. This was also seen in the global-average picture, in section 4.1.1. For the LW fluxes, this is reflective of the similar temperature profiles of the SST's and atmosphere, especially its lower layers, which are subject to a shorter path length to the surface, and hence less atmospheric absorption. For the turbulent heat fluxes, it reflects the similar parameterisations used, given by equations (2.4.3) and (2.4.4), both being subject to changes in the surface wind. Moreover, following the Clausius-Clapeyron relation - equation (2.4.7) - a rise in temperature gives rise to an exponential rise in saturation vapour pressure. Thus, a rise in SST will necessarily be accompanied by a rise in surface humidity, and similar for the bottom atmospheric layer.

By-and-large, the latent heat fluxes appear to dominate in the tropics (especially for U01 and T01), and sensible heat fluxes in the extratropics, although the latent heat flux contributions in the small basin are significant. The radiative fluxes show a pattern of being dominated in the tropics by anomalous downward LW, and in the extratropics by anomalous upward LW. This is the case, except for U01, for which the anomalous downward LW radiative flux is significant at all latitudes, although the upward LW appears significant in shaping the zonal anomalies in

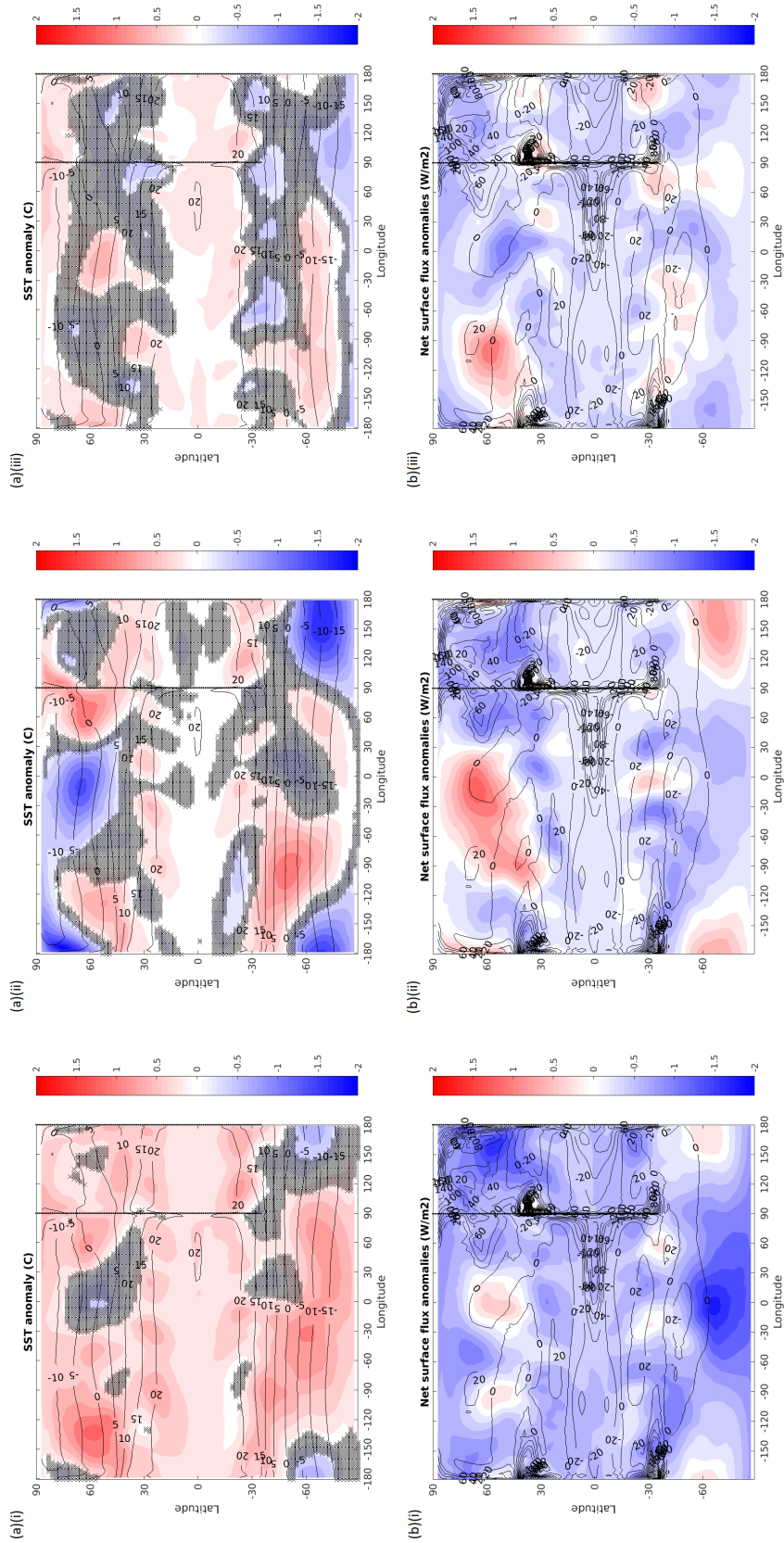


Figure 4.1.4: Control values (contours) and anomalies (colours) in (a) sea surface temperatures (top panels), and (b) net surface heat fluxes (bottom panels), positive upwards, averaged over years 0-10, for experiments: (i) U01 (left panels), (ii) P01 (middle panels), and (iii) T01 (right panels), in slab-ocean double-drake set-up. Hatching in the top panels indicates regions in which the confidence levels in the experiment vs control values are below 95%, as measured by a two-tail student's t-test.

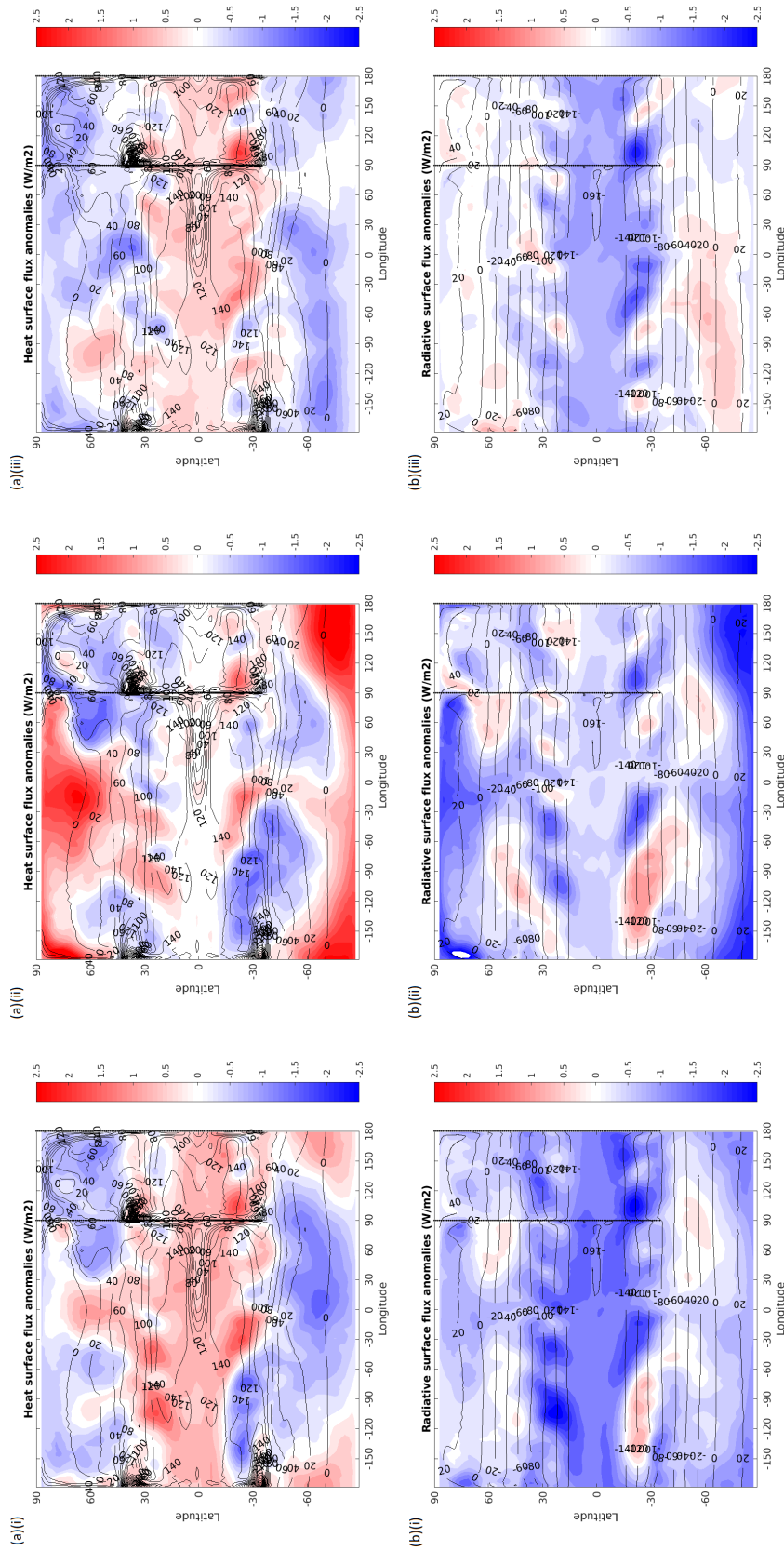


Figure 4.1.5: Control values (contours) and anomalies (colours) in surface (a) turbulent heat fluxes (top panels), and (b) radiative fluxes (bottom panels), positive upwards, averaged over years 0-10, for experiments: (i) U01 (left panels), (ii) P01 (middle panels), and (iii) T01 (right panels), in slab-ocean double-drake set-up.

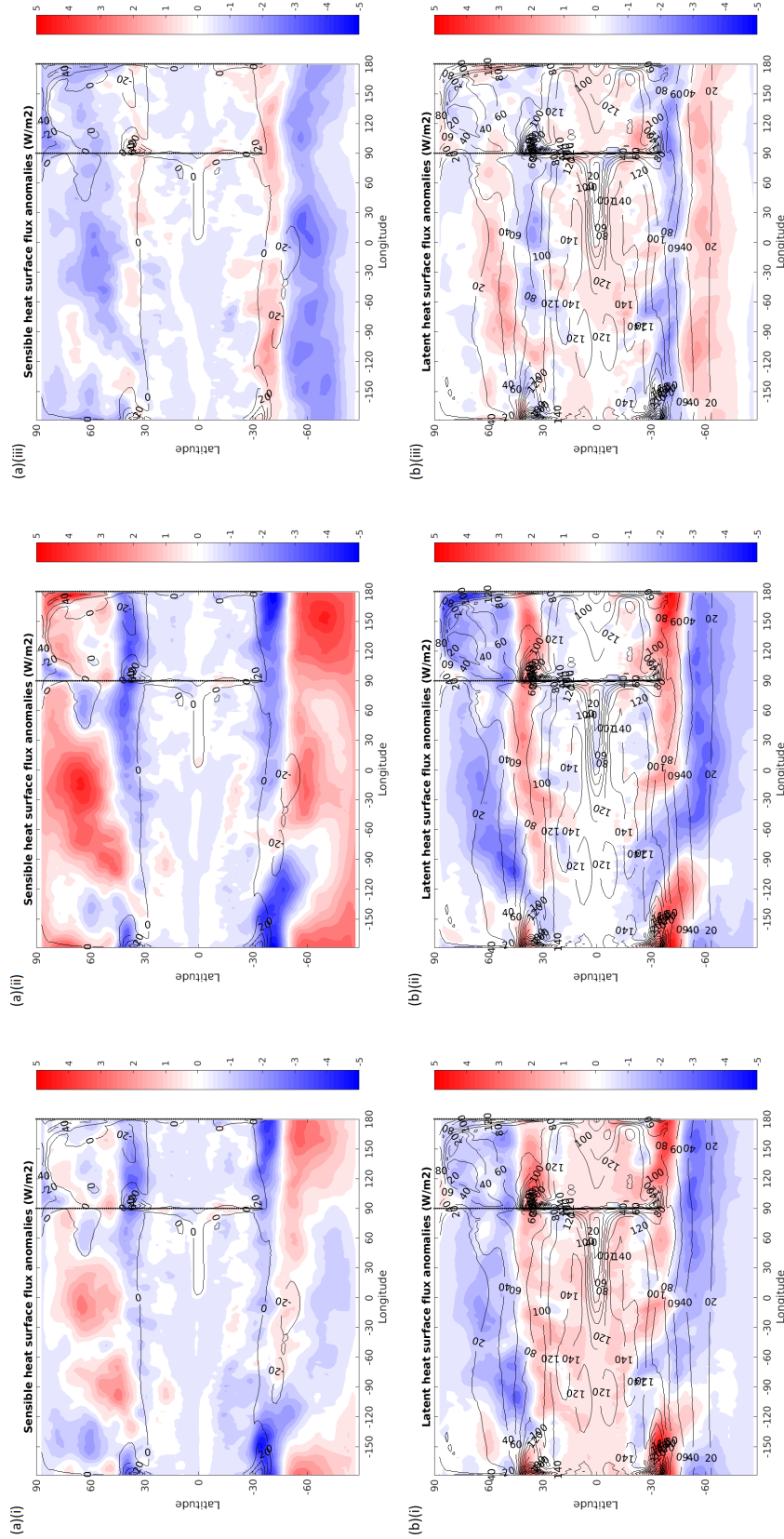


Figure 4.1.6: Control values (contours) and anomalies (colours) in surface (a) sensible heat fluxes (top panels), and (b) latent heat fluxes (bottom panels), positive upwards, averaged over years 0-10, for experiments: (i) U01 (left panels), (ii) P01 (middle panels), and (iii) T01 (right panels), in slab-ocean double-drake set-up.

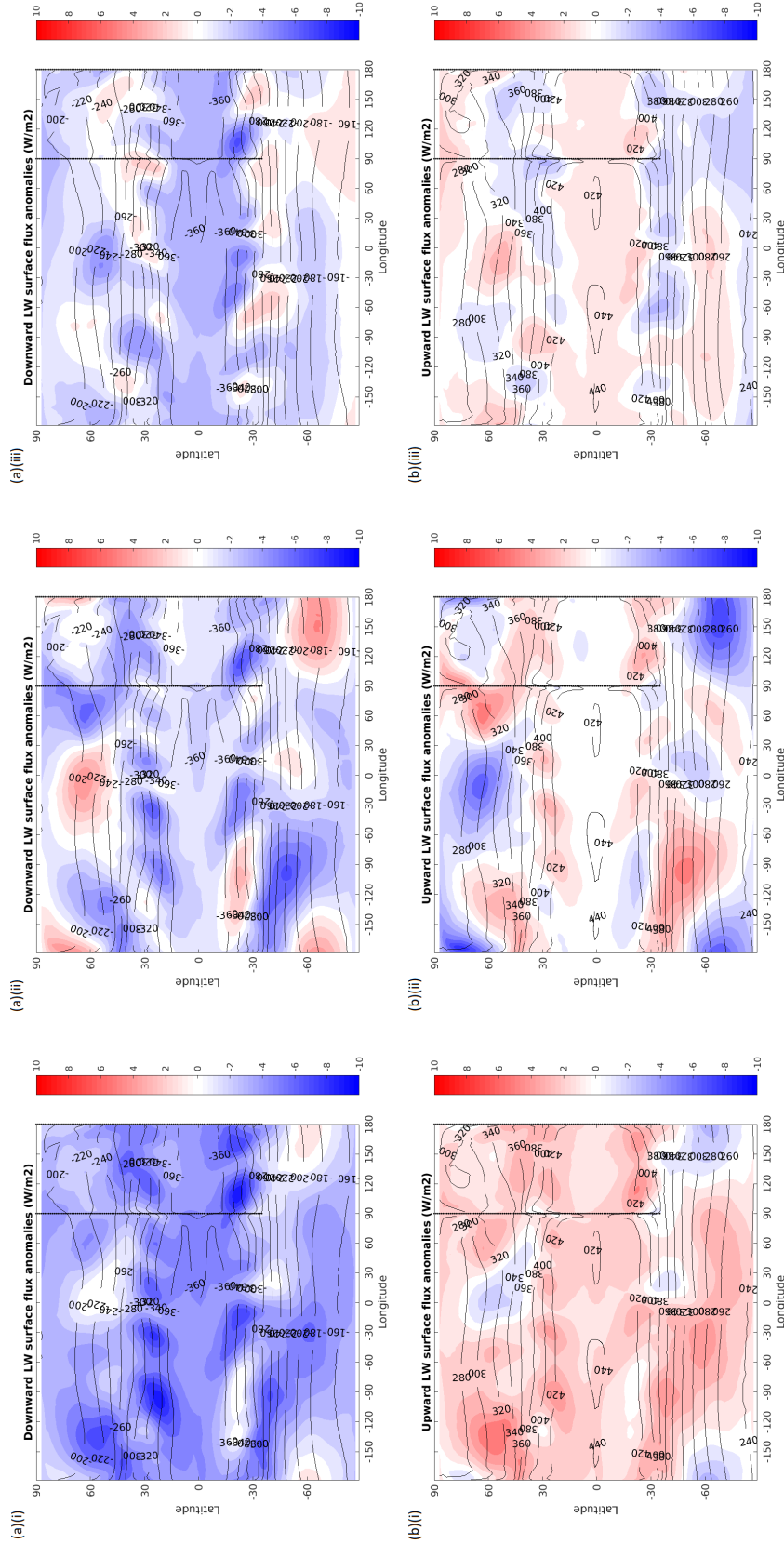


Figure 4.1.7: Control values (contours) and anomalies (colours) in surface longwave fluxes: (a) downward LW fluxes (top panels), and (b) upward LW fluxes (bottom panels), positive upwards, averaged over years 0-10, for experiments: (i) U01 (left panels), (ii) P01 (middle panels), and (iii) T01 (right panels), in slab-ocean double-drake set-up.

the extratropics. Broadly speaking, it therefore appears that downward LW fluxes drive SST changes in the tropics, damped by latent heat fluxes, and sensible heat fluxes in the extratropics, damped by latent heat and upward LW fluxes.

Summary

- The SST zonal-mean meridional profile is largely set within the first ~ 1000 days for experiments P01 and T01, and within the first 2000-3000 days for experiment U01, similar to the global-average SST;
- SST changes are driven by anomalous:
 - downward LW radiative fluxes in the tropics, damped by upward LW + latent heat fluxes;
 - sensible heat fluxes in the extratropics, damped by upward LW + latent heat fluxes.
- In experiment U01, downward LW and latent heat fluxes also make a positive contribution to SST increases in the extratropics;
- Sensible/latent heat, and downward/upward LW flux anomalies tend to be equal and opposite to one another, as do turbulent heat/radiative flux anomalies.

4.1.3 Drivers of turbulent heat flux anomalies

To understand better what is driving the changes in turbulent surface fluxes, which appear crucial to the driving of SST changes in the extratropics, we turn our attention towards the individual contributions to these fluxes by the changes in surface wind, $\sqrt{(u_s^*)^2} = \sqrt{u_s^2 + v_s^2}$, and by surface humidity/temperature gradients, $(SST - T_s)$ or $(q_{sat} - q_s)$. Due to the nature of the parameterisations of surface drag coefficients used in the model, their values are highly variable and difficult to calculate accurately. We will therefore focus simply on the product of these two variables - surface wind times surface humidity/temperature gradient - as a proxy for surface latent and sensible heat flux. The anomalous values for these quantities (left panels), and their individual contributions due to changes in the surface wind (middle panels) and humidity/temperature gradient (right panels), are shown in figure 4.1.8 for experiment P01.

If we compare the total anomalies (left panels) with the anomalous sensible and latent heat fluxes - shown in the middle panels of figure 4.1.6 - we observe a generally good correspondence between the two, especially in the midlatitudes. Moreover, it would appear that the contribution due to changes in surface wind strength (middle panels) drives most of the changes in turbulent surface heat flux, especially, again, in the midlatitudes, where it reproduces positive/negative dipole anomalies seen in the latent and sensible heat flux anomalies. That said, the changes in surface temperature and humidity gradient are not negligible, especially in the lower midlatitudes, 30° to 45° , where enhanced surface temperature and humidity gradients (more

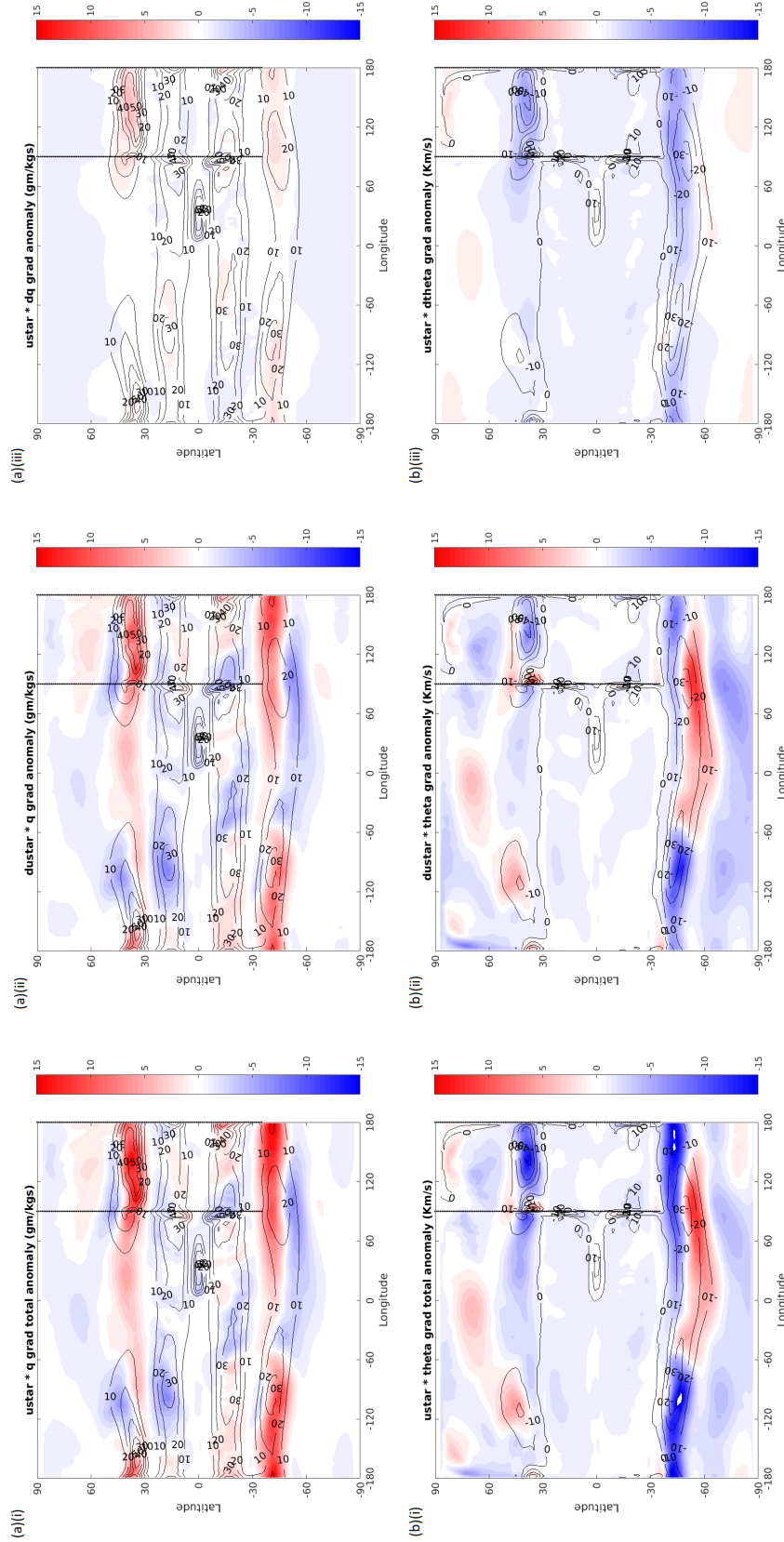


Figure 4.1.8: Control values (contours) and anomalies (colours) of surface wind times: (a) surface humidity difference, $u_s^*(q_{sat} - q_s)$ (top panels), and (b) surface temperature difference, $u_s^*(SST - T_s)$ (bottom panels), averaged over years 0-10 of experiment P01 in slab-ocean double-drake setup. From left-to-right, the anomalies in the panels give the (i) total anomaly, $\Delta(u_s^*(X_{sea} - X_{air}))$ (left panels), (ii) anomaly due to changes in surface wind, $(\Delta u_s^*)(X_{sea} - X_s)$ (middle panels), and (iii) anomaly due to changes in surface temperature/humidity difference, $u_s^*(\Delta(X_{sea} - X_s))$ (right panels).

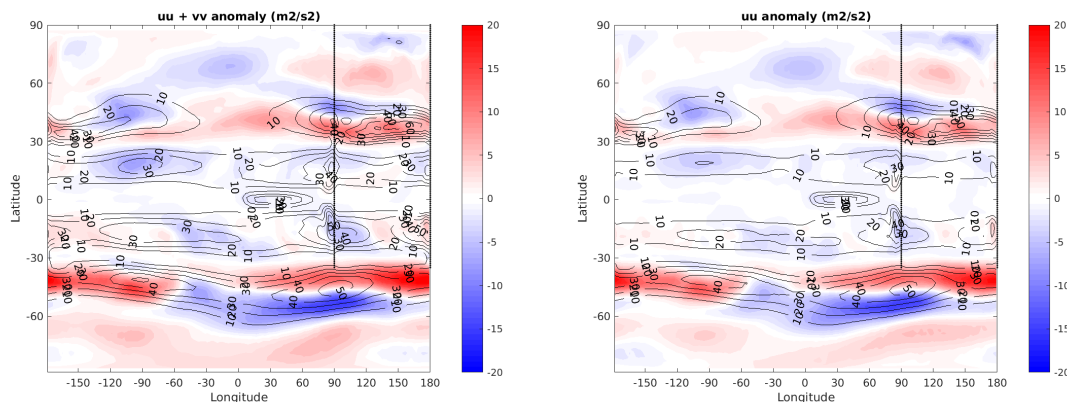


Figure 4.1.9: Control values (contours) and anomalies (colours) in surface wind squared: (a) total, $u^2 + v^2$ (left) and (b) zonal, u^2 (right), averaged over years 0-10 of experiment P01 in slab-ocean double-drake set-up.

negative/positive) contribute to correspondingly stronger turbulent heat fluxes in those regions. Moreover, in the high latitudes - a region of small surface wind time humidity/temperature gradient - this approach generally fails to adequately explain the observed turbulent heat flux anomalies, especially those seen in the sensible heat fluxes. This is possibly related to the relatively small overall values of surface wind and temperature/humidity gradients in the high latitudes. Thus, we might expect the drag coefficients - themselves complex functions of surface wind, and local temperature and humidity gradients - to play a more significant role in shaping the overall turbulent heat flux anomalies in these regions.

To determine what is driving the observed changes in surface wind, the anomalous surface wind squared, $(u_s^*)^2 = u_s^2 + v_s^2$, and the anomalous zonal wind squared only, are shown in figure 4.1.9, averaged over years 0-10 of experiment P01. Clearly, the changes in surface zonal wind dominate the overall surface wind anomalies. Moreover, when we look back at the zonal-average anomalies in zonal winds seen in response to stratospheric heating perturbations - given in figure 3.1.1 of section 3.1 - we see that the correspondence with the turbulent heat flux anomalies in figure 4.1.6 in the extratropics is generally very good, with increased/decreased magnitudes of latent and sensible heat fluxes in regions of accelerated/decelerated westerly zonal wind.

Thus, the emerging picture is that of the changing patterns of tropospheric zonal wind being responsible for the observed turbulent heat flux anomalies in the extratropics. In the high latitudes, where the surface zonal winds and temperature and humidity gradients are relatively weak, this is probably in part manifested by changes in the drag coefficient.

What is still not clear from all of the above analysis, however, is what is driving longer-term trends in the turbulent heat fluxes: in particular, it is unclear what is driving the long-term increases in upward latent heat fluxes in the global-mean, seen in figures 4.1.2, across our experiments in the slab-ocean setup. To aid in our attempts to understand this trend, global-

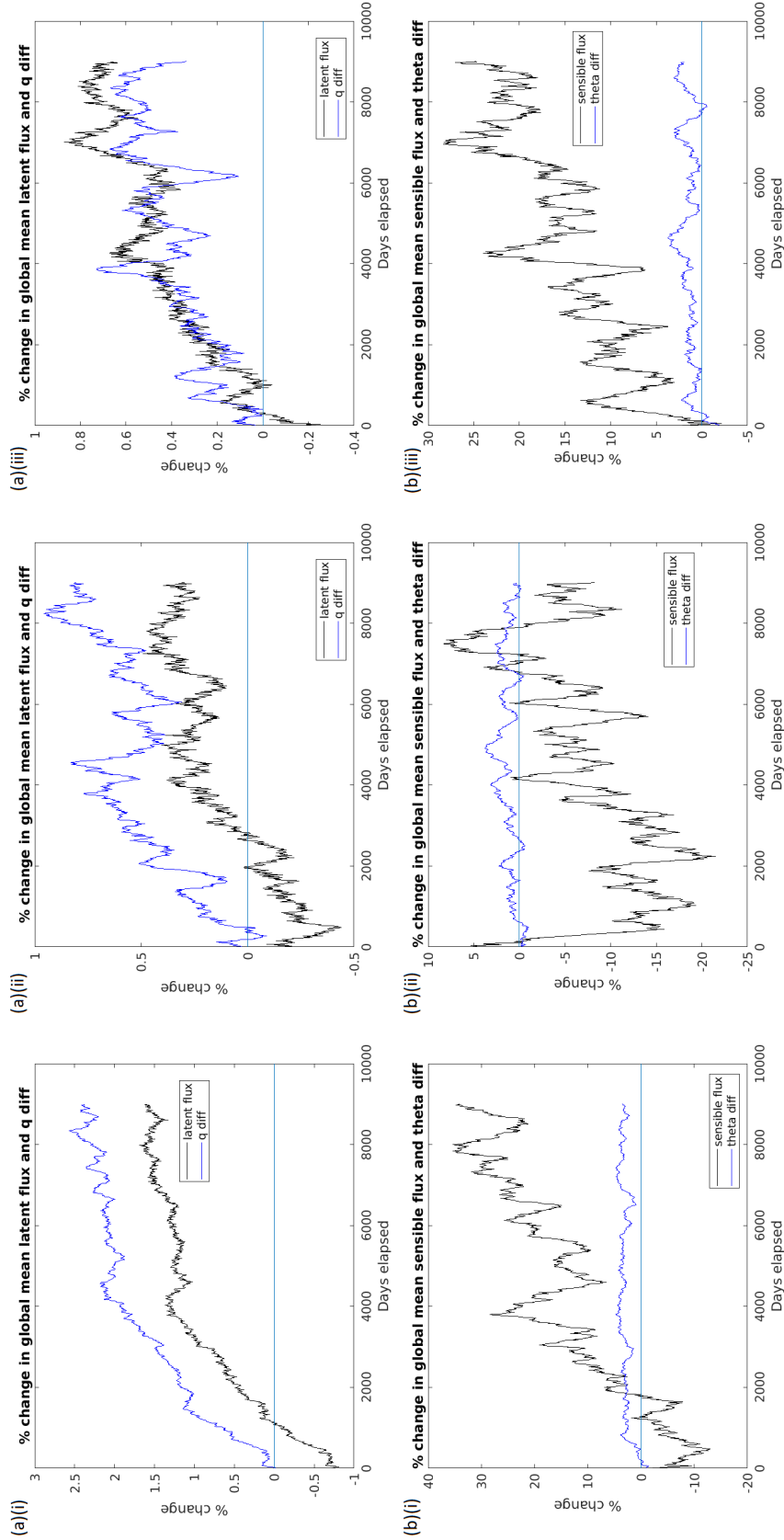


Figure 4.1.10: Time-evolution of global-average latent (top panels) /sensible (bottom panels) heat flux anomalies (black lines), and global-average surface wind times: (a) surface temperature difference, $u_s^* (SST - T_s)$ (top panels), and (b) surface humidity difference, $u_s^* (q_{sat} - q_s)$ (bottom panels) anomalies (blue lines), in experiments (i) U01 (left panels), (ii) P01 (middle panels), and (iii) T01 (right panels), in slab-ocean double-drake setup.

average values for the sea-air humidity/temperature difference and latent/sensible heat fluxes were calculated, and their anomalies divided by their control values to provide a percentage changes in both quantities, enabling comparison between the two quantities and their time-evolution. The timeseries of these variables for experiments U01, P01 and T01 in the slab-ocean setup are shown in figure 4.1.10.

When it comes to the overall trend in latent heat flux and humidity difference (top panels), there appears to be a connection, with both global-average quantities exhibiting similar increasing (more positive) trends. This connection is perhaps most convincing for experiment U01 (top-left), for which the line plots of both variable seem almost identical, separated by an almost fixed percentage change difference of about 0.5%. For both experiments P01 (top-middle) and U01, the changes in humidity difference systemically exceed those of latent heat flux, indicating that changing patterns of surface winds and drag coefficients act to dampen the overall changes in global-average latent heat flux in these experiments. In any case, it seems apparent that the long-term trends in surface humidity gradient do indeed drive those of the latent heat fluxes, which we know from before are largely confined to the tropics.

For the surface sensible heat fluxes and temperature differences (bottom panels), however, there seems to be much less of a connection, with the global-average changes in the former generally dwarfing that of the latter. Thus, for the sensible heat fluxes, the changes in surface wind and drag coefficients, appear important in driving the longer-term trends.

Summary

- The changes in turbulent heat fluxes in the extratropics - midlatitudes especially - are well-explained by the changes in surface wind times surface humidity/temperature gradient, in turn accounted for mostly by changes in surface zonal wind;
- Longer-term trends in the global-average latent heat fluxes are driven by increasing sea-air humidity gradients, primarily in the low latitudes.

4.1.4 Summary & main conclusions

To summarise the main conclusions from this subsection looking at the SST changes in the slab-ocean setup and their drivers, what appears to be happening is as follows:

1. Initially ($\lesssim 1000$ days), an anomalous, net downward turbulent - largely latent - heat flux, driven primarily by changes in surface zonal wind, drives global-average SST changes;
2. Subsequently, increased atmospheric temperatures, humidities, and surface humidity gradients drive large anomalous net downward/upward fluxes of LW/latent heat (+ SW) fluxes, overall driving further global-average SST increases, but at a slower rate and which diminishes with time.

Whilst all experiments take approximately ~ 11 years to fully equilibrate for a 50m mixed-layer depth, for experiments P01 and T01, the SST meridional profile is largely set within the first 1000 days, and thus largely driven by process (1). For experiment U01, whereas, it is largely set within the first 2000-3000 days, and thus, driven by both of the above processes, (1) and (2).

Also, there are latitudinal deviations in what is driving SST changes, with SST changes being broadly driven by anomalous:

- downward LW fluxes in the tropics (balanced by upward latent heat fluxes), largely driven by increased atmospheric temperatures;
- sensible heat fluxes in the extratropics (balanced by upward LW + latent heat fluxes), largely driven by changes in surface zonal wind; in experiment U01, downward LW and latent heat fluxes also contribute positively in the extratropics.

4.2 SST time-evolution and drivers: Fully-coupled setup

Having analysed the SST changes seen in the slab-ocean version of the model and their drivers, we now turn to analysing the SST changes seen in the fully-coupled atmosphere-ocean version of the model. In the globally-averaged picture, it is the case - as in the slab-ocean model - that only changes in net surface heat flux can alter oceanic heat content, as the globally-averaged oceanic heat transport comes to zero. That said, when we are looking at changes in sea surface temperature in this version of the model - both locally and globally - it becomes important to consider anomalous oceanic heat transport, which may lead to a redistribution of oceanic heat content - vertically and horizontally - and thereby alter the SST's.

We will begin this subsection with an analysis similar to that of the previous subsection, focused on the influence of global-average net surface heat fluxes on global-average SST, as well as the time-evolution of the SST's. Later on, however, we will move to looking at the contributions of individual terms to the SST-tendency equation (2.4.1), analysing the influences of both surface heat fluxes and ocean heat transport fluxes.

4.2.1 Global mean SST and surface fluxes time-evolution

The top and bottom panels of figure 4.2.1 display the time-evolution of the global-average sea surface temperatures (top panel) and surface heat fluxes (bottom panel) (positive upward) of the STP experiments in the fully-coupled setup, over the first 300 years of their evolution from when the perturbations are switched on. Note that, unlike the corresponding graphs given for the slab-ocean setup in the previous subsection, they are based upon timeseries that are not running means of the underlying data, but the discrete 1-year averaged values output by the model.

As in the slab-ocean experiment, in experiments U01 and P01 we observe a long-term pattern of rising global-average SSTs, driven primarily by an anomalous downward radiative flux, and

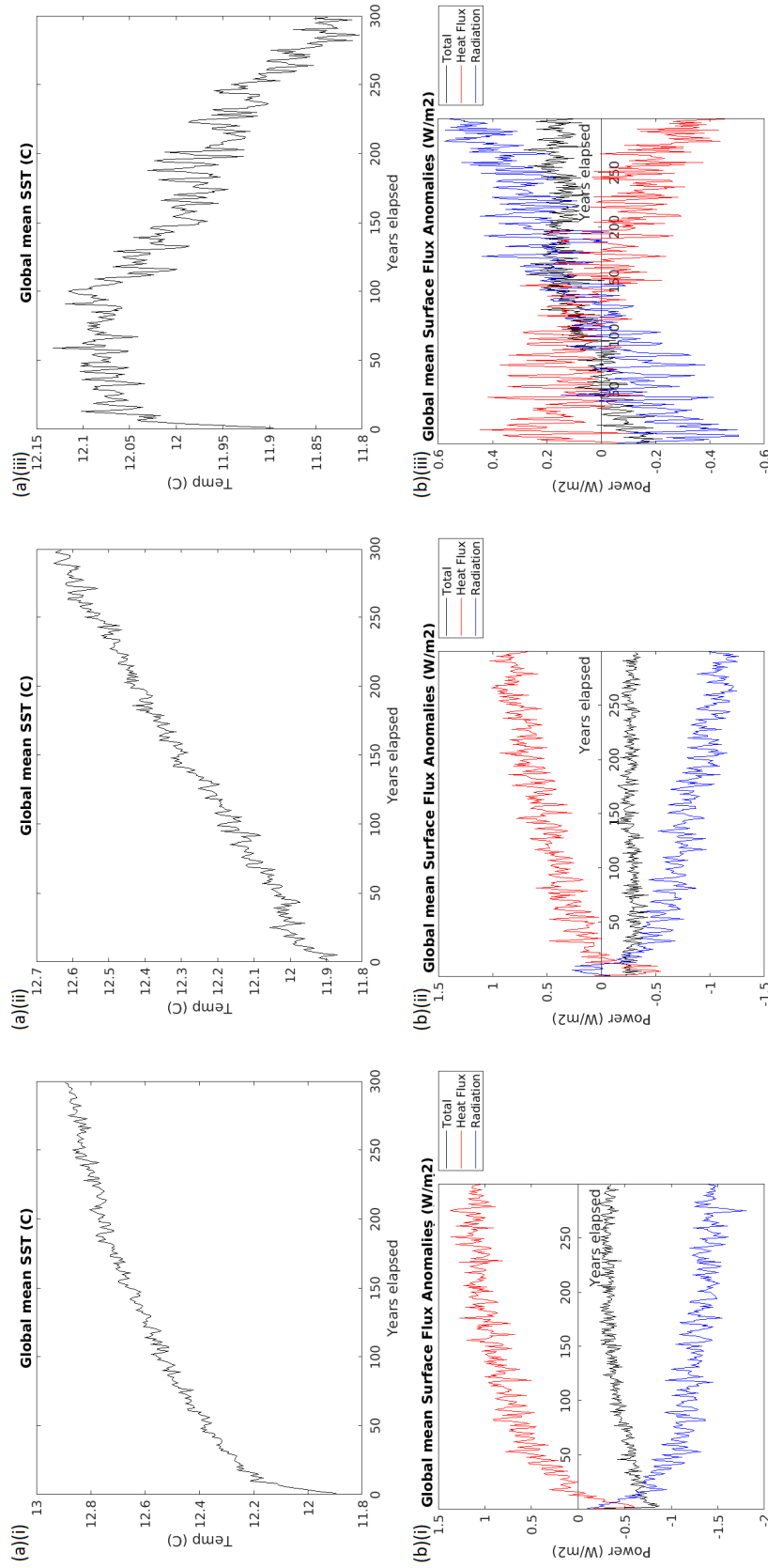


Figure 4.2.1: Time-evolution of global-average (a) sea surface temperatures (top panels), and (b) surface heat flux anomalies (black), and its radiative (blue) and turbulent heat (red) flux components (bottom panels), for experiments (left-to-right): (i) U01 (left panels), (ii) P01 (middle panels), and (iii) T01 (right panels), in fully-coupled double-drake set-up.

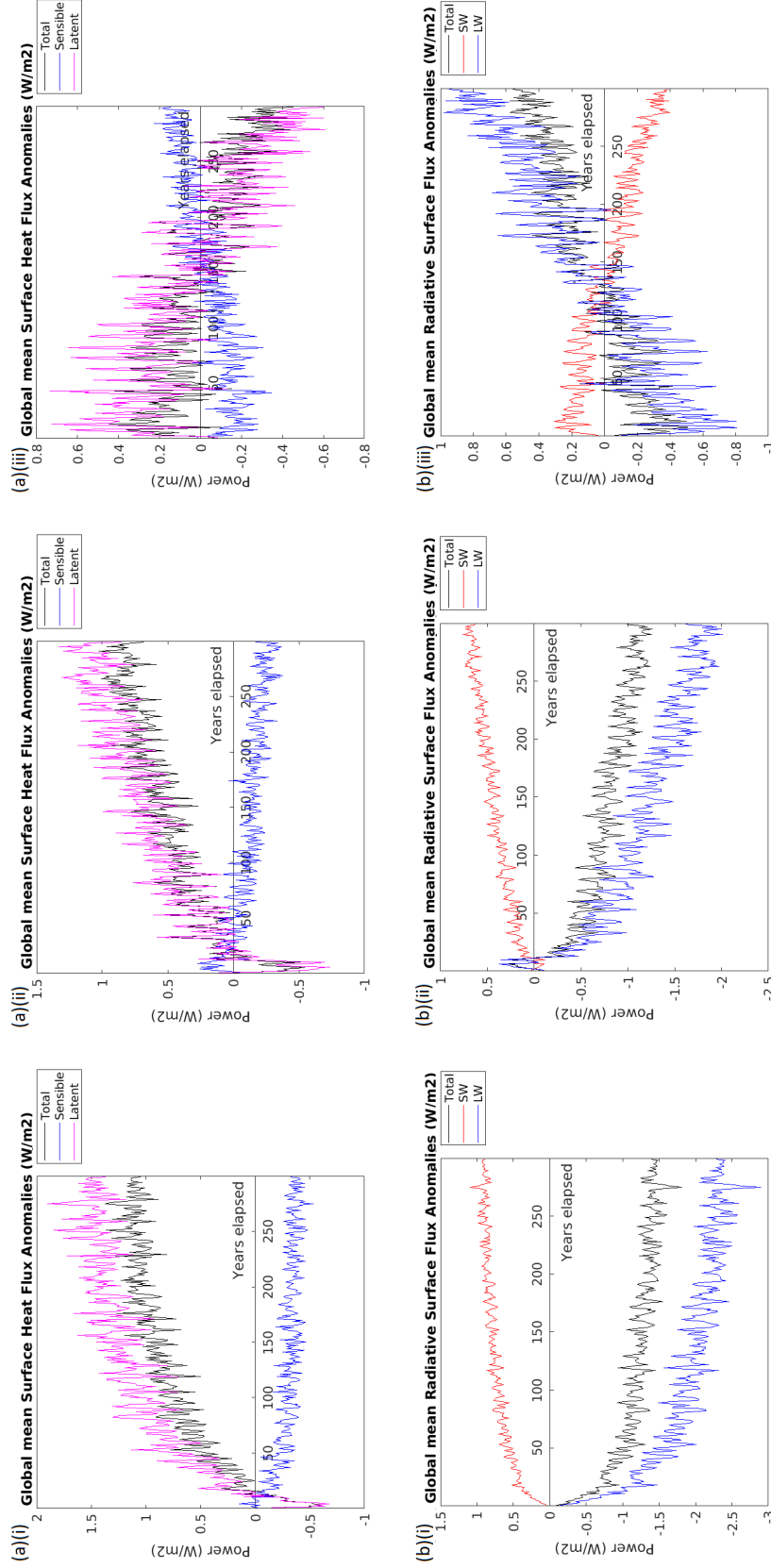


Figure 4.2: Time-evolution of global-average anomalous (a) turbulent surface fluxes (top panels), and (b) radiative surface fluxes (bottom panels), positive upwards, for experiments (left-to-right): (i) U01 (left panels), (ii) P01 (middle panels), and (iii) T01 (right panels), in fully-coupled double-drake set-up.

damped by an anomalous upward turbulent heat flux. For T01, this is the case for the first 100 years approximately, after which the signs of radiative and turbulent heat fluxes swap, resulting in a net upward surface heat flux. This drives net heat losses of the ocean to the atmosphere, and causes the global-average SST to steadily decrease. Also, similar to the first ~ 1000 days of the slab-ocean setup, we find that the turbulent heat fluxes appear to be driving the increases in global-average SST for experiments U01 and P01 during the first ~ 15 years. What's more, looking at the decomposition of the global-average turbulent and radiative fluxes into their individual components, shown in figure 4.2.2, we can again affirm that they are being driven principally in each experiment by anomalous latent heat fluxes, and anomalous downward longwave radiative fluxes respectively, with the sensible heat, upward LW and SW fluxes effectively acting as dampeners on the former fluxes.

If we wish to understand what is behind these changes in global-average turbulent and radiative fluxes, it is instructive to look at the changes in the individual components of global-average radiative flux, shown in the bottom panels of figure 4.2.2. For experiments U01 and P01, we see a similar pattern to the slab-ocean setup, with long-term anomalous upward/downward SW/LW fluxes, which increase with time, giving a net downward radiative flux which gets stronger with time. This is true also for T01 for the initial ~ 100 years, after which the sign of the two fluxes swap to give a net upward radiative flux. As noted in section 4.1.1, a net upward/downward SW surface radiative flux means a reduced/increased downward flux of SW radiation. This must be attributable to an overall increased/decreased optical depth in the atmosphere above, leading to more/less absorption of downward SW radiation, and can only be caused by an overall increase/decrease in atmospheric water vapour. Likewise, a net downward/upward LW radiative flux must correspond to increased/decreased fluxes of downward LW radiation, which in turn must be attributable to increased/decreased atmospheric heat content, leading to increased/decreased atmospheric LW emission. We also know, from section 4.1.3, that long-term upward latent heat flux anomalies tend to be primarily forced by increased sea-air humidity gradients, and it also stands to reason that the converse will hold for long-term downward latent heat flux anomalies.

Thus, what appears to be happening is, in experiments U01 and P01, atmospheric heat content, humidity, and sea-air humidity gradient all appear to be gradually increasing with time, leading to increased fluxes of downward LW radiation and upward latent heat, and decreased downward SW radiation. In experiment T01, we appear to start with this situation initially, however over time the increases in atmospheric heat content, humidity, and sea-air humidity gradient gradually reduce, going to zero at around 100 years. After this, they become anomalously negative - i.e. we see an overall reduction in atmospheric heat content, humidity, and sea-air humidity gradient - and they become more negative with time, leading to reduced fluxes of downward LW radiation and upward latent heat, and increased downward SW radiation.

If we apply our previous threshold value of 0.1 W/m^2 to determine when a new equilibrium has been reached, we see that, even after 300 years, no experiment has fully equilibrated, save for the fact that T01 remains below this value in a quasi-stationary state, with global-average

SST changing little, between years 50-100. If we modify this threshold value to account for the greater mixed-layer depth of our model, which was calculated for the control setup to have a global-average value of 119m, giving a new threshold value of approximately $\frac{119\text{m}}{50\text{m}} \times 0.1\text{W/m}^2 \approx 0.2\text{W/m}^2$, we could say that T01 reaches equilibrium almost instantly, whereas U01 and P01 hover close to it, yet show no sign of reaching it after 300 years. Moreover, as we see in the figures, even after the model has reached 'equilibrium', substantial SST changes are still possible over timeperiods of centuries or longer, with a global-average SST change of up to approximately $0.015^\circ\text{C}/\text{year} \times 100\text{years} = 1.5^\circ\text{C}$ possible over a century.

Another interesting point to note is the scale of the changes in SST and global-average heat fluxes, compared to those we saw in the slab-ocean setup. In experiment U01 the overall changes are comparable, with global-average SST and surface turbulent/radiative heat flux anomalies of around $+0.9^\circ\text{C}$ and 1.5 W/m^2 after 300 years and an initial net surface heat flux anomaly of around -0.8W/m^2 . In P01, however, whilst of the same sign, the overall, long-term changes are greater than in the slab-ocean setup, with global-average SST and surface turbulent/radiative heat flux anomalies of around $+0.7^\circ\text{C}$ and 1 W/m^2 , although the initial surface heat flux anomaly is comparable, at around -0.3W/m^2 . Experiment T01, meanwhile, exhibits similar magnitude but opposite sign overall SST and surface heat flux anomalies to the slab-ocean setup, at around -0.2°C (from the peak at 100 years) and 0.4W/m^2 after 300 years. What's more, its initial behaviour during the first ~ 15 years is very comparable to the behaviour seen in the slab-ocean setup, with similar signs and magnitudes of SST and surface heat flux changes seen.

Summary

- Experiments U01 and P01 experience a steady rise in global-average SST over the initial 300 years, similar to that seen in U01 in the slab-ocean setup over the first 25 years;
- Experiment T01 experiences an initial rise in global-average SST over the first ~ 15 years, remains in a quasi-steady state up until ~ 100 years, and then experiences a subsequent, gradual fall in global-average SST, with both increases/decreases in SST comparable in size to that seen in the slab-ocean setup;
- All long-term global-average SST increases/decreases appear to be driven by changes in downward LW fluxes, damped by changes in latent heat (+ downward SW) fluxes, in turn attributable to increases/decreases in atmospheric heat, water vapour, and surface sea-air humidity gradient.
- The initial ~ 15 years of global-average SST increase in experiments U01 and P01 appear to be powered by anomalous turbulent surface fluxes, which are themselves powered by anomalous downward latent heat fluxes.

4.2.2 Zonal mean SST time-evolution

The bottom panel of figure 4.2.3 shows the changes in zonal-average SST over the initial 300 years of each spinup. As with the slab-ocean setup, the overall SST meridional profile appears to be set quite early on, within the first 25 years, at least for experiments U01 (bottom-left) and P0 (bottom-middle)¹. This is further affirmed by looking at the top panels of figure 4.2.3, which show similar meridional SST profiles averaged over years 0-25 (red), 125-250 (green) and 250-275 (blue) for experiments U01 (top-left) and P01 (top-middle), minus broadly latitudinally-uniform SST increases - mainly over the first 125-150 years - that occur outside of the Southern Ocean region, north of about 60°S. That said, the subsequent SST changes outside of the Southern Ocean region are clearly significant, even if they have little impact on the SST meridional gradients. In experiment T01 (left panels), the SST changes appear somewhat more gradual, the meridional profile taking about 50 years to set, and subsequent, steady cooling occurring over the next 250 years north of about 60°S. This all stands in sharp contrast with what was found in the slab-ocean setup, in which all significant SST changes happened within the first 3-10 years. Given the very gradual changes in global-average SST and surface heat fluxes, as detailed in the previous section, this is not altogether surprising.

Another interesting feature of the time-evolution of the zonal-average SST anomalies in experiments P01 and T01 - confined to the Southern Ocean region - is how the initial SST anomalies appear qualitatively different to the long-term SST anomaly patterns. In experiment T01, we see initial cold anomalies south of 45°S, which subsequently become warm anomalies after about 5 years, whilst in experiment P01, warm anomalies which initially reach up to 75°S recede to equatorwards of 60°S, after the first ~10 years. This is quite reminiscent of the two-timescale SST evolution discussed in Frierson et al. (2015), in which the sign of high-latitude SH SST anomalies - in response to abrupt stratospheric ozone depletion - would change from cold to warm after the first 2-20 years. Furthermore, there appears to be some interesting inter-hemispheric differences occurring, with the high-latitude NH generally exhibiting much warmer/cooler SST anomalies in experiments U01 and P01/T01, compared to the Southern Ocean, especially as the model evolves with time.

Summary

- The SST meridional gradient profile is largely set within the first ~25-50 years, and subsequent evolution largely corresponds with uniform, steady heating/cooling in experiments U01 and P01/T01, north of about 60°S, occurring over the subsequent ~250-275 years;
- Experiment P01/T01 shows a sign-change in its high-latitude SH SST anomalies over the first ~5-10 years, from warm/cold to cold/warm;
- SST anomalies in the high-latitude NH are generally much warmer/cooler than those seen in the Southern Ocean in experiments U01 and P01/T01.

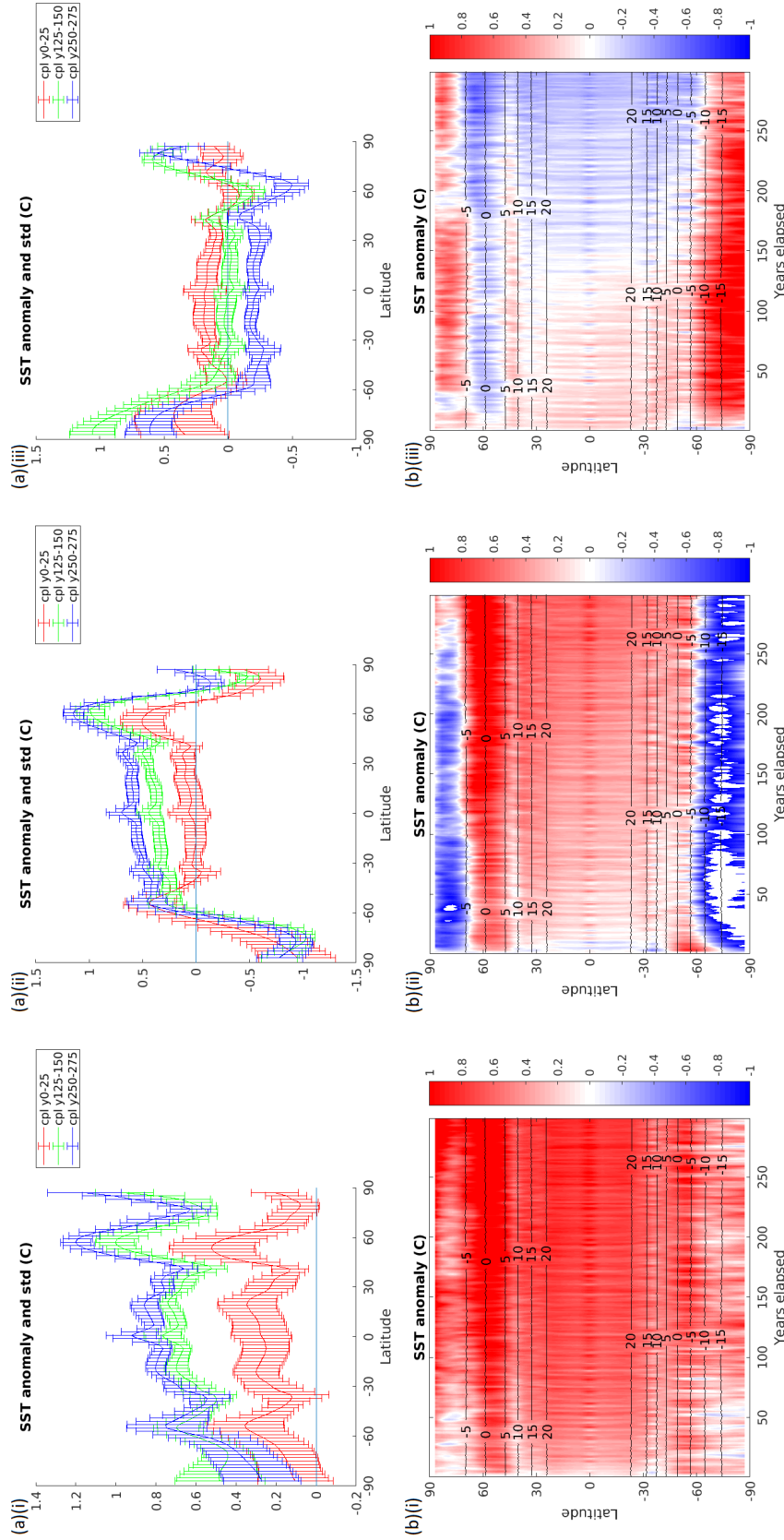


Figure 4.2.3: (a) (Top panels) Changes in zonal-mean sea surface temperatures in fully-coupled setup, averaged over years 0-25 (red), 125-150 (green), and 250-275 (blue), and (b) (bottom panels) time-evolution of control values (contours) and anomalies (colours) in zonal-average sea surface temperatures, in experiments (left-to-right): (i) U01 (left panels), (ii) P01 (middle panels), and (iii) T01 (right panels). Errorbars in the top panel are based upon the ensemble-mean values, calculated along the time dimension.

4.2.3 Changes in pseudo-mixed layer heat content

Having established the broad SST changes which occur in the fully-coupled model in response to stratospheric heating, the timescales over which they occur, and what drives them on a global-scale, we will now turn to diagnosing what is driving these changes in SST locally. Our analysis in this section will focus upon the oceanic heat budget, vertically-integrated over the top 144m, corresponding to our 'pseudo-mixed' layer. By doing so, we essentially - as seen in section 2.6.3 - make the diffusive heat transport negligible in most parts of the global ocean, allowing for a more tangible heat budget and causal attribution. As with much of our analyses in chapter 3, we will neglect the results of U01, which generally resemble a weakened version of P01, and focus only on the result of experiments P01 and T01.

Figure 4.2.4 shows the anomalous ocean heat content (left panel), surface heat fluxes (middle panel), and oceanic heat transport fluxes (right panel), integrated over our pseudo-mixed layer, and averaged over years 250-300 (left panels)/0-300 (middle and right panels) of experiments P01 (top panels) and T01 (bottom panels) in the fully-coupled model. Note the difference in the direction of net surface heat fluxes compared with similar plots for the slab-ocean setup in section 4.1.2, with positive/negative fluxes corresponding to net downward/upward fluxes, i.e. warming/heating of the pseudo-mixed layer.

By comparing between the left and right panels, we observe that, polewards of around 50°S and 30°N, changes in ocean heat content appear to be driven primarily by the changes in oceanic heat transport. These changes act, in P01/T01 to decrease/increase the transport of heat away from the midlatitudes and into the polar latitudes, thereby enhancing/weakening the meridional SST gradient in the high latitudes. These changes in midlatitude oceanic heat transport (of T01) are similar to those simulated by Cai (2006) in response to wind stress curl trends, corresponding to stratospheric ozone depletion, and also to increasing GHG's (Cai et al. 2005; Cai & Cowan 2007).

Equatorwards of this, it would appear that, overall, it is the changes in net surface heat flux which are driving local changes in heat content, with an overall downward/upward flux causing local increases/decreases in heat content in P01/T01. We also note the similar anomalous patterns in heat content and fluxes between the different experiments, with the changes seen experiment T01 looking like an inverted version of that seen in P01. In the rest of our analysis in this section, therefore, we will focus only on the results of experiment P01.

Figure 4.2.5 shows the anomalies in net surface heat fluxes (top-left), net ocean heat fluxes (bottom-left), and their individual component terms (middle and right panels), averaged over years 0-300 of experiment P01. Looking at the changes in net surface heat flux first, we see how the radiative flux anomalies (top-middle) appear to dominate in the tropics, driving the SST increases we see in that region. In the midlatitudes, the turbulent heat flux anomalies (top-right) appear dominant, driving a +/- heating dipole centred around 50°S in the midlatitudinal Southern Ocean region. In the polar latitudes, both radiative and turbulent heat flux anomalies appear significant in driving the overall damping of SST changes seen in those regions, although

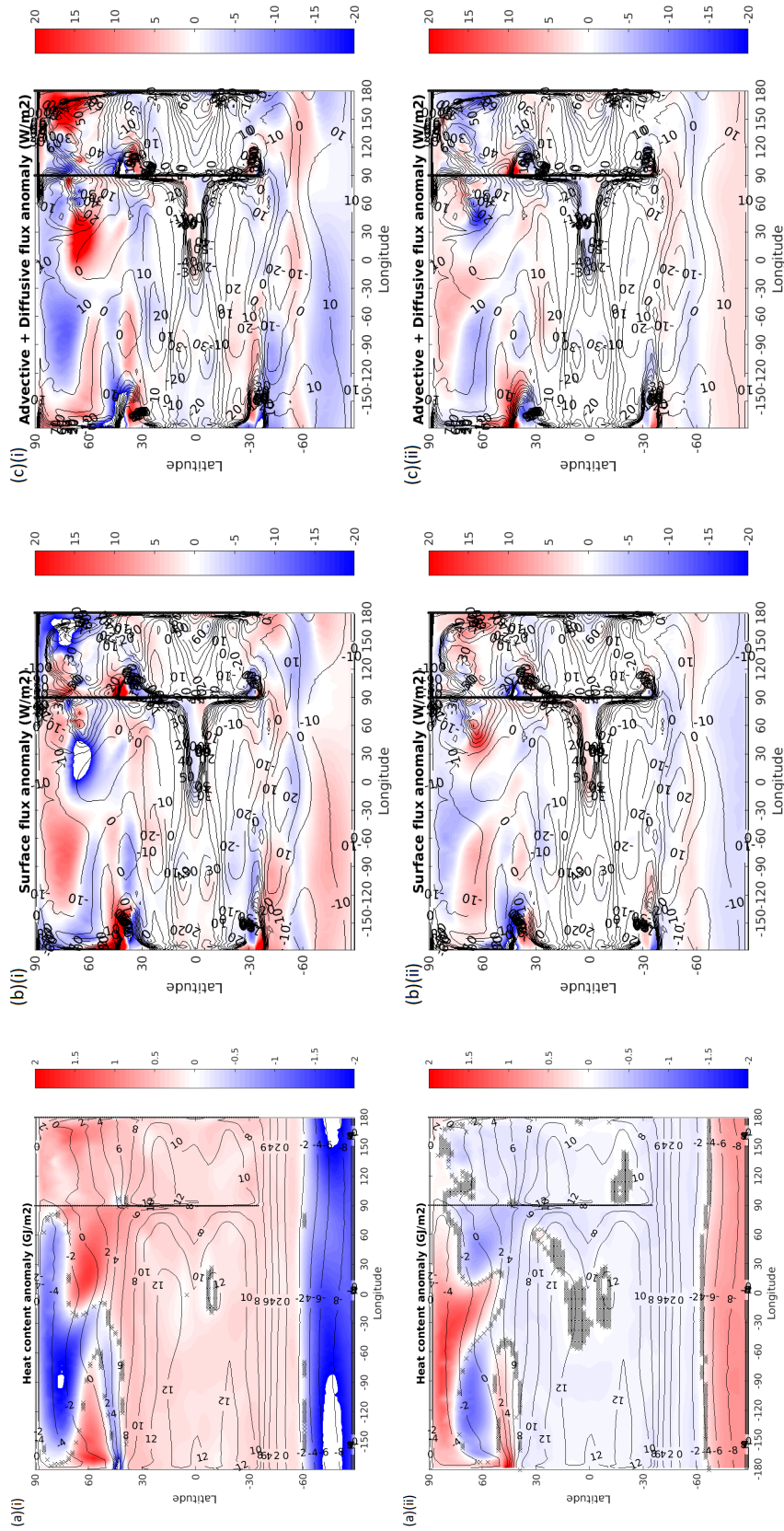


Figure 4.2.4: Control values (contours) and anomalies (colours) in vertically-integrated (0-144m): (a) heat content, averaged over years 250-300 (left panels), (b) net surface heat fluxes, averaged over years 0-300 (middle panels), and (c) net advective + diffusive fluxes, averaged over years 0-300 (right panels), (positive = warming), in experiments: (i) P01 (top panels), and (ii) T01 (bottom panels) in fully-coupled double-drake setup. Hatching in the left panels indicates regions in which the confidence levels in the experiment vs control values are below 95%, as measured by a two-tail student's t-test.

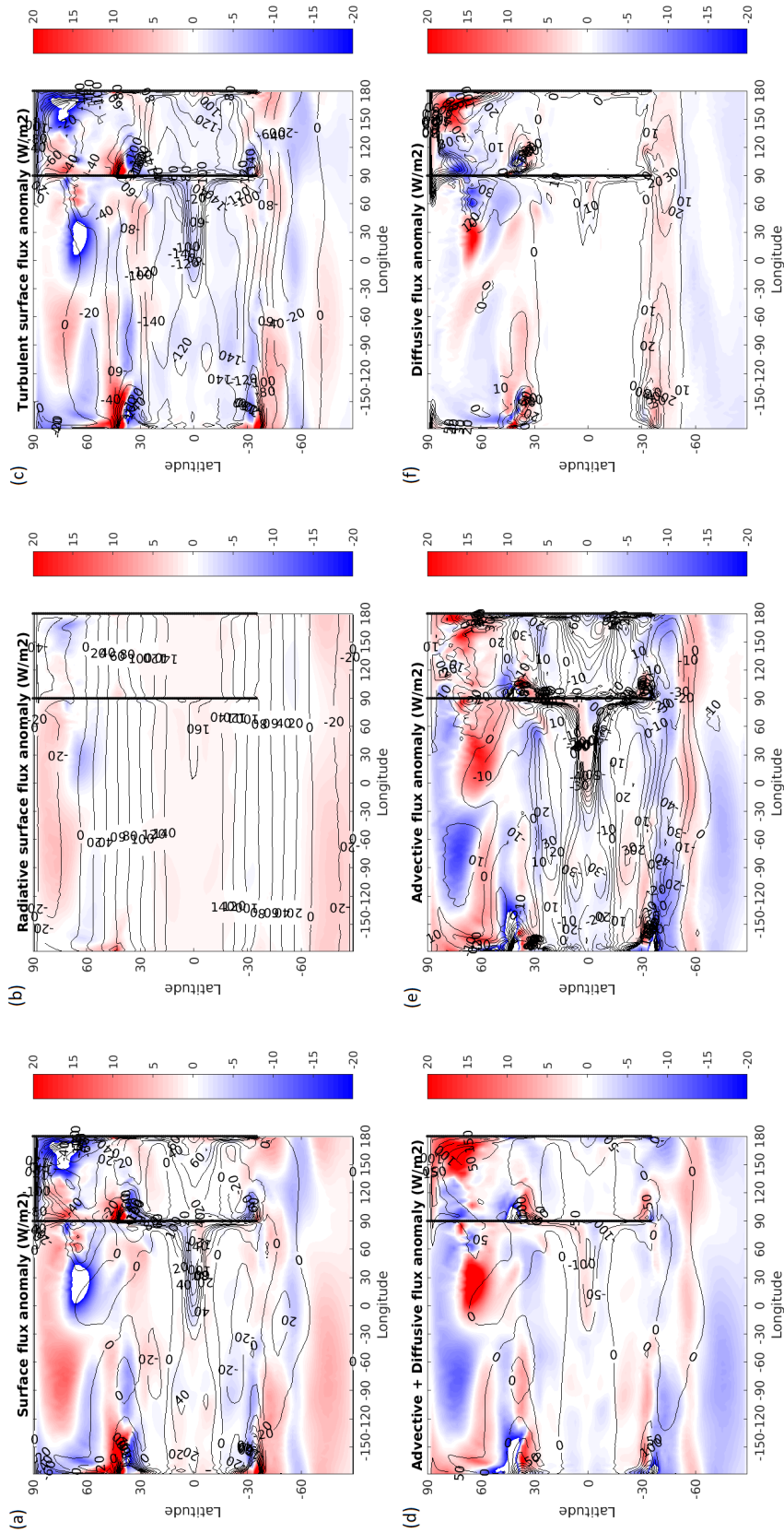


Figure 4.2.5: Control values (contours) and anomalies (colours) in total vertically-integrated (0-144m): (a) net surface heat fluxes (radiative + turbulent) (top-left), (b) radiative heat fluxes (top-right), (c) turbulent heat fluxes (bottom-left), (d) net ocean heat transport fluxes (advective + diffusive) (bottom-right), (e) advective heat fluxes (bottom-middle), and (f) diffusive heat fluxes (bottom-right), (positive = warming), averaged over years 0-300 of experiment P01 in fully-coupled setup.

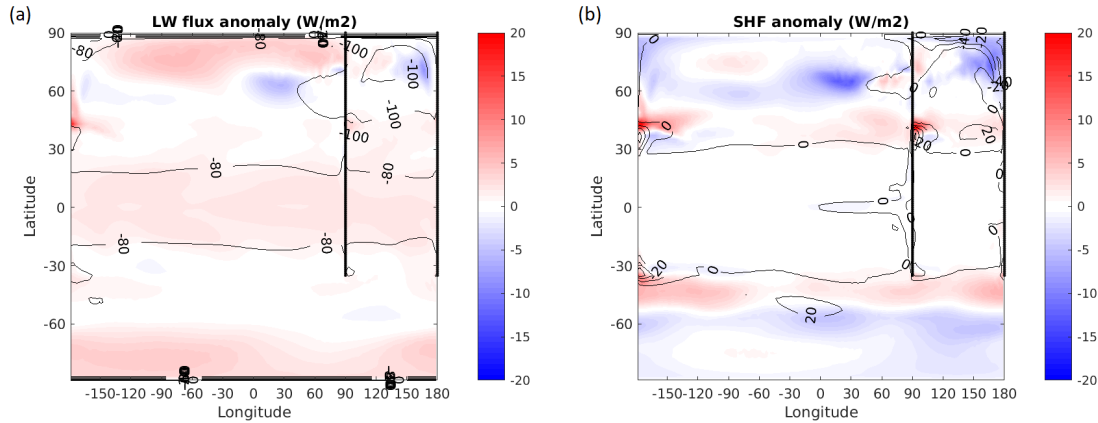


Figure 4.2.6: Control values (contours) and anomalies (colours) in total vertically-integrated (0-144m) surface heat fluxes: (a) net longwave (left), and (b) sensible heat (right), (positive = warming), averaged over years 0-300 of experiment P01 in fully-coupled double-drake set-up.

the radiative flux anomalies are somewhat more significant in the polar Southern Ocean region.

Further, when we decompose the individual radiative and turbulent heat flux components, we find that the LW flux anomalies (left of figure 4.2.6) dominate the overall radiative flux anomalies, and the sensible heat flux anomalies (right of figure 4.2.6) dominate the turbulent heat flux anomalies in the midlatitude Southern Ocean, where they also drive SST changes locally (30°-50°S).

Overall, the picture we are getting of the changes in net surface heat fluxes in the lower latitudes - where they drive changes in ocean heat content - in this fully-coupled setup, is highly similar to that found in the slab-ocean setup, described in section 4.1.3. Downward LW flux anomalies drive increases in ocean heat content 0°-30°, and sensible heat fluxes 30°-50°S. Moreover, the patterns of anomalous sensible heat fluxes in the extratropics are highly similar - compare right panel of figure 4.2.6 with the top-middle panel of 4.1.6 (note the sign changes between the plots). Since these were found in section 4.1.3 to be driven by the changes in surface zonal winds, which is similar between the setups, this is to be expected.

Turning to the changes in ocean heat fluxes, comparison of the overall anomalies in P01 (bottom-left of figure 4.2.5) with its individual contributions by the changes in oceanic heat advection (bottom-middle of figure 4.2.5) and diffusion/convection (bottom-right of figure 4.2.5) reveals that it is largely driven by the changes in the advective heat fluxes. The diffusive heat flux anomalies, whereas, are negligible in the tropics, and provide only a small negative feedback on the advective flux anomalies in the extratropics, except for the far North Atlantic region, and part of the Southern Ocean, south of 60°S. Here, the diffusive anomalies are dominant/provide a weakly positive contribution. The dominance of diffusion in the polar North Atlantic region can be understood as a consequence of the very high mixed layer depths - over 500m, and as high as 3400m i.e. the entire model ocean depth - seen in that region, as discussed in section

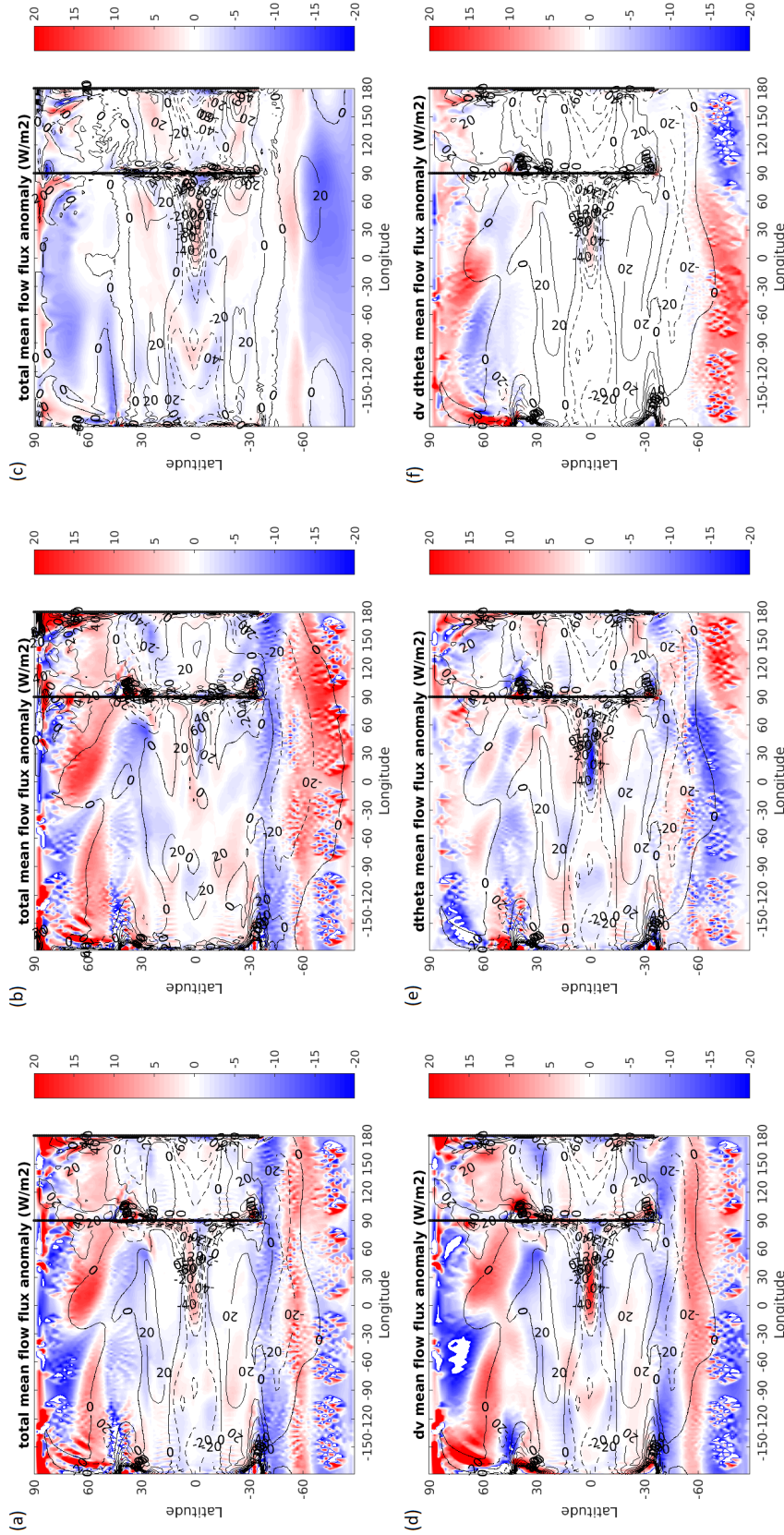


Figure 4.2.7: Control values of advective heat fluxes (contours), and anomalies in mean flow advective heat fluxes, $-\bar{\mathbf{u}} \cdot \nabla \bar{\theta}$ (colours) due to changes in: (a) total, $-\Delta(\bar{\mathbf{u}} \cdot \nabla \bar{\theta})$, (top-left), (b) horizontal advection, $\Delta(-\bar{u} \partial_x \bar{\theta} - \bar{v} \partial_y \bar{\theta})$ (top-middle), (c) vertical advection, $-\Delta \bar{w} \partial_z \bar{\theta}$ (top-right), (d) mean flow, $-(\Delta \bar{\mathbf{u}}) \cdot \nabla \bar{\theta}$ (bottom-left), (e) potential temperatures, $-\bar{\mathbf{u}} \cdot \Delta(\nabla \bar{\theta})$ (bottom-middle), and (f) mean flow and potential temperatures, $-(\Delta \bar{\mathbf{u}}) \cdot \Delta(\nabla \bar{\theta})$ (bottom-right), (positive = warming), averaged over years 0-300 of P01 in fully-coupled setup.

2.6.3.

Dissecting the anomalous advective heat transport of P01 further, we look at its total contribution from the mean flow, $-\Delta(\bar{\mathbf{u}} \cdot \nabla \bar{\theta})$ (top-left of figure 4.2.7), as well as the individual contributions due to changes in the mean flow, $\Delta\bar{\mathbf{u}}$ (bottom-left of figure 4.2.7), changes in the potential temperature, $\Delta\bar{\theta}$ (bottom-middle of figure 4.2.7), and both simultaneously (bottom-right of figure 4.2.7), as per the following decomposition:

$$\Delta(\bar{\mathbf{u}} \cdot \nabla \bar{\theta}) = (\Delta\bar{\mathbf{u}}) \cdot \nabla \bar{\theta} + \bar{\mathbf{u}} \cdot \Delta(\nabla \bar{\theta}) + (\Delta\bar{\mathbf{u}}) \cdot \Delta(\nabla \bar{\theta}) \quad (4.2.1)$$

Comparing top-left of figure 4.2.7 with the bottom-middle of figure 4.2.5, it appears that the anomalous advective heat transport is dominated by the changes in heat advection by the mean flow. Moreover, when we look at the individual contributions to this term - as per equation (4.2.1) - in the bottom panels of figure 4.2.7, it itself appears to be dominated by the first term on the RHS of equation (4.2.1), the contribution due to changes in the mean flow, $(\Delta\bar{\mathbf{u}}) \cdot \nabla \bar{\theta}$. This appears to be the case for most of the global ocean, except around the poleward boundaries of the subtropical western boundary currents, especially the one in the Northern Hemisphere large basin (centred around 30°N), and a part of the Southern Ocean, poleward of 60°S and extending from around 120°W to 90°E. In these regions, the contribution of the second term, due to changes in the potential temperature, $\Delta\bar{\theta}$, are significant. The third term tends to mainly act as a negative feedback on the first/second term, primarily in the high-latitude regions, where it increases the local heat fluxes into the polar latitudes, contrary to the net ocean heat flux pattern.

We can also dissect the anomalous mean-flow advective heat transport into its contributions by the horizontal mean-flows (top-middle of figure 4.2.7) and vertical mean-flows (top-right of figure 4.2.7). Comparing with total mean-flow advective heat flux anomalies (top-left of figure 4.2.7), we see that the anomalous horizontal fluxes appear to dominate at most latitudes, except around the equator, and in the high latitudes, polewards of 60°, in the Southern Ocean and Northern hemisphere large basin. At these latitudes, and in the Southern Ocean region especially, the anomalous vertical heat fluxes are significant/dominant, with large cooling contributions in those regions. It is also interesting to note slight interhemispheric differences in these anomalies, with the Southern Ocean region generally exhibiting stronger vertical advective heat flux anomalies, and the small basin showing virtually no contribution. The former is possibly a consequence of the very strong vertical temperature gradients seen in the Southern Ocean region, as detailed in section 2.6.3.

We also note how, in this high-latitude region - again, especially in the Southern Ocean - anomalous horizontal and vertical advective heat fluxes appear in opposition to each other, with anomalous positive meridional heat transport from the midlatitudes into the poles, whilst anomalous vertical advection around the poles causes cooling. Again, this is reminiscent of the results of Frierson et al. (2015), in which a poleward-shift in zonal winds induced anomalous upwards- and equatorwards-moving Ekman currents, causing competing advective effects of

high-latitude warming (vertical heat transport) and cooling (meridional heat transport).

Summary

- Changes in ocean heat content within the pseudo-mixed layer are driven by anomalous:
 - surface heat fluxes (0° - 30° N/ 50° S), driven by anomalous:
 - * downward LW fluxes (0° - 30°);
 - * sensible heat fluxes (30° S- 50° S);
 - ocean heat fluxes (30° N/ 50° S- 90°), driven by anomalous mean-flow advective heat transport, which is in turn driven by changes in:
 - * the mean flow, $\Delta \bar{\mathbf{u}}$ (except around WBC's, and parts of the Southern Ocean, where $\Delta \bar{\theta}$ also contributes):
 - the horizontal mean flow, (30° N/ 50° S- 60°);
 - the vertical mean flow, (60° - 90°).
- In the polar latitudes, and especially in the Southern Ocean, the effects of changes in horizontal/vertical mean-flow heat advection are in opposition to each other, causing increased ocean heat transport into/out of that region in experiments U01 and P01, and the opposite for T01.

4.2.4 Ocean circulation changes

From section 4.2.3, it is clear that the changes in advective heat flux - responsible for most of the changes in extratropical heat content in our experiments - are largely driven by changes in the mean flow, both horizontal and vertical. In order to ascertain what exactly is driving these changes, we will now analyse the changes in meridional and zonal mass transport, integrated over the top 144m/pseudo-mixed layer, and vertical velocities at the bottom of this layer, and compare with the changes in the Ekman and geostrophic currents, as defined by equations (2.2.3), (2.2.2), and (2.2.5).

The anomalous meridional (left panels) and zonal mass (middle panels) transports, calculated from vertically-integrating over the top 144m both the mean fields output by the model - $U = \int_{-144m}^0 \rho u dz$ and $V = \int_{-144m}^0 \rho v dz$ - and also the vertical velocities at the $z=-144m$ bottom boundary (right panels), are shown in figure 4.2.8 for experiments P01 (top panels) and T01 (bottom panels). We observe how, equatorwards of about 50° , most currents are essentially strengthened/weakened in P01/T01, with stronger/weaker gyres, upwelling and downwelling currents, and strengthened/weakened equatorwards mass transport in the low-midlatitudes. Polewards of 50° , the relationship flips, and we get a weaker/stronger circumpolar current, anomalous downwelling/upwelling, a weakened/strengthened equatorwards mass transport in the high-midlatitudes, and a weakened/strengthened polewards mass transport in the high-latitudes. We also get a stronger/weaker and equatorward-/poleward- shifted polar gyre in

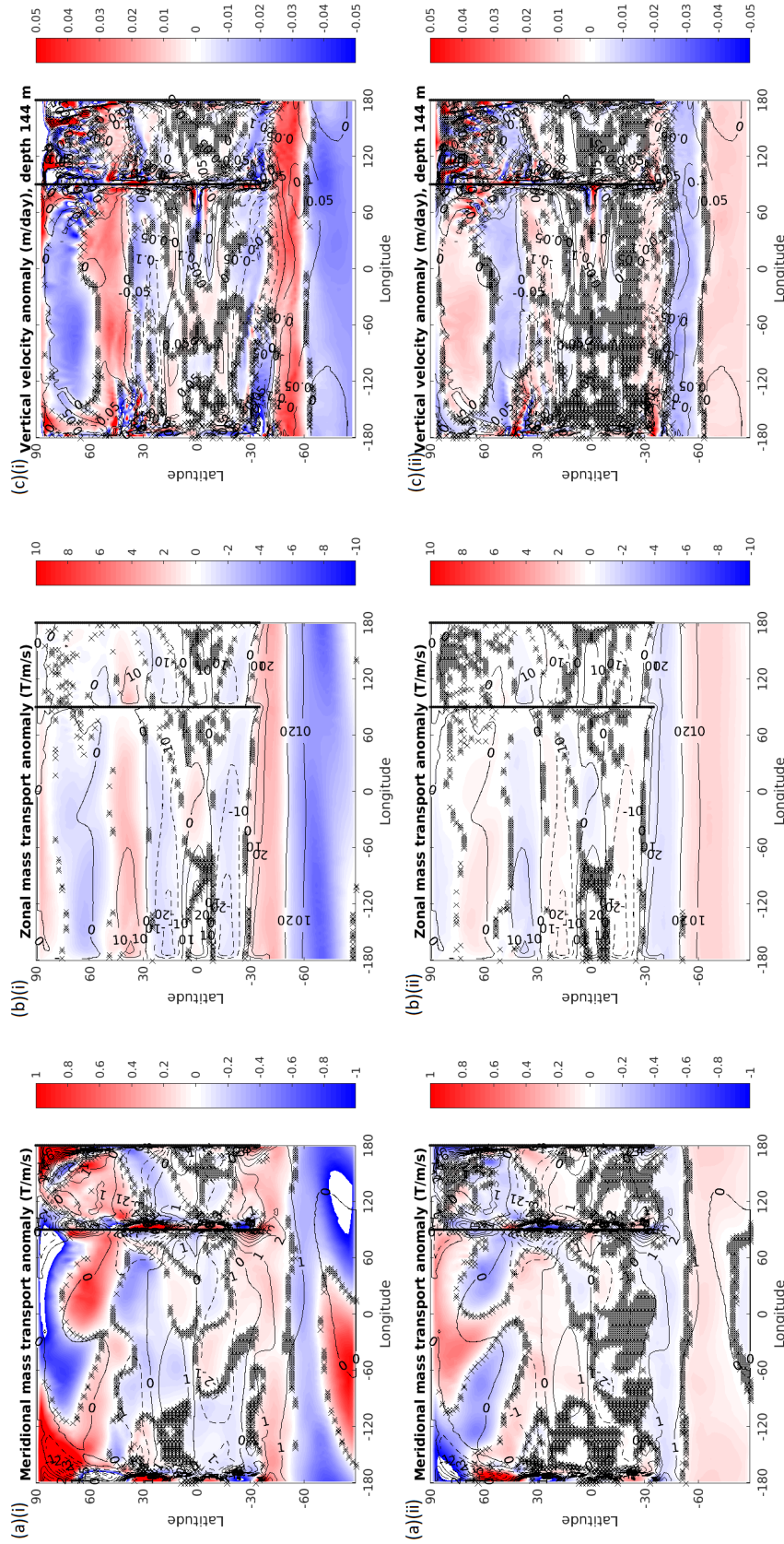


Figure 4.2.8: Control values (contours) and anomalies (colours) in: (a) vertically-integrated (0-144m) meridional mass transport, $V = \int_{-144m}^0 \rho v dz$ (positive northward; left panels), (b) vertically-integrated (0-144m) zonal mass transport, $U = \int_{-144m}^0 \rho u dz$ (positive eastward; middle panels), and (c) vertical velocities at $z=144m$ (positive upward; right panels), for experiments (i) P01 (top panels), and (ii) T01 (bottom panels), averaged over years 0-300 of fully-coupled setup. Hatching indicates regions in which the confidence levels in the experiment vs control values are below 95%, as measured by a two-tail student's t-test.

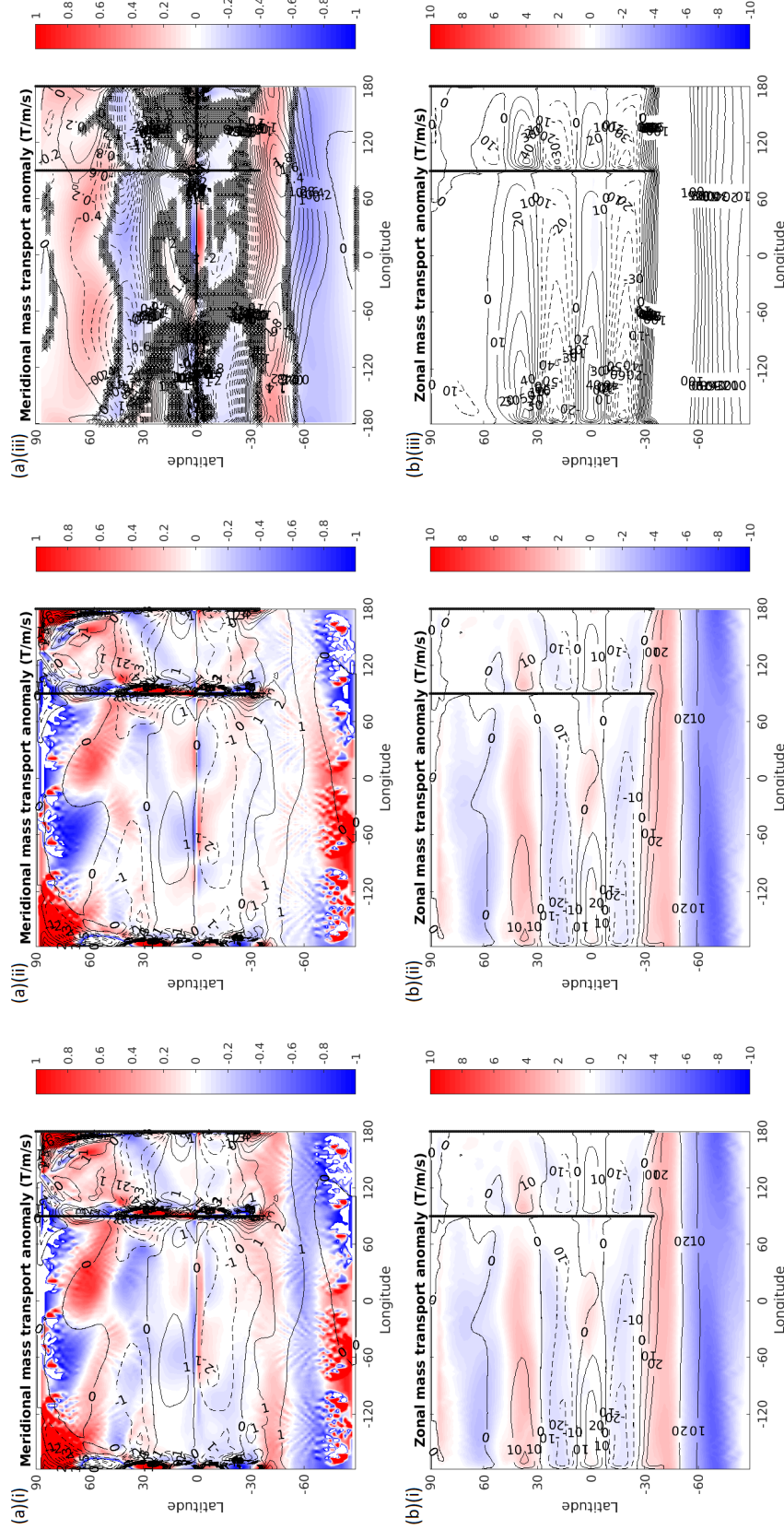


Figure 4.2.9: Control values (contours) and anomalies (colours) in vertically-integrated (0-144m): (a) meridional mass transport, $V = \int_{-144m}^0 \rho v dz$ (positive northward; top panels), and (b) zonal mass transport, $U = \int_{-144m}^0 \rho u dz$ (positive eastward; bottom panels), driven by changes in the: (i) Ekman + geostrophic flows, $\mathbf{u_E} + \mathbf{u_G}$ (left panels), (ii) geostrophic flows only, $\mathbf{u_G}$ (middle panels), and (iii) Ekman flows only, $\mathbf{u_E}$ (right panels), averaged over years 0-300 of experiment P01 in fully-coupled setup. Hatching in the top-right panel indicates regions in which the confidence levels in the experiment vs control values are below 95%, as measured by a two-tail student's t-test.

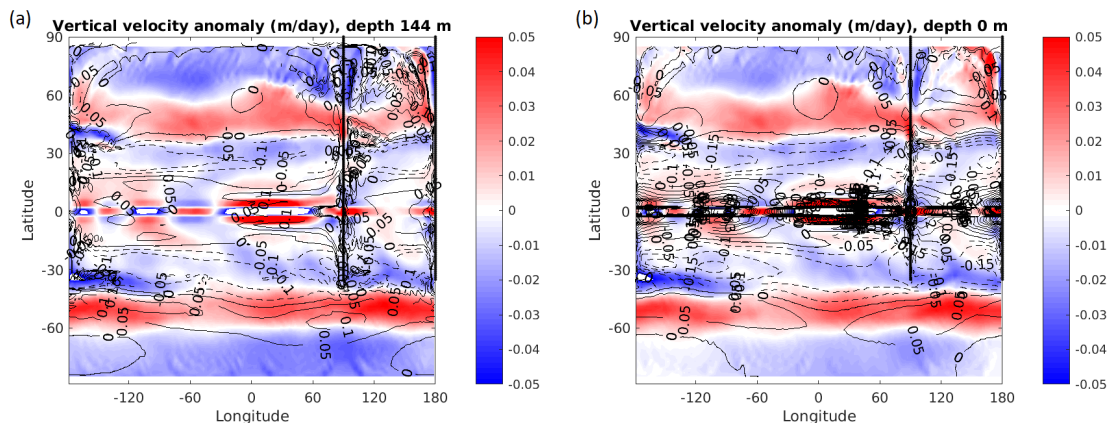


Figure 4.2.10: Control values (contours) and anomalies (colours) in the geostrophic vertical velocities, w_G , at depth: (a) $z=-144\text{m}$ (left panel), and (b) $z=0\text{m}$ (right panel), averaged over years 0-300 of experiment P01 in fully-coupled setup.

the NH large basin, in experiments P01/T01. These results (T01), again, are similar to those simulated by Cai (2006) in response to surface wind-stress changes in the Southern Hemisphere, caused by stratospheric ozone depletion, and also increasing GHG's (Cai et al. 2005; Cai & Cowan 2007), which found a southward-strengthening of the midlatitude ocean circulation.

Figure 4.2.8 shows the changes in vertically-integrated zonal- (bottom panels) and meridional- (top panels) mass transport by the geostrophic (middle panels) and Ekman (right panels) currents, and their sum (left panels), averaged over years 0-300 of experiment P01. We see that the combined geostrophic + Ekman mass transports fairly well capture the overall horizontal mass transports within the top 144m, both qualitatively and quantitatively - compare the top-left and top-middle panels of figure 4.2.8 with the top-left and bottom-left panels of figure 4.2.9 respectively.

Looking at the individual geostrophic- and Ekman-current contributions, the meridional mass transport seems to be driven in part by both geostrophic and Ekman currents. The Ekman current contribution is broadly zonally- and hemispherically-symmetric, whereas the geostrophic current contributes primarily by introducing zonal asymmetries to the meridional mass transport. This makes sense, given that the meridional geostrophic current, given by equation (2.2.2), is directly proportional to the longitudinal pressure gradient, $\partial_x p$, which must zonally average to give only boundary terms. In the Southern Hemisphere, between 30°S to 60°S , this contribution goes to zero, and the meridional mass transport comes from the Ekman current contribution there alone.

In the case of the zonal mass transport anomalies and its individual contributions - bottom panels of figure 4.2.8 - we observe that the Ekman current contribution is negligible, with the geostrophic current changes alone powering the overall changes in zonal mass transport. The geostrophic vertical velocity anomalies - calculated at depths $z=-144\text{m}$ (left panel) and $z=0\text{m}$

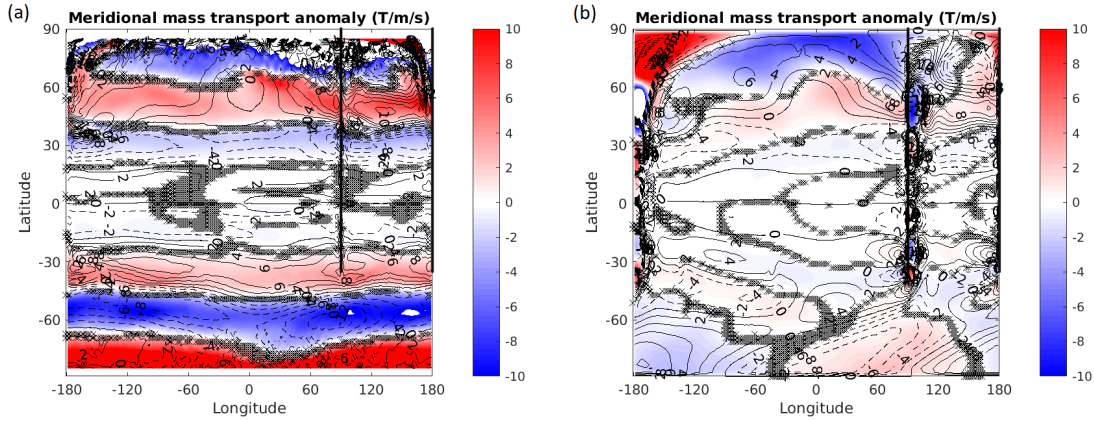


Figure 4.2.11: Control values (contours) and anomalies (colours) in the total column-integrated meridional mass transport, $V = \int_{-3400m}^0 \rho v dz$ (positive northward), calculated from the: (a) Sverdrup mass balance (equation (2.2.7); left panel), and (b) Eulerian mean fields (right panel), averaged over years 0-300 of experiment P01 in fully-coupled setup. Hatching indicates regions in which the confidence levels in the experiment vs control values are below 95%, as measured by a two-tail student's t-test.

(right panel), as per equation (2.2.2) - averaged over years 0-300 of experiment P01 are shown in figure 4.2.10. Like the zonal mass transport, all changes in the vertical velocities at $z=-144m$ can be attributed to changes in the geostrophic current - compare the top-right of figure 4.2.8 with the left panel of figure 4.2.10. However, comparing with the right panel of figure 4.2.10 - which shows the geostrophic vertical velocity at the surface ($z=0m$) which, by equation (2.2.4), must be equal and opposite to the vertical Ekman current - we see that the two anomalies are identical, meaning that the geostrophic vertical velocity at $z=-144m$ is more-or-less purely induced by the surface Ekman current.

Having established that, within the top 144m, the anomalous ocean currents and mass transports can be well-explained by their decomposition into Ekman and geostrophic components, as per equation (2.2.1), what remains is to explain definitively what is driving these changes. Whilst the Ekman currents are clearly wind-driven, responding to the surface wind stress curl as per equation (2.2.3), this is not necessarily the case for the geostrophic currents. However, we know from section 2.2 that the total column-integrated Sverdrup meridional mass transport, V_S - which itself can be decomposed into geostrophic and Ekman contributions - is directly driven by the surface wind-stress curl.

Figure 4.2.11 shows the changes in the total column-integrated (0-3400m) meridional mass transport, calculated from Sverdrup balance (left; equation (2.2.7)) and the Eulerian mean field (right), averaged over years 0-300 of experiment P01. There are notable differences between the two plots, with the anomalous Eulerian mass transport significantly weaker than the anomalous Sverdrup mass transport, and also significant deviations in the Southern Ocean region, with the Sverdrup mass transport showing an almost zonally-uniform strengthening and

equatorward-contraction of the underlying currents, whilst the Eulerian mass transport is more zonally-asymmetric. This latter point might be partially the result of the control Eulerian meridional mass transport being more zonally-asymmetric in general, as can be seen by looking at the contours, and the experiment is forcing a response that is less zonally-asymmetric. Regardless, the Sverdrup mass transport does capture the general pattern of zonally-averaged changes in meridional mass transport. It is especially effective at describing what is happening in the Northern Hemisphere, where the changes in meridional mass transport are more zonally-symmetric. Moreover, the changes in Sverdrup meridional mass transport also show a good, perhaps better, qualitative correspondence with the changes in meridional mass transport integrated over the top 144m (top-left of figure 4.2.8). This is all therefore very suggestive of the changes in meridional mass transport - integrated over both the top 144m, and the full 3400m - being induced by changes in the wind-driven Sverdrup mass transport.

Taken together, it therefore appears that most of the changes in ocean currents and mass transport can be attributed to changes in the wind-stress curl, via the Ekman currents, and Sverdrup balance.

Summary

- Experiment P01/T01 causes a strengthening/weakening of the ocean currents equatorwards of 50° , and a weakening/strengthening polewards of 50° ;
- The changes in zonal and meridional mass transports within the top 144m, and the changes in vertical velocity at $z=-144\text{m}$, can be entirely explained by the changes in the geostrophic and Ekman currents;
- The patterns of anomalous meridional mass transport - integrated over both the top 144m and full 3400m - appear to be powered by the changes in Sverdrup mass transport, and the anomalous vertical velocities by Ekman pumping, both powered by changes in the surface wind-stress curl.

4.2.5 Changes in vertical temperature structure

Thus far, we have focused primarily on changes in SST, and heat content, integrated over the top three model layers, and their drivers. Whilst this is perfectly appropriate to diagnosing the drivers of SST change in our model, by solely focusing on the top model layers, we risk missing the bigger picture of what is happening with the ocean's vertical temperature structure as a whole, and any implications that might have for the surface temperatures. In particular, in regions in which the changes in surface temperature cannot be explained by changes in ocean heat transport - i.e. the tropics and low-midlatitude Southern Ocean - discrepancies between the SST anomalies seen in the fully-coupled versus slab-ocean setup may not be adequately explained. We will thus turn briefly in this section to the changes in vertical temperature structure seen in the fully-coupled model, and their drivers.



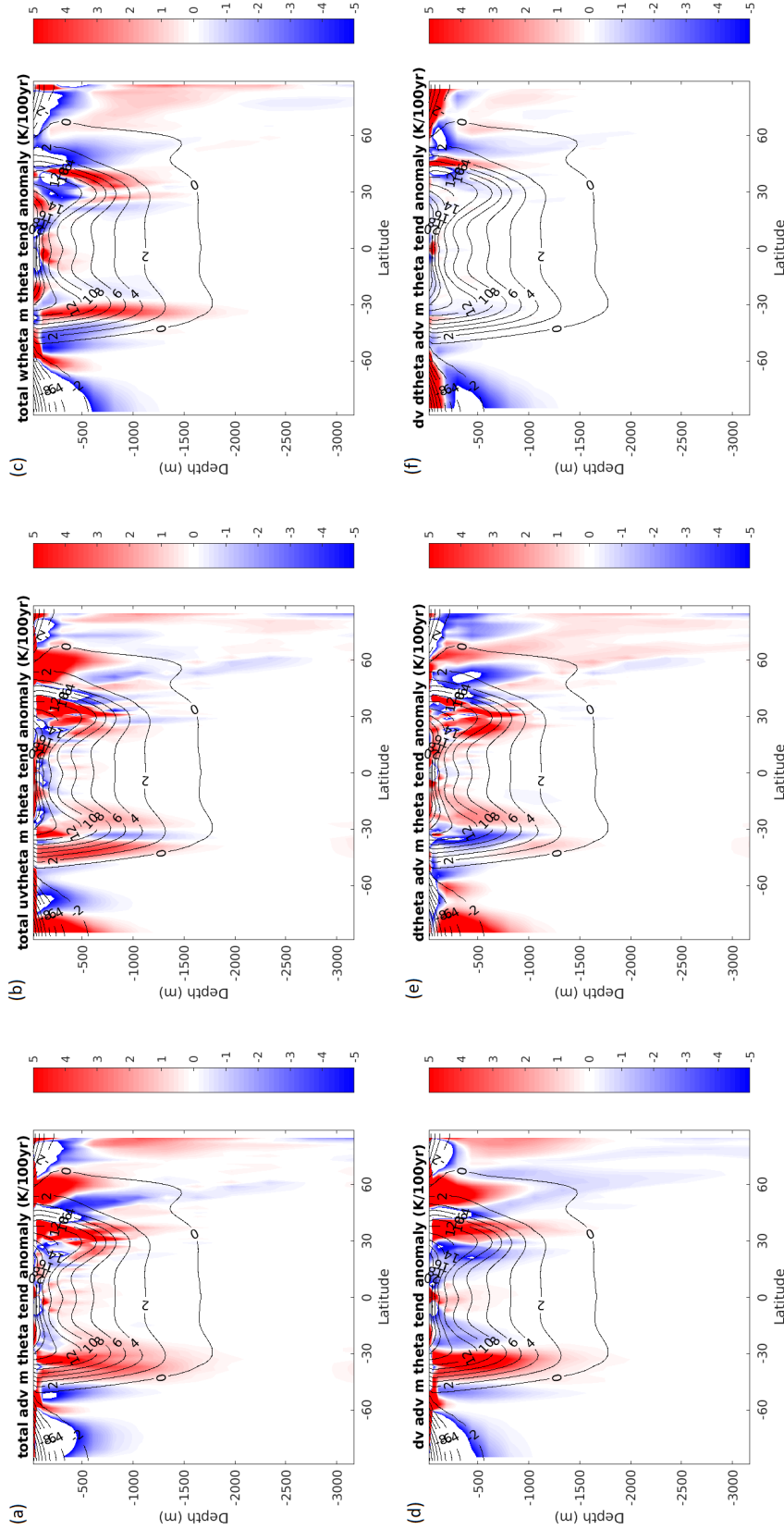


Figure 4.2.13: Control values of potential temperature (contours), and anomalies (colours) in zonal-mean oceanic stationary-mean advective potential temperature tendency, $-\bar{\mathbf{u}} \cdot \nabla \bar{\theta}$, due to changes: (a) total, $-\Delta(\bar{\mathbf{u}} \cdot \nabla \bar{\theta})$, (top-left), (b) meridional advection, $-\Delta \bar{v} \partial_y \bar{\theta}$ (top-middle), (c) vertical advection, $-\Delta \bar{w} \partial_z \bar{\theta}$ (top-right), (d) mean flow, $-(\Delta \bar{\mathbf{u}}) \cdot \nabla \bar{\theta}$ (bottom-left), (e) potential temperatures, $-\bar{\mathbf{u}} \cdot \Delta(\nabla \bar{\theta})$ (bottom-middle), and (f) mean flow and potential temperatures, $-(\Delta \bar{\mathbf{u}}) \cdot \Delta(\nabla \bar{\theta})$ (bottom-right), (positive = warming), averaged over years 0-300 of P01 in fully-coupled setup.

Figure 4.2.12 shows the changes in oceanic potential temperatures, zonally-averaged over the entire longitude circle (both large and small basins), seen in each experiment, averaged over years 0-10 (top panels) and 250-300 (bottom panels). First, the similarity between experiments U01 (left panels) and P01 (middle panels) is quite striking, over both timeperiods, with the U01 temperature response resembling a similar/weakened version of that seen in P01 in the low-/high-latitudes. Also, the vertical-uniformity of the temperature response - across both timeperiods and sets of experiment - seen throughout the thermocline is quite striking. Further analysis of the changes in velocities and salinities, as well as the various heat budget terms, reveals a similar vertical-uniformity. This provides extra validation for our integration over the top three model layers - down to $z=-144\text{m}$ - in our prior analysis of the ocean heat budget.

What is also quite striking is the qualitative resemblance in temperature response seen between the two timeperiods. Clearly, the thermocline is very quick to respond to changes in the surface climate. Furthermore, in the tropics, we see a sudden downward/upward and equatorward/poleward shift in the deep, poleward edge of the tropical thermocline, around 30° , in experiments U01 and P01/T01. This effect is strongest below the surface, between 300 to 1500m, where the thermocline is steep, and has a large meridional gradient. Moreover, it appears to arise in this region before becoming evident at the surface, as seen by looking at years 0-10 of experiment T01 (top-right), which shows an initial surface warming, in contrast to the sub-surface cooling, which grows over time, and subsequently shows up at the surface (bottom-right).

Figure 4.2.13 shows the changes in total advective heating rate by the stationary mean flow (top-left), and its contribution by changes in the mean flow (bottom-left), potential temperature gradient (bottom-middle), and both simultaneously (bottom-right), decomposed as per equation (4.2.1), for P01, zonally and time-averaged over the full longitude circle and years 0-300. Comparing with the overall temperature changes (bottom-left of figure 4.2.12), it is clear that the bulk of the sub-surface temperature changes within the thermocline are driven by anomalous advective heating/cooling by the mean flow. Moreover, comparing between the top-left and bottom panels of figure 4.2.13, it is clear that the bulk of these heat flux anomalies are driven by changes in the mean flow itself, $\Delta \bar{u}$, with the exception of the tropical thermocline region, 5° to 30° , and 200 to 1000m. Here, the changes in potential temperature gradient (bottom-middle) appear dominant. The third term on the RHS of equation (4.2.1) (bottom-right) only contributes significantly at high-latitudes, where it drives heat flux anomalies that are generally in opposition to that forced by changes in potential temperature gradient.

The top-middle and top-right panels of figure 4.2.13, show a similar decomposition of the changes in advective heating rate by the mean flow in P01, displaying its contributions by changes in meridional (top-middle) and vertical (top-right) mean-flow advection. Comparing with the overall advective heating anomalies (top-left), it appears that the vertical heating anomalies dominate in the Southern Ocean region and around the equator, changes in meridional advection in most of the tropics, and a combination of both in the Northern Hemisphere extratropics, and also around the poleward edges of the tropical thermocline. Following Kostov

et al. (2017), we hypothesise that the stronger vertical heating anomalies in the high-latitude SH vs. NH are the consequence of the stronger vertical temperature gradients, evident by counting the contours of control potential temperatures and comparing between the two regions.

Putting this all together, what appears to be happening is that, polewards of around 30° , and equatorwards of 5° , sub-surface potential temperature changes are driven by changes in the vertical and or/meridional flow, causing excessive heating/cooling at low-/high-latitudes in experiment P01, and the opposite for T01. Within the tropical thermocline (away from the equator), it is the passive meridional advection of excess hot/cold anomalies towards the equator, away from the poleward edges of the tropical thermocline, which drives temperature changes there. The net result is an overall deeper/shallower thermocline in experiments U01 and P01/T01, at all latitudes.

Summary

- Experiments U01 and P01/T01 show increases/decreases in thermocline depth, causing increases/decreases in heat content in the tropical thermocline, and decreases/increases in the polar thermoclines;
- These changes in thermocline depth originate in the sub-surface, before showing up at the surface;
- The changes in sub-surface ocean heat content are driven by changes in the mean-flow advective heat fluxes, driven by changes in the:
 - vertical mean flow, $-(\Delta\bar{w})\partial_z\bar{\theta}$ (equator, SH polar thermocline);
 - meridional + vertical mean flows, $-(\Delta\bar{w})\partial_z\bar{\theta} - (\Delta\bar{v})\partial_z\bar{\theta}$ (poleward edges of tropical thermocline, NH polar thermocline);
 - meridional potential temperature gradient, $-\bar{v}(\Delta\partial_y\bar{\theta})$ (interior of tropical thermocline).

4.2.6 Summary & main conclusions

To summarise the main conclusions from this subsection on the SST/ocean heat content changes in the fully-coupled double drake setup and their drivers:

- Global-average SST rises steadily over the initial 300 years for U01 and P01, and rises for the first 100 years and then falls for T01, driven by:
 - anomalous latent heat fluxes short-term (first ~ 10 -20 years);
 - anomalous downward longwave radiative fluxes long-term ($\gtrsim 10$ -20 years).
- Latitudinally, the changes in heat content in the pseudo-mixed layer are driven by changes in:

- ocean heat advection (30°N and 50°S to 90°), driven by changes in the:
 - * horizontal mean-flow (30°N and 50°S to 60°S);
 - * vertical mean-flow (60°S to 90°S);
 - * horizontal and vertical mean-flow (60°N to 90°N).
- surface heat fluxes (0° to 30°N and 50°S), driven by changes in the:
 - * downwelling longwave radiative fluxes (0° to 30°);
 - * sensible heat fluxes (30°S to 50°S).
- Below the surface, there is an increase/decrease in thermocline depth in experiments U01 and P01/T01, driven by changes in the mean flow advection of heat, driven by changes in the:
 - vertical mean flow, $-(\Delta\bar{w})\partial_z\bar{\theta}$ (equator, SH polar thermocline);
 - meridional + vertical mean flows, $-(\Delta\bar{w})\partial_z\bar{\theta} - (\Delta\bar{v})\partial_z\bar{\theta}$ (poleward edges of tropical thermocline, NH polar thermocline);
 - meridional potential temperature gradient, $-\bar{v}(\Delta\partial_y\bar{\theta})$ (interior of tropical thermocline).
- Via bulk formulae, Ekman/geostrophic currents, and Sverdrup balance, virtually all changes in the extratropical turbulent heat fluxes and oceanic mean flows within the pseudo-mixed layer can be attributed to changes in the surface winds, specifically surface zonal winds;

4.3 SST change: Fully-Coupled vs Slab-Ocean Setups

Having analysed the changes in SST/ocean heat content and their drivers - seen in response to stratospheric forcing - in our two coupled setups individually, we will in this subsection attempt to bring this all together, comparing and contrasting the changes in SST seen in each setup, what drives them, and the reasons for the differences we see between the two setups.

4.3.1 Differences in SST anomalies

The top panel of figure 4.3.1 displays the zonal-average SST anomalies produced by each type of STP in the slab-ocean and fully-coupled setups, time-averaged over the initial 0-50 years for both setups, and also over the initial 250-300 years for the fully-coupled setup. The bottom panel displays the difference in zonal-average SST anomaly between the two setups (fully-coupled SST - slab-ocean SST) for both fully-coupled timeperiods. Errorbars are plotted at each latitude for each given SST anomaly, estimated from the standard deviation (calculated along the time dimension) of the ensemble-mean SST anomaly at that latitude over the specified time period.

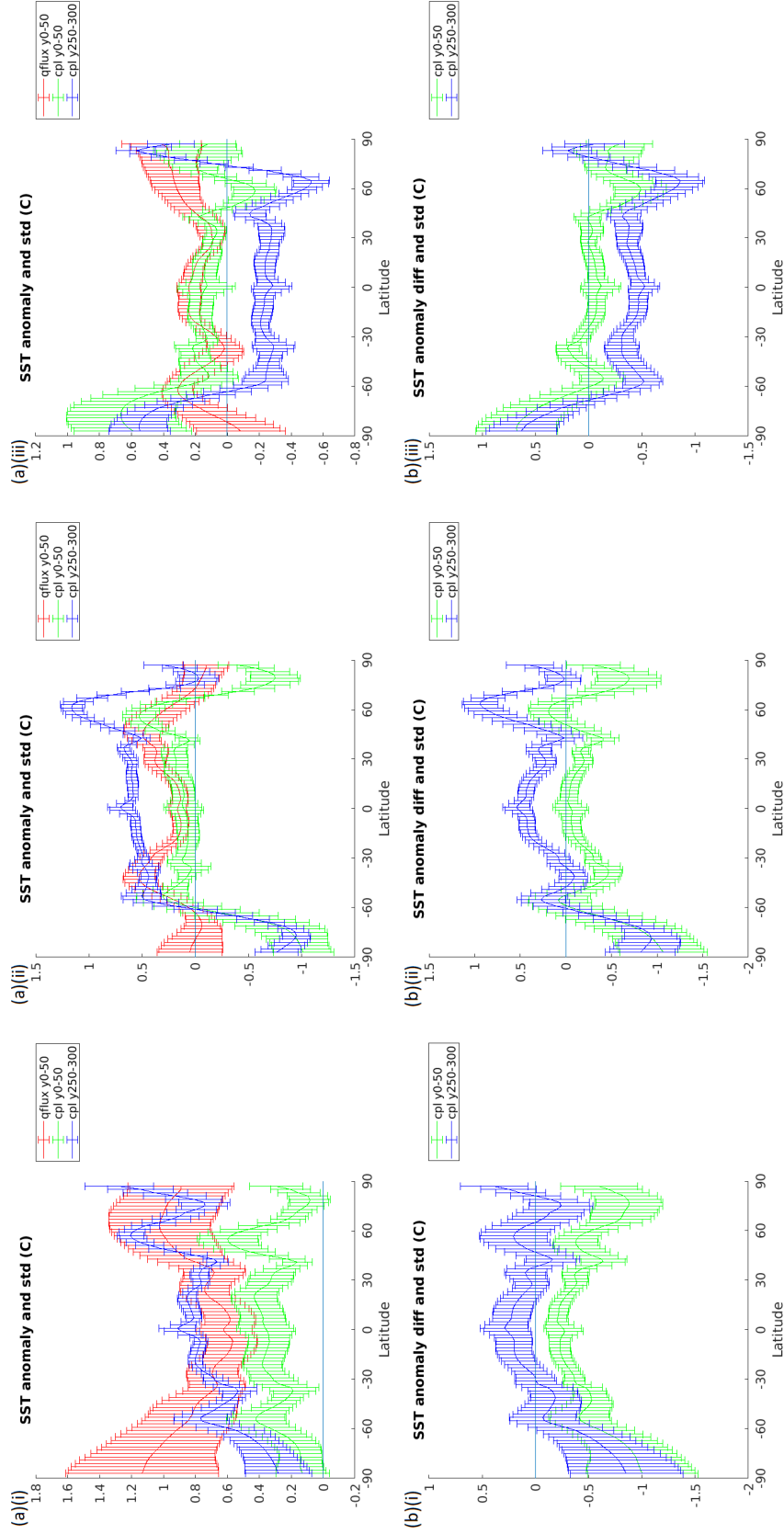
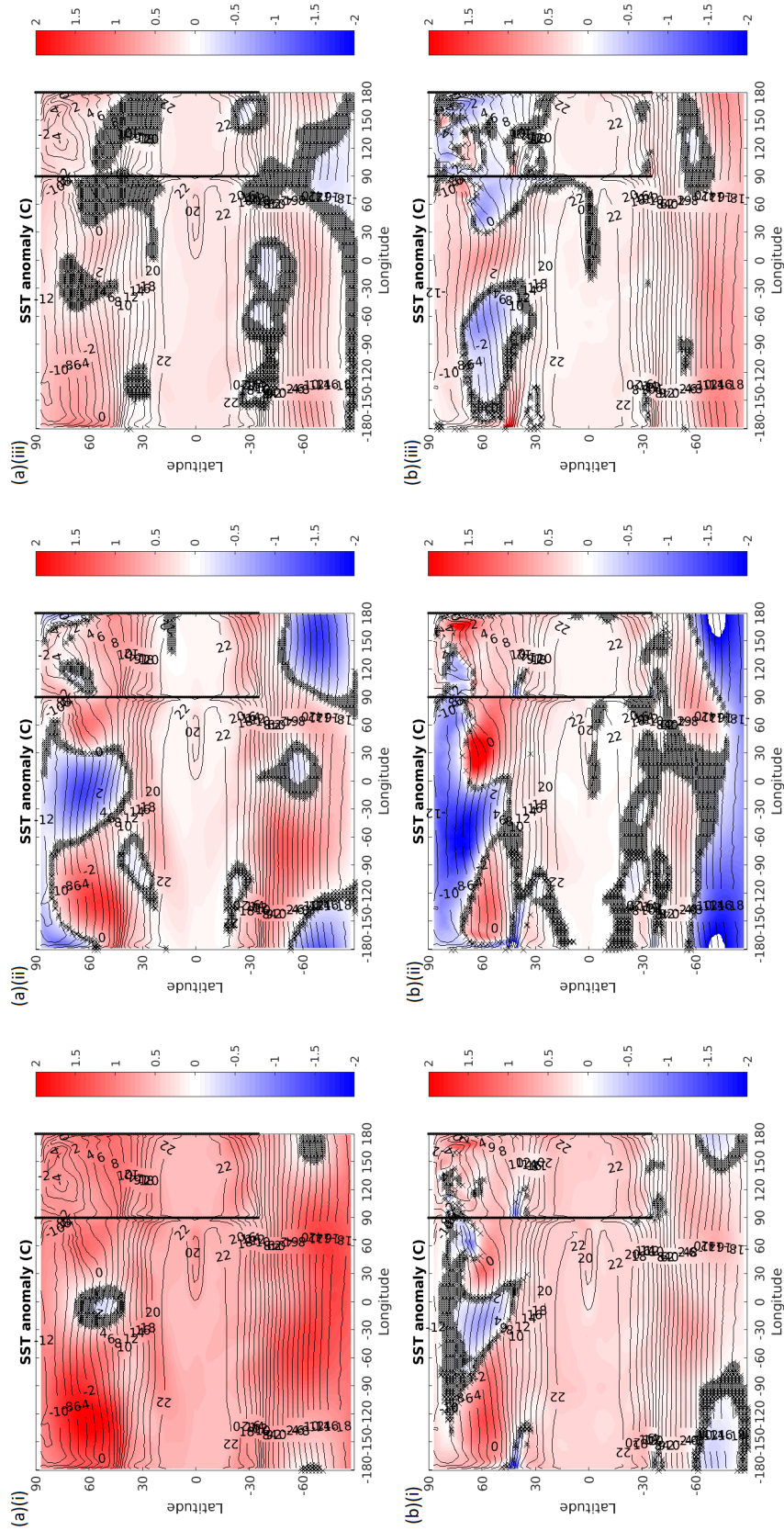


Figure 4.3.1: (a) (Top panel) Absolute changes in zonal-mean sea surface temperatures in slab-ocean setup years 0-50 (red line) and fully-coupled setup years 0-50 (green line) and 250-300 (blue line). (b) (Bottom panel) Difference in zonal-mean sea surface temperature anomalies between fully-coupled setup years 0-50/250-300 (green/blue line) and slab-ocean setup years 0-50. Shown for experiments (left-to-right): (i) U01 (left panels), (ii) P01 (middle panels) and (iii) T01 (right panels). Errorbars plotted are based on standard deviations of the ensemble-average SST anomalies, calculated along time dimension.



Comparing between the fully-coupled and slab-ocean setups over the initial 0-50 years, there are no significant differences in the SST anomalies in the low-to-mid latitudes for both experiments P01 and T01. The only region that appears to exhibit significant and large differences in SST anomaly are the high-latitude Southern Ocean, south of 60°S, where there are large negative/positive SST differences of up to -1°C/+0.5°C in the P01/T01 experiments between the setups. Significant differences in SST anomalies are also seen in parts of the high-latitude Northern Hemisphere: poleward of around 60°N in P01, and 45°N to 70°N in T01, where there are negative SST differences of about -0.5°C. In the U01 experiment, the defining difference between the SSTs appears to be a significant reduction and flattening of the positive SST anomaly in the fully-coupled setup compared to the slab-ocean setup. The cooling is most significant around the poles, with reductions in SST there of up to -1°C.

From subsection 4.2, we understand that, over the subsequent 250 years in the fully-coupled setup, the U01 and P01/T01 experiments experience a global-average increase/decrease in SST, and with amplified heating/cooling in the high-latitude Northern Hemisphere - north of about 50°N - and diminished SST changes in the Southern Ocean region, south of about 30°S. This impacts upon the difference in SST's between the fully-coupled and slab-ocean setups for experiments P01/T01, by making the tropical SST's comparatively warmer/colder, by around +/-0.5°C, and also by making the high-latitude NH SST's less cold/warm, and more similar to that seen in the slab-ocean setup. For experiment U01, the SST increases act to make the differences in SST outside of the high-latitude Southern Ocean between the two setups essentially negligible.

Figure 4.3.2 displays the changes in SST seen in both slab-ocean (top panels) and fully-coupled (bottom-panels) model setups, averaged over the initial 0-50 years, on latitude-longitude grids. Aside from the zonal-average differences outlined above, one striking difference between the two setups' induced SST anomalies is their much greater zonal-uniformity in the fully-coupled setup. Indeed, in the slab-ocean setup, there appears to be significant wavenumber-1/-2 zonal asymmetries in the SST anomalies in the Southern/Northern hemisphere extratropics, extending from about 40°N and 50°S up to the poles. This is especially apparent in experiment P01 in the slab-ocean setup (top-middle), where we observe alternating hot/cold SST anomalies across the zonal axis. Conversely, in the fully-coupled setup, although these type of SST zonal-asymmetries are present to some degree, they are generally less pronounced, and confined to a more narrow latitudinal band: 60°S to 90°S in the Southern Hemisphere, and 45°N to 80°N in the Northern Hemisphere. This greater zonal-uniformity in the extratropics is probably partly why the zonal-average SST anomalies there are generally more pronounced for experiments P01/T01 in the fully-coupled setup, especially in the high latitudes.

Summary

The main differences seen in SST anomalies induced by stratospheric-forcing experiments, between the slab-ocean and fully-coupled setups are:

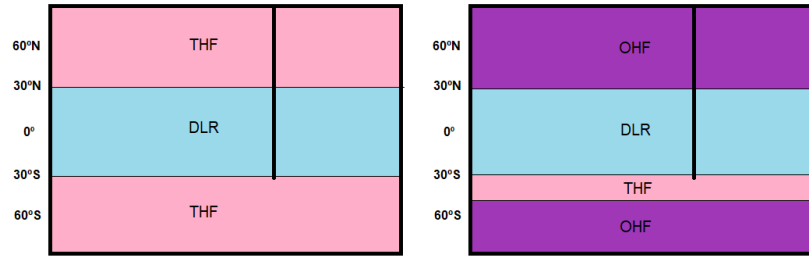


Figure 4.3.3: Schematic showing the main drivers of SST changes seen in the slab-ocean (left) and fully-coupled setup (right), in different regions of the global ocean (DLR = downward longwave radiation; THF = turbulent heat fluxes; OHF = ocean heat fluxes).

- Colder/Warmer SST's in the Southern Ocean in experiments U01 and P01/T01, fully-coupled setup years 0-50 and 250-300;
- Colder SST's in the NH large basin in P01, and at all latitudes in U01, fully-coupled setup years 0-50;
- Warmer/Colder SST's in tropics in experiments P01/T01, fully-coupled setup years 250-300;
- More zonally-uniform extratropical SST anomalies in fully-coupled setup.

4.3.2 Drivers of SST differences

By experimental design, the two differences between the slab-ocean and fully-coupled setups are, first, the mixed-layer depths (50m vs global-average of 119m), and second, the ability of the ocean heat transport - parameterised as the Q_{flux} term in equation (2.4.1) for the slab-ocean setup - to respond to changes in the atmosphere above. Any differences in SST between the two setups must therefore be traceable to one or both of these factors.

Figure 4.3.3 shows schematics of the main drivers of SST changes in different regions of the global-ocean, in both the slab-ocean (left) and fully-coupled setups (right), as deduced from our analyses in sections 4.1 and 4.2. Both setups have similar drivers of SST change in the lower latitudes, with downward longwave radiative (DLR) fluxes - powered by warmer/cooler atmospheric temperatures - driving SST changes in the tropics, and turbulent heat fluxes (THF) - powered by changes in surface zonal wind - driving changes in the Southern Hemisphere low-midlatitudes. Polewards of about 30°N/50°S, however, there is deviation between the two setups, with the slab-ocean remaining driven by the turbulent heat flux anomalies, whilst for the fully-coupled model, it is here that the wind-driven changes in ocean heat flux kick-in, with overall reduced/enhanced poleward heat transport from the mid- to high-latitudes in experiment U01 and P01/T01. This is probably owing to the fact that the zonally-averaged Ekman vertical

velocities and Sverdrup meridional mass transports - which, as shown in section 4.2.4, drive changes in the depth-integrated mass transports and vertical velocities - respond to changes in the meridional surface zonal wind gradient, $\partial_y u_s$ (through the zonally-averaged surface wind stress curl), as per equations (2.2.7) and (2.2.3). Hence, changes in the zonally-averaged circulation will generally be poleward-displaced relative to changes in absolute surface zonal wind. This is in contrast to the changes in turbulent heat fluxes, which - as per the bulk formulae, equations (2.4.3) and (2.4.4) - respond to local changes in absolute surface zonal wind. This most likely explains the differences we see between the different setups' SST anomalies in the mid-to-high latitudes, with significant changes in meridional SST gradient in the fully-coupled setup generally occurring at higher latitudes, relative to those seen in the slab-ocean setup. Moreover, the lack of an ability for zonal asymmetries in the SST field to respond to each other in the slab-ocean setup - as provided by e.g. the changes in ocean heat advection caused by changes in temperature gradient, $-\bar{\mathbf{u}} \cdot \Delta(\nabla\bar{\theta})$, in the fully-coupled setup (see section 4.2.3) - explains their presence in the mid-to-high latitudes in that setup, which in turn explains their relative low-amplitudes in the zonally-averaged picture.

In the low-latitudes, surface heat flux anomalies are the dominant drivers of SST changes in both slab-ocean and fully-coupled setups. In spite of this commonality, however, we do see differences in the SST anomalies in these regions between the setups over long timeperiods, with significantly warmer/colder tropical SST's seen in years 250-300 of experiment P01/T01 in the fully-coupled setup. From section 4.2.5, we know that, below the surface, changes in ocean heat content within the tropical thermocline are controlled by hot/cold anomalies at its poleward boundaries, and also around the equator, forced by wind-driven downwelling/upwelling currents, and reduced/enhanced poleward flows, in experiments P01/T01. These anomalies then get redistributed throughout the tropical thermocline via passive meridional advection. Such changes initially occur below the surface, around the poleward tropical thermocline boundaries, and slowly show up at the surface. We can therefore understand the discrepancies in tropical SST's between the setups over long timeperiods as, in effect, a consequence of the changing depth of the tropical thermocline. This shows up at the surface as an enhanced surface heating/cooling by the longwave fluxes.

Summary

- Differences in SST anomalies between the slab-ocean and fully-coupled setup are largely attributable to changes in the wind-driven ocean circulation and Ekman pumping, causing changes in the thermoclines' meridional boundaries and depths, and thereby altering the individual heat contents within the clines.

4.4 Main conclusions

In this last subsection, we will attempt to summarise the main take-away points from this chapter on the oceanic impact of STP's. From section 4.3.1, the main changes in SST were found to be, in experiments P01/T01 and the different coupled models:

- Slab-ocean:
 - Positive SST anomaly centred around $40^{\circ}/60^{\circ}$ in each hemisphere, plus a small positive anomaly in the tropics (T01 only);
- Fully-coupled:
 - Positive/Negative SST anomaly centred around 60°N , and negative/positive anomaly polewards of 60° in each hemisphere;
 - Positive/Negative SST anomaly in low-to-midlatitudes (0° to 60°) in each hemisphere ($\gtrsim 100$ years only);

Thus, even on relatively short timescales (\sim decades), and using a relatively low-resolution model, we saw significant differences in the SST anomalies induced between the different coupled models, with differences in the extratropics becoming apparent initially, and in the tropics subsequently. This supports the need to use a fully-interactive ocean when seeking to understand the oceanic response to STP's, especially on longer ($\gtrsim 100$ years) timescales.

The main drivers of these SST changes were summarised in section 4.3.2 and by the schematic in figure 4.3.3, although the subsequent increases/decreases in SST in the low-to-midlatitudes seen in the fully-coupled setup ($\gtrsim 100$ years) were also concluded to be attributable to the changes in ocean heat transport, with experiments P01/T01 exhibiting a decrease/increase in poleward ocean heat transport away from the tropical thermocline, as well increased Ekman downwelling/upwelling currents along its poleward boundary. At higher latitudes, poleward ocean heat transport was strengthened/weakened, with more/less heat being advected away from the midlatitudes into the poles by meridional currents. However, anomalous polar downwelling/upwelling, which would cause polar cooling/warming, ended up dominating the overall response.

The T01 scenario was in agreement with the results of previous studies looking at the oceanic impact of a poleward jet shift, such as Cai et al. (2005), Cai (2006), and Cai & Cowan (2007). Also, the increased vertical upwelling seen around the poles in experiment T01 is like the 'slow' response described by Ferreira et al. (2015) to abrupt ozone depletion, whilst the decreased poleward heat transport into the higher latitudes is like the 'fast' response. Evidence of a corresponding two-timescale behaviour was present in experiments P01 and T01, in the Southern Ocean region, with the 'fast' response only lasting about 5-10 years, probably owing to the strong vertical stratification in that region.

Thus, whilst on a global-scale and thermodynamically, radiative fluxes drive SST changes, locally, changes in ocean heat transport/turbulent heat fluxes were found to be more significant, through their control of the meridional redistribution of heat. Furthermore, whilst in experiments P01/T01 in the fully-coupled setup, radiatively, we would expect local increases in SST in the poles/tropics, in response to increased downward LW in the region of applied STP's (see section 4.1.2), the changes in ocean heat transport meant that we ended up seeing local SST *decreases* in those regions. In a sense, therefore, the radiative and turbulent/ocean heat fluxes appeared to act in ways that were in opposition to each other. And as both turbulent and ocean heat transport fluxes were ultimately found to be wind-driven (see sections 4.2.4 and 4.1.3), we could say that in experiments P01 and T01, the effects of changes in atmospheric thermodynamics (through radiation) and dynamics (through the surface winds) were essentially in competition with each other in terms of their impact on extratropical SST's.

Experiment U01, on-the-other-hand, saw similar SST changes in both coupled models - albeit progressing at different timescales owing to the differences in mixed-layer depths (50m slab-ocean vs. global-average of 119m fully-coupled) - characterised by a near-uniform increase in SST. The main difference was in the Southern Ocean region, which saw suppressed SST increases in the fully-coupled model, in turn attributable to the changes in ocean heat transport in that region. Thus, for this type of STP, it would appear that - at least on the timescales explored in this chapter (0-300 years) - a fully dynamical ocean is not necessary to capture the most salient SST changes, with a slab-ocean of appropriate mixed-layer depth sufficing. For, the changes in SST are mostly governed by the increases in downward LW radiation, seen at all latitudes, in response to the uniformly applied STP.

Chapter 5

Effect of atmosphere-ocean coupling

In previous chapters, we sought to delineate the precise effects of different STP's, upon both the troposphere below (chapter 3), and upon a double-drake global ocean, with either only thermal, or both thermal and dynamical couplings present (chapter 4). Having achieved this, what remains is to understand the interaction between these two components of the global climate system: how does the presence of atmosphere-ocean coupling affect the atmospheric response to STP's, if at all? This question will be the subject of this chapter.

5.1 Model hierarchy results comparison

Having conducted our STP experiments in a model hierarchy of three different setups, and over different timeperiods, it makes sense to start by comparing the atmospheric response to stratospheric forcing between these three different setups. Figures 5.1.1-5.1.3 display the difference between the anomalies in the zonal winds and mass streamfunctions - induced by the STP experiments - in the coupled vs the atmosphere-only setups. In other words, they show the difference in atmospheric response to said perturbations - shown in figure 3.1.1 of chapter 3 for the atmosphere-only configuration - when going from the atmosphere-only configuration of chapter 3, to the slab-ocean and fully-coupled configurations of chapter 4. For the fully-coupled setup, because of the significant changes in SST we see over hundreds of years, we show plots which display the differences in the anomalies seen over both the initial 0-50 years (figure 5.1.2) and over years 250-300 (figure 5.1.3).

Starting with the slab-ocean setup, averaged over years 0-50, and the difference in zonal wind a streamfunction anomalies seen in this setup vs atmosphere-only, shown in figure 5.1.1, we see a clear signal for experiment U01 (left panels): the midlatitude jets and Ferrel cells are all strengthened, whilst the Hadley cells and high-latitude westerlies are weakened, up to

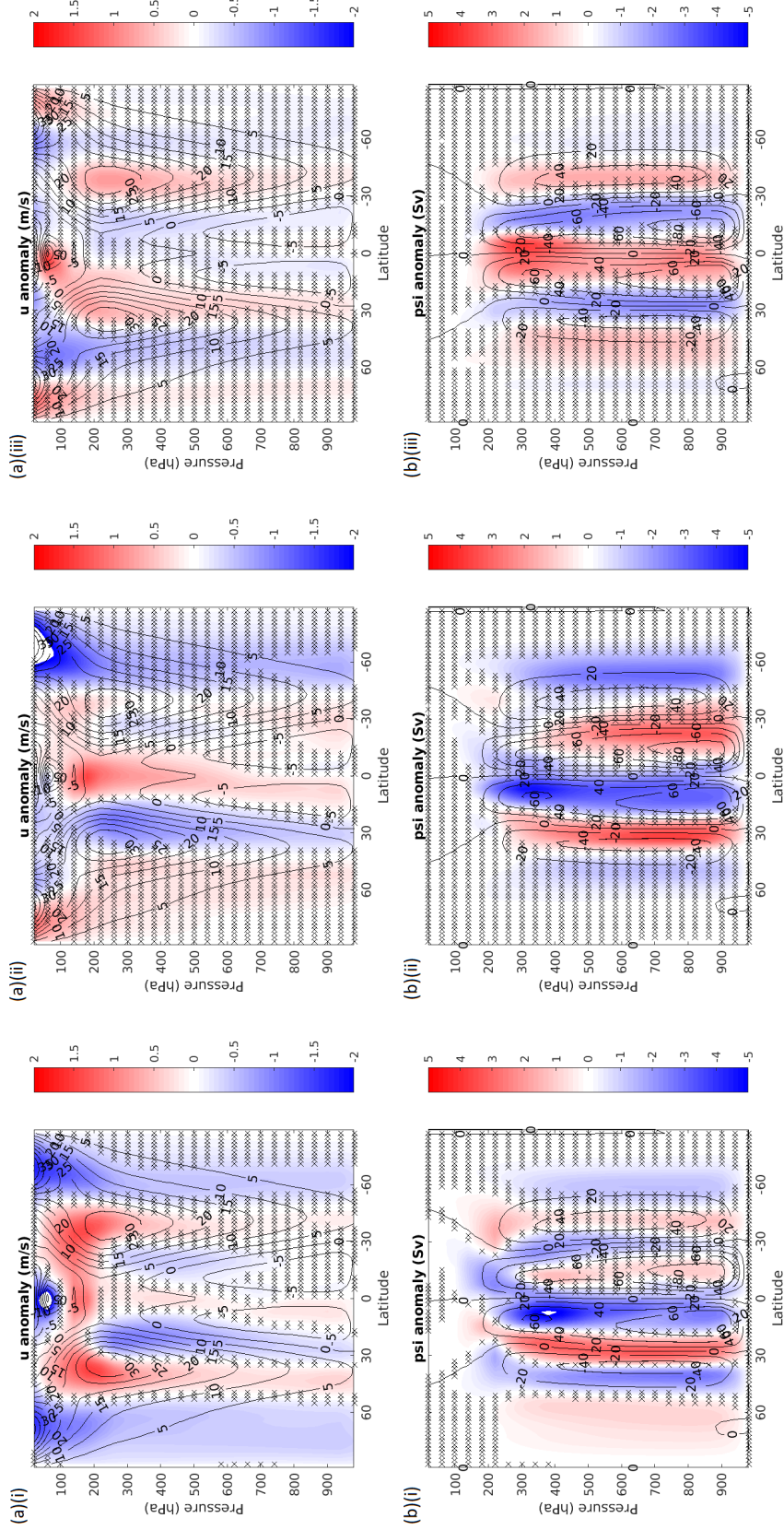


Figure 5.1.1: Changes (colours) in (a) zonal wind (top panel) and (b) mass streamfunction (bottom panel) anomalies in (left-to-right): (i) U01 (left panels), (ii) P01 (middle panels) and (iii) T01 (right panels), in slab-ocean setup years 0-50 vs atmosphere-only setup years 0-30. Contours display the control values in the atmosphere-only setup. Hatching indicates regions in which the confidence levels in the coupled anomalies vs uncoupled anomalies are below 95%, as measured by a two-tail student's t-test.

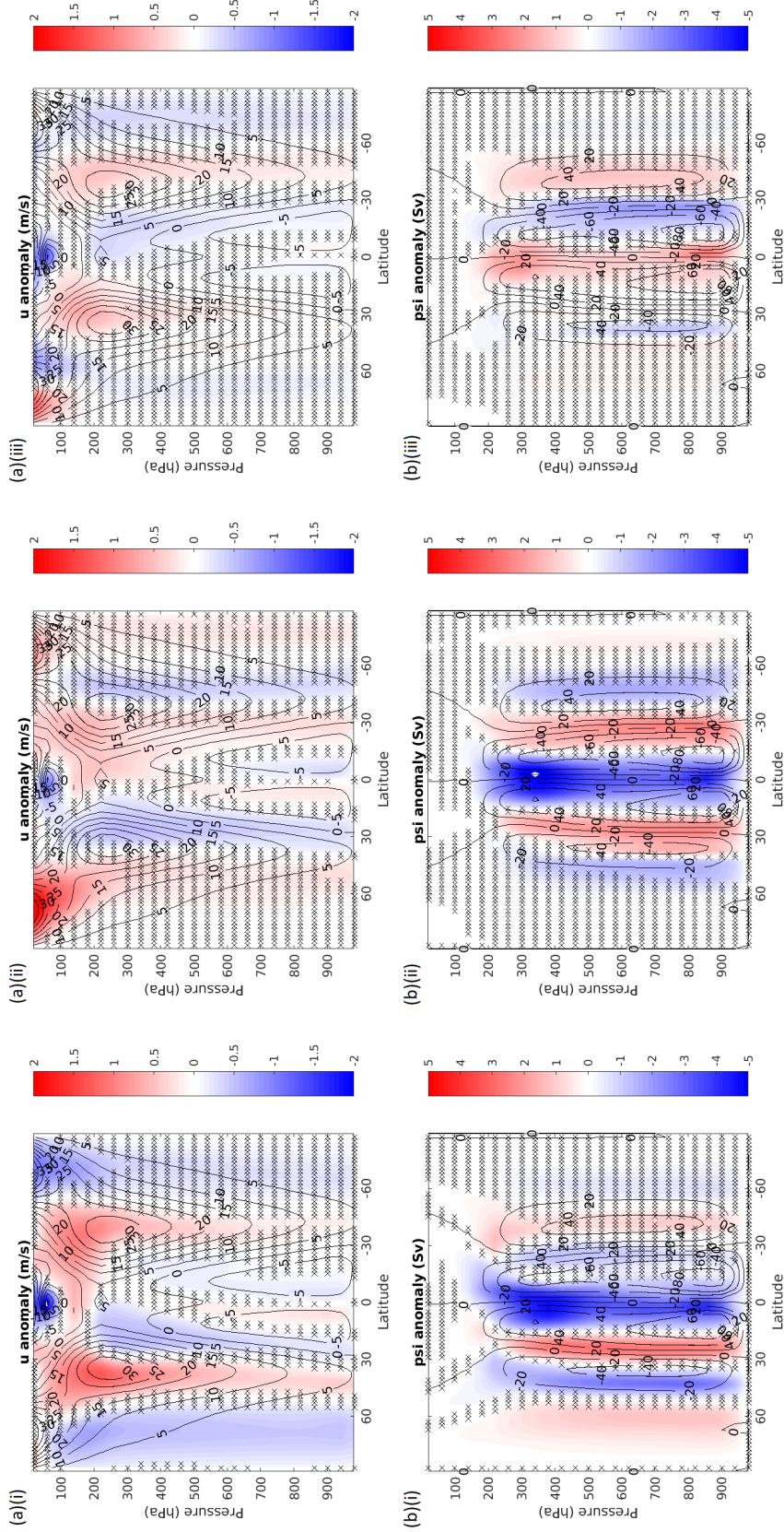


Figure 5.1.2: Changes (colours) in (a) zonal wind (top panel) and (b) mass streamfunction (bottom panel) anomalies in (left-to-right): (i) U01 (left panels), (ii) P01 (middle panels) and (iii) T01 (right panels), in fully-coupled setup years 0-50 vs atmosphere-only setup years 0-30. Contours display the control values in the atmosphere-only setup. Hatching indicates regions in which the confidence levels in the coupled anomalies vs uncoupled anomalies are below 95%, as measured by a two-tail student's t-test.

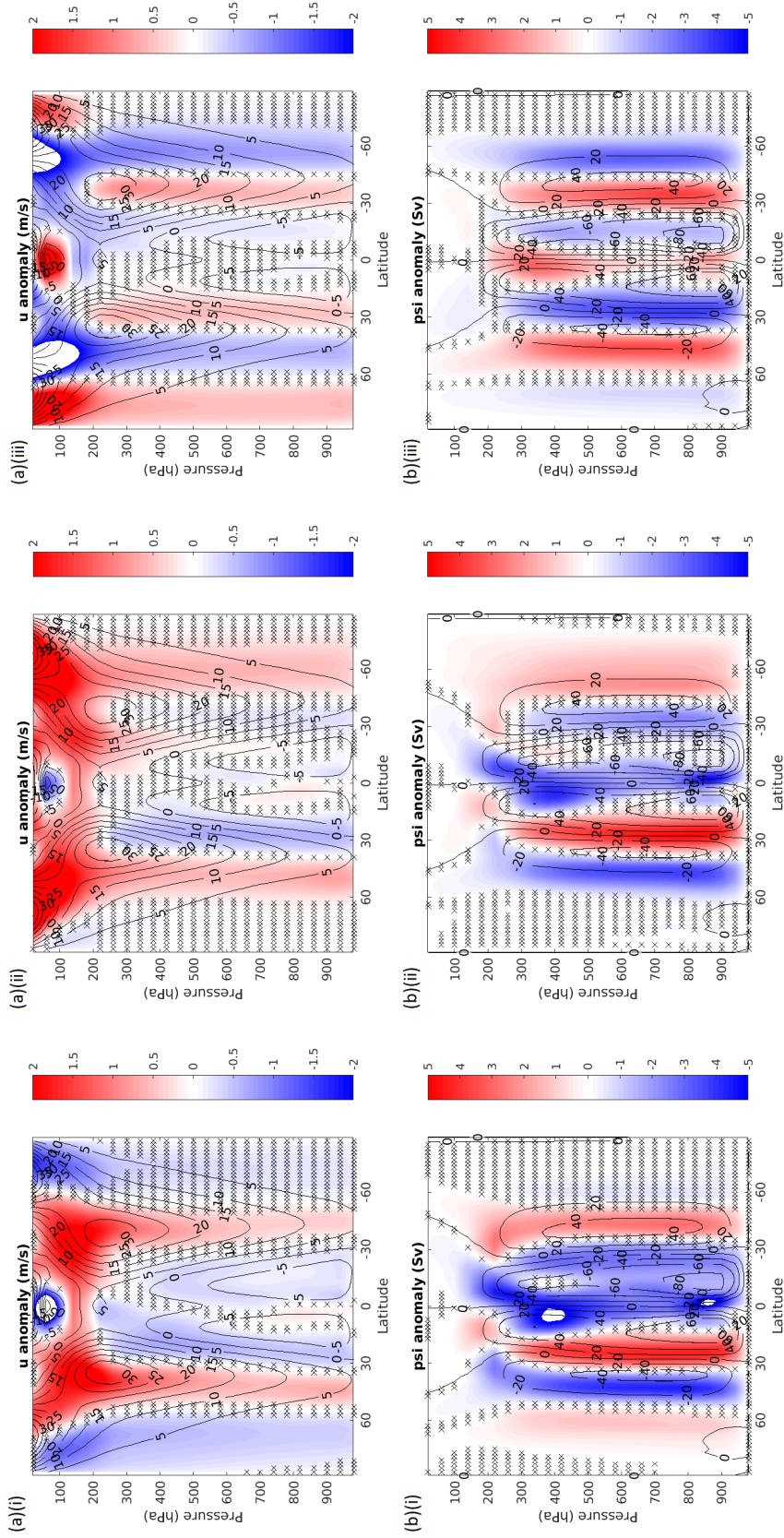


Figure 5.1.3: Changes (colours) in (a) zonal wind (top panel) and (b) mass streamfunction (bottom panel) anomalies in (left-to-right): (i) U01 (left panels), (ii) P01 (middle panels) and (iii) T01 (right panels) experiments, in fully-coupled setup years 250-300 vs atmosphere-only setup years 0-30. Contours display the control values in the atmosphere-only setup. Hatching indicates regions in which the confidence levels in the coupled anomalies vs uncoupled anomalies are below 95%, as measured by a two-tail student's t-test.

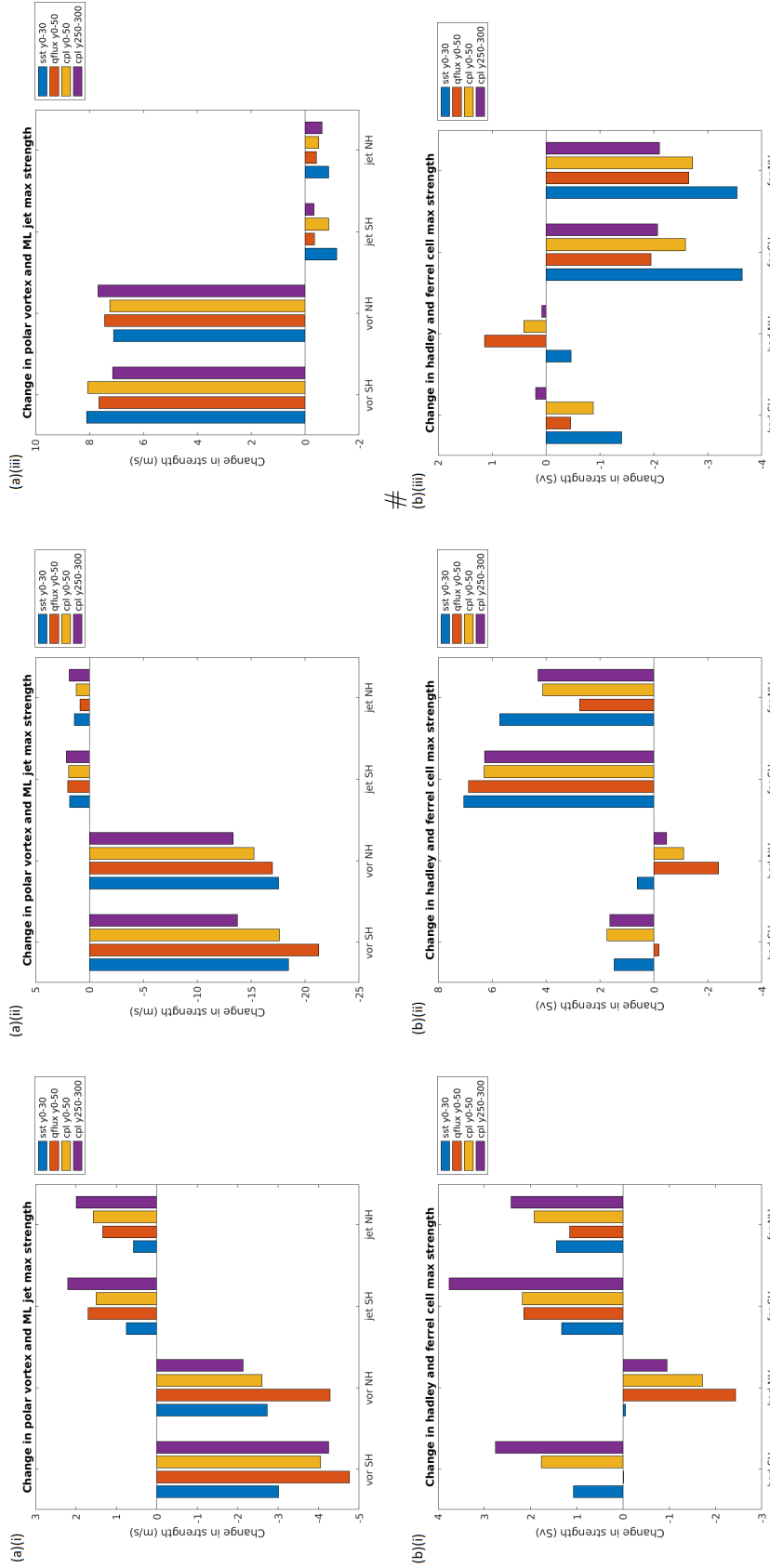


Figure 5.1.4: Changes in (a) maximum polar vortex (vor) and midlatitude jet (jet) strength (top panel), and (b) maximum tropical Hadley (had) and Ferrel cell (fer) strength (bottom panel) in (left-to-right): (i) U01 (left panels), (ii) P01 (middle panels) and (iii) T01 (right panels) experiments, in atmosphere-only (sst), slab-ocean-only (sst), and fully-coupled (cpl) setups, averaged over years indicated (yX-Y).

and including the stratospheric polar vortices, as are the poleward boundaries of the Ferrel cells. For experiments P01 (middle panels)/T01 (right panels), we only see a clear signal at low latitudes, with weakened/strengthened Hadley cells and tropical easterlies, and a slight weakening/strengthening of the subtropical flank of the midlatitude jet and Ferrel cell in the Northern Hemisphere.

When we compare with the base-level anomalies in the atmosphere-only setup - shown in figure 3.1.1 of chapter 3 - we see that these changes generally lead to a weakening of the underlying anomalies at low latitudes. For experiment U01, given the qualitative resemblance of the changes in anomalies in the extratropics to those of the base-level anomalies of experiment P01, the setup also leads to an overall strengthening and poleward-shift in the extratropical atmospheric anomalies. This can be seen when we look at figure 5.1.4, which displays the quantitative changes seen in maximum polar vortex, midlatitude jet, Hadley and Ferrel cell strength in each hemisphere, for each experiment in each setup. When we look at the changes in maximum polar vortex/midlatitude jet (vor/jet, top-left panel), and Ferrel cell strength (fer, bottom-left panel) for experiment U01, we see that the slab-ocean setup (orange, qflux y0-50) generally increases all quantities in both hemispheres - except for the NH Ferrel cell - by in the range of +50 to +100%.

In the fully-coupled setup, averaged over years 0-50, the differences in the anomalies compared with the atmosphere-only setup are shown in figure 5.1.2, and appear qualitatively very similar to those in the slab-ocean setup, but quantitatively somewhat weaker. This is confirmed by the weaker shifts in maximum polar vortex (NH + SH) and midlatitude jet (SH) strength seen in experiment U01, shown in the left panels of figure 5.1.4 (yellow, cpl y0-50). Over years 250-300 of the fully coupled setup - differences in the anomalies shown in figure 5.1.3 - for experiment U01 (left panels), we see a similar signal in the mid-to-high latitudes as in the slab-ocean setup, with stronger midlatitude jets and Ferrel cells, and weakened high-latitude westerlies, whilst at low latitudes it is quite different, with strengthened and slightly poleward-expanded Hadley cells and tropical easterlies. For experiments P01 (middle panels)/T01 (right panels), whilst there is not such a clear signal at low latitudes as in the slab-ocean setup, there is one in the extratropics, with the midlatitude jets and Ferrel cells appearing to strengthen/weaken and shift polewards/equatorwards. There is also a fairly clear change in the polar vortices across the experiments, shifting equatorwards/polewards in experiments U01/T01, and getting stronger in experiment P01.

When we compare these changes in response, seen in years 250-300 of the fully-coupled setup, with the base-level anomalies, we see that - similar to what we saw for experiment U01 in the other coupled setups - these changes generally lead to a poleward-shift in the underlying extratropical anomalies, weakening the subtropical anomalies, and strengthening and expanding polewards the low-midlatitude anomalies. It also causes, for experiment U01, an overall stronger response, in both the tropics and extratropics, with greater increases in maximum Hadley cell, Ferrel cell, and midlatitude jet strength, of around +50% to +300%, as shown in the left panels of figure 5.1.4 (purple, cpl y250-300). For experiment T01 (right panels), we see an overall

weakened response in the midlatitudes, with smaller decreases in maximum midlatitude jet and Ferrel cell strength, to around 20% to 60% of the original values, whilst for P01 (middle panels), we see reduced increases/decreases in Ferrel cell/polar vortex strength, by around -10% to -30%.

Summary

- U01 experiment:
 - Across setups: midlatitude jets and Ferrel cells strengthened, high-latitude westerlies weakened;
 - * Strengthening and slight poleward-expansion of signal in extratropics;
 - Slab-ocean setup years 0-50: Hadley cells and polar vortices weakened;
 - * Signal in tropics weakened; signal in high-latitude stratosphere strengthened.
 - Fully-coupled setup years 250-300: Hadley cells and tropical easterlies strengthened, polar vortices equatorward shifted.
 - * Signal in tropics strengthened.
- P01 experiment:
 - Slab-ocean and fully-coupled setups years 0-50: Hadley cells and tropical easterlies weakened, equatorial flank of NH midlatitude jet and Ferrel cell weakened;
 - * Signal in low-latitudes weakened.
 - Fully-coupled setup years 250-300: Poleward expansion of midlatitude jets and Ferrel cells, polar vortices strengthened;
 - * Signal in low-midlatitudes expands polewards; signal in high-latitude stratosphere weakened.
- T01 experiment:
 - Slab-ocean and fully-coupled setups years 0-50: Hadley cells and tropical easterlies strengthened, equatorial flank of NH midlatitude jet and Ferrel cell strengthened;
 - * Signal in low-latitudes weakened.
 - Fully-coupled setup years 250-300: Equatorward contraction of midlatitude jets, Ferrel cells and polar vortices;
 - * Signal in low-midlatitudes expands polewards.

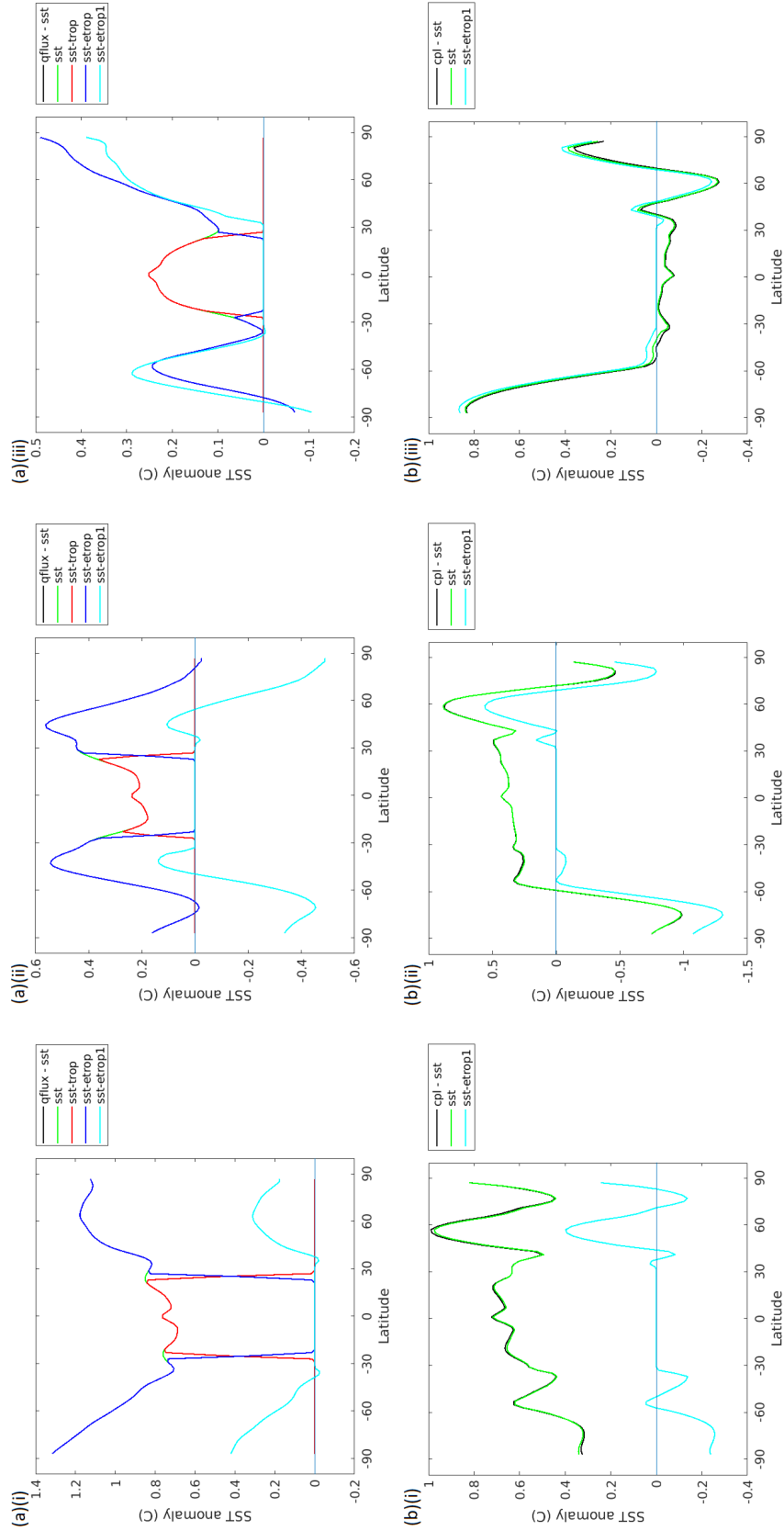


Figure 5.2.1: Sea surface temperature anomalies used in SST perturbation experiments, derived from SST changes in the (a) slab-ocean setup (top panel), and (b) fully-coupled setup (bottom panel) in experiments (left-to-right): (i) U01 (left panels), (ii) P01 (middle panels) and (iii) T01 (right panels).

SST Name	Description
sst	Full coupled-setup Δ SST applied
sst-trop	Coupled-setup Δ SST applied only in tropics, 0 to 25°
sst-etrop	Coupled-setup Δ SST applied only in extratropics, 25° to 90°
sst-etrop1	Coupled-setup Δ SST - Δ SST($\phi=30^\circ$) applied in extratropics, 30° to 90°
sst-Xk/-0Xk	Uniform SST increase of +X°C/+0.X°C
sst--Yk/--0Yk	Uniform SST decrease of -Y°C/-0.Y°C
np	No STP applied in both control and SST-perturbed run
p	STP applied in both control and SST-perturbed run, corresponding to original perturbation (U01/P01/T01) that gave rise to the SST anomaly in coupled setup; sst-1k/--1k p uses U01 perturbation.

Table 5.2.1: List of descriptors used to describe and identify the different SST-perturbation experiments.

5.2 SST perturbation experiments

In order to better understand what exactly is responsible for the observed changes in climate dynamics in the different coupled setups versus the atmosphere-only setup, various experiments were run in the atmosphere-only configuration, in which the SST's were altered to mimic all, part of, or aspects of the SST changes seen in the STP experiments in the coupled setups. Descriptions of these SST perturbation experiments are provided in table 5.2.1, and illustrations of the zonal-average applied SST perturbations are provided in figure 5.2.1. These perturbed SST's are constructed from the ensemble-mean SST anomalies seen in each STP experiment - U01(left panels), P01 (middle panels) and T01 (right panels) - in each coupled setup - both slab-ocean (qflux, top panels of figure 5.2.1), and fully-coupled (cpl, bottom panels of figure 5.2.1) - time-averaged over the entire run: 0-50 and 0-300 years respectively. Thus, each time- and ensemble-average SST anomaly has its own set of derived SST-perturbations, as shown in figure 5.2.1. These SST-perturbations are then applied in the atmosphere-only/fixed-SST setup, and run for 5 years with an ensemble size of 6. This is done both with, and without, the corresponding STP's present (p and np in table 5.2.1). The results of the runs are then compared with those of corresponding control runs, in which everything is the same - including whether or not the equivalent STP is present - except the SST, which is held at its control, unperturbed profile. Thus, for each type of SST-perturbation applied, we obtain two estimates for its impact upon the climate: one with, and one without stratospheric forcing present. In comparing the two, we can get an idea of the importance of nonlinear feedbacks between the applied SST and STP's.

Figure 5.2.2 shows the results of these experiments: each coloured dot represents the result of a different SST-perturbation experiment, with the x- and y-values being the projection of the zonal wind and mass streamfunction anomalies respectively onto the difference in the corresponding anomalies between the coupled- and atmosphere-only setups, for each STP experiment.

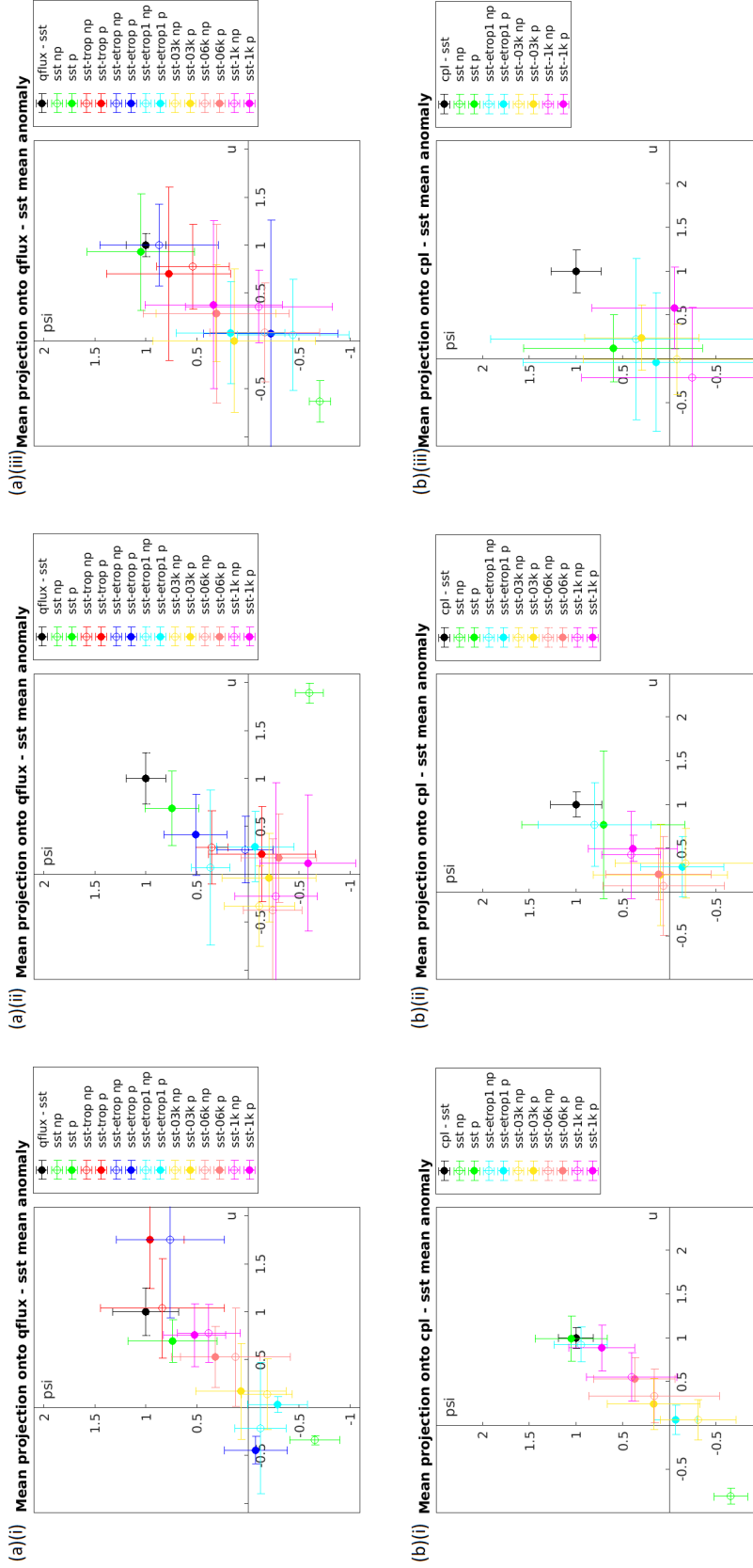


Figure 5.2.2: Projections of the full zonal wind (u) and mass streamfunction (psi) anomalies, seen in response to SST-perturbation experiments, onto difference in anomalies between atmosphere-only and (a) slab-ocean setup, years 25-50 (top panel), (b) fully-coupled setup, years 0-300 (bottom panel), in experiments (left-to-right): (i) U01 (left panels), (ii) P01 (middle panels) and (iii) T01 (right panels). The black dots indicate the result of projecting the difference in the anomalies between the different setups onto itself, and the error bars' length are set as the standard deviation of the time-average projections of the different ensemble members.

Thus, if the changes in the zonal winds and mass streamfunctions in a given SST-perturbation experiment exactly matched the difference in the anomalies seen between the corresponding STP experiment in the coupled versus atmosphere-only setup, the projections of both fields would equal 1, and so the point would have coordinates (1,1). This indeed is what we see when we project those changes in the anomalies back onto themselves, as represented by the black dots in the plots. Errorbars in both horizontal and vertical directions are also placed on the dots, estimated by taking the standard deviation between the time-averaged projection values of different ensemble members.

Focusing first on the results of SST-perturbation experiments, corresponding to the changes in SST seen in the slab-ocean setup, shown in the top panel of figure 5.2.2, across the different experiments, we find that the experiment in which the full Δ SST is imposed in the presence of stratospheric forcing, sst p (green filled dot) does a good job at capturing the changes in u and ψ , with projections onto those fields of 90-120%, and with errorbars that place them within range of 100%. Also, for the SST-experiments corresponding to experiments U01 (top-left) and T01 (top-right) in the slab-ocean setup, we see that experiments with tropical-SST, sst-trop (red dots) and uniform-heating SST anomalies, sst-1k, sst-06k, and sst-03k (yellow, orange and pink dots respectively), produce u and ψ anomalies that generally project positively onto the full (qflux - sst) anomalies. Of these, the tropical-SST anomalies project the most positively, with mean projections of 60-200%, followed by the uniform-heating SST anomalies, with the larger amplitude SST anomalies generally yielding the more positive projections. Conversely, the experiments with the extratropical-SST anomalies, sst-etrop/sst-etrop1 (blue/cyan dots), tend to have projections that are close to zero, or negative, for experiments U01 and T01, the most negative projections being that of the sst-etrop p (blue filled dots) experiments.

This all appears to point towards the increases in SST, and in particular the increases in tropical SST, as being responsible for driving the observed changes in the zonal winds and streamfunctions, between the slab-ocean and atmosphere-only setups, for experiments U01 and T01, whilst the extratropical-SST changes either act to dampen (U01), or have no real effect (T01). Indeed, when we analyse the results of the individual SST-perturbation experiments, it is found that the atmospheric response induced by applying only the change in tropical-SST corresponding to these experiments, sst-trop, is very similar to that caused by a uniform SST increase (top panels of figure 5.2.3), whilst the atmospheric response caused by applying only the changes in extratropical-SST, sst-etrop, is very similar to that caused by a uniform decrease in SST (bottom panels of figure 5.2.3), for experiments U01 and T01. Looking back at section 5.1, we note also the strong resemblance between the results of the uniform $+1^\circ\text{C}$ SST increase experiment (top panels of figure 5.2.3), and the changes in the anomalies seen in experiment U01 in years 250-300 of the fully-coupled setup (left panels of figure 5.1.3).

The SST experiments corresponding with experiment P01 in the slab-ocean setup - top-middle panel of figure 5.2.2 - appear to show almost the opposite results, insofar as the experiment with the most positive projection is sst-etrop p (blue filled dot), at projections of around 40-60%, whilst all the other experiments appear to exhibit either weakly positive (sst-etrop1/sst-

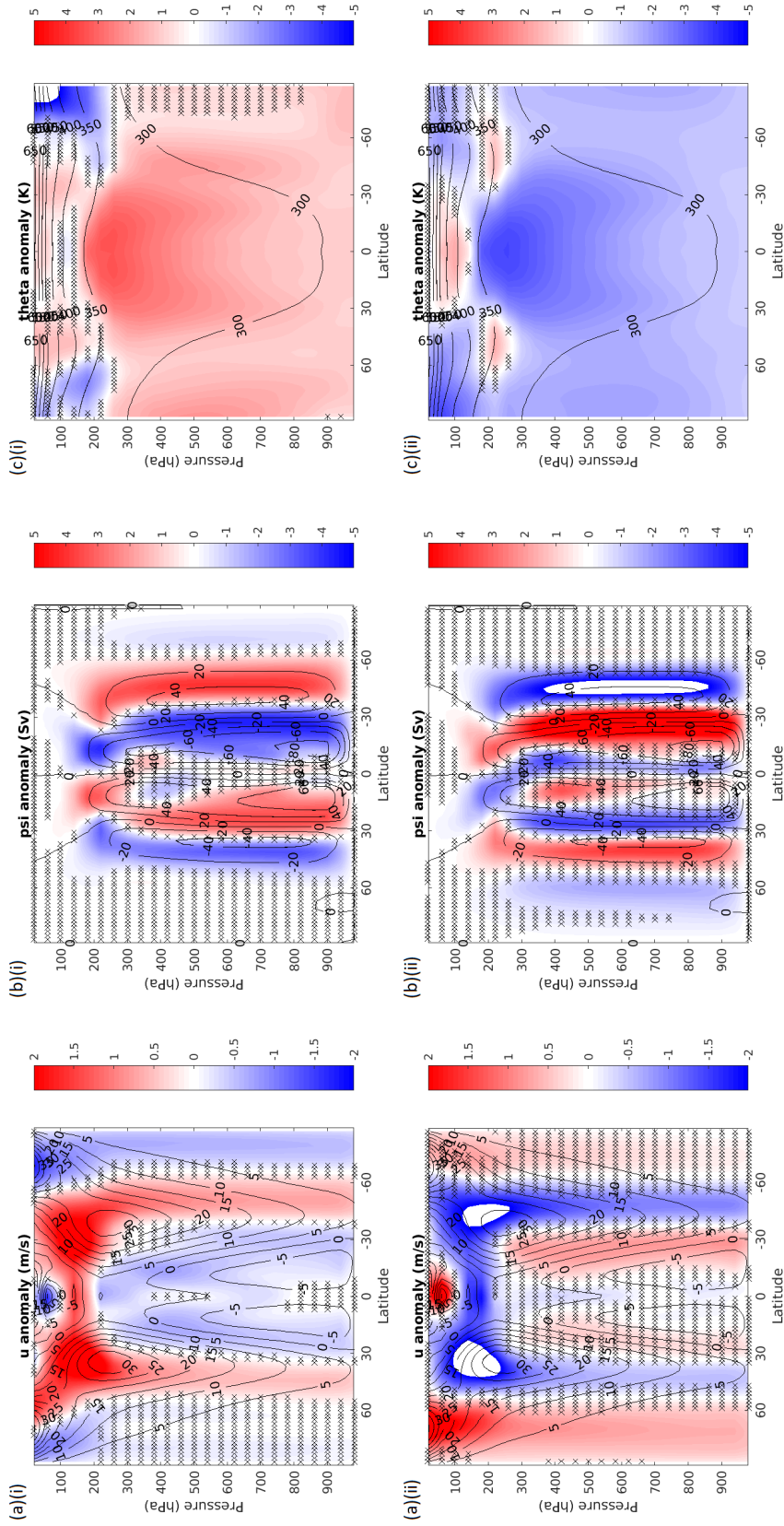


Figure 5.2.3: Control values (contours) and anomalies (colours) in (a) zonal wind (left panels), (b) mass streamfunction (middle panels), and (c) potential temperature (right panels), in response to uniform SST-perturbation experiments: (i) sst-1k np (top panels), and (ii) sst-1k up (bottom panels). Hatching indicates regions in which the confidence levels in the experiment vs control values are below 95%, as measured by a two-tail student's t-test.

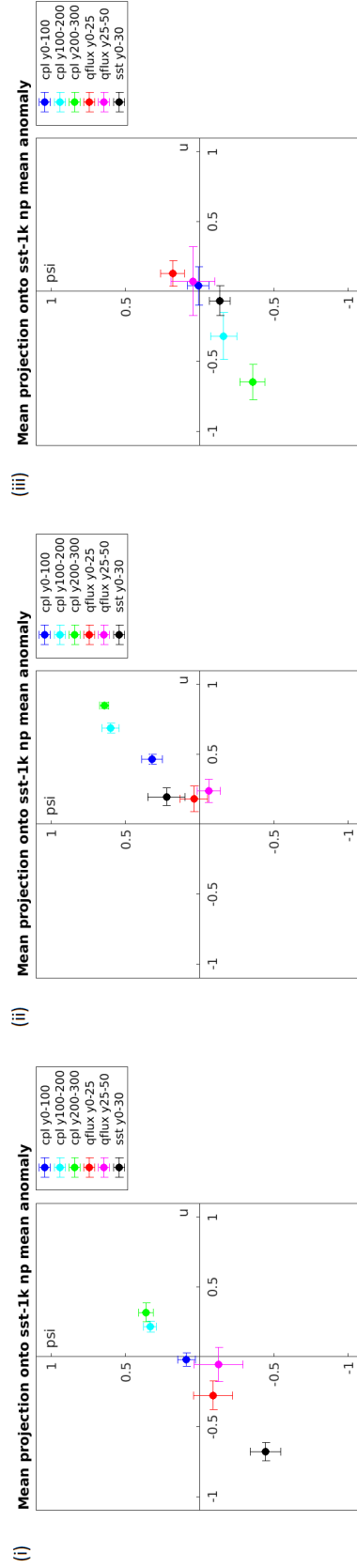


Figure 5.2.4: Projections of zonal wind (u) and mass streamfunction (psi) anomalies in atmosphere-only (sst), slab-ocean (qflux) and fully-coupled (cpl) setups, averaged over years 0-30, 0-50, and 250-100 as stated, in experiments (left-to-right): (i) U01 (left panels), (ii) P01 (middle panels) and (iii) T01 (right panels), onto corresponding anomalies seen in SST perturbation experiment sst-1k np. Errorbars' length are set as the standard deviations between ensemble members.

trop; cyan/red dots) or weakly negative (sst-03k, sst-06k, sst-1k; yellow/orange/pink dots) projections, with error ranges that could place them at around zero. This appears to indicate that, for experiment P01 in the slab-ocean setup, it is mainly the changes in extratropical-SST - both absolute SST changes, and changes in its meridional gradient - that appear to be driving most of the changes in u and ψ anomalies, when compared with the atmosphere-only setup. Again, the atmospheric changes caused by the changes in tropical- and extratropical-SST are found to correspond qualitatively to those of uniform increases and decreases in SST respectively.

Turning our attention to the results of experiments emulating the SST changes seen in the fully-coupled setup, displayed in the bottom panels of figure 5.2.2, we see that, for both experiments U01 (bottom-left) and P01 (bottom-middle), the experiment sst p (green filled dot) - in which the full SST anomaly is applied in the presence of the relevant STP - does reasonably well at emulating the difference in response between the fully-coupled and atmosphere-only setups, with projections in the range of 80-100%. We also observe that the experiments involving uniform increases in SST have positive projections, with experiment sst-1k p (pink dots) having the most positive, at 80-100% for U01, and around 50% for P01. When we compare the full atmospheric anomalies, shown in figure 5.1.3, with that caused by a uniform $+1^{\circ}\text{C}$ SST increase, shown in the top panels of figure 5.2.3, we see again a good correspondence for U01, whilst for P01 the full anomaly appears to be slightly poleward shifted, a $-/+$ tropospheric zonal wind anomaly dipole occurring centred around 40° in both hemispheres, as opposed to around 30° in U01 and sst-1k np. This may be in part due to the changes SST at high-latitudes, as investigated by experiments with the extratropical SST anomaly, sst-etrop1 (cyan dots). These experiments are found to produce an atmospheric response similar to that of a uniform SST decrease, shown in the bottom panels of figure 5.2.3.

The difference in atmospheric response to experiment T01 in the fully-coupled vs atmosphere-only setup, and its cause, is not so easy to explain (bottom-right panel of figure 5.2.2). Whilst the experiments sst p (green filled dot) and sst--03k p (yellow filled dot) both have positive projections onto the full anomaly, they are weak and within range of 0, as are the other experiments. This may be due to the comparatively weak changes in atmospheric dynamics involved in experiment T01, and its associated SST changes. Qualitatively, the anomalous atmospheric response, shown in the right panels of figure 5.1.3, is like that of experiment sst--1k np (-1°C uniform SST decrease), shown in the bottom panels of figure 5.2.3, but shifted polewards by about $+10^{\circ}$. As with P01, this may be related to the changes in SST at high latitude, but nothing can be concluded from what we observe.

To round things off, figure 5.2.4 displays the projections of the zonal wind and mass stream-function anomalies, seen in the model-hierarchy of setups, in response to the applied STP's, onto the corresponding anomalies seen in experiment sst-1k np, in which a uniform SST perturbation of $+1^{\circ}\text{C}$ is applied (top panels of figure 5.2.3). We see that, for both experiments U01 (left panel) and P01 (middle panel), the general pattern is that the fully-coupled setup (blue/cyan/green dots) makes the projections more positive, whilst for experiment T01 (right panel), it makes them more negative. Moreover, the projections become more positive/negative with time. It is

also the case that, while the slab-ocean setup (red/pink dots) appears to make the projection more positive for experiment U01, with values falling between that of the atmosphere-only and fully-coupled setups, for experiment P01/T01 it appears to make little difference, and indeed, might lead to a slightly more negative/positive projection.

Summary

- In general, the changes in atmospheric response in the coupled setups vs atmosphere-only setup can be accounted for by the changes in SST in the presence of stratospheric forcing (sst p);
- The bulk of the difference in atmospheric response appears driven by the changes in:
 - Uniform/Tropical SST (U01 qflux + cpl, P01 cpl, T01 qflux + cpl);
 - Extratropical SST (P01 qflux):
 - * Produces a similar atmospheric response to that of a lowering of uniform/tropical SST;
- In the slab-ocean setup, the changes in tropical- and extratropical- SST changes appear to force atmospheric responses in qualitative opposition to each other for experiments U01 and P01.

5.3 U01-QFLUX SST experiment

Since, from the previous subsection, the majority of changes in the atmospheric response to STP's in our coupled models vs the atmosphere-only model appear driven by changes in tropical and/or uniform SST, and that, moreover, the atmospheric responses to both are highly similar, it makes sense to further investigate the atmospheric response to at least one of these types of SST perturbation, and attempt to diagnose the driving factors behind the atmospheric response.

To that end, we will in this subsection further investigate the atmospheric response to the SST anomaly found in the U01 experiment in the slab-ocean setup, sst-qflux-U01 np, shown in the top-left panel of figure 5.2.1 (sst; green). Whilst this SST anomaly is not perfectly uniform, with a slight negative meridional gradient in the extratropics, the atmospheric response is very close to that found in response to a uniform rise in SST of similar magnitude, sst-1k np, and also to that found when the SST anomaly is applied only in the tropics, sst-trop np. We can thus be confident that changes in extratropical SST meridional gradient have only a secondary influence on the atmosphere above, and can be safely ignored in our analysis. Furthermore, given the fact that the atmospheric response to a uniform lowering of SST is more-or-less the exact opposite to that of a uniform raising of SST - compare the top and bottom panels of figure 5.2.3 - the conclusions of this analysis can also be applied to that of a uniform lowering of SST, but with the sign of the anomalies reversed.

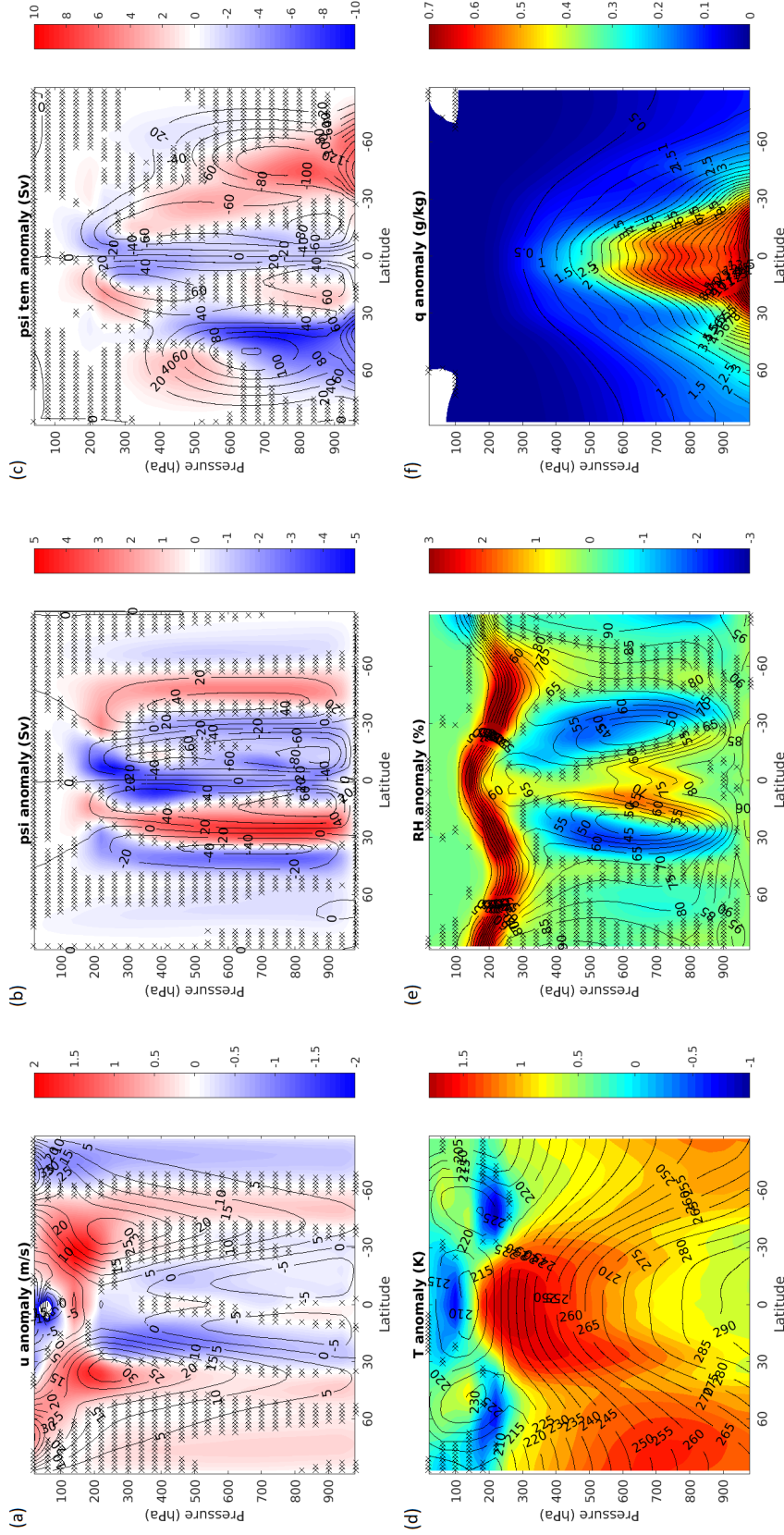


Figure 5.3.1: Control values (contours) and anomalies (colours) in various climatological fields in response to SST perturbation experiment sst-qflux-U01 np, averaged over years 0-5: (a) zonal wind (top-left), (b) Eulerian streamfunction (top-middle), (c) TEM residual streamfunction (top-right), (d) temperature (bottom-left), (e) relative humidity (bottom-middle), and (f) absolute humidity (bottom-right). Hatching indicates regions in which the confidence levels in the experiment vs control values are below 95%, as measured by a two-tail student's t-test.

Figure 5.3.1 displays the changes in various mean climatological fields in response to the applied SST anomaly. Again, we note the strong similarity of the changes in zonal winds (top-left) and streamfunction (top-middle), with those of experiment sst-1k np, shown in the top-left and top-middle panels of figure 5.2.3. In the zonal winds, the most distinctive features are the accelerations of the tropical easterlies and midlatitude westerlies, with maximum positive accelerations around the core of the midlatitude jets, at 40° and 200hPa. As we know from chapter 3, the zonal wind changes tend to be geostrophic, i.e. in agreement with changes in meridional temperature gradient via the thermal wind equation. Looking at the changes in temperature, shown in the bottom-left panel of figure 5.3.1, we see that there is indeed a strong increase (more negative) in its meridional gradient between 30° and 45° , and 1000 to 200hPa, with the strongest increase at around 40° and 200hPa, which is a region close to the tropopause, and where the tropopause pressure level is decreasing substantially with increasing latitude. Moreover, throughout most of the tropical troposphere, there also appears to be a fairly strong decrease in meridional temperature gradient, between 0° to 30° and 1000 to 300hPa. These changes in meridional temperature gradient would, through the thermal wind equation, be in agreement with observed accelerations in midlatitude westerlies and tropical easterlies respectively.

5.3.1 Momentum budget

The top panel of figure 5.3.2 displays the changes in the individual component terms of the quasigeostrophic zonal wind tendency equation (2.1.12). If we compare with the overall zonal wind changes (top-left of figure 5.3.1), we see that, for the most part, zonal wind accelerations in the extratropical upper troposphere appear driven by changes in the $[u^*v^*]$ eddies (top-middle of figure 5.3.2), with the exception of zonal wind accelerations in the subtropical upper troposphere, equatorward of around 40° , which, as with the zonal wind changes in the tropical troposphere, appear more driven by changes in Coriolis acceleration, $f[v]$ (top-left of figure 5.3.2). Changes in this latter term can be fairly well understood with reference to the circulation changes we observe in the top-middle panel figure 5.3.1, with westerly acceleration/deceleration occurring in the upper/lower branches of the strengthened Hadley cells, and the converse in upper/lower branches of the strengthened Ferrel cells.

The bottom panel of figure 5.3.2 displays the changes in TEM residual circulation (bottom-left), EP fluxes/divergences (bottom-middle), and meridional PV gradient (bottom-right). In the lower midlatitude troposphere, we observe a general reduction in the residual circulation strength, and an increase aloft, above about 600hPa. This is echoed by the anomalous EP fluxes, which exhibit an anomalous downward/upward pattern in the midlatitude lower/upper troposphere, indicating decreases/increases in the vertical EP fluxes in these regions. Accompanying the anomalous upward EP fluxes in the upper midlatitudes are anomalous equatorward fluxes in the upper troposphere, converging around the subtropical flanks of the midlatitude jets. This pattern of anomalous upward and equatorward EP fluxes in the upper extratropical

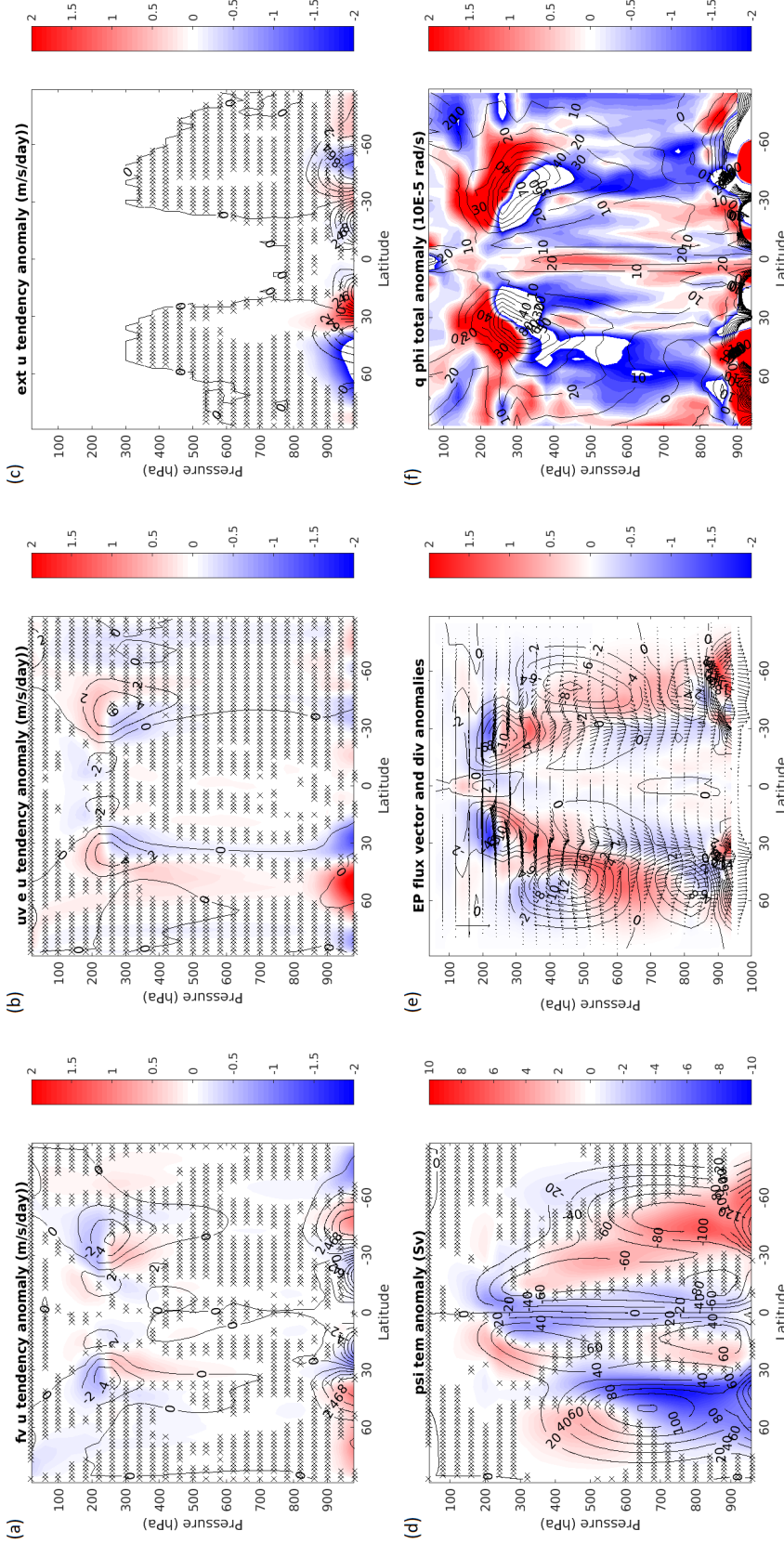


Figure 5.3.2: Control values (contours) and anomalies (colours) in: (a) Coriolis westerly acceleration, $f[v]$ (top-left), (b) westerly acceleration by uv eddies, $-\frac{\partial[u^*v^*]}{\partial y}$ (top-middle), (c) frictional deceleration, $\overline{F_x}$ (top-right), (d) TEM residual circulation (bottom-left), (e) EP fluxes (arrows) and divergences (colours = control values) (bottom-middle), and (f) meridional PV gradient, q_ϕ (bottom-right), in response to SST perturbation experiment sst-qflux-U01 up, averaged over years 0-5. In the EP flux diagram, the fluxes are mass-weighted as per equations (2.1.32) and (2.1.33), the EP flux divergences are in units of $10^{15} m^3$, and the arrows are scaled such that the horizontal and vertical arrows in the top-left have lengths $5 \times 10^{13} m^3$ and $5 \times 10^{19} m^3 Pa$ respectively. Hatching in all but the bottom-middle and bottom-right panels indicates regions in which the confidence levels in the experiment vs control values are below 95%, as measured by a two-tail student's t-test.

troposphere is well-explained by the pattern of meridional PV gradients in that region, which exhibit an upward shift in the midlatitude upper troposphere, with increases aloft and decreases below. All these changes in the residual circulation and EP fluxes indicate increases in the poleward fluxes of westerly momentum and heat, $\overline{u'v'}$ and $\overline{v'\theta'}$, in the subtropical and midlatitude upper troposphere respectively, which would have the effect of redistributing westerly momentum away from the subtropical flanks of the tropospheric jet cores, and into the eddy-driven component of the jet in the midlatitudes, the $\overline{v'\theta'}$ eddies acting to redistribute the momentum throughout the jets' height (via their forcing of the Ferrel circulations), reducing their vertical shears/baroclinicity.

Figure 5.3.3 shows the changes in Eady growth rate, σ_B (top panel), the third component of meridional PV gradient (bottom panel; $q_{\phi,p}$ in equation (2.1.28)), and their components, due to the changes in vertical zonal wind (middle panels), temperature gradients (right panels), and in total (left panels). Again, the similarity between the changes in $q_{\phi,p}$ (bottom-left) and q_ϕ (bottom-right of figure 5.3.2), shows the dominance of the former in driving the latter. The zonal wind gradient contributions to both Eady growth rate (top-middle) and meridional PV gradient (bottom-middle) exhibit, broadly speaking, positive anomalies throughout the subtropical troposphere above the boundary layer, centered around 30° , and broad decreases in the extratropical troposphere, polewards of about 40° , indicating increased/decreased vertical zonal wind shear, $\partial_z \bar{u}$, and, again, via thermal wind arguments, increased/decreased meridional temperature gradients, in these regions respectively. The temperature gradient contributions to both terms (right panels) display decreases/increases in the lower-to-middle/upper troposphere. Overall, the zonal wind gradient contributions to the Eady growth rate appear dominant, the temperature gradient contributions generally acting to damp the former in regions of strong vertical temperature gradient, namely the subtropical troposphere and tropopause regions. For the meridional PV gradient component $q_{\phi,p}$, both contributions appear significant. When we combine this with the observed Coriolis acceleration patterns previously noted, which act to increase/decrease vertical zonal wind shear in the subtropics/midlatitudes, it would appear that - regardless of whether or not they are driving the changes in absolute zonal wind - the circulation changes appear to be forcing the changes in vertical zonal wind shear, and thereby, much of the observed changes in baroclinicity and meridional PV gradient.

Figure 5.3.4 shows the changes in zonal winds, mass streamfunction, Coriolis and eddy-momentum flux acceleration, EP fluxes and divergences, and PV meridional gradient in the first 5 days of the spinup. We see an immediate, large positive/negative circulation anomaly in the NH/SH equatorial-to-midlatitude troposphere, and corresponding positive/negative Coriolis accelerations in the upper/lower troposphere, leading to the +/- zonal wind anomaly dipole we observe in the troposphere. We also observe, in the EP fluxes, a similar pattern to the equilibrated anomalies, with anomalous upward EP fluxes in the upper midlatitude troposphere, and mid-level divergence and upper-level convergence in the midlatitude and subtropical troposphere. If we compare this pattern with the anomalous meridional PV gradient due to changes in the vertical zonal wind shear, again, this shows a strong correspondence with the patterns of EP

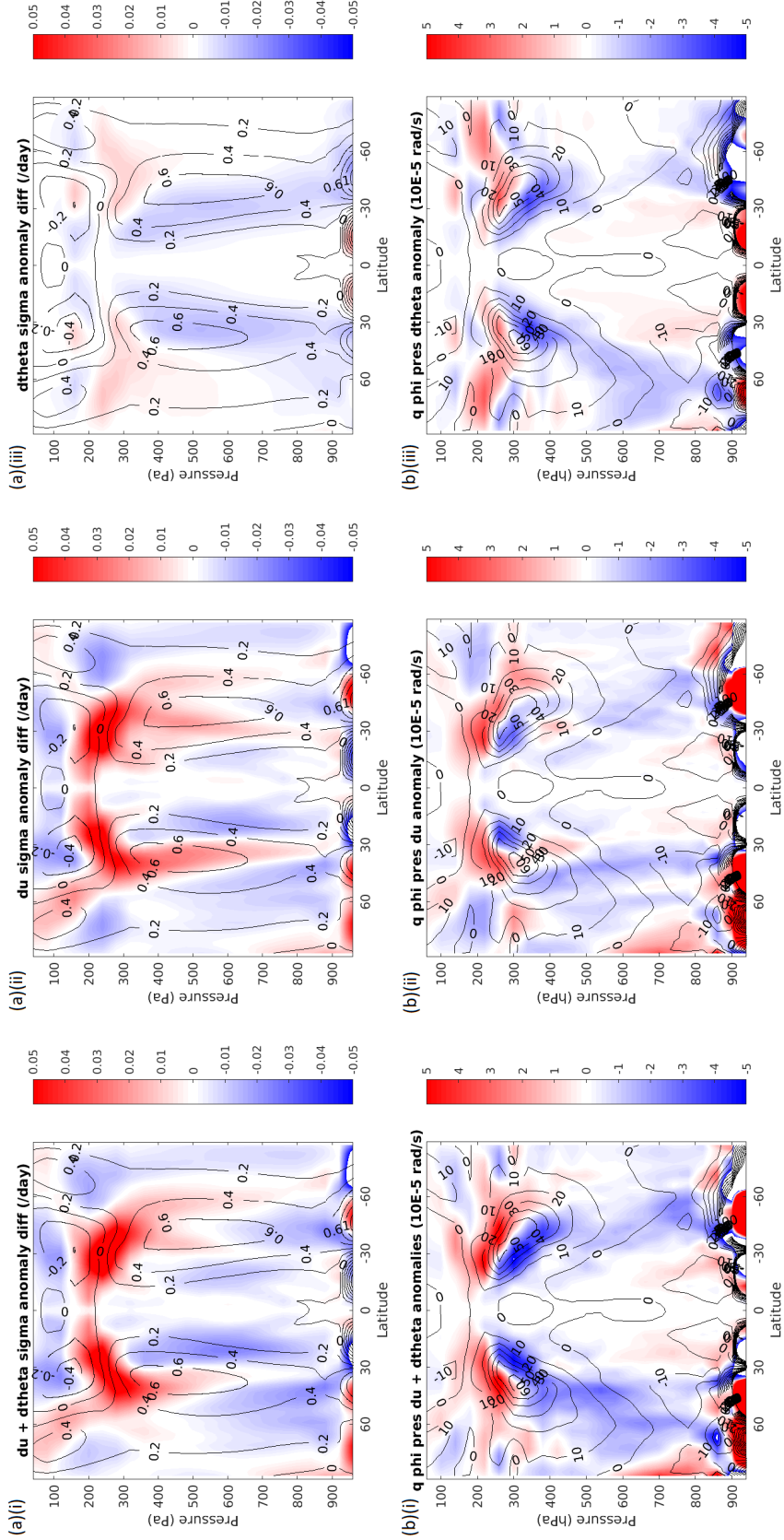


Figure 5.3.3: Control values (contours) and anomalies (colours) in (a) Eady growth rate, σ_B (top panel), and (b) 3rd meridional PV gradient component, $q_{\phi,p}$ (bottom panel), due to changes in: (i) both vertical potential temperature and zonal wind gradients, $\Delta \partial_p \theta$ and $\Delta \partial_p u$ (left panel), (ii) vertical zonal wind gradient only, $\Delta \partial_p u$ (middle panel), and (iii) vertical potential temperature gradient only, $\Delta \partial_p \theta$ (right panel), in response to SST perturbation experiment sst-qflux-U01 np, averaged over years 0-5.

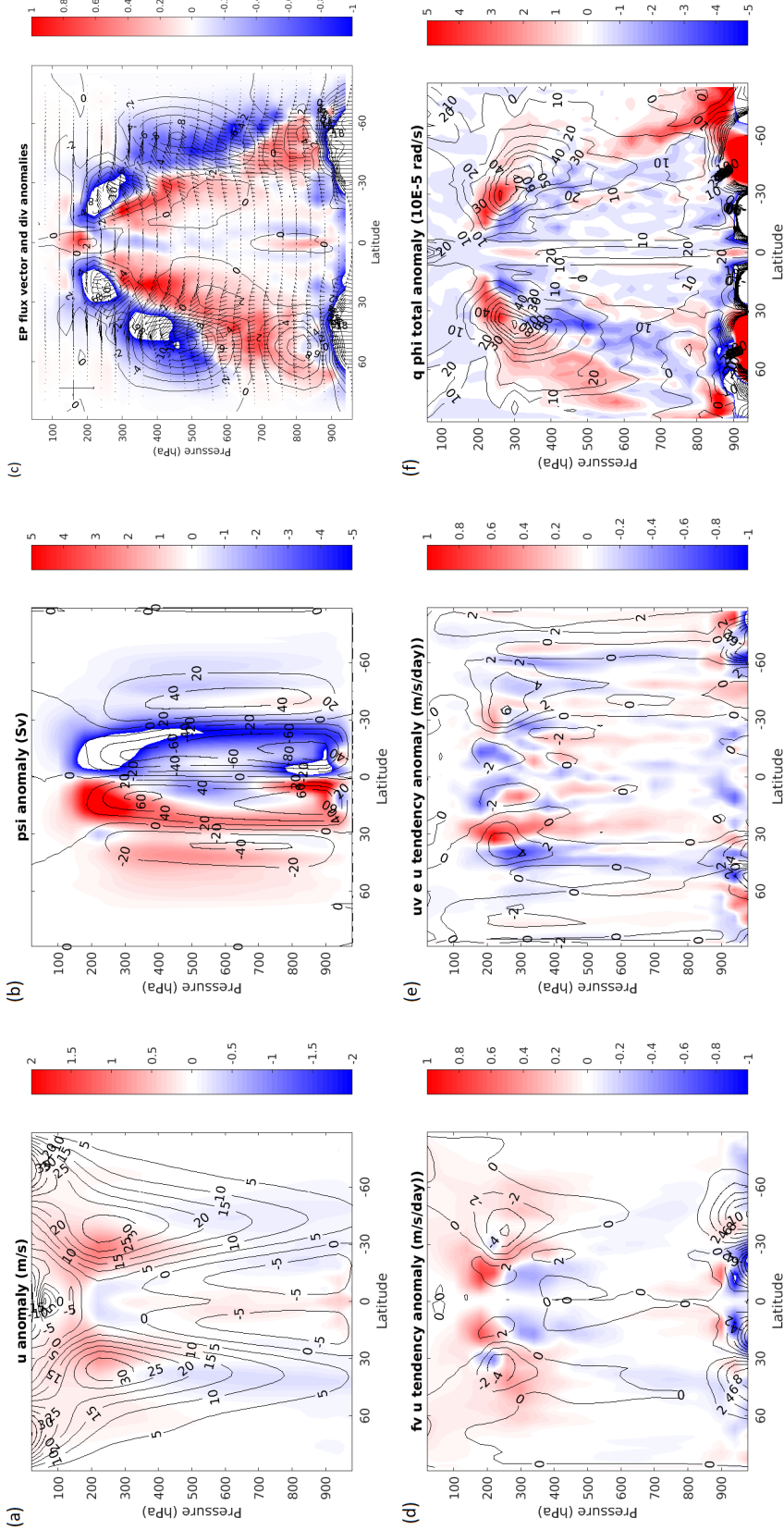


Figure 5.3.4: Control values (contours) and anomalies (colours) in: (a) zonal winds (top-left), (b) mass streamfunction (top-middle), (c) EP fluxes (arrows) and divergences (colours = anomalies; colours = control values) (top-right), (d) Coriolis acceleration, $f[v]$ (bottom-left), (e) acceleration by uv eddies, $-\frac{\partial[u^*v^*]}{\partial y}$ (bottom-middle), and (f) meridional PV gradient, q_ϕ (bottom-right), in response to SST perturbation experiment sst-qflux-U01 np, averaged over days 0-5. In the EP flux diagram, the fluxes are mass-weighted as per equations (2.1.32) and (2.1.33), the EP flux divergences are in units of 10^{15}m^3 , and the arrows are scaled such that the horizontal and vertical arrows in the top-left have lengths $5 \times 10^{13}\text{m}^3$ and $5 \times 10^{19}\text{m}^3\text{Pa}$ respectively.

flux convergence, with excess convergence/divergence in areas of anomalous negative/positive PV gradient. We therefore see how these initial changes in the zonal winds - forced by a much stronger tropical Hadley cell, extending into the midlatitudes - are able to force changes in the patterns of EP flux convergence, which will subsequently act to drive the observed midlatitude circulation and zonal wind changes we see in the fully equilibrated model response.

Taken all together, what appears to be happening is as follows: the low-latitude SST changes drive a strengthening and polewards-expansion of the tropical Hadley cells. This in turn drives an increased vertical zonal wind shear in the subtropics and midlatitudes, increasing the baroclinicity and meridional PV gradients. Via thermal wind, this must be accompanied by locally increased meridional temperature gradients, and is probably also paired with changes in the vertical temperature gradients, which act to reinforce the changes in subtropical meridional PV gradient. Such changes in turn drive changes in the poleward eddy fluxes of westerly momentum and heat in the extratropics, or equivalently changes in the EP fluxes, driving stronger Ferrel cells and eddy-driven midlatitude jets. Essentially, by driving stronger mean flows in the tropics, we increase the amount of available eddy potential energy, increasing the strength of the eddies which transport heat and momentum away from the tropics and into the extratropics, leading in turn to enhanced mean flows in the midlatitudes.

5.3.2 Heat budget

Using thermal wind arguments to go back to the changes in meridional temperature gradient as being the source of observed changes in zonal winds, several things appear to be driving said changes. First, the tropopause is moving slightly upwards, as indicated by the positive/negative temperature anomalies immediately below/above (bottom-left of figure 5.3.1). Paired with the fact that the height of the tropopause diminishes with latitude in the midlatitudes, this leads to the observed strengthened meridional temperature gradient around the midlatitude jet core, and hence a stronger and slightly upward-shifted core. Second, lower down into the troposphere, the tropics appear to heat up more than the midlatitudes, especially in the upper troposphere, above about 500hPa, also leading to a stronger meridional temperature gradient and hence stronger westerlies there. Third, within the tropics, the vertical temperature gradients - i.e. the lapse rates - weaken throughout troposphere, with warmer anomalies at higher altitudes, however there are significant meridional differences in the degree of weakening of the lapse rates we observe. Around the equator, the lapse rate appears to decrease more with height the higher up one gets, with stronger/weaker decreases in the regions of higher/lower underlying lapse rate, whilst around the subtropics the decrease in lapse rate appears fairly uniform with height, as are the control value lapse rates. This leads to the positive meridional temperature gradient we see within the tropical troposphere, and corresponding strengthening of the tropical easterlies. Indeed, this point about the meridional variation in lapse rates can also be used to explain the changes in meridional temperature gradients in the midlatitudes as, outside of the tropics, the lapse rate changes in a different way: it weakens in the lower troposphere, and strengthens

in the upper troposphere, with maximal temperature changes around the middle troposphere, between 700 to 500hPa. This, paired with the weakening of the lapse rate throughout most of the tropical troposphere, would lead to the strengthened meridional temperature gradient we see in the midlatitudes, and correspondingly strengthened zonal winds there. Another thing worth mentioning is the decrease in strength of the zonal winds in the high-latitude Southern Hemisphere, south of 60°, throughout the troposphere and stratosphere, which again, appears to be connected to local decreases in meridional temperature gradient.

Figure 5.3.5 displays the changes in potential temperature tendency, caused by changes in the different diabatic heating terms, as per the heat budget equation (2.1.9). Looking at the changes in total diabatic heating rate in the top-left panel, and comparing with the overall changes in temperature (bottom-left of figure 5.3.1), it appears to be the case that most of the changes in potential temperature - absolute and its gradients - in the troposphere are driven largely by changes in the diabatic heating rate. Indeed, around the equator we see anomalous heating which appears to get stronger higher up, whilst in the extratropics we see $-/+/-$ tripoles and $+/-$ dipoles. These changes in heating rate would reproduce the main observed changes in the vertical temperature gradient - i.e. lapse rate - in the troposphere. That said, cooling anomalies in certain regions of the troposphere suggest that there might be a degree of negative feedback occurring in certain regions, thus absolute causality is not clear.

Furthermore, when we look at the changes in the advective heating rate and its individual components, shown in figure 5.3.6, we see that in the stratosphere, and much of the extratropical upper troposphere, the changes in advective heating rate (top-left) appear to dominate, driven largely by changes in the TEM residual heating rate (top-middle), and also by changes in the heating by $[\omega^*\theta^*]$ eddies (bottom-middle) in the extratropical upper troposphere. When we look at the individual components of the overall diabatic heating rate anomalies, we see that the convective heating anomalies (top-middle) appear dominant throughout tropical troposphere, as expected, whilst the extratropical troposphere appears dominated by a combination of condensative (top-right) and radiative (bottom-left) heating anomalies, with each being more dominant in the lower and upper tropospheres respectively.

Figure 5.3.7 displays the changes in absolute potential temperature (left), and its total diabatic (middle) and convective (right) tendencies, during the first 15 days of the spinup. Already, the temperature signal in the tropical troposphere is resembling that of the equilibrated signal, with a temperature change that gets larger with height, and decreases/increases in the meridional temperature gradient in the equatorial/subtropical regions. It is also clear that the initial temperature increases we see throughout the tropical and lower extratropical troposphere are driven by diabatic heating anomalies, with the tropical temperature changes - absolute and gradient - being driven more-or-less exclusively by convective heating anomalies. This therefore confirms the centrality of the convective heating in driving the observed tropical tropospheric temperature changes, which are so important in forcing the observed zonal wind changes in the tropics and into the midlatitudes.

From a more theoretical perspective, we can understand the observed changes in convective

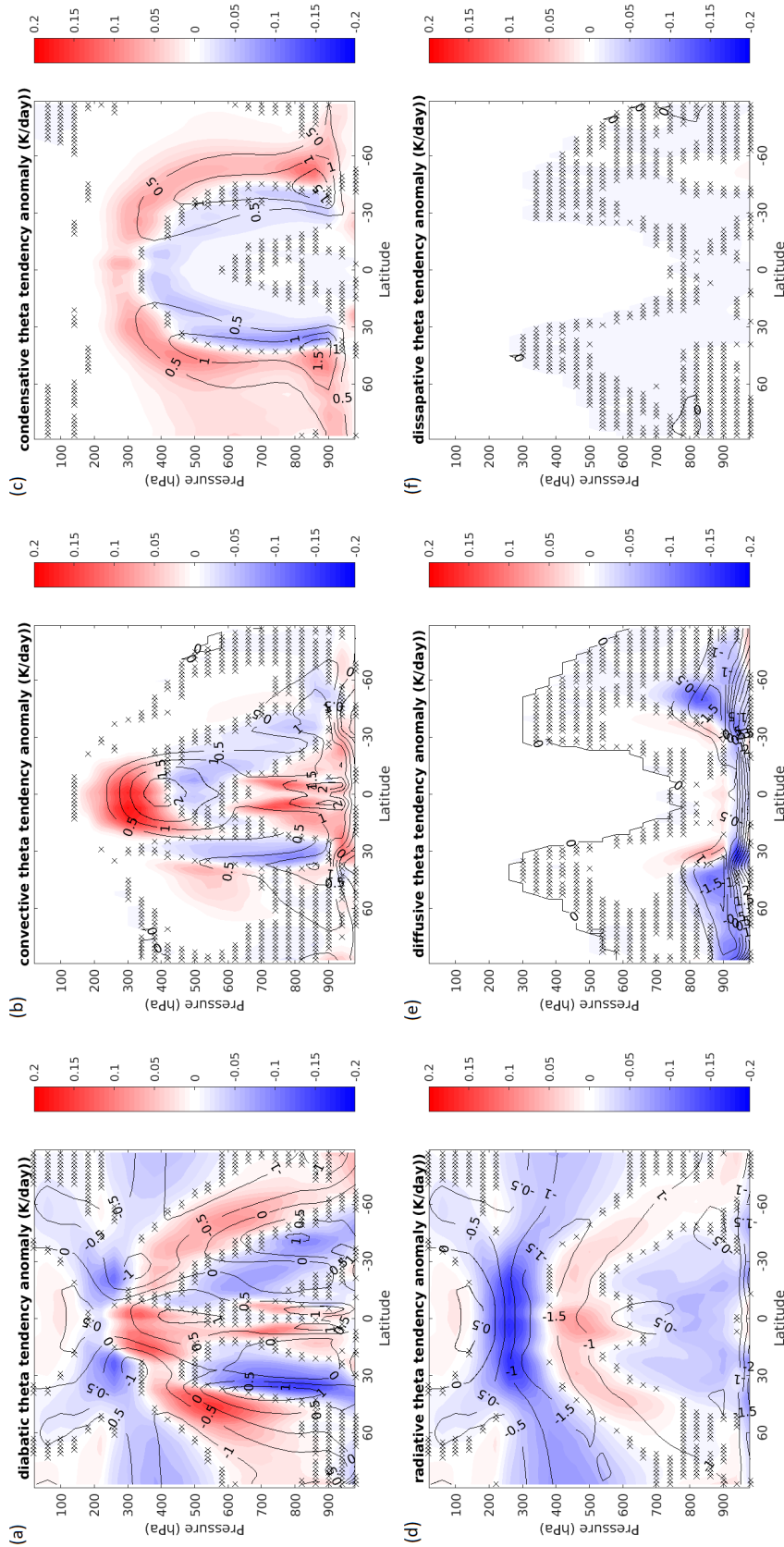


Figure 5.3.5: Control values (contours) and anomalies (colours) in diabatic potential temperature tendencies in response to SST perturbation experiment sst-qflux-U01 np, averaged over years 0-5, due to changes in: (a) all diabatic processes (top-left), (b) convection (top-middle), (c) condensation (top-right), (d) radiation (bottom-left), (e) diffusion (bottom-middle), and (f) dissipation (bottom-right). Hatching indicates regions in which the confidence levels in the experiment vs control values are below 95%, as measured by a two-tail student's t-test.

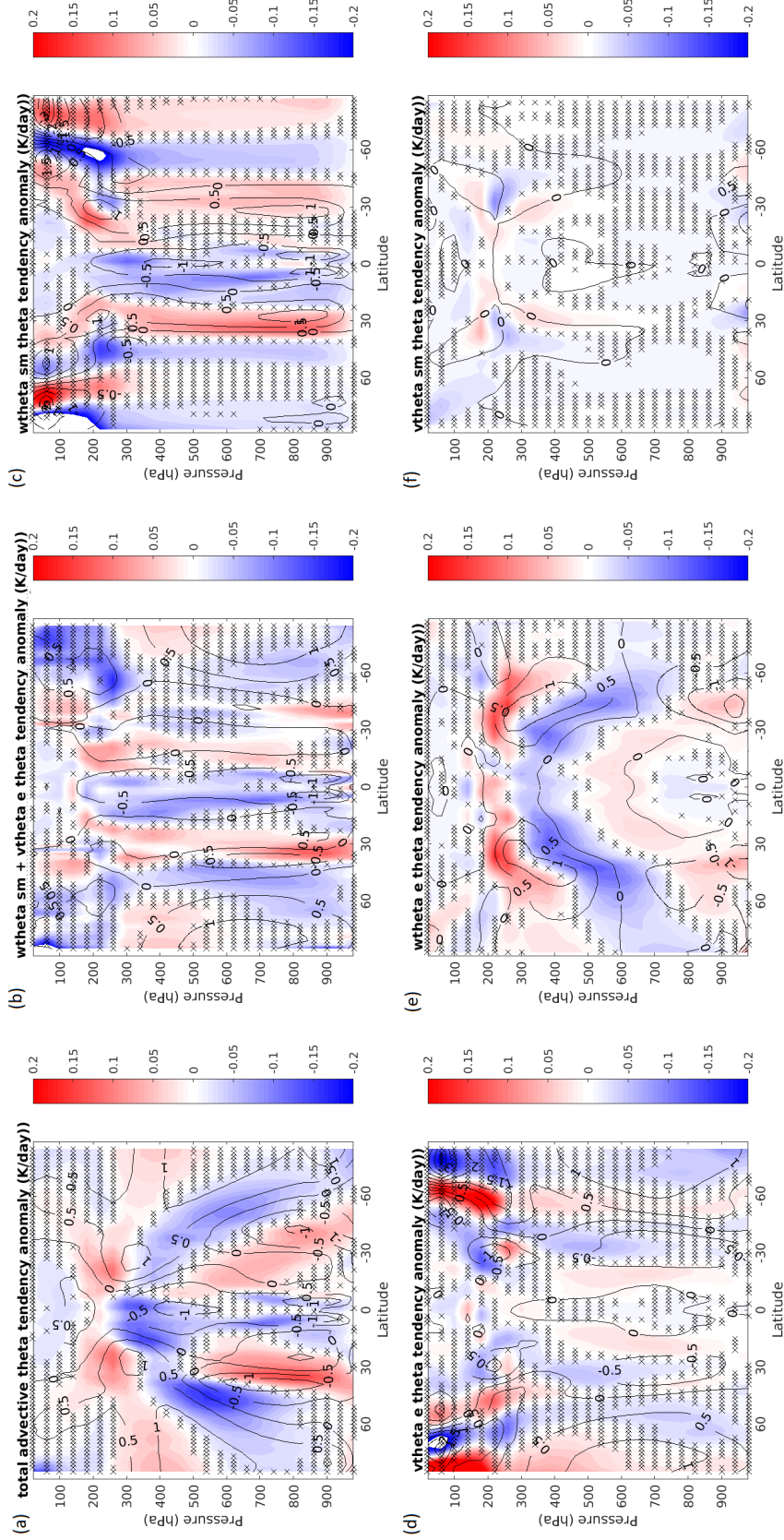


Figure 5.3.6: Control values (contours) and anomalies (colours) in advective potential temperature tendencies in response to SST perturbation experiment sst-qflux-U01 np, averaged over years 0-5, due to changes in heating by: (a) total advection (top-left), (b) TEM residual mean flow, $\tilde{\omega}[\theta]$, (top-middle), (c) vertical mean flow, $[\omega][\theta]$ (top-right), (d) meridional eddies, $[u^*v^*]$ (bottom-left), (e) vertical eddies, $[\omega^*\theta^*]$ (bottom-middle), and (f) meridional mean flow, $[v][\theta]$ (bottom-right). Hatching indicates regions in which the confidence levels in the experiment vs control values are below 95%, as measured by a two-tail student's t-test.

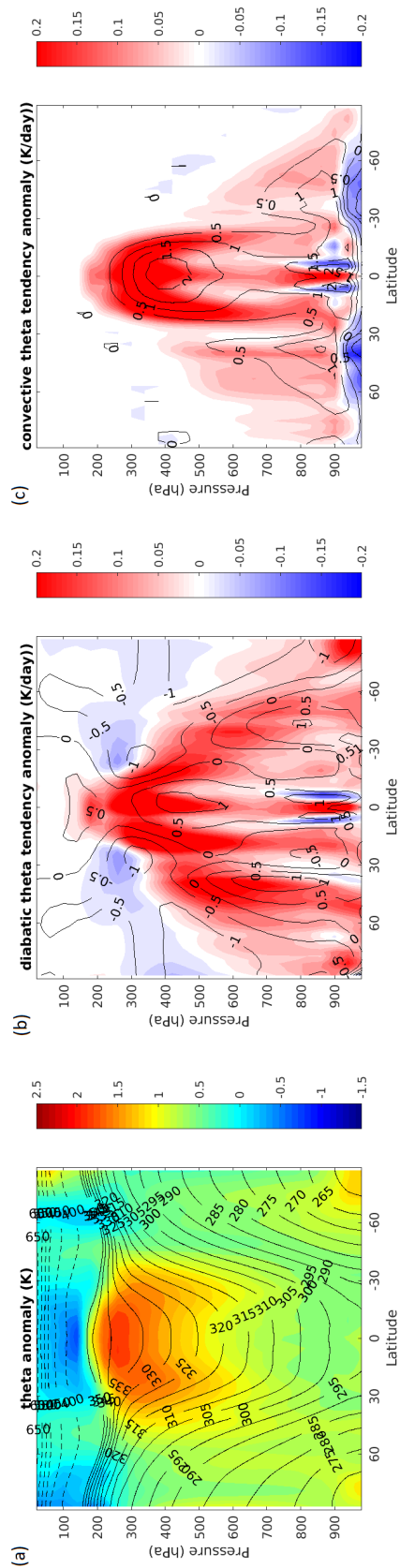


Figure 5.3.7: Control values (contours) and anomalies (colours) in (a) potential temperature (left), (b) diabatic potential temperature tendencies (middle), and (c) convective potential temperature tendencies (right), in response to SST perturbation experiment sst-qflux-U01 np, averaged over days 0–15.

heating, and therein changes in tropical temperature, by taking into account the Clausius-Clapeyron relation, equation (2.4.7). This equation implies an exponential growth in saturation vapour pressure with temperature, thus allowing warmer air to carry significantly more water vapour, and thereby making the tropics carry much more moisture than elsewhere in the atmosphere - see bottom-right panel of figure 5.3.1. Likewise, it also implies that, given a fixed increase in surface temperature, the warmer the underlying temperature field, the greater the amount of moisture it is going to liberate from the ocean. These factors explain why, given a fixed increase in sea surface temperature, the tropics experience a much stronger change in convective heating rates, due to the much larger changes in column-integrated moisture, triggering deep convection.

As for explaining the difference in convective heating and temperature gradient anomalies within the tropics, we note that, whilst the meridional humidity gradients between 0° and 10° are relatively flat, from 10° to around 25° they slope downwards significantly, making the subtropics extremely dry, as can be seen by the low relative humidities in that region - see bottom-middle panel of figure 5.3.1. Thus, whilst a similar amount of humidity might be initially injected throughout the tropics, only in the regions of high relative humidity - around the equator, and at low-levels in the subtropics - will that increase in humidity cause an excess of moisture that triggers deep convection. There will thus be more deep convection around the equator than the subtropics, causing a greater degree of vertical heat redistribution, with more heat accumulating at high-altitude and less at low-altitude, and with a sharper vertical temperature curvature, the temperature profile more closely following that of a moist adiabat.

Summary

- Changes in the zonal winds can be attributed to:
 - strengthening of the Hadley cells/tropical convective heating rate (0° to 40°);
 - strengthened EP fluxes/poleward eddy transport of heat and momentum (40° to 90°);
- The changes in tropical convective heating/Hadley circulation strength appear to emerge first, and appear key to driving the observed atmospheric changes, in both the tropics and extratropics.

5.4 P01-QFLUX SST experiment

Having examined and explained the changes in atmospheric zonal winds, circulations, and temperature arising from a perturbation to the tropical/uniform SST's, we will in this last subsection briefly examine the atmospheric changes we see in response to extratropical SST perturbations. As discussed in section 5.2, such SST anomalies tend to be of secondary influence compared to tropical SST anomalies of comparable amplitude. That said, in certain experiments in which the changes in tropical SST are much smaller/negligible compared to the changes in extratropical

SST, their atmospheric influence can be significant. This is the situation in experiment P01 in the slab-ocean setup.

The top panels of figure 5.4.1 shows the changes in zonal winds (top-left), mass streamfunction (top-middle), and temperature (top-right) we see in experiment sst-qflux-P01 np, in which an SST perturbation, corresponding to that seen in experiment P01 in the slab-ocean setup (top-middle of figure 5.2.1, green curve), is applied in the fixed-SST/atmosphere-only model setup. Again, we note the similarity with the middle panels of figure 5.1.1, affirming that it is the changes in SST which are forcing the differences in atmospheric response between the slab-ocean and atmosphere-only setup for this experiment. We also note the contrast with the results of the $+1^{\circ}\text{C}$ uniform SST perturbation experiment, shown in the top panels of figure 5.2.3, with the atmospheric changes being almost the exact opposite, similar to the -1°C uniform SST perturbation experiment, shown in the bottom panels. At the same time, we know that the tropical/uniform SST perturbation in experiment sst-qflux-P01 np is positive. Thus - because we know from section 5.2 that a uniform SST perturbation yields similar results qualitatively to a same-sign tropical SST perturbation - we know that the atmospheric changes we see in response to this SST perturbation cannot result from the tropical SST changes, and must therefore result from perturbations to the extratropical SST.

Also, if we compare the changes in zonal winds and temperature, we see that the regions of westerly acceleration/deceleration correspond to regions of local increase/decrease in the meridional temperature gradient, in agreement with equation (2.1.11). The bottom-right panel of figure 5.4.1 shows the anomalous diabatic heating rate. Decomposition of these heating rate anomalies yields the same results as in section 5.3.2, with the anomalies driven in the tropical troposphere by changes in the convective heating rate, and in the extratropics by changes in the condensative/radiative heating rate in the lower/upper troposphere. We also note the correspondence between the warm anomalies in the midlatitude troposphere, and similar warm anomalies in both the midlatitude diabatic heating rate, and in the SST perturbation pattern (top-middle panel of figure 5.2.1). This is all therefore strongly suggestive of the increases in midlatitude SST forcing the observed warm anomalies we see in the troposphere in that region, through changes in the diabatic heating rate.

Figure 5.4.2 shows the changes in EP fluxes and divergences (top-left), meridional PV gradient (bottom-left), and their individual components (top-/bottom-middle and right), as per equations (2.1.22)-(2.1.24) and (2.1.28). As in section 5.3, we note a strong correspondence between regions of anomalous EP flux convergence/divergence and regions of anomalous positive/negative meridional PV gradient. We also see how the anomalous meridional EP flux divergence pattern (top-middle) is reflective of the pattern of anomalous zonal winds, wind westerly acceleration/deceleration in regions of anomalous divergence/convergence. This is reflected in the vertical EP fluxes and their divergence patterns (top-right) too, with anomalous upward/downward fluxes in regions of horizontal divergence/convergence.

All-in-all, the extratropical zonal wind anomalies we see appear to be powered by the changes in EP fluxes and their divergences, with anomalous upward fluxes poleward of around 50° , which

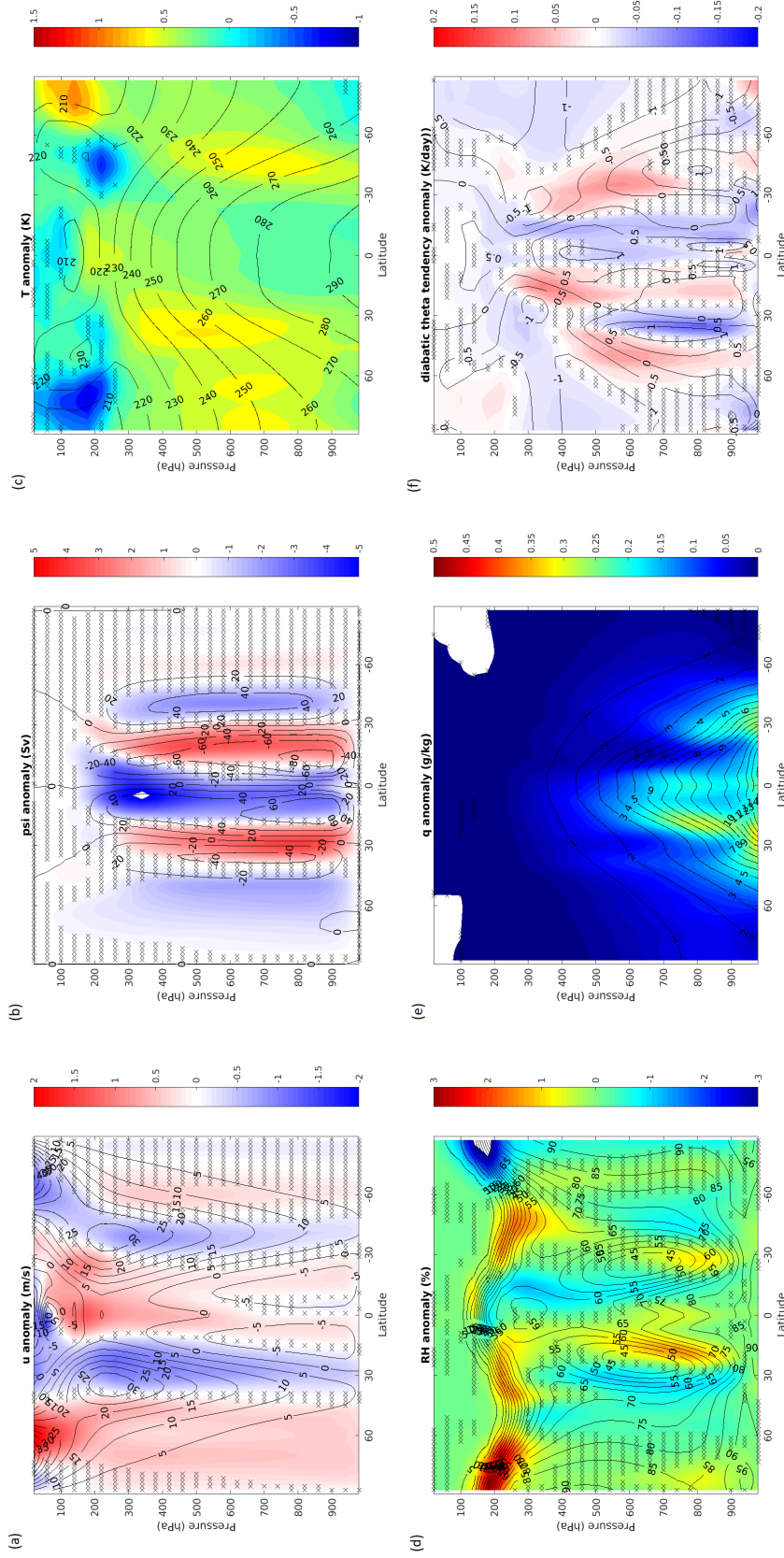


Figure 5.4.1: Control values (contours) and anomalies (colours) in various climatological fields in response to SST perturbation experiment sst-qflux-P01 np, averaged over years 0-5: (a) zonal wind (top-left), (b) Eulerian streamfunction (top-middle), (c) temperature (top-right), (d) relative humidity (bottom-left), (e) absolute humidity (bottom-middle), and (f) diabatic potential temperature tendency (bottom-right). Hatching indicates regions in which the confidence levels in the experiment vs control values are below 95%, as measured by a two-tail student's t-test.

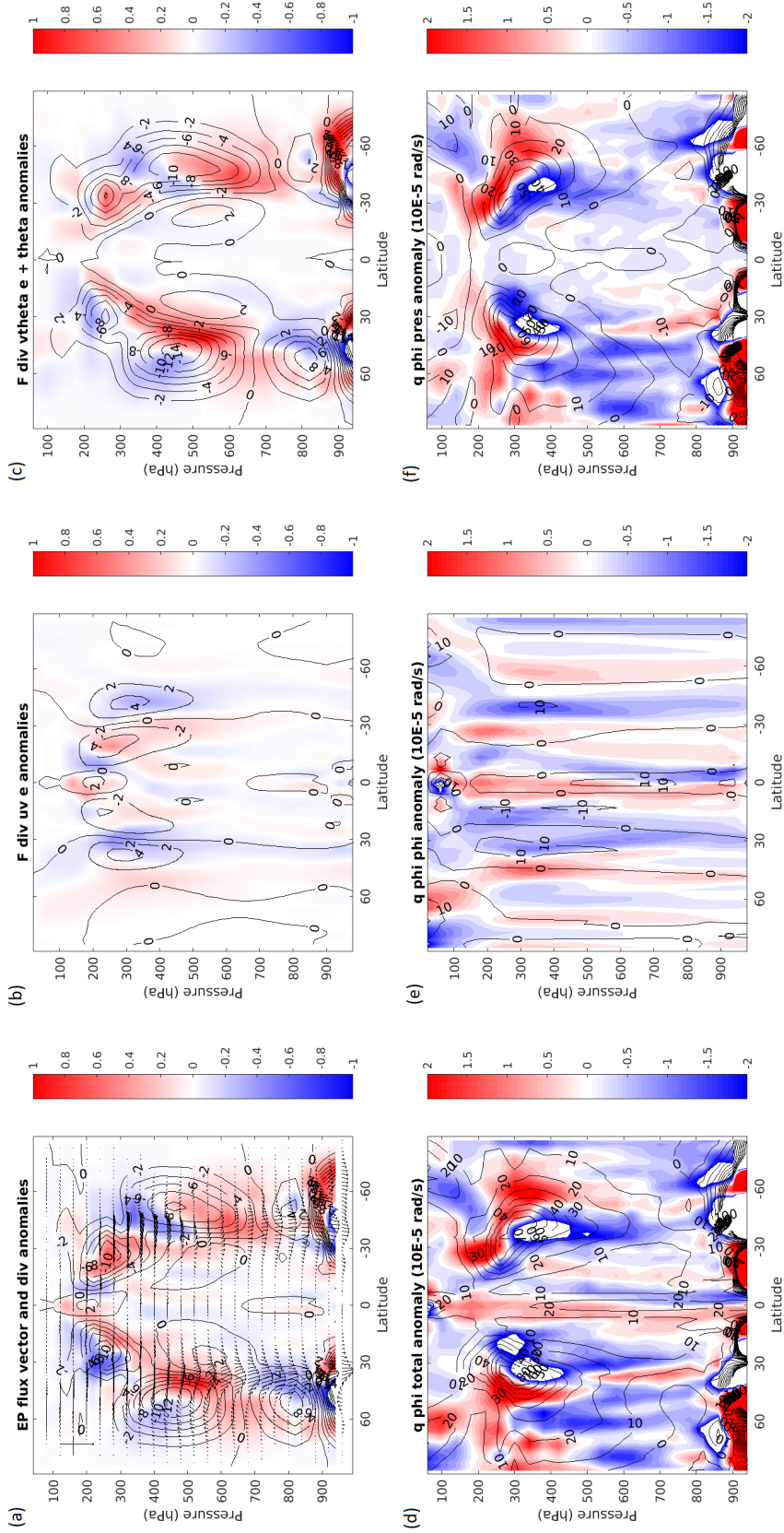


Figure 5.4.2: Control values (contours) and anomalies (colours) in: (a) EP flux divergence, $\nabla \cdot \mathbf{F}$, including anomalous EP fluxes (arrows) (top-left), (b) meridional EP flux gradient, $\frac{\partial F_y}{\partial y}$ (top-middle), (c) vertical EP flux gradient, $\frac{\partial F^p}{\partial p}$ (top-right), (d) meridional PV gradient, q_ϕ (bottom-left), (e) meridional PV gradient 2nd component in equation (2.1.28), $q_{\phi,y}$ (bottom-middle), and (f) (e) meridional PV gradient 3rd component in equation (2.1.28), $q_{\phi,p}$ (bottom-right), in response to SST perturbation experiment sst-qflux-P01 up, averaged over years 0-5. In the EP flux diagram, the fluxes are mass-weighted as per equations (2.1.32) and (2.1.33), the EP flux divergences are in units of 10^{15}m^3 , and the arrows are scaled such that the horizontal and vertical arrows in the top-left have lengths $5 \times 10^{13} \text{m}^3$ and $5 \times 10^{19} \text{m}^3 \text{Pa}$ respectively.

converge around the upper troposphere, move equatorward to around 30° , and then downward. These changes in EP flux propagation are very similar to those outlined in section 5.3.1, except that they are polewards-shifted, hence the difference in pattern of zonal wind anomalies. The same can be said for the anomalous PV meridional gradients, with the pattern generally being shifted downward and poleward, causing the positive anomalies seen in the upper subtropical troposphere in experiment sst-qflux-U01 np to migrate into the midlatitudes.

Figure 5.4.3, which shows the changes in total (left panels) Eady growth rate (top panels) and 3rd meridional PV gradient component (bottom panels), and their individual contributions (middle/right panels), echoes this poleward-shifted pattern (compare with figure 5.3.3). Crucially, whereas in experiment sst-qflux-U01 np we saw increases in subtropical tropospheric baroclinicity, and decreases poleward, both driven primarily by changes in the zonal wind shear, here we see more-or-less the opposite picture here, with reductions in the subtropics and increases in the midlatitudes, also largely driven by the zonal wind shear changes (middle panels). Such changes in baroclinicity would cause - as the 3rd meridional PV gradient component is proportional to the vertical gradient of baroclinicity (compare RHS of equation (2.1.18) and 3rd component on RHS of equation (2.1.28)) - the observed changes in meridional PV gradient, with reductions/increases in the upper subtropical/midlatitude troposphere, where we see a more negative/positive vertical baroclinicity gradient.

What therefore appears to be happening in this experiment is as follows. The extratropical SST changes cause corresponding changes in the atmospheric temperature field via diabatic heating, with maximal heating in the midlatitudes, around the peaks in the applied SST perturbation. This causes a reduction/enhancement in meridional temperature gradient in the subtropics-to-low midlatitudes/high midlatitudes-to-poles. This is necessarily accompanied by decreases/increases in baroclinicity in these regions, as per equation (2.1.11), and also causes a dipole anomaly in meridional PV gradient to emerge in the upper troposphere, with negative/positive anomalies in the subtropics/midlatitudes. These changes in meridional PV and temperature gradient cause changes in the patterns of EP flux propagation and divergence/convergence, with anomalous downward/upward fluxes in the subtropics-to-low midlatitudes/high midlatitudes-to-poles, and anomalous equatorward fluxes in the upper midlatitude troposphere. This corresponds to a poleward-shift in their patterns of propagation, and therefore causing a similar poleward-shift in the extratropical zonal winds and circulations, with reductions in the low-latitudes, and enhancements in the high-latitudes, as the eddy heat and momentum fluxes shift polewards.

This mechanism is quite similar to that outlined in section 5.3, except that: (i) the changes in baroclinicity are directly responding to changes in SST-induced meridional temperature gradient, and not those induced by a strengthened/weakened Hadley cell, and (ii) the extratropical changes are poleward-shifted, owing to the poleward-shift in the region of increased meridional temperature gradient, from the subtropics, into the high midlatitudes. Moreover, the shift in the extratropical zonal winds, storm tracks (through vertical EP fluxes), and circulations away from/towards the regions of decreased/increased SST meridional gradient and baroclinic-

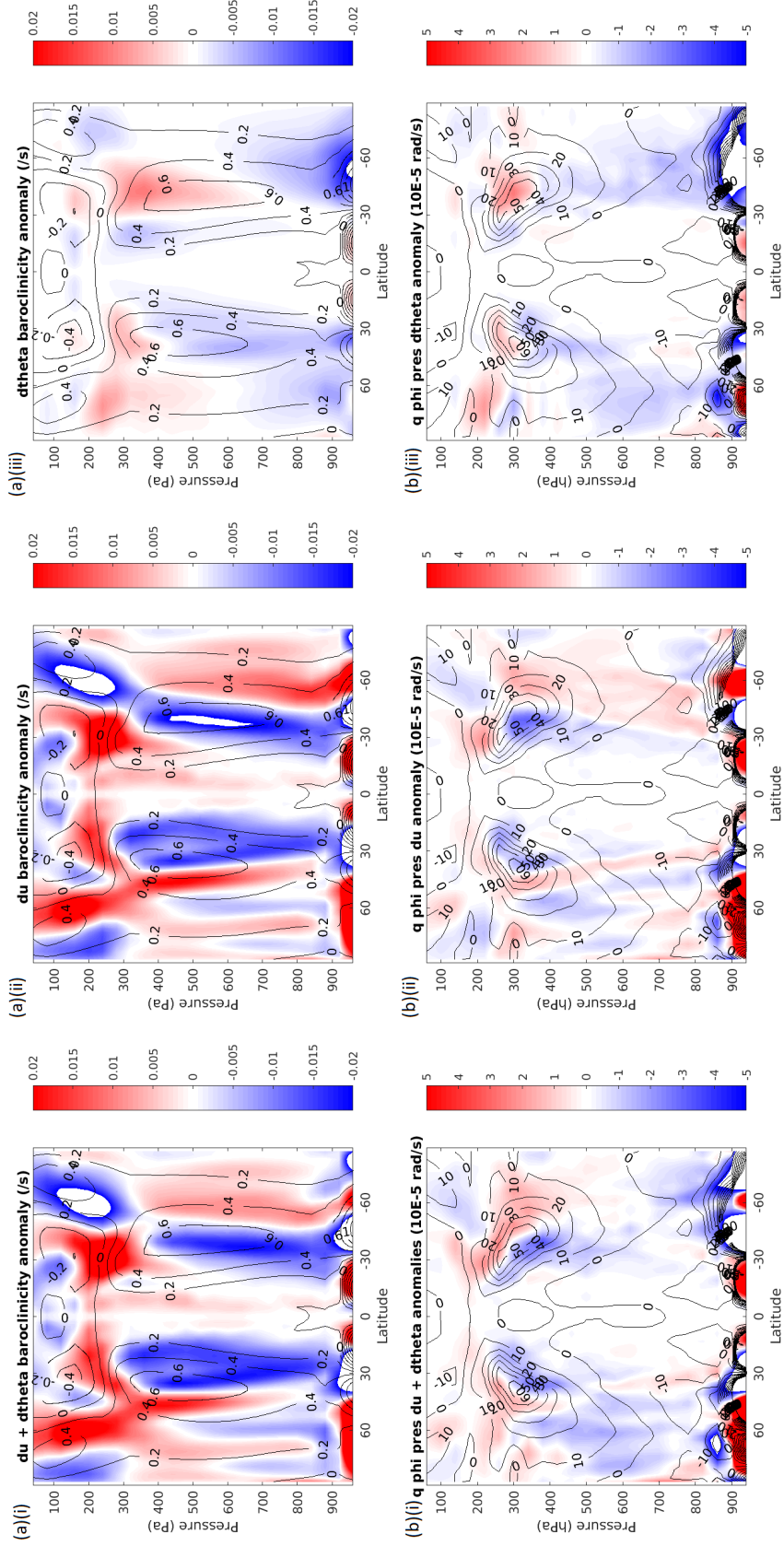


Figure 5.4.3: Control values (contours) and anomalies (colours) in (a) Eady growth rate, σ_B (top panel), and (b) 3rd meridional PV gradient component, $q_{\phi,p}$ (bottom panel), due to changes in: (i) both vertical potential temperature and zonal wind gradients, $\Delta\partial_p\theta$ and $\Delta\partial_p u$ (left panel), (ii) vertical zonal wind gradient only, $\Delta\partial_p u$ (middle panel), and (iii) vertical potential temperature gradient only, $\Delta\partial_p\theta$ (right panel), in response to SST perturbation experiment sst-qflux-P01 np, averaged over years 0-5.

ity makes the mechanism more-or-less identical to that of Brayshaw et al. (2008) and Chen et al. (2010).

We can perhaps also understand the slight poleward-expansion of the NH Hadley cell (see top-middle of figure 5.4.1) as a consequence of this reduction in subtropical baroclinicity, allowing for a polewards-shift in the Hadley cell critical latitude. This is however only seen in the NH, probably a consequence of the somewhat sharper subtropical SST gradient perturbations applied to that hemisphere (see top-middle panel of figure 5.2.1).

5.5 Chapter Conclusions

To draw this chapter to an end, we will now summarise its main conclusions. It was found in section 5.1 that the main effects of having a double-drake ocean present when STP's are applied were, in general terms, either: for experiments P01 and T01, to initially weaken, over the first ~ 50 years, the underlying atmospheric changes in the low-latitudes (P01 + T01, cpl + qflux y0-50), and, over the subsequent ~ 100 s years, to strengthen and shift the midlatitude anomalies poleward, whilst also weakening the high-latitude anomalies (P01 + T01 cpl y250-300). Or, for experiment U01, to cause a strengthening and polewards expansion of the extratropical atmospheric changes over ~ 10 s years, which subsequently gets stronger over ~ 100 s years (U01 qflux + cpl), whilst the tropical signal initially gets weaker (U01 qflux + cpl y0-50), and subsequently stronger (U01 cpl y250-300). Moreover, the fully-coupled and slab-ocean setups were found not to give significantly different results in their impact upon the atmospheric response to stratospheric forcing in the short-term (qflux + cpl y0-50), and with only experiment U01 showing significant modifications to the atmospheric response at all latitudes in that time-frame. Longer-term, over ~ 100 s years, the fully-coupled setup was found to provide a significantly different and stronger feedback onto the underlying atmospheric responses (cpl y250-300).

Experiments with various different SST perturbations in section 5.2 found the primary driving factor behind the majority of these modifications to atmospheric response to be changes in the tropical SST. Changes in extratropical SST were found to either have a secondary impact, or to be significant only when the changes in tropical SST were very small in comparison (e.g. P01 qflux y0-50). Moreover, the atmospheric changes produced by changes in tropical or extratropical SST were found all to be similar to those produced by either uniform increases or decreases in SST. Further investigation into the atmospheric response to a near-uniform SST increase sst-qflux-U01 np in section 5.3 found that it was driven primarily by increased convective heating in the tropics, leading to an enhancement of Hadley circulation strength and extent, and increased vertical wind shear/meridional temperature gradient in the subtropics and into the midlatitudes. Such changes would - through their effects on meridional PV and temperature gradients - force changes in extratropical eddy-activity, enhancing the poleward eddy transport of heat and westerly momentum, and thereby strengthening the eddy-driven midlatitude jets and circulations. Figure 5.5.1 shows this mechanism schematically. The emergence of a dipole

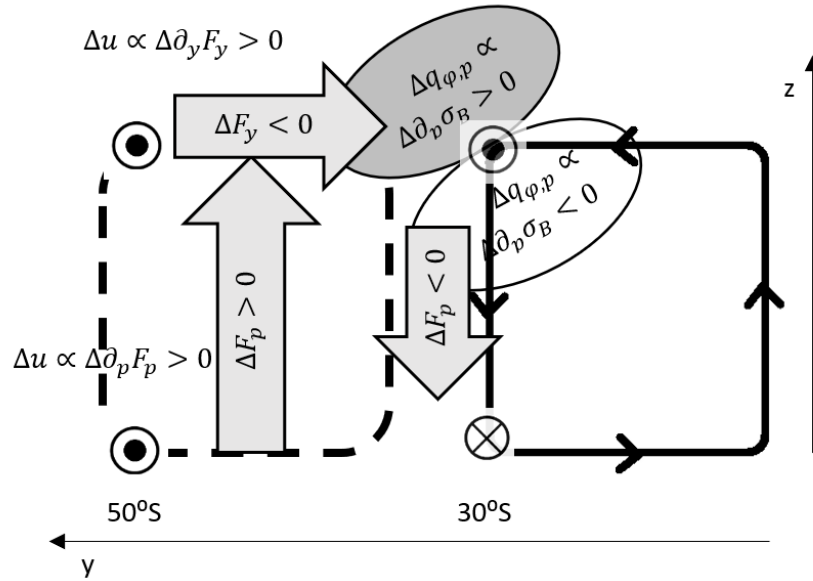


Figure 5.5.1: Schematic showing mechanism whereby a strengthened and expanded Hadley cell (solid black rectangle) leads to an increase in subtropical baroclinicity, with westerly/easterly acceleration (dotted/crossed circles) in the upper/lower subtropical troposphere. This causes a dipole anomaly in the third meridional PV gradient component - $q_{\varphi,p}$ in equation (2.1.28) - above/below the region of maximum baroclinicity increase (grey/white ovals), which acts as a waveguide, causing anomalous upward and equatorward EP fluxes in the midlatitudes, as well as anomalous downward EP fluxes in the subtropics (arrows), as the waves move towards/away from regions of increased/decreased meridional PV gradient. This induces a strengthening of the midlatitude zonal winds and circulation, with westerly zonal wind acceleration throughout the midlatitude troposphere, and a strengthened Ferrel cell (dashed black rectangle). Please note that the exact positions of the anomalous EP flux arrows and meridional PV gradient anomalies are not to be taken as precise, and are intended more for illustrative purposes. Mechanism is depicted for the Southern Hemisphere, with approximate latitudes of the zonal wind anomalies indicated along the (horizontal) latitude axis.

anomaly in meridional PV gradient around the region of maximum baroclinicity increase is supported by both the equilibrium and transient model response to an abrupt SST increase, detailed in section 5.3 (see figures 5.3.2-5.3.4). This mechanism is highly similar to that proposed by Hou (1998), and agrees with previous studies looking at both the effect of tropical diabatic heating on the Hadley circulation itself (Held & Hou 1980; Held 2000; Frierson 2007), and its downstream impact on the strength and latitude of midlatitude jets, circulations and storm tracks (Kang & Polvani 2011; Ceppi & Hartmann 2013; Mbengue & Schneider 2018).

Investigation into the atmospheric changes seen in response to changes in midlatitude SST in section 5.4 revealed that a similar mechanism was at work there, except that the changes in meridional temperature and PV gradients and baroclinicity appeared to be more of a direct response to SST-induced midlatitude temperature anomalies. The extratropical circulations, storm tracks and jets would respond by moving away from/towards the region of decreased/increased meridional SST gradient and baroclinicity, similar to Brayshaw et al. (2008) and Chen et al. (2010).

Furthermore, if we return to the results of the STP experiments in the atmosphere-only setup in chapter 3, displayed in figure 3.1.1, and compare with the results of a uniform SST increase/decreases, shown in figure 5.2.3, analogies can be drawn between the two sets of experiments. Essentially, the atmospheric response to experiments U01 and P01 is qualitatively similar to that of a uniform SST increase, and that of experiment T01 to a uniform SST decrease, save for some latitudinal shifts. The strengthened/weakened Hadley cell and tropical easterlies extend up to 40° in the uniform SST experiments vs up to 20° - 30° in the associated S-T coupling experiment(s). Also, the strengthened/weakened Ferrel cells and midlatitude westerlies extend up to 60° in the uniform SST experiments vs up to 40° - 50° in the associated S-T coupling experiment(s). Thus, we may say that the atmospheric response to a uniform increase/decrease in SST is qualitatively similar to that of a uniform or polar/tropical STP, but polewards shifted by about $+10^\circ$ to $+20^\circ$. The reason for this similarity is that, fundamentally, both couplings lead - through mechanisms outlined in figures 3.4.1 and 5.5.1 - to the same type of atmospheric response, especially in the midlatitudes. However, whereas the stratosphere-troposphere coupling operates by directly modifying the extratropical PV gradients and EP flux patterns, and has - through its inability to affect a change in tropical temperatures and static stability - limited impact on the tropical circulations, the atmosphere-ocean coupling operates by altering the tropical static energy content, causing considerable changes in the strength and extent of the Hadley cells, which then leads to downstream impacts upon the extratropical mean flows. It is therefore the ability to modify tropical temperatures and static energy, via changes in tropical SST, that fundamentally differentiates the fully-coupled stratosphere-troposphere-ocean response from the fixed-SST, stratosphere-troposphere response.

Given this, and what we know of the SST changes seen in the different coupled experiments and their time-evolution, discussed in chapter 4, we can explain the impact upon the different S-T coupling experiments as follows. Initially (~ 10 s years), experiments P01 and T01 both see fairly insignificant rises in tropical SST in both fully-coupled and slab-ocean setups, leading

to fairly insignificant modifications of atmospheric response. The response that we do see is a slight reduction in atmospheric signal at low-latitudes, as extratropical SST changes cause modifications to local baroclinicity, causing changes in strength and position of the eddy-driven jet and Ferrel cell. Later on (~ 100 s years), both see significant increases/decreases in tropical SST in the fully-coupled setup, leading to an enhancement and poleward expansion of the underlying atmospheric response. Experiment U01 sees significant rises in tropical SST across the coupled setups and timescales, leading to an enhancement and poleward expansion of the underlying atmospheric response across the different coupled setups and timescales.

Chapter 6

Conclusions & Future Work

In this last chapter, we will summarise the main results from chapters 3-5, and put them together to form an overall picture of stratosphere-troposphere-ocean coupling, as it pertains to our modeling experiments. We will then - returning to the bigger picture - place them in the context of the broader body of literature, as reviewed in chapter 1, discuss their implications within this context, and any future work which might be done to build upon or generalise the results.

6.1 Summary & Conclusions

In chapter 3, the results of STP experiments - as outlined in section 2.7 - in the atmosphere-only model configuration were discussed. It was found that the P01/T01 experiments caused the following changes:

- Polar vortices weakened/strengthened;
- Hadley cells and tropical easterlies strengthened/weakened;
- Ferrel cells and midlatitude jets strengthened/weakened and contracted/expanded equatorwards/polewards;
- Poleward eddy heat fluxes - and associated EP fluxes, divergences and TEM circulation patterns - in the mid-to-high latitudes weakened/strengthened.

Experiment U01 was found to produce a response akin to a weakened version of P01, similar to P01 (strong) + T01 (weak). These results were in good qualitative agreement with those of previous studies with simplified GCM's, such as Haigh et al. (2005) and Garfinkel et al. (2013), and also quantitative agreement with the observed and modelled SH DJF response to ozone depletion/recovery (Polvani et al. 2011; Son et al. 2010, 2018), with experiments T01/P01 resembling the atmospheric response to ozone depletion/recovery. Moreover - via such quantities

as the EP flux divergence and meridional PV gradient - changes in the mean flows, and changes in the poleward eddy fluxes of heat and westerly momentum, were found to be inextricably linked together. The trigger for these changes was then found to be provided by the direct impact of the STP's on vertical zonal wind and temperature gradients, at the latitude of their application, around the tropopause, in a mechanism akin to that described by figure 1.1.4. These then propagate downwards throughout the troposphere, via feedbacks between changes in the vertical zonal wind shear, and changes in the EP fluxes, with the link between the two being provided by changes in the meridional PV gradient - see section 3.4 and figure 3.4.1 for more details. This is a similar mechanism to that detailed in Simpson et al. (2009), and the details of its operation in experiment P01 were found to be highly similar to that detailed in White et al. (2020). All this served to underscore the generic nature of this type of stratosphere-troposphere coupling, with no apparent dependence upon e.g. topography, land-sea contrasts, and physical parameterisations.

Chapter 4 looked at the SST changes seen in response to the STP experiments, in both the slab-ocean and fully-coupled model setups, and their drivers. In the global-average picture, both models appeared to respond similarly, albeit at different timescales, with initial (first ~3/11-15 years) SST changes driven by anomalous latent heat fluxes, and subsequent changes driven by anomalous downward LW radiative fluxes. Latitudinally, however, there was variation, with extratropical SST anomalies in the slab-ocean setup being chiefly driven by anomalous turbulent heat fluxes, whilst in the fully-coupled setup, such anomalies were mainly driven by anomalous ocean heat advection. Both were ultimately driven by changes in surface zonal wind, but whilst the surface heat fluxes were sensitive to changes in absolute surface zonal wind, the ocean heat transport was sensitive to changes in the meridional gradient of surface zonal wind which, minus boundary terms, is equivalent to the surface wind stress curl when zonally-averaging. Overall, this led to deviations in the extratropical SST anomalies between the setups, with the fully-coupled SST anomalies being generally more zonally-uniform - and thereby larger when zonally-averaged - and poleward-displaced, relative to those seen in the slab-ocean setup. Furthermore, the changes in ocean heat transport also caused a general increased/decreased depth of the tropical thermocline in experiment P01/T01, allowing the tropical SST's to warm/cool significantly in the fully-coupled setup, compared to the slab-ocean setup.

Chapter 5 then looked at the impact of these changes in SST upon the atmospheric response to the applied STP's. It found the main changes in atmospheric state to be a strengthening and poleward expansion/shift of the underlying atmospheric response, at both short (~10s years) and long (~100s years) timescales for experiment U01, and at long timescales ($\gtrsim 100$ years) for experiments P01/T01. These changes were found to be driven primarily by changes in tropical SST, with increases/decreases leading to a strengthening/weakening and poleward expansion/contraction of the Hadley cells and tropical easterlies, with corresponding downstream impacts upon the Ferrel cells, midlatitude jets, and storm tracks - see section 5.5 and figure 5.5.1 for more details. These results on the atmospheric impact of alterations in tropical SST

were in good qualitative with the results of previous studies, including both the impact on the Hadley circulation (Held & Hou 1980; Held 2000; Ferreira 2007), and the downstream impact on the extratropical mean fields and storm tracks (Hou 1998; Kang & Polvani 2011; Ceppi & Hartmann 2013; Mbengue & Schneider 2018). This type of response was also highly similar to that of experiments P01/T01, but poleward-shifted, explaining the apparent strengthening and poleward-shifting of the underlying atmospheric responses in the fully-coupled runs of those experiments. This was fundamentally attributed to the modification of tropical SST's, allowing for much greater changes in the Hadley cell strength and extent, which would otherwise not be possible in an atmosphere-only setup. A less significant, initial weakening (~ 10 s years) of the atmospheric response in the low-midlatitudes was also seen with experiments P01/T01, in both slab-ocean and fully-coupled setups. As the tropical SST anomalies were fairly small ($\lesssim 0.1^\circ\text{C}$) in these instances, they were most likely the result of local decreases/increases in the meridional SST gradient around the midlatitude jet axis, themselves induced by anomalous turbulent heat exchange as a result of a strengthened/weakened midlatitude jet. These would cause corresponding changes in the atmospheric temperature field via diabatic heating anomalies, causing alterations to the tropospheric baroclinicity, with general reductions/increases in the regions of underlying westerly acceleration/deceleration. This would thereby trigger changes in the meridional PV gradient and EP fluxes, driving a generally negative feedback on the zonal winds and circulations.

Figure 6.1.1 displays schematics illustrating the different ways in which the slab-ocean (left) and fully-coupled (right) ocean models react to atmospheric changes induced by experiment P01; identical schematics could also apply to experiment T01 in both setups, but with the signs of all changes inverted. In the slab-ocean setup (left diagram), the extratropical SST is essentially controlled by changes in sensible heat flux, with regions of enhanced/reduced surface westerlies (+/-) experiencing a net increase/decrease in downward sensible heat flux (downward/upward red arrows), and thereby causing local SST increases/decreases. In the fully-coupled setup (right diagram), as per equations (2.2.3) and (2.2.4), the Ekman meridional and vertical velocities are controlled by the absolute values and meridional gradients of surface zonal wind stress respectively. As such, we get local equatorward/poleward surface currents around a westerly/easterly surface wind anomaly, as well as upwelling/downwelling currents on its poleward flank, and the opposite on its equatorial flank. This leads to the Ekman circulation patterns shown in the right panel of figure 6.1.1, within the top ocean layers. Downwelling/upwelling currents in the low-latitudes ($\sim 15^\circ$ to 40°) in experiments U01 and P01/T01 cause the tropical thermocline to get deeper/shallower, allowing surface temperatures to rise/fall farther than in the slab-ocean setup. Upwelling/downwelling currents in the midlatitudes cause a shallower/deeper thermocline, and the reverse in the polar latitudes. However, because of the different oceanic vertical temperature structures there - with cold surface temperatures and warmer sub-surface waters which get warmer with increasing depth - these anomalous vertical currents have the reverse effect to in the low-latitudes, causing anomalous heating/cooling in the midlatitudes, and the reverse in the polar latitudes. At the surface, anomalous heating/cooling in the tropics is me-

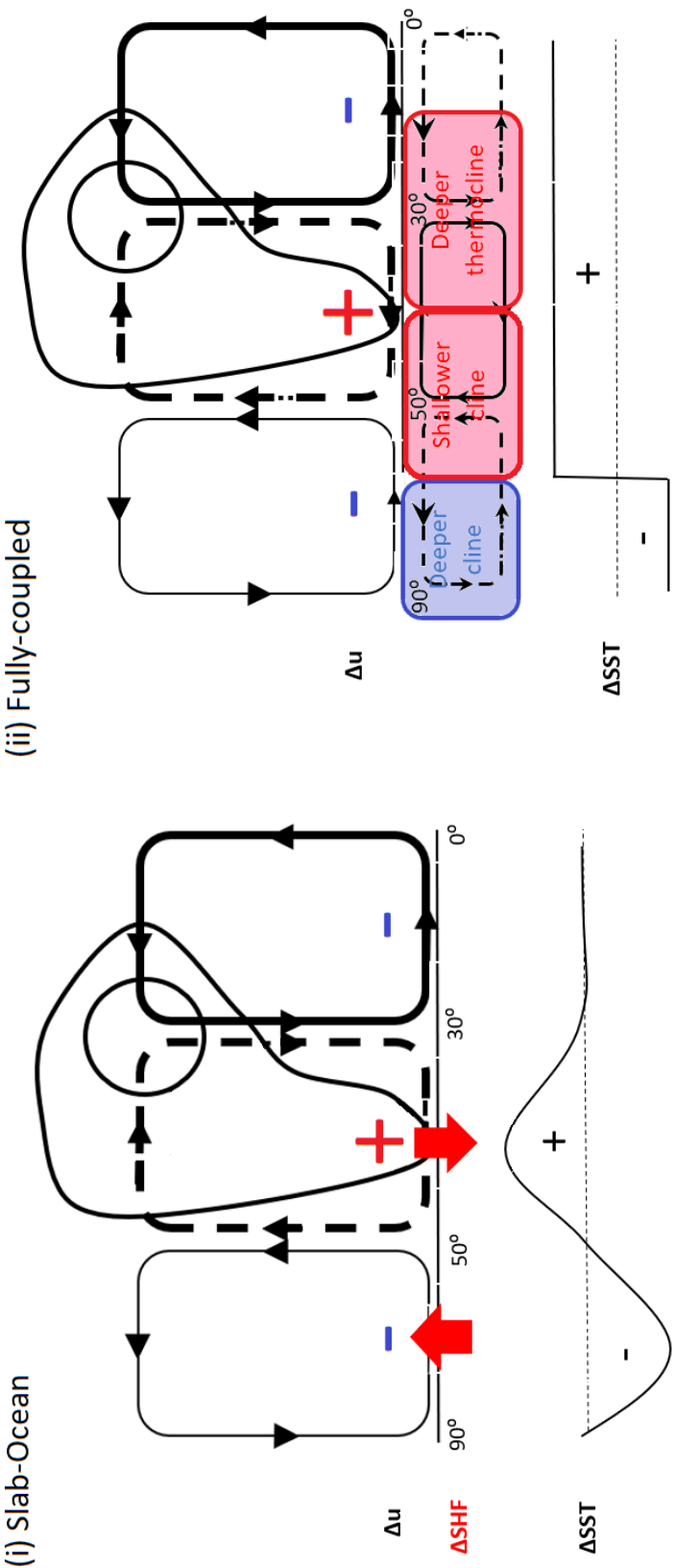


Figure 6.1.1: Schematics showing the changes in atmospheric and oceanic circulation patterns (solid and dashed black cells), surface zonal winds (red pluses/blue minuses), surface sensible heat fluxes (red arrows) and SST, in experiment P01, setups: (i) slab-ocean (left), and (ii) fully-coupled (right). Red/blue shading indicate regions of heating/cooling by the changes in ocean vertical currents, causing local changes in the penetration depth of the thermocline.

diated by anomalous LW radiation, in the SH midlatitudes by anomalous sensible heat fluxes - of the same sign to those seen in the slab-ocean setup - and elsewhere, in the mid-to-high latitudes, directly by the ocean currents. Put all together, this causes the observed SST pattern, with low-to-midlatitude warming/cooling, and high-latitude cooling/warming, in experiments P01/T01.

Once established, the SST anomalies then exert their influence on the atmosphere above in the following ways. Tropical SST anomalies - via a Held & Hou (1980), and Held (2000) type of mechanism - induce changes in tropical convective heating rates and Hadley circulation strengths, with warm/cold SST anomalies causing a strengthening/weakening and polewards-expansion/equatorwards-contraction, as the amount of static energy in the tropics rises, as per equations (1.2.1)-(1.2.3). These in turn cause strengthened/weakened subtropical meridional temperature and PV gradients, causing local increases/decreases in vertical zonal wind shear - i.e. a stronger/weaker subtropical jet. This then has a downstream effect on the eddy momentum and temperature fluxes, with enhanced/weakened eddy fluxes into the midlatitudes. This in turn drives stronger/weaker and polewards-/equatorwards-shifted Ferrel cells and eddy-driven midlatitude jets. Given that experiments U01 (slab-ocean and fully-coupled) and P01/T01 (fully-coupled) cause increases/decreases in tropical SST, the net effect is therefore a strengthening and polewards-expansion of the underlying atmospheric response to the STP.

The influence of extratropical SST anomalies is comparatively weak in the model, and appears to be felt mostly through their meridional gradients, which cause local zonal wind accelerations/deceleration in regions of enhanced/weakened meridional SST gradient, through its modification of the local baroclinicity, in a mechanism similar to that of Brayshaw et al. (2008). Since, in the slab-ocean setup experiments P01/T01, these anomalies are centred around surface zonal wind anomalies - owing to their induction by turbulent heat flux anomalies - they cause a weak deceleration/acceleration on the equatorial and acceleration/deceleration on the poleward flank of the midlatitude jets. The net effect is thereby to cause a slight weakening and poleward-shift in the underlying atmospheric response to the STP.

Lastly, we must give special mention to the results of experiment U01. In this experiment, the surface zonal wind anomalies - which are similar to those of P01, but weaker - did induce changes in the turbulent and ocean heat fluxes that were, again, similar to those in P01. However, in terms of controlling the most significant SST changes, it was the changes in downward LW fluxes which proved most important. This is owing to the large and latitudinally-uniform STP applied in U01, leading to a large global-average anomalous downward LW flux, spread across the entire global surface, causing near-uniform rises in SST. And whilst changes in the anomalous turbulent and ocean heat fluxes could cause local modifications to the extratropical SST anomalies - e.g. the anomalous polar downwelling causing a notable reduction in the high-latitude SST anomalies in the fully-coupled setup vs. the slab-ocean setup - they were not strong enough to override the anomalous downward LW fluxes.

Moreover, it was the changes in tropical SST which dominated the coupled atmosphere-ocean response to this applied STP in this experiment, in both coupled models, and across

all timescales. Such changes are entirely controlled by anomalous downward LW fluxes in the slab-ocean model, and can only be overridden in the long-term (~ 100 s years) in the fully-coupled model by changes in sub-surface ocean heat transport, causing adjustments to the depth of the tropical thermocline. In U01, the changes in ocean heat transport were such that they increased tropical thermocline depth, allowing for greater surface warming by downward LW fluxes. This, paired with the increased mixed-layer depth in the fully-coupled setup, causing a longer adjustment time, meant that there was no significant difference in tropical SST anomalies between the slab-ocean and fully-coupled setup. Thus, in contrast to experiments P01 and T01, ocean dynamics are not necessary to reproduce the most important SST changes seen in response to experiment U01, which are controlled by large anomalous downward LW fluxes.

6.2 Applications

In this subsection, we will discuss the possible real-world and research implications and applications of these results. First of all, it should be noted that, with the exception of experiment U01, SST changes capable of providing a very significant feedback onto the atmosphere were only seen at relatively long timescales in the STP experiments, of the order of hundreds of years. Thus, based upon our results, the effects of atmosphere-ocean coupling may not be significant when looking at phenomena involving STP's of/over relatively short timescales, e.g. sudden stratospheric warming events (~ 2 -3 weeks), volcanic aerosols (~ 2 -3 years), and solar variability (~ 11 years). When looking at the long-term ($\gtrsim 100$ years) effects of changes in stratospheric chemical composition - caused by e.g. ozone and CO₂ - atmosphere-ocean coupling becomes important to account for.

Furthermore, given the relatively simple, aquaplanet double-drake setup which was used, our results have more relevance to, for instance, the Southern Hemisphere, and in particular the Southern Ocean region. This is owing to the relative lack of land in these regions, making them more similar to the corresponding model regions, and with correspondingly stronger atmosphere-ocean coupling present. Given all of the aforementioned, the scenario our results have most relevance to is stratospheric ozone recovery/depletion in the Southern Hemisphere. This would be analogous to our polar stratospheric heating experiment, P01, with the sign of the anomalies the same/reversed for ozone recovery/depletion. Accordingly, based upon the results of that experiment, we would expect stratospheric ozone depletion/recovery to lead a weakening/strengthening of the zonal winds and circulations in the subtropics to low-midlatitudes (25° to 45°), and a strengthening/weakening in the higher latitudes (45° to 75°), including the polar vortices. This is indeed what is observed/predicted from reanalysis data and simulations, to a fairly remarkable degree - qualitatively and quantitatively - during austral summertime (DJF) conditions, when ozone recovery is at its strongest (Son et al. 2008; 2010; 2018). Again, this suggests that the mechanism(s) involved in transmitting such a signal from the stratosphere to the troposphere below rely upon large-scale dynamics, and are not especially sensitive to

physical parameterisations, model resolution, or accurate topographies.

Medium term (~ 10 s years) - based upon the fully-coupled results - we would expect a dipole of negative/positive SST anomalies in the midlatitudes, and the opposite at polar latitudes, caused by the poleward-/equatorward-shift in zonal winds inducing a decreased/increased poleward flux of heat from the low-midlatitudes into the higher latitudes, and anomalous upwelling/downwelling around the pole, with the latter process dominating in the polar region long-term ($\gtrsim 5$ -10 years). These responses by the meridional and vertical ocean advective heat fluxes are similar to the 'fast' and 'slow' responses discussed in Frierson et al. (2015). The net result may be a very slight weakening and poleward-shift in the underlying atmospheric response in the midlatitudes, although its magnitude compared to the atmospheric internal variability would be very small and hard to detect. Longer-term ($\gtrsim 100$ years), these changes in ocean heat transport will also affect the lower latitudes, causing the tropical thermocline to get shallower/deeper, which will show up as surface cooling/warming. This will greatly impact the atmosphere above, the decreases/increases in tropical SST inducing a weaker/stronger and narrower/wider Hadley cell, with downstream impacts on the extratropics, causing weaker/stronger Ferrel cells and midlatitude jets, and the opposite at higher latitudes. The net result will be a strengthening and poleward-shifting of the underlying atmospheric response.

This work therefore suggests that the poleward-shift in the SH summertime (DJF) mid-latitude jet, observed in the period of ozone depletion, 1960-2000, might have been slightly reinforced by accompanying SST changes. Looking into the future, the effects of stratospheric ozone recovery and rising greenhouse gases are projected to broadly cancel each other out in the Southern Hemisphere initially (until ~ 2050), with a possible subsequent further poleward-shift of the zonal winds occurring under certain high-emissions scenarios like RCP 8.5 (Previdi & Polvani, 2014). Thus, provided there is no sudden drop in GHG emissions, it seems likely that this poleward-shift in the SH jet either remains or accelerates over the whole 21st century. Over such a timeperiod, our results suggest that accompanying poleward-shifts in the ocean circulation will induce an amplification/reduction of projected SST increases poleward/equatorward of around 60° , pushing the SH midlatitude jet further poleward yet, and continue to do so beyond the initial period of forcing, as the ocean circulation changes continue to cause adjustments to oceanic heat content patterns. This process, if not countered by restoring the atmosphere to its pre-forced state via e.g. removal of anthropogenic CO₂ emissions, will likely continue for centuries to come, as the global ocean adjusts to its new equilibrium state.

6.3 Limitations

It should be noted that one of the main limitations of my work is its utilisation of a highly-simplified, double-drake aquaplanet setup, with no land and sea ice, and very cold polar SST's. Whilst these limitations should be less of a concern when considering extrapolation of its results to the Southern Hemisphere, and the Southern Ocean especially, they may still have an impact,

and should be taken into consideration. In particular, the lack of sea ice may have led to an exaggeration of polar SST changes in our experiments. Also, the strong vertical temperature stratification seen in our model's Southern Ocean may have led to much stronger and faster warming/cooling by anomalous upwelling/downwelling currents around the poles than would be seen in the real world. This is probably the reason why the initial, 'fast' high-latitude SH cooling, suggested by Frierson et al. (2015), and which we would expect to see in experiment T01, quickly gave way to the 'slow', warming response, after only about 5 years (see bottom-right of figure 4.2.3). It is therefore possible that the projected amplified warming of polar SST's - caused by ozone depletion/rising GHGs, forcing a poleward-shift in the SH midlatitude jet - suggested by my study, may take much longer (~ 10 s years) to occur. This may also be one reason why previous studies with more realistic model oceans, such as Sigmond et al. (2010), found no discernible impact of atmosphere-ocean coupling on the tropospheric response to stratospheric ozone perturbations, especially given that that particular study was only looking at the response over the first 100 years.

Another limitation is the apparent strong/weak atmospheric response to tropical/extratropical SST anomalies seen in the model, as discussed in chapter 5. As discussed in section 1.2, one would expect atmosphere-ocean coupling to be stronger in the tropics than the extratropics - based simply on the higher temperatures and the exponential Clausius-Clapeyron scaling of water vapour. However, it has been noted in recent years that, as model resolution increases to around 10-100km, further extratropical atmosphere-ocean coupling processes get excited, leading to stronger overall extratropical atmosphere-ocean coupling, closer to that seen in the real-world (Czaja et al. 2019). Given the relatively coarse resolution of our model ($3^\circ\text{-}4^\circ \approx 300\text{-}400\text{km}$), extratropical atmosphere-ocean coupling is therefore likely underestimated by the model. This could lead to a potentially significant modification to the feedback of induced extratropical SST anomalies on the atmosphere. Arguably, it could mean that the initial (~ 10 s years) weakening of the tropical-to-low midlatitudinal atmospheric response to STP's - seen in P01 and T01 in both slab-ocean and fully-coupled setups - is stronger than that estimated by the model. On-the-other hand, it might impact the overall long-term (~ 100 s years) modification of the atmospheric signal by atmosphere-ocean coupling, with greater competition between the varying effects of tropical and extratropical SST anomalies. More work with higher-resolution GCM's will therefore be needed, to establish what the precise impact of stronger and more realistic extratropical atmosphere-ocean coupling is upon the overall coupled stratosphere-troposphere-ocean response to applied STP's.

Another model-related potential limitation is the sign of anomalous sensible heat fluxes, as driven by stronger/weaker surface winds, and discussed in sections 4.1.2, 4.1.3 and 4.2.3. In the model, whilst latent heat fluxes are positive upwards across the globe, giving an overall positive turbulent heat flux from the oceans into the atmosphere, the sensible heat fluxes are only positive upwards in the tropics. In the extratropics, they become positive downwards, meaning that surface wind accelerations/decelerations will locally increase/decrease the fluxes of sensible heat from atmosphere into the ocean in that region. This is what was found in

the aforementioned sections, and is potentially problematic, as it conflicts with the real world, in which the sensible heat fluxes are positive upward throughout most of the air-sea interface, including in the extratropics (e.g. Peixoto & Oort 1992). This is mostly an issue for the slab-ocean model runs, and in particular for experiment P01, for which an equatorward-shift in the zonal winds caused, via sensible heat flux anomalies, SST increases locally around the strengthened surface zonal winds in the low-midlatitudes. This therefore calls into question the validity of these extratropical SST changes and, by extension, the atmospheric response to said SST changes. It is less of an issue, on-the-other-hand, for experiments U01 and T01 in this setup, for which atmospheric changes were mostly mediated by the changes in tropical SST, controlled by downward LW fluxes. It is also not such an issue for the fully-coupled setup, for which the changes in ocean heat fluxes were dominant in driving extratropical SST changes.

6.4 Future Work

Looking ahead to ways in which the body of work presented by this thesis could be built upon/improved/extended, it would first be logical to address some of the limitations outlined in the previous subsection. Key to many of these limitations, were differences between the model and the real-world: in particular, differences in the mean state of the global ocean, and aspects of atmosphere-ocean coupling, such as sea-air sensible heat fluxes, and the strength of such coupling in the extratropics. It would therefore be ideal to perform similar STP experiments again, however, using a different coupled atmosphere-ocean model or model setup. Such a model setup should have a more accurate representation of the mean state of the oceans - with weaker thermal stratification in the Southern Ocean region - and of the direction of air-sea turbulent heat exchange. This would allow for a more direct analogy between the simulated changes seen in the model, and that which we would expect on Earth, and also between the timescales of such changes. It would also ideally have the option of being run at different resolutions: one that is comparable to that used within this thesis (3° - $4^{\circ} \approx 300$ - 400 km), and a higher-resolution one, capable ideally of fully representing atmosphere-ocean coupling due to mesoscale ocean eddies ($\lesssim 100$ km). This would allow one to see what effect an increased model resolution, and thereby, stronger and more realistic extratropical atmosphere-ocean coupling, has upon the fully-coupled stratosphere-troposphere-ocean response to STP's.

In the spirit of performing simulations that are more directly applicable to Earth phenomena, it might also be a good idea to perform simulations involving the imposition of zonally-asymmetric STP's, as caused by e.g. stratospheric ozone depletion/recovery. It has been suggested by Crook et al. (2008) and Waugh et al. (2009) that asymmetric STP's yield a greater overall atmospheric response. It would be interesting to see if this is echoed by the oceanic response, and if that in-turn leads to a greater overall adjustment to the underlying atmospheric response. Similarly, it might also be advisable to perform simulations with STP's - primarily polar ones - that are active in the Southern Hemisphere only, also analogous to stratospheric

ozone depletion/recovery. Also, one might also want to study the effects of stratospheric cooling perturbations, as in response to e.g. ozone depletion.

Furthermore, as well as studying the effects of an abrupt stratospheric heating/cooling perturbation, it would be interesting to then see what happens when said perturbation is switched off in the different coupled models, at different points in their evolution. This would be akin to studying the effects of e.g. an initial depletion, and subsequent recovery, in stratospheric ozone levels, a scenario which is currently in the process of playing out in Southern Hemisphere. One would expect - especially when switched off at later points in the fully-coupled model integration - the changes in SST to maintain some of the previous changes in the atmospheric state, as suggested by Nakamura et al. (2004), at least until the ocean has itself returned to its original equilibrium state. This is certainly what one would expect based upon my results, in which the long-term SST changes reinforce and shift polewards the underlying atmospheric changes.

To then move into ways to build upon/explore further the results of the existing experiments, within this thesis, we have mainly been focussed upon zonally-averaged and hemispherically-symmetric changes to the atmosphere and oceans. It therefore might be interesting to explore some of the zonally-asymmetric changes: for instance, the different changes in ocean circulation, heat and salinity content, between the small and large basins. The control-values of these fields were shown in section 2.6.3 to be significantly different between the basins, and so it would stand to reason that their changes in response to STP's would also be quite different. Likewise, it would also be interesting to explore interhemispheric asymmetries. For example, one interesting result was that, in the fully-coupled model, the NH and SH extratropics appeared to exhibit slightly different SST anomalies, with the extratropical NH generally having warmer/cooler SST's in response to experiments U01 and P01/T01. This appeared to be a result of the NH/SH extratropical SST's being more controlled by meridional/vertical heat advection, causing opposing SST tendencies, similar to in Frierson et al. (2015). Lastly, in my analysis of ocean circulation changes in section 4.2.4, I focused on changes to the wind-driven circulation. It would therefore be interesting to investigate changes to the thermohaline circulation, its drivers, and how the buoyancy- and wind-driven ocean circulation changes all fit together.

Bibliography

- [1] Adcroft, A., Campin, J.M., Dutkiewicz, S., Evangelinos, C., Ferreira, D., Forget, G., Fox-Kemper, B., Losch, M., Marshall, J., Maze, G. and Menemenlis, D., 2018. MITgcm User Manual.
- [2] Alexander, M.A., Deser, C. and Timlin, M.S., 1999. The reemergence of SST anomalies in the North Pacific Ocean. *Journal of climate*, 12(8), pp.2419-2433.
- [3] Andrews, D.G. and McIntyre, M.E., 1976. Planetary waves in horizontal and vertical shear: The generalized Eliassen-Palm relation and the mean zonal acceleration. *Journal of the Atmospheric Sciences*, 33(11), pp.2031-2048.
- [4] Andrews, D.G., Holton, J.R. and Leovy, C.B., 1987. *Middle atmosphere dynamics* (No. 40). Academic press.
- [5] Andrews, D.G., 2010. *An introduction to atmospheric physics*. Cambridge University Press.
- [6] Andrews, M.B., Knight, J.R. and Gray, L.J., 2015. A simulated lagged response of the North Atlantic Oscillation to the solar cycle over the period 1960–2009. *Environmental Research Letters*, 10(5), p.054022.
- [7] Armour, K.C., Marshall, J., Scott, J.R., Donohoe, A. and Newsom, E.R., 2016. Southern Ocean warming delayed by circumpolar upwelling and equatorward transport. *Nature Geoscience*, 9(7), pp.549-554.
- [8] Baldwin, M.P. and Dunkerton, T.J., 1999. Propagation of the Arctic Oscillation from the stratosphere to the troposphere. *Journal of Geophysical Research: Atmospheres*, 104(D24), pp.30937-30946.
- [9] Baldwin, M.P., Thompson, D.W., Shuckburgh, E.F., Norton, W.A. and Gillett, N.P., 2003. Weather from the stratosphere?. *Science*, 301(5631), pp.317-319.
- [10] Barnett, T.P., 1981. On the nature and causes of large-scale thermal variability in the central North Pacific Ocean. *Journal of Physical Oceanography*, 11(7), pp.887-904.

- [11] Bjerknes, J., 1966. A possible response of the atmospheric Hadley circulation to equatorial anomalies of ocean temperature. *Tellus*, 18(4), pp.820-829.
- [12] Bjerknes, J., 1969. Atmospheric teleconnections from the equatorial Pacific. *Monthly weather review*, 97(3), pp.163-172.
- [13] Brayshaw, D.J., Hoskins, B. and Blackburn, M., 2008. The storm-track response to idealized SST perturbations in an aquaplanet GCM. *Journal of the Atmospheric Sciences*, 65(9), pp.2842-2860.
- [14] Cai, W., Shi, G., Cowan, T., Bi, D. and Ribbe, J., 2005. The response of the Southern Annular Mode, the East Australian Current, and the southern mid-latitude ocean circulation to global warming. *Geophysical Research Letters*, 32(23).
- [15] Cai, W., 2006. Antarctic ozone depletion causes an intensification of the Southern Ocean super-gyre circulation. *Geophysical Research Letters*, 33(3).
- [16] Cai, W. and Cowan, T., 2007. Trends in Southern Hemisphere circulation in IPCC AR4 models over 1950–99: Ozone depletion versus greenhouse forcing. *Journal of Climate*, 20(4), pp.681-693.
- [17] Cayan, D.R., 1992. Latent and sensible heat flux anomalies over the northern oceans: Driving the sea surface temperature. *Journal of Physical Oceanography*, 22(8), pp.859-881.
- [18] Cayan, D.R., 1992. Latent and sensible heat flux anomalies over the northern oceans: The connection to monthly atmospheric circulation. *Journal of climate*, 5(4), pp.354-369.
- [19] Cayan, D.R., 1992. Variability of latent and sensible heat fluxes estimated using bulk formulae. *Atmosphere-Ocean*, 30(1), pp.1-42.
- [20] Ceppi, P. and Hartmann, D.L., 2013. On the speed of the eddy-driven jet and the width of the Hadley cell in the Southern Hemisphere. *Journal of Climate*, 26(10), pp.3450-3465.
- [21] Chang, E.K., Lee, S. and Swanson, K.L., 2002. Storm track dynamics. *Journal of climate*, 15(16), pp.2163-2183.
- [22] Chen, G., Plumb, R.A. and Lu, J., 2010. Sensitivities of zonal mean atmospheric circulation to SST warming in an aqua-planet model. *Geophysical Research Letters*, 37(12).
- [23] Chen, G., Lu, J. and Sun, L., 2013. Delineating the eddy–zonal flow interaction in the atmospheric circulation response to climate forcing: Uniform SST warming in an idealized aquaplanet model. *Journal of the Atmospheric Sciences*, 70(7), pp.2214-2233.
- [24] Cohen, J., Barlow, M., Kushner, P.J. and Saito, K., 2007. Stratosphere–troposphere coupling and links with Eurasian land surface variability. *Journal of Climate*, 20(21), pp.5335-5343.

- [25] Crook, J.A., Gillett, N.P. and Keeley, S.P., 2008. Sensitivity of Southern Hemisphere climate to zonal asymmetry in ozone. *Geophysical Research Letters*, 35(7).
- [26] Cuff, D. and Goudie, A., 2009. *The Oxford companion to global change*. Oxford University Press.
- [27] Czaja, A. and Frankignoul, C., 1999. Influence of the North Atlantic SST on the atmospheric circulation. *Geophysical Research Letters*, 26(19), pp.2969-2972.
- [28] Czaja, A. and Frankignoul, C., 2002. Observed impact of Atlantic SST anomalies on the North Atlantic Oscillation. *Journal of Climate*, 15(6), pp.606-623.
- [29] Czaja, A., Frankignoul, C., Minobe, S. and Vannière, B., 2019. Simulating the midlatitude atmospheric circulation: What might we gain from high-resolution modeling of air-sea interactions?. *Current Climate Change reports*, 5(4), pp.390-406.
- [30] Domeisen, D.I., Sun, L. and Chen, G., 2013. The role of synoptic eddies in the tropospheric response to stratospheric variability. *Geophysical research letters*, 40(18), pp.4933-4937.
- [31] Domeisen, D.I., Butler, A.H., Charlton-Perez, A.J., Ayarzagüena, B., Baldwin, M.P., Dunn-Sigouin, E., Furtado, J.C., Garfinkel, C.I., Hitchcock, P., Karpechko, A.Y. and Kim, H., 2020. The role of the stratosphere in subseasonal to seasonal prediction: 2. Predictability arising from stratosphere-troposphere coupling. *Journal of Geophysical Research: Atmospheres*, 125(2), p.e2019JD030923.
- [32] Eady, E.T., 1949. Long waves and cyclone waves. *Tellus*, 1(3), pp.33-52.
- [33] Edmon Jr, H.J., Hoskins, B.J. and McIntyre, M.E., 1980. Eliassen-Palm cross sections for the troposphere. *Journal of Atmospheric Sciences*, 37(12), pp.2600-2616.
- [34] Eliassen, A., 1960. On the transfer of energy in stationary mountain waves. *Geophy. Publ.*, 22, pp.1-23.
- [35] Eyring, V., Cionni, I., Bodeker, G.E., Charlton-Perez, A.J., Kinnison, D.E., Scinocca, J.F., Waugh, D.W., Akiyoshi, H., Bekki, S., Chipperfield, M.P. and Dameris, M., 2010. Multi-model assessment of stratospheric ozone return dates and ozone recovery in CCMVal-2 models. *Atmospheric Chemistry and Physics*, 10(19), pp.9451-9472.
- [36] Ferranti, L., Molteni, F. and Palmer, T.N., 1994. Impact of localized tropical and extra-tropical SST anomalies in ensembles of seasonal GCM integrations. *Quarterly Journal of the Royal Meteorological Society*, 120(520), pp.1613-1645.
- [37] Ferreira, D., Marshall, J., Bitz, C.M., Solomon, S. and Plumb, A., 2015. Antarctic Ocean and sea ice response to ozone depletion: A two-time-scale problem. *Journal of Climate*, 28(3), pp.1206-1226.

- [38] Foussard, A., Lapeyre, G. and Plougonven, R., 2019. Storm track response to oceanic eddies in idealized atmospheric simulations. *Journal of Climate*, 32(2), pp.445-463.
- [39] Frame, T.H. and Gray, L.J., 2010. The 11-yr solar cycle in ERA-40 data: An update to 2008. *Journal of Climate*, 23(8), pp.2213-2222.
- [40] Frankignoul, C. and Reynolds, R.W., 1983. Testing a dynamical model for mid-latitude sea surface temperature anomalies. *Journal of physical oceanography*, 13(7), pp.1131-1145.
- [41] Frankignoul, C., Sennéchal, N., Kwon, Y.O. and Alexander, M.A., 2011. Influence of the meridional shifts of the Kuroshio and the Oyashio Extensions on the atmospheric circulation. *Journal of Climate*, 24(3), pp.762-777.
- [42] Frierson, D.M., Held, I.M. and Zurita-Gotor, P., 2006. A gray-radiation aquaplanet moist GCM. Part I: Static stability and eddy scale. *Journal of the atmospheric sciences*, 63(10), pp.2548-2566.
- [43] Frierson, D.M., 2007. The dynamics of idealized convection schemes and their effect on the zonally averaged tropical circulation. *Journal of the atmospheric sciences*, 64(6), pp.1959-1976.
- [44] Frierson, D.M., Lu, J. and Chen, G., 2007. Width of the Hadley cell in simple and comprehensive general circulation models. *Geophysical Research Letters*, 34(18).
- [45] Garfinkel, C.I., Waugh, D.W. and Gerber, E.P., 2013. The effect of tropospheric jet latitude on coupling between the stratospheric polar vortex and the troposphere. *Journal of Climate*, 26(6), pp.2077-2095.
- [46] Geen, R., 2015. The effects of latent heat release on the climate of an aquaplanet model (Doctoral dissertation, Imperial College London).
- [47] Gent, P. R., and J. C. McWilliams, Isopycnal mixing in ocean circulation models, *J. Phys. Oceanogr.*, 20, 150-155, 1990.
- [48] Gent, P. R., J. Willebrand, T. J. McDougall, and J. C. McWilliams, Parameterizing eddy-induced tracer transports in ocean circulation models, *J. Phys. Oceanogr.*, 25, 463-474, 1995.
- [49] Gerber, E.P. and Polvani, L.M., 2009. Stratosphere-troposphere coupling in a relatively simple AGCM: The importance of stratospheric variability. *Journal of Climate*, 22(8), pp.1920-1933.
- [50] Gerber, E.P., Baldwin, M.P., Akiyoshi, H., Austin, J., Bekki, S., Braesicke, P., Butchart, N., Chipperfield, M., Dameris, M., Dhomse, S. and Frith, S.M., 2010. Stratosphere-troposphere coupling and annular mode variability in chemistry-climate models. *Journal of Geophysical Research: Atmospheres*, 115(D3).

- [51] Gerber, E.P. and Son, S.W., 2014. Quantifying the summertime response of the austral jet stream and Hadley cell to stratospheric ozone and greenhouse gases. *Journal of Climate*, 27(14), pp.5538-5559.
- [52] Gill, A.E., 1980. Some simple solutions for heat-induced tropical circulation. *Quarterly Journal of the Royal Meteorological Society*, 106(449), pp.447-462.
- [53] Gray, L.J., Crooks, S.A., Palmer, M.A., Pascoe, C.L. and Sparrow, S., 2006. A possible transfer mechanism for the 11-year solar cycle to the lower stratosphere. *Space Science Reviews*, 125(1-4), pp.357-370.
- [54] Gray, L.J., Rumbold, S.T. and Shine, K.P., 2009. Stratospheric temperature and radiative forcing response to 11-year solar cycle changes in irradiance and ozone. *Journal of the Atmospheric Sciences*, 66(8), pp.2402-2417.
- [55] Gray, L.J., Beer, J., Geller, M., Haigh, J.D., Lockwood, M., Matthes, K., Cubasch, U., Fleitmann, D., Harrison, G., Hood, L. and Luterbacher, J., 2010. Solar influences on climate. *Reviews of Geophysics*, 48(4).
- [56] Gray, L.J., Scaife, A.A., Mitchell, D.M., Osprey, S., Ineson, S., Hardiman, S., Butchart, N., Knight, J., Sutton, R. and Kodera, K., 2013. A lagged response to the 11 year solar cycle in observed winter Atlantic/European weather patterns. *Journal of Geophysical Research: Atmospheres*, 118(24), pp.13-405.
- [57] Gray, L.J., Woollings, T.J., Andrews, M. and Knight, J., 2016. Eleven-year solar cycle signal in the NAO and Atlantic/European blocking. *Quarterly Journal of the Royal Meteorological Society*, 142(698), pp.1890-1903.
- [58] Haigh, J.D., 1994. The role of stratospheric ozone in modulating the solar radiative forcing of climate. *Nature*, 370(6490), pp.544-546.
- [59] Haigh, J.D., Blackburn, M. and Day, R., 2005. The response of tropospheric circulation to perturbations in lower-stratospheric temperature. *Journal of Climate*, 18(17), pp.3672-3685.
- [60] Haigh, J.D. and Blackburn, M., 2006. Solar influences on dynamical coupling between the stratosphere and troposphere. *Space Science Reviews*, 125(1-4), pp.331-344.
- [61] Held, I.M. and Hou, A.Y., 1980. Nonlinear axially symmetric circulations in a nearly inviscid atmosphere. *Journal of the Atmospheric Sciences*, 37(3), pp.515-533.
- [62] Held, I. M., 2000. The general circulation of the atmosphere, paper presented at 2000 Woods Hole Oceanographic Institute Geophysical Fluid Dynamics Program, Woods Hole Oceanogr. Inst., Woods Hole, Mass. (Available at <https://darchive.mblwhoilibrary.org/handle/1912/15>)

- [63] Hitchcock, P. and Simpson, I.R., 2014. The downward influence of stratospheric sudden warmings. *Journal of the Atmospheric Sciences*, 71(10), pp.3856-3876.
- [64] Hitchcock, P. and Simpson, I.R., 2016. Quantifying eddy feedbacks and forcings in the tropospheric response to stratospheric sudden warmings. *Journal of the Atmospheric Sciences*, 73(9), pp.3641-3657.
- [65] Hoskins, B.J. and Karoly, D.J., 1981. The steady linear response of a spherical atmosphere to thermal and orographic forcing. *Journal of Atmospheric Sciences*, 38(6), pp.1179-1196.
- [66] Hou, A.Y., 1998. Hadley circulation as a modulator of the extratropical climate. *Journal of Atmospheric Sciences*, 55(14), pp.2437-2457.
- [67] Kang, S.M. and Polvani, L.M., 2011. The interannual relationship between the latitude of the eddy-driven jet and the edge of the Hadley cell. *Journal of Climate*, 24(2), pp.563-568.
- [68] Karoly, D.J. and Hoskins, B.J., 1982. Three dimensional propagation of planetary waves. *Journal of the Meteorological Society of Japan. Ser. II*, 60(1), pp.109-123.
- [69] Kostov, Y., Marshall, J., Hausmann, U., Armour, K.C., Ferreira, D. and Holland, M.M., 2017. Fast and slow responses of Southern Ocean sea surface temperature to SAM in coupled climate models. *Climate Dynamics*, 48(5-6), pp.1595-1609.
- [70] Kushnir, Y., Robinson, W.A., Bladé, I., Hall, N.M.J., Peng, S. and Sutton, R., 2002. Atmospheric GCM response to extratropical SST anomalies: Synthesis and evaluation. *Journal of Climate*, 15(16), pp.2233-2256.
- [71] Kushner, P.J. and Polvani, L.M., 2004. Stratosphere–troposphere coupling in a relatively simple AGCM: The role of eddies. *Journal of climate*, 17(3), pp.629-639.
- [72] Kushner, P.J. and Polvani, L.M., 2006. Stratosphere–troposphere coupling in a relatively simple AGCM: Impact of the seasonal cycle. *Journal of climate*, 19(21), pp.5721-5727.
- [73] Kwon, Y.O., Alexander, M.A., Bond, N.A., Frankignoul, C., Nakamura, H., Qiu, B. and Thompson, L.A., 2010. Role of the Gulf Stream and Kuroshio–Oyashio systems in large-scale atmosphere–ocean interaction: A review. *Journal of Climate*, 23(12), pp.3249-3281.
- [74] Lau, N.C., 1997. Interactions between global SST anomalies and the midlatitude atmospheric circulation. *Bulletin of the American Meteorological Society*, 78(1), pp.21-33.
- [75] Lindzen, R.S. and Hou, A.V., 1988. Hadley circulations for zonally averaged heating centered off the equator. *Journal of Atmospheric Sciences*, 45(17), pp.2416-2427.
- [76] Lorenz, D.J. and Hartmann, D.L., 2001. Eddy–zonal flow feedback in the Southern Hemisphere. *Journal of the atmospheric sciences*, 58(21), pp.3312-3327.

- [77] Lorenz, D.J. and DeWeaver, E.T., 2007. Tropopause height and zonal wind response to global warming in the IPCC scenario integrations. *Journal of Geophysical Research: Atmospheres*, 112(D10).
- [78] Ma, X., Chang, P., Saravanan, R., Montuoro, R., Nakamura, H., Wu, D., Lin, X. and Wu, L., 2017. Importance of resolving Kuroshio front and eddy influence in simulating the North Pacific storm track. *Journal of Climate*, 30(5), pp.1861-1880.
- [79] Marshall, J., Adcroft, A., Hill, C., Perelman, L. and Heisey, C., 1997. A finite-volume, incompressible Navier Stokes model for studies of the ocean on parallel computers. *Journal of Geophysical Research: Oceans*, 102(C3), pp.5753-5766. Vancouver
- [80] Marshall, J., Ferreira, D., Campin, J.M. and Enderton, D., 2007. Mean climate and variability of the atmosphere and ocean on an aquaplanet. *Journal of the Atmospheric Sciences*, 64(12), pp.4270-4286.
- [81] Marshall, J., Armour, K.C., Scott, J.R., Kostov, Y., Hausmann, U., Ferreira, D., Shepherd, T.G. and Bitz, C.M., 2014. The ocean's role in polar climate change: asymmetric Arctic and Antarctic responses to greenhouse gas and ozone forcing. *Philosophical Transactions of the Royal Society A: Mathematical, Physical and Engineering Sciences*, 372(2019), p.20130040.
- [82] Matsuno, T., 1966. Quasi-geostrophic motions in the equatorial area. *Journal of the Meteorological Society of Japan. Ser. II*, 44(1), pp.25-43.
- [83] Mbengue, C. and Schneider, T., 2018. Linking Hadley circulation and storm tracks in a conceptual model of the atmospheric energy balance. *Journal of the Atmospheric Sciences*, 75(3), pp.841-856.
- [84] Met Office. 2021. Numerical weather prediction models. [online] Available at: <<https://www.metoffice.gov.uk/research/approach/modelling-systems/unified-model/weather-forecasting>> [Accessed 28 April 2021].
- [85] Michel, C. and Rivière, G., 2014. Sensitivity of the position and variability of the eddy-driven jet to different SST profiles in an aquaplanet general circulation model. *Journal of the Atmospheric Sciences*, 71(1), pp.349-371.
- [86] Miller, R.L., Schmidt, G.A. and Shindell, D.T., 2006. Forced annular variations in the 20th century intergovernmental panel on climate change fourth assessment report models. *Journal of Geophysical Research: Atmospheres*, 111(D18).
- [87] Minobe, S., Kuwano-Yoshida, A., Komori, N., Xie, S.P. and Small, R.J., 2008. Influence of the Gulf Stream on the troposphere. *Nature*, 452(7184), pp.206-209.

- [88] Misios, S., Mitchell, D.M., Gray, L.J., Tourpali, K., Matthes, K., Hood, L., Schmidt, H., Chiodo, G., Thiéblemont, R., Rozanov, E. and Krivolutsky, A., 2016. Solar signals in CMIP-5 simulations: effects of atmosphere–ocean coupling. *Quarterly Journal of the Royal Meteorological Society*, 142(695), pp.928-941.
- [89] Nakamura, H., Sampe, T., Tanimoto, Y. and Shimpo, A., 2004. Observed associations among storm tracks, jet streams and midlatitude oceanic fronts. *Earth’s Climate: The Ocean–Atmosphere Interaction*, *Geophys. Monogr.* 147, pp.329-345.
- [90] Newchurch, M.J., Yang, E.S., Cunnold, D.M., Reinsel, G.C., Zawodny, J.M. and Russell, J.M., 2003. Evidence for slowdown in stratospheric ozone loss: First stage of ozone recovery. *Journal of Geophysical Research: Atmospheres*, 108(D16).
- [91] Ogawa, F., Omrani, N.E., Nishii, K., Nakamura, H. and Keenlyside, N., 2015. Ozone-induced climate change propped up by the Southern Hemisphere oceanic front. *Geophysical Research Letters*, 42(22), pp.10-056.
- [92] O’Gorman, P.A. and Schneider, T., 2008. The hydrological cycle over a wide range of climates simulated with an idealized GCM. *Journal of Climate*, 21(15), pp.3815-3832. Vancouver
- [93] O’Reilly, C.H. and Czaja, A., 2015. The response of the Pacific storm track and atmospheric circulation to Kuroshio Extension variability. *Quarterly Journal of the Royal Meteorological Society*, 141(686), pp.52-66.
- [94] Pan, Y.H. and Oort, A.H., 1983. Global climate variations connected with sea surface temperature anomalies in the eastern equatorial Pacific Ocean for the 1958–73 period. *Monthly Weather Review*, 111(6), pp.1244-1258.
- [95] Parfitt, R., Czaja, A. and Kwon, Y.O., 2017. The impact of SST resolution change in the ERA-Interim reanalysis on wintertime Gulf Stream frontal air-sea interaction. *Geophysical Research Letters*, 44(7), pp.3246-3254.
- [96] Pedlosky, J., 1996. *Ocean Circulation Theory*. Springer Science & Business Media.
- [97] Peixoto, J.P. and Oort, A.H., 1992. *Physics of Climate*, 520 pp. Am. Inst. of Phys., New York.
- [98] Polvani, L.M. and Kushner, P.J., 2002. Tropospheric response to stratospheric perturbations in a relatively simple general circulation model. *Geophysical Research Letters*, 29(7).
- [99] Polvani, L.M., Waugh, D.W., Correa, G.J. and Son, S.W., 2011. Stratospheric ozone depletion: The main driver of twentieth-century atmospheric circulation changes in the Southern Hemisphere. *Journal of Climate*, 24(3), pp.795-812.

- [100] Previdi, M. and Polvani, L.M., 2014. Climate system response to stratospheric ozone depletion and recovery. *Quarterly Journal of the Royal Meteorological Society*, 140(685), pp.2401-2419.
- [101] Randall, C.E., Harvey, V.L., Singleton, C.S., Bailey, S.M., Bernath, P.F., Codrescu, M., Nakajima, H. and Russell III, J.M., 2007. Energetic particle precipitation effects on the Southern Hemisphere stratosphere in 1992–2005. *Journal of Geophysical Research: Atmospheres*, 112(D8).
- [102] Rasmusson, E.M. and Wallace, J.M., 1983. Meteorological aspects of the El Niño/southern oscillation. *Science*, 222(4629), pp.1195-1202.
- [103] Redi, M. H., Oceanic isopycnal mixing by coordinate rotation, *Journal of Physical Oceanography*, 12, 1154-1158, 1982.
- [104] Robinson, W.A., 2000. A baroclinic mechanism for the eddy feedback on the zonal index. *Journal of the Atmospheric Sciences*, 57(3), pp.415-422.
- [105] Sampe, T., Nakamura, H., Goto, A. and Ohfuchi, W., 2010. Significance of a midlatitude SST frontal zone in the formation of a storm track and an eddy-driven westerly jet. *Journal of Climate*, 23(7), pp.1793-1814.
- [106] Sardeshmukh, P.D. and Hoskins, B.J., 1988. The generation of global rotational flow by steady idealized tropical divergence. *Journal of Atmospheric Sciences*, 45(7), pp.1228-1251.
- [107] Scaife, A.A., Ineson, S., Knight, J.R., Gray, L., Kodera, K. and Smith, D.M., 2013. A mechanism for lagged North Atlantic climate response to solar variability. *Geophysical Research Letters*, 40(2), pp.434-439.
- [108] Schneider, T., 2006. The general circulation of the atmosphere. *Annu. Rev. Earth Planet. Sci.*, 34, pp.655-688.
- [109] Seager, R., Kushnir, Y., Visbeck, M., Naik, N., Miller, J., Krahmann, G. and Cullen, H., 2000. Causes of Atlantic Ocean climate variability between 1958 and 1998. *Journal of Climate*, 13(16), pp.2845-2862.
- [110] Seviour, W.J.M., Codron, F., Doddridge, E.W., Ferreira, D., Gnanadesikan, A., Kelley, M., Kostov, Y., Marshall, J., Polvani, L.M., Thomas, J.L. and Waugh, D.W., 2019. The southern ocean sea surface temperature response to ozone depletion: a multimodel comparison. *Journal of Climate*, 32(16), pp.5107-5121.
- [111] Shepherd, T.G., 2002. Issues in stratosphere-troposphere coupling. *Journal of the Meteorological Society of Japan. Ser. II*, 80(4B), pp.769-792.
- [112] Sigmond, M., Fyfe, J.C. and Scinocca, J.F., 2010. Does the ocean impact the atmospheric response to stratospheric ozone depletion?. *Geophysical research letters*, 37(12).

- [113] Sigmond, M., Scinocca, J.F., Kharin, V.V. and Shepherd, T.G., 2013. Enhanced seasonal forecast skill following stratospheric sudden warmings. *Nature Geoscience*, 6(2), pp.98-102.
- [114] Simpson, I.R., 2009. Solar influence on stratosphere-troposphere dynamical coupling (Doctoral dissertation, Imperial College London).
- [115] Simpson, I.R., Blackburn, M. and Haigh, J.D., 2009. The role of eddies in driving the tropospheric response to stratospheric heating perturbations. *Journal of the Atmospheric Sciences*, 66(5), pp.1347-1365.
- [116] Simpson, I.R., Blackburn, M., Haigh, J.D. and Sparrow, S.N., 2010. The impact of the state of the troposphere on the response to stratospheric heating in a simplified GCM. *Journal of climate*, 23(23), pp.6166-6185.
- [117] Ślownik, W.M.O., 1992. International meteorological vocabulary, 1992. WMO/OMM/IMGW, 182, Geneva.
- [118] Smirnov, D., Newman, M., Alexander, M.A., Kwon, Y.O. and Frankignoul, C., 2015. Investigating the local atmospheric response to a realistic shift in the Oyashio sea surface temperature front. *Journal of Climate*, 28(3), pp.1126-1147.
- [119] Smith, K.L. and Scott, R.K., 2016. The role of planetary waves in the tropospheric jet response to stratospheric cooling. *Geophysical Research Letters*, 43(6), pp.2904-2911.
- [120] Son, S.W., Polvani, L.M., Waugh, D.W., Akiyoshi, H., Garcia, R., Kinnison, D., Pawson, S., Rozanov, E., Shepherd, T.G. and Shibata, K., 2008. The impact of stratospheric ozone recovery on the Southern Hemisphere westerly jet. *Science*, 320(5882), pp.1486-1489.
- [121] Son, S.W., Gerber, E.P., Perlwitz, J., Polvani, L.M., Gillett, N.P., Seo, K.H., Eyring, V., Shepherd, T.G., Waugh, D., Akiyoshi, H. and Austin, J., 2010. Impact of stratospheric ozone on Southern Hemisphere circulation change: A multimodel assessment. *Journal of Geophysical Research: Atmospheres*, 115(D3).
- [122] Son, S.W., Han, B.R., Garfinkel, C.I., Kim, S.Y., Park, R., Abraham, N.L., Akiyoshi, H., Archibald, A.T., Butchart, N., Chipperfield, M.P. and Dameris, M., 2018. Tropospheric jet response to Antarctic ozone depletion: An update with Chemistry-Climate Model Initiative (CCMI) models. *Environmental Research Letters*, 13(5), p.054024.
- [123] Solomon, S., 1999. Stratospheric ozone depletion: A review of concepts and history. *Reviews of Geophysics*, 37(3), pp.275-316.
- [124] Soukharev, B.E. and Hood, L.L., 2006. Solar cycle variation of stratospheric ozone: Multiple regression analysis of long-term satellite data sets and comparisons with models. *Journal of Geophysical Research: Atmospheres*, 111(D20).

- [125] Staten, P.W. and Reichler, T., 2014. On the ratio between shifts in the eddy-driven jet and the Hadley cell edge. *Climate dynamics*, 42(5-6), pp.1229-1242.
- [126] Taguchi, B., Nakamura, H., Nonaka, M. and Xie, S.P., 2009. Influences of the Kuroshio/Oyashio Extensions on air-sea heat exchanges and storm-track activity as revealed in regional atmospheric model simulations for the 2003/04 cold season. *Journal of Climate*, 22(24), pp.6536-6560.
- [127] Thompson, D.W., Baldwin, M.P. and Solomon, S., 2005. Stratosphere-troposphere coupling in the Southern Hemisphere. *Journal of the atmospheric sciences*, 62(3), pp.708-715.
- [128] Thompson, D.W. and Wallace, J.M., 2000. Annular modes in the extratropical circulation. Part I: Month-to-month variability. *Journal of climate*, 13(5), pp.1000-1016.
- [129] Thompson, D.W., Wallace, J.M. and Hegerl, G.C., 2000. Annular modes in the extratropical circulation. Part II: Trends. *Journal of Climate*, 13(5), pp.1018-1036.
- [130] Trenberth, K.E. and Hoar, T.J., 1996. The 1990–1995 El Niño–Southern Oscillation event: Longest on record. *Geophysical research letters*, 23(1), pp.57-60.
- [131] Trenberth, K.E., Branstator, G.W., Karoly, D., Kumar, A., Lau, N.C. and Ropelewski, C., 1998. Progress during TOGA in understanding and modeling global teleconnections associated with tropical sea surface temperatures. *Journal of Geophysical Research: Oceans*, 103(C7), pp.14291-14324.
- [132] Troen, I.B. and Mahrt, L., 1986. A simple model of the atmospheric boundary layer; sensitivity to surface evaporation. *Boundary-Layer Meteorology*, 37(1-2), pp.129-148.
- [133] Vallis, G.K., 2006. *Atmospheric and Oceanic Fluid Dynamics: Fundamentals and Large-scale Circulation*.
- [134] Vallis, G.K., Zurita-Gotor, P., Cairns, C. and Kidston, J., 2015. Response of the large-scale structure of the atmosphere to global warming. *Quarterly Journal of the Royal Meteorological Society*, 141(690), pp.1479-1501.
- [135] Walker, C.C. and Schneider, T., 2006. Eddy influences on Hadley circulations: Simulations with an idealized GCM. *Journal of the atmospheric sciences*, 63(12), pp.3333-3350.
- [136] Wang, G., Cai, W. and Purich, A., 2014. Trends in Southern Hemisphere wind-driven circulation in CMIP5 models over the 21st century: Ozone recovery versus greenhouse forcing. *Journal of Geophysical Research: Oceans*, 119(5), pp.2974-2986.
- [137] Waugh, D.W., Oman, L., Newman, P.A., Stolarski, R.S., Pawson, S., Nielsen, J.E. and Perlwitz, J., 2009. Effect of zonal asymmetries in stratospheric ozone on simulated Southern Hemisphere climate trends. *Geophysical Research Letters*, 36(18).

- [138] White, I.P., Garfinkel, C.I., Gerber, E.P., Jucker, M., Hitchcock, P. and Rao, J., 2020. The generic nature of the tropospheric response to sudden stratospheric warmings. *Journal of Climate*, 33(13), pp.5589-5610.
- [139] Williamson, D.L., Blackburn, M., Hoskins, B.J., Nakajima, K., Ohfuchi, W., Takahashi, Y.O., Hayashi, Y.Y., Nakamura, H., Ishiwatari, M., McGregor, J.L. and Borth, H., 2012. The APE atlas.
- [140] Zhou, S., Miller, A.J., Wang, J. and Angell, J.K., 2002. Downward-propagating temperature anomalies in the preconditioned polar stratosphere. *Journal of climate*, 15(7), pp.781-792.

Appendix A

Atmospheric equations

A.1 Equations of motion

The equations of motion for an atmosphere in hydrostatic equilibrium are, in horizontal Cartesian and vertical pressure coordinates:

$$\frac{du}{dt} - fv + \frac{\partial \Phi}{\partial x} = \mathcal{F}_x \quad (\text{A.1.1})$$

$$\frac{dv}{dt} + fu + \frac{\partial \Phi}{\partial y} = \mathcal{F}_y \quad (\text{A.1.2})$$

$$\frac{d\Phi}{dp} = -\frac{1}{\rho} \quad (\text{A.1.3})$$

$$\frac{\partial u}{\partial x} + \frac{\partial v}{\partial y} + \frac{\partial \omega}{\partial p} = 0 \quad (\text{A.1.4})$$

$$p = \rho R_d T \quad (\text{A.1.5})$$

$$\frac{d\theta}{dt} = Q \quad (\text{A.1.6})$$

$$\frac{dq}{dt} = E - P \quad (\text{A.1.7})$$

where u , v and ω are the zonal, meridional, and vertical wind components, respectively, f is the Coriolis parameter, Φ is the geopotential height, \mathcal{F}_x and \mathcal{F}_y are the zonal and meridional components of friction, respectively, ρ is the density, R_d is the specific gas constant for dry air,

θ is the potential temperature, defined by:

$$\theta = T \left(\frac{p}{p_0} \right)^{-R_d/c_p} \quad (\text{A.1.8})$$

where p_0 is a reference pressure, set to 1000hPa, c_p is the specific heat capacity of dry air at constant pressure for standard temperature, Q is the diabatic heating rate, q is the specific humidity, and E and P are the evaporation and precipitation rates, respectively. The material derivative, $\frac{d}{dt}$, is defined by:

$$\frac{d}{dt} = \frac{\partial}{\partial t} + u \frac{\partial}{\partial x} + v \frac{\partial}{\partial y} + \omega \frac{\partial}{\partial p} \quad (\text{A.1.9})$$

and describes the rate of change of any given quantity following a fluid parcel. The first two equations express horizontal momentum conservation, and are known as the momentum equations, the third is the hydrostatic pressure equation, the fourth is the continuity equation, expressing conservation of mass, the fifth is the ideal gas equation for the atmosphere, and the sixth and seventh equations express conservation of heat and water vapour, respectively.

A.2 Geostrophic wind

When the atmosphere is in equilibrium, such that $\frac{du}{dt} = \frac{dv}{dt} = 0$, and neglecting friction, the momentum equations simplify to give geostrophic balance:

$$v_g = \frac{1}{f} \frac{\partial \Phi}{\partial x} \quad (\text{A.2.1})$$

$$u_g = -\frac{1}{f} \frac{\partial \Phi}{\partial y} \quad (\text{A.2.2})$$

Taking the vertical derivative, and combining with the hydrostatic pressure and ideal gas equations gives the thermal wind-shear equations:

$$\frac{\partial v_g}{\partial p} = \frac{1}{f} \frac{\partial^2 \Phi}{\partial x \partial p} = -\frac{R_d}{pf} \frac{\partial T}{\partial x} = -\frac{R_d}{pf} \frac{\partial \theta}{\partial x} \quad (\text{A.2.3})$$

$$\frac{\partial u_g}{\partial p} = -\frac{1}{f} \frac{\partial^2 \Phi}{\partial y \partial p} = \frac{R_d}{pf} \frac{\partial T}{\partial y} = \frac{R_d}{pf} \frac{\partial \theta}{\partial y} \quad (\text{A.2.4})$$

A.3 Relationships between PV meridional gradient & EP flux divergence

Under the assumption that $[v^* \theta^*] = -\kappa_\theta \partial_y [\theta]$, where κ_θ is some constant - i.e. that the meridional eddy heat fluxes are downgradient - and given the thermal wind relation, equation

(2.1.11), $[q]_{\phi,p}$ and $\frac{dF^p}{dp}$ can be directly related as:

$$\begin{aligned} [q]_{\phi,p} &= \frac{Rf}{R_d} \frac{\partial}{\partial p} \left(\frac{p[\theta]}{[T]} \frac{f \partial_p [u]}{\partial_p [\theta]} \right) = \frac{Rf}{R_d} \frac{\partial}{\partial p} \left(\frac{p[\theta]}{[T]} \frac{\partial_y [\theta]}{\rho[\theta] \partial_p [\theta]} \right) = \frac{Rf}{R_d} \frac{\partial}{\partial p} \left(\frac{\rho R_d [T]}{[T]} \frac{\partial_y [\theta]}{\rho \partial_p [\theta]} \right) \\ &= Rf \frac{\partial}{\partial p} \left(\frac{\partial_y [\theta]}{\partial_p [\theta]} \right) \quad (\text{A.3.1}) \end{aligned}$$

$$\frac{dF^p}{dp} = Rf \cos \phi \frac{\partial}{\partial p} \left(\frac{[v^* \theta^*]}{\partial_p [\theta]} \right) = -\kappa_\theta Rf \cos \phi \frac{\partial}{\partial p} \left(\frac{\partial_y [\theta]}{\partial_p [\theta]} \right) = -[q]_{\phi,p} \kappa_\theta \cos \phi \quad (\text{A.3.2})$$

Similarly, under the assumption of downgradient meridional potential vorticity eddy fluxes, $[v^* q^*] = -\kappa_q \partial_y [q]$ where κ_q is another constant, and using the fact that $\nabla \cdot \mathbf{F} = [v^* q^*]$, we can construct a relationship between q_ϕ and $\nabla \cdot \mathbf{F}$ as follows:

$$\nabla \cdot \mathbf{F} = [v^* q^*] = -\kappa_q \partial_\phi [q] = -\kappa_q [q]_{\phi,\beta} - \kappa_q [q]_{\phi,y} - \kappa_q [q]_{\phi,p} \quad (\text{A.3.3})$$

At the same time, using equations (2.1.24) and (A.3.2), we arrive at another expression for $\nabla \cdot \mathbf{F}$:

$$\nabla \cdot \mathbf{F} \equiv \frac{dF^y}{dy} + \frac{dF^p}{dp} = \frac{dF^y}{dy} - [q]_{\phi,p} \kappa_\theta \cos \phi \quad (\text{A.3.4})$$

By considering changes in $\nabla \cdot \mathbf{F}$ instead of its absolute value, we eliminate the 1st term on the RHS of equation (A.3.3). Then, under the assumption that $\kappa_q = \kappa_\theta \cos \phi$, we can combine equations (A.3.3) and (A.3.4) to arrive at an expression for changes in the horizontal EP flux component, $\frac{dF^y}{dy}$:

$$\Delta \frac{dF^y}{dy} = -\kappa_q \Delta [q]_{\phi,y} = -\kappa_\theta \cos \phi \Delta [q]_{\phi,y} \quad (\text{A.3.5})$$

Alternatively, we consider the case where the eddy momentum fluxes drive local changes in the zonal winds, such that $\Delta [u] = -\kappa_u \Delta \partial_y [u^* v^*] = \kappa_u R \Delta \partial_y F^y$. This is the case in the midlatitude upper troposphere. Now consider a local positive/negative zonal wind anomaly. It would create a positive/negative meridional zonal wind gradient anomaly on its equatorward flank, and a negative/positive anomaly on its poleward flank. This would therefore result in a negative/positive meridional zonal wind curvature anomaly in the neighborhood of the positive/negative zonal wind anomaly, so that $\partial_{yy}^2 [u] \propto -\Delta [u]$, and we would arrive at the following equation for the changes in the 2nd component of meridional PV gradient, $\Delta [q]_{\phi,y}$:

$$\Delta [q]_{\phi,y} = -R \Delta \partial_{yy}^2 [u] \propto \Delta [u] = \kappa_u R \Delta \partial_y F^y \quad (\text{A.3.6})$$

Appendix B

Oceanic equations

B.1 Fundamental equations

The momentum, hydrostatic and continuity equations take fundamentally the same form when applied to the ocean as when applied to the atmosphere. However, it is best in this instance to work with height, z , rather than pressure, p , as the vertical coordinate. Moreover, the frictional force \mathbf{F} felt over the mixed layer is proportional to the surface wind stress exerted on it by the atmosphere above, τ , as per:

$$\mathbf{F} = (\mathcal{F}_x, \mathcal{F}_y) = \frac{1}{\rho} \left(\frac{\partial \tau_x}{\partial z}, \frac{\partial \tau_y}{\partial z} \right) = \frac{1}{\rho} \tau \quad (\text{B.1.1})$$

Thus, the momentum, hydrostatic and continuity equations become:

$$\frac{d\mathbf{u}}{dt} + f\hat{k} \times \mathbf{u} = -\frac{1}{\rho} \left(\nabla_{\mathbf{H}} p - \frac{\partial \tau}{\partial z} \right) \quad (\text{B.1.2})$$

$$\frac{dp}{dz} = -\rho g \quad (\text{B.1.3})$$

$$\nabla_{\mathbf{H}} \cdot \mathbf{u} + \frac{\partial w}{\partial z} = 0 \quad (\text{B.1.4})$$

where we have combined the zonal and meridional velocity components into the horizontal velocity vector $\mathbf{u} = (u, v)$, and we take $\nabla_{\mathbf{H}}$ to mean the horizontal gradient operator, $\nabla_{\mathbf{H}} = \left(\frac{\partial}{\partial x}, \frac{\partial}{\partial y} \right)$. Whilst the atmosphere has an approximate equation of state in the ideal gas law, the ocean does not have an equivalent equation. In its case, density is a complex function of temperature, T , salinity, S , and pressure, p , with no analytical form; the best we have are complicated empirical formulae. Thus, we suffice with the following equation of state for the ocean:

$$\rho = \rho(T, S, p) \quad (\text{B.1.5})$$

Lastly, we have the conservation laws expressing conservation of heat energy and salinity. These take the following form:

$$\frac{d\theta}{dt} = Q \quad (\text{B.1.6})$$

$$\frac{dS}{dt} = 0 \quad (\text{B.1.7})$$

$$\theta(z) = T(z) - \int_{p_0}^{p(z)} \left(\frac{dT}{dp'} \right)_{ad} dp' \quad (\text{B.1.8})$$

Appendix C

Third-party works & permissions

Page No.	Type of work:	Name of work	Source of work	Copyright holder and contact	Permission requested on	I have permission yes /no	Permission note
32	Figure	Figure 1.1.1	Thompson et al. 2011	© American Meteorological Society	26.05.21	Yes	Written permission
33	Figure	Figure 1.1.2	Polvani et al. 2011	© American Meteorological Society	26.05.21	Yes	Written permission
36	Figure	Figure 1.1.3	Haigh et al. 2005	© American Meteorological Society	26.05.21	Yes	Written permission
39	Figure	Figure 1.1.4	Simpson et al. 2009	© American Meteorological Society	26.05.21	Yes	Written permission
41	Figure	Figure 1.2.1	Bjerknes et al. 1966	Tellus	n/a	Yes	Open Access article distributed under the terms of the Creative Commons Attribution License
42	Figure	Figure 1.2.2	Hoskins & Karoly 1981	© American Meteorological Society	26.05.21	Yes	Written permission
43	Figure	Figure 1.2.3	Hou 1998	© American Meteorological Society	26.05.21	Yes	Written permission
45	Figure	Figure 1.2.4	Kushnir et al. 2002	© American Meteorological Society	26.05.21	Yes	Written permission
47	Figure	Figure 1.2.5	Nakamura et al. 2004	Wiley Books	08.06.21	Yes	Electronic permission obtained via RightsLink, https://s100.copyright.com/
48	Figure	Figure 1.2.6	Minobe et al. 2008	Nature	27.05.21	Yes	Electronic permission obtained via RightsLink, https://s100.copyright.com/
51	Figure	Figure 1.3.1	Ferreira et al. 2015	© American Meteorological Society	08.06.21	Yes	Written permission
63	Figure	Figure 2.3.1	Williamson et al. 2012	Williamson, D. L. and Coauthors	n/a	Yes	Licensed under a Creative Commons Attribution NonCommercial 4.0 International License.
64	Figure	Figure 2.3.2	Williamson et al. 2012	D.L. Williamson and Coauthors	n/a	Yes	Licensed under a Creative Commons Attribution NonCommercial 4.0 International License.
65	Figure	Figure 2.4.1	Adcroft et al. 2018	A. Adcroft and Coauthors	n/a	Yes	Licensed under a Creative Commons Attribution 3.0 United States

66	Figure	Figure 2.4.2	Adcroft et al. 2018	A. Adcroft and Coauthors	n/a	Yes	Licensed under a Creative Commons Attribution 3.0 United States
74	Figure	Figure 2.5.1	John Marshall's personal webpages at www.oceans.mit.edu	John Marshall	08.06.21	Yes	Written permission